AD_____

Award Number: W81XWH-06-1-0484

TITLE: Simulations to Evaluate Accuracy and Patient Dose in Neutron-Stimulated, Emission-Computed Tomography (NSECT) for Diagnosis of Breast Cancer

PRINCIPAL INVESTIGATOR: Anuj J. Kapadia

CONTRACTING ORGANIZATION: Duke University
Durham, NC 27708

REPORT DATE: April 2009

TYPE OF REPORT: Annual Summary

PREPARED FOR: U.S. Army Medical Research and Materiel Command
Fort Detrick, Maryland 21702-5012

# REPORT DOCUMENTATION PAGE

*Form Approved*
*OMB No. 0704-0188*



| 1. REPORT DATE | 2. REPORT TYPE | 3. DATES COVERED |
|---|---|---|
| 01-04-2009 | Annual Summary | 31 Mar 2006 – 30 Mar 2009 |

**4. TITLE AND SUBTITLE**

Simulations to Evaluate Accuracy and Patient Dose in Neutron-Stimulated, Emission-Computed Tomography (NSECT) for Diagnosis of Breast Cancer

**5a. CONTRACT NUMBER**

**5b. GRANT NUMBER**
W81XWH-06-1-0484

**5c. PROGRAM ELEMENT NUMBER**

**6. AUTHOR(S)**

Anuj J. Kapadia

Email: anuj.kapadia@duke.edu

**5d. PROJECT NUMBER**

**5e. TASK NUMBER**

**5f. WORK UNIT NUMBER**

**7. PERFORMING ORGANIZATION NAME(S) AND ADDRESS(ES)**

Duke University
Durham, NC 27708

**8. PERFORMING ORGANIZATION REPORT NUMBER**

**9. SPONSORING / MONITORING AGENCY NAME(S) AND ADDRESS(ES)**
U.S. Army Medical Research and Materiel Command
Fort Detrick, Maryland 21702-5012

**10. SPONSOR/MONITOR'S ACRONYM(S)**

**11. SPONSOR/MONITOR'S REPORT NUMBER(S)**

**12. DISTRIBUTION / AVAILABILITY STATEMENT**
Approved for Public Release; Distribution Unlimited

**13. SUPPLEMENTARY NOTES**
Original contains colored plates: ALL DTIC reproductions will be in black and white.

**14. ABSTRACT** We have developed a new tomographic technique called Neutron Stimulated Emission Computed Tomography (NSECT) for early detection of breast cancer. NSECT is sensitive to metabolic changes in trace element concentrations that are seen in tumors at very early stages of development. Detecting and measuring these element concentrations has the potential to detectbreast cancer very early. While the use of neutrons as the imaging radiation leads to concerns about radiation dose, preliminary experiments suggest that it may be possible to perform NSECT scans with dose levels comparable to mammography. A key aspect of successful clinical translation is to deliver the minimum dose possible. This project aims at evaluating the effects of NSECT dose-reduction techniques on the accuracy of detecting breast cancer. Four dose-reduction techniques are under evaluation: reduction of – neutron flux; spatial projections; angular positions; and the use of multiple detectors. As separate evaluation of each factor using experimental studies is prohibitively time consuming, we have investigated each effect using Monte-Carlo simulations as an alternative. We developed a Monte-Carlo simulation of the NSECT tomographic scanning system in GEANT4 and designed phantoms of benign and malignant breast tissue. The simulation was tested and validated against experimentally acquired data from several different types of phantoms. After successful validation, the simulation was used to generate spectral data from NSECT scans of the benign and malignant breast and obtain an estimate of the radiation dose. Tomographic images were then generated from a single-element disease model using a maximum-likelihood algorithm. Finally, weanalyzed the effects of the four dose-reduction techniques on system accuracy for both, nontomographic acquisitions and tomographic images. Based on the results, we identified an optimal acquisition strategy for each scanning method. The results demonstrate that NSECT has the ability to detect cancer-marking elements in the breast at reasonable levels of patient dose as well as differentiate benign and malignant tissue.

**15. SUBJECT TERMS**
Neutron, spectroscopy, NSECT, breast, tomography, imaging, MLEM, Monte Carlo simulation, Geant4.

| 16. SECURITY CLASSIFICATION OF: | | | 17. LIMITATION OF ABSTRACT | 18. NUMBER OF PAGES | 19a. NAME OF RESPONSIBLE PERSON |
|---|---|---|---|---|---|
| a. REPORT | b. ABSTRACT | c. THIS PAGE | | | USAMRMC |
| U | U | U | UU | 199 | 19b. TELEPHONE NUMBER *(include area code)* |

## Table of Contents

## INTRODUCTION

Breast cancer is the leading type of cancer to affect women all over the world. In the United States alone, breast cancer is expected to account for 32% of all new cancer cases among women. The American Cancer Society has estimated that 184,450 new cases of breast cancer will be detected in 2008, and 40,930 of these will result in death [1]. Early detection has proved to be the most effective technique to increase survival rates for this disease. Screening x-ray mammography is presently the only FDA approved screening tool for early detection of breast cancer. While it has proved to be effective, screening mammography has several limitations in trying to detect masses and spiculations in mammograms. First, it requires that the mammograms have good contrast, which is often difficult to achieve in women with dense breasts. Second, it uses an anatomic approach in trying to identify abnormalities in mammograms, making it essential that the abnormality be developed enough to show masses and calcifications clearly. This development usually comes at advanced stages of tumor growth. Finally, it has limitations in classifying detected abnormalities as benign or malignant. Several artificial intelligence tools, developed to classify detected lesions as benign or malignant have been investigated, but none have been FDA approved yet. These tools, such as computer aided diagnosis (not to be confused with the FDA approved computer aided detection systems now available), make their decisions based on morphological features such as shape, size, texture, etc. While they are fairly effective in classifying a detected lesion as benign or malignant, their dependence on analyzing an already visible lesion reduces their decision-making ability for lesions in very early stages of development.

To overcome these limitations, we are developing a technique that is sensitive to metabolic changes seen in malignant tumors during very early developmental stages. Various experiments conducted on trace elements in the human body have shown that malignant tumors exhibit changes in trace elements concentrations during early stages of development [2-7]. Quantifying these element concentrations, such as those of rubidium, cesium, aluminum and antimony, could potentially enable diagnosis of breast cancer at very early stages much before the tumor grows large enough to be detected by existing imaging techniques.

### Principle

Our technique, called Neutron Stimulated Emission Computed Tomography (NSECT), uses a spectroscopic approach to analyze changes in element concentrations at molecular levels in breast tissue [8-10]. NSECT analyzes spectral information obtained from inelastic scattering between a neutron and a target atomic nucleus to identify the atom and determine its concentration in the tissue. Neutrons striking a stable atomic nucleus stimulate it to emit gamma radiation which is unique to that element. Measuring the energy and quantity of the emitted radiation allows direct determining of the emitting element concentration. Ratios of trace element concentrations detected can then be used to classify the tissue as benign or malignant. Our preliminary data suggests that this technique has great potential in developing into an effective screening tool for breast cancer diagnosis.

Using neutrons as the imaging radiation leads to significant concerns about patient dose. At the energies we propose neutrons are known to damage the body 10 times more than x-rays. Reducing patient dose is a critical task in making NSECT feasible as a diagnostic technique for breast cancer. Our preliminary experiments show that it is possible to achieve an effective patient dose of about 15 mSv, which is comparable to the typical dose from an abdominal CT scan. This is possible because though individual neutrons cause more tissue damage than x-rays, it takes an immensely smaller number of neutrons to create an NSECT image than x-rays to create a CT image. A primary objective of this project is to reduce dose further to allow NSECT to be easily accepted as a screening tool.

Reducing patient dose in NSECT will be accompanied by a reduction in detection accuracy. This project aims at evaluating the trade-offs between patient dose and accuracy in NSECT, for 4 proposed dose-reduction techniques, and determine the minimal values of patient dose for which accuracy in the system remains high enough to effectively diagnose breast cancer.

The 4 different techniques proposed for dose-reduction in NSECT are a) neutron flux reduction, b) reduction in projection spatial sampling, c) reduction in angular sampling (fewer angles), and d) using multiple detectors. The first 3 techniques will reduce dose by reducing the amount of radiation incident on the body, while using multiple detectors will extract maximum information from the incident radiation. It is very difficult to evaluate the effects of each of these techniques individually using experimental NSECT studies, as these studies, which are at present performed in a nuclear accelerator lab, are prohibitively time consuming. We propose to approach this experiment using Monte-Carlo simulations as an alternative.

**BODY**

**Task 1: Build a Monte Carlo simulation of the tomographic scanning system using GEANT4**
(Months 1-10)

a) Simulate neutron beam source with user-defined neutron flux and neutron beam width
b) Simulate gantry with user-defined spatial and angular beam sampling rates
c) Simulate 2 types of gamma detectors under consideration with user-defined radius, efficiency and location: bismuth germanate (BGO), and high-purity germanium (HPGe)

**Status:** This task has been completed exactly as proposed.

The first task of this project is to develop a simulation tool to model the interactions between incoming neutrons and atomic nuclei as a practical alternative to evaluate the effects of dose-reduction techniques on detection accuracy. This is performed using stochastic modeling methods in GEANT4, a high-energy-physics object-oriented Monte-Carlo programming toolkit for simulating the passage of particles through matter. Developed by a worldwide collaboration of about 100 scientists in Europe, Russia, Japan, Canada and the United States, GEANT4 accounts for all the diverse interactions of particles with matter across a wide energy range. It incorporates a powerful set of random number generators, physics units and constants, and provides all the tools required for detector simulation, including geometry, tracking, detector response management, visualization and user interface. Its programming package allows individual simulation of different types of user-defined "objects" such as neutron sources and detectors composed of a single element or a mixture of elements, which can be integrated into a single module separately through its object-oriented nature.

**Preliminary experimental model:** The simulation is based on the experimental model, which works as follows. A neutron, incident on a body, travels freely along its projected path until it collides with an atomic nucleus. If the neutron scatters inelastically with a target atomic nucleus, the nucleus gets excited into one of its quantized, higher-energy states. This excited nucleus then rapidly decays to a lower state, emitting a gamma ray photon, whose energy is equal to the difference between the two states. These non-overlapping energy states are well established and unique to each element and isotope. Detection and analysis of the emitted gamma ray spectrum enables identification of the target atom. An energy-sensitive gamma detector is used to capture the emitted gamma photons. Tomography is performed using the translate-rotate configuration, as in first generation CT scanners, by translating the beam horizontally through the entire sample length, then rotating the beam through a fixed angle and repeating the process. Tomographic reconstruction of these scanned projections yields a two-dimensional slice of element concentration and distribution in the sample. The translate-rotate geometry is appropriate for initial proof of concept studies using phantom, specimen or small animals. Once feasibility is demonstrated, other geometries can be used in future clinical systems.

**Simulated Model:** The simulated model consists of 4 parts – (a) World, (b) Neutron Source, (c) Tomographic Gantry, and (d) Gamma Detectors. Each part has been designed as a separate GEANT4 object to facilitate modifying individual parameters on one object independently of the others.

(a) **World:** GEANT4 requires creation of a finite virtual space called the 'world', which acts as the world for the experiment. This world defines the virtual space within which the experiment will occur. All sources, detectors and samples are placed in the world. Particle interactions are tracked only as long as they occur in this world, and particles exiting the world are considered spent events. For this study, the world was defined as a cube with edge 1m, and filled with air.

(b) **Neutron Source:** The neutron source is created by defining a 'GEANT4 Particle Gun', with user defined options for particle type and energy. For breast studies, the incident particles are set to 2.5 MeV neutrons. The gun is placed at the left edge of the world so that every particle exiting the gun enters directly into the world to form a neutron beam. The exit position of the particle from the gun is given a user-defined width, which determines the width of the emitted neutron beam. GEANT4 processes each neutron as an individual event instead of a beam. Hence to create a beam with a finite width, a random number generator is used to select the point of emission of the individual neutron within a certain distance about the center of the gun. This distance about the gun center forms the

beam width of the emitted neutron beam. For this experiment, the beam-width was set at 1cm. The result of the GEANT4 'source' object is a collection of individual neutron events distributed randomly within a 1cm width about the gun-center, forming a 2.5 MeV neutron beam with a 1cm user-defined width.

(c) **Tomographic Gantry:** Tomography in NSECT is currently performed in a manner similar to first generation CT with a stationary beam and single element detector. The phantom is translated through the beam, then rotated through a finite angle and translated through the beam again. In the simulation, this translation-rotation is facilitated by the tomographic gantry. The tomographic gantry is designed by creating a gantry chamber within the world, filling it with the same material as the world (air), and placing it in the center of the world. The chamber can be rotated to any angle from 0-180 degrees in clockwise or anticlockwise direction, and can be moved to any desired xyz lateral position within the world. The user defines the number of translation and rotation positions along with the translation and rotation increments. Once a phantom is created, it can simply be placed inside this gantry chamber, and the sample can then be rotated and translated along with the gantry using gantry parameters. Typical values for rotation and translation in breast study experiments are 15 lateral steps at 7mm intervals and 8 angles at 22.5 degree intervals.

(d) **Gamma Detectors:** Gamma detectors are created as solid cylinders with user-defined diameter and height. Each cylinder is filled with one of 2 detector materials:

(i) High-purity germanium, HPGe (density= 5.32 g/cm$^3$)

(ii) Bismuth Germanate, BGO (density= 7.13 g/cm$^3$, 67.1% Bi, 17.5% Ge, and 15.4% O).

The detector material is 'sensitized', i.e. defined to track particle interactions and record the energy deposited at each interaction. The detector can be placed at any location in the world. In the current configuration, the detector is modeled as a 9cm diameter cylinder with 8cm height, similar to the detectors used in the physical NSECT experiments. The detector is placed at a backward angle of 135 degrees in the beam plane, mimicking the position of the detector in the physical experiment where a backward angle is used to minimize damage to the detector from forward scattered neutrons. Detector efficiency is modeled by collecting information from all events occurring in the detector and then retaining only a required fraction of these events. For example, for a 60% efficient HPGe detector, 100% of events will be recorded, but only 60% of these will be used to generate spectral results.

Figure 1 shows an example of this geometry with the world housing the gamma detectors and the phantom. The target gantry is an invisible box around the ellipsoid breast phantom. The gun is an invisible source at the left edge of the figure, emitting neutrons (shown in blue) that illuminate the breast.

**Task 2: Build GEANT4 phantoms for benign and malignant breast tissue based on element concentrations reported in various experimental studies.** (Months 11-12)

**Status:** This task has been completed as proposed.

This task aims at designing GEANT4 phantoms of the benign and malignant breast, which will be scanned using the simulated NSECT system. Two sets of phantoms are designed for this study – (a) Breast Phantom (b) Dose Phantom.

(a) **Breast Phantom:** Breast phantoms are simulated in GEANT4 as ellipsoids of 10cm x 6 cm x 5cm height. The phantom is filled with benign or malignant breast tissue, which is classified on the basis of its elemental composition as shown in table 1 below. Apart from the regular elements found in human breast tissue, i.e. hydrogen, oxygen, carbon and nitrogen, the breast tissue models are given trace elements in concentrations corresponding to benign and malignant breast tissue as reported in [2-6, 11]. The density of breast tissue was defined as 0.93 g/cm$^3$.

(b) **Dose Phantom:** A separate phantom of the torso is designed to perform dose measurements. This phantom consists of the whole torso including the breast, and accounts for the larger anatomic structures encountered by a neutron beam when scanning a patient. The torso is modeled as a larger ellipsoid, 40cm x 30cm x 30 cm height, similar to a human torso. The breasts are modeled as hemispheres located on one edge of the torso. As neutron dose

depends primarily on the hydrogen content of tissue, the torso and breast regions are both filled with water to approximate the hydrogen content of the body. This phantom is sensitized to measure the energy deposited in it, which can then be converted to an absorbed dose equivalent. As energy measurements are made within the phantom, separate gamma detectors are not required.

| | Normal (%) | Malignant (%) |
|---|---|---|
| **Oxygen** | 61.429 | 61.429 |
| **Carbon** | 22.857 | 22.857 |
| **Hydrogen** | 12.649 | 12.510 |
| **Nitrogen** | 2.571 | 2.571 |
| **Chlorine** | 1.98E-2 | 2.15E-2 |
| **Sodium** | 1.85E-2 | 2E-2 |
| **Potassium** | 8.94E-2 | 1.96E-2 |
| **Iron** | 9.8E-3 | 7.85E-3 |
| **Calcium** | 8.29E-3 | 1.13E-2 |
| **Zinc** | 1.17E-3 | 1.14E-3 |
| **Bromine** | 7.07E-4 | 6.55E-4 |
| **Aluminum** | 6.67E-4 | 5.7E-4 |
| **Rubidium** | 5.98E-4 | 5.84E-4 |
| **Manganese** | 3.88E-5 | 3.16E-5 |
| **Cobalt** | 2.06E-5 | 1.98E-5 |
| **Cesium** | 3.27E-7 | 3.6E-7 |

Table 1: Breast tissue composition for normal and malignant models (from [12]). The percentages were calculated by first converting dry weights to wet weights.

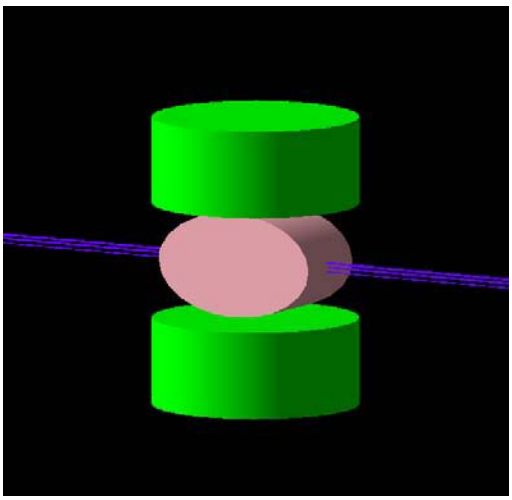

Figure 1. Breast phantom flanked by gamma detectors on either side. The black region represents the world, the pink region is the breast, and green cylinders correspond to gamma detectors. Neutrons passing through the breast are shown in blue.

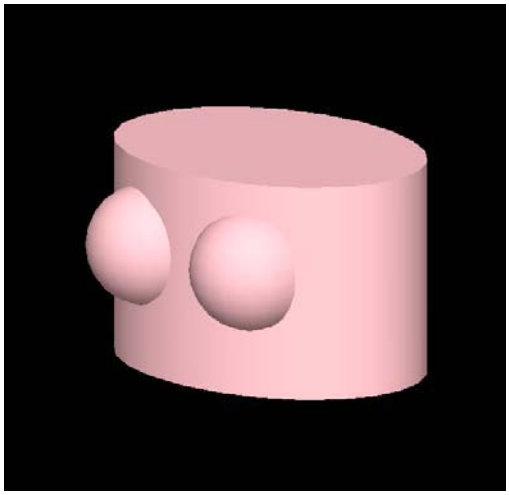

Figure 2. Dose phantom showing the torso and the relative position of the breasts. For dose estimation simulations, the torso and breasts are all filled with water. As dose is calculated by measuring the energy deposited in the torso and breasts, gamma detectors are not required.

**Task 3: Integrate simulations built in tasks 1 and 2 into a single module to allow simulation of a complete NSECT patient scan from patient irradiation to spectrum acquisition.** (Months 11-12)

**Status:** Completed as proposed.

GEANT4 is an object oriented programming package, which allows creation of each part as an individual object. This task integrates all the objects to create a complete simulation of the NSECT acquisition system. The phantoms created in Task 2 were integrated with the gantry created in Task 1. While GEANT4 contains libraries for a large number of high-energy physics interactions for a host of particles, it is left to the user to select which interactions to model for each application.

**Task 4: Determine element concentrations from simulated gamma spectra using spectral analysis and compare with pre-defined concentration levels in simulated phantom.** Months (13-15)

**Status:** Completed as proposed.

The breast phantom simulations built in tasks 1-3 were used to obtain quantitative estimates of the concentration differences in the benign and malignant breast. The results, described in [12] and corroborated by the experimental measurements in [9], demonstrated that with the currently available instrumentation hardware, NSECT has the detection sensitivity to identify concentration changes between benign and malignant tissue. Table 1 above shows the elemental composition of the normal and malignant breast tissue simulated in GEANT4. The corresponding gamma spectrum obtained for this sample is shown in Figure 3. As can be observed in the spectrum, statistically significant differences were observed primarily for three elements – $^{81}$Br, $^{87}$Rb and $^{133}$Cs. While several other elements were also observed in the gamma spectra, these three elements demonstrated maximum statistical detection accuracy for identifying malignant tissue.

Figure 4 shows experimentally acquired spectra from (a) benign and (b) malignant breast tissue specimens obtained from biopsy. The three elements noted above, $^{81}$Br, $^{87}$Rb and $^{133}$Cs, were observed to exhibit significant concentration differences between the two specimens, thereby confirming the results of the simulation experiments.

These two studies led to the publication of two manuscripts in peer-reviewed journals - references [9, 12].

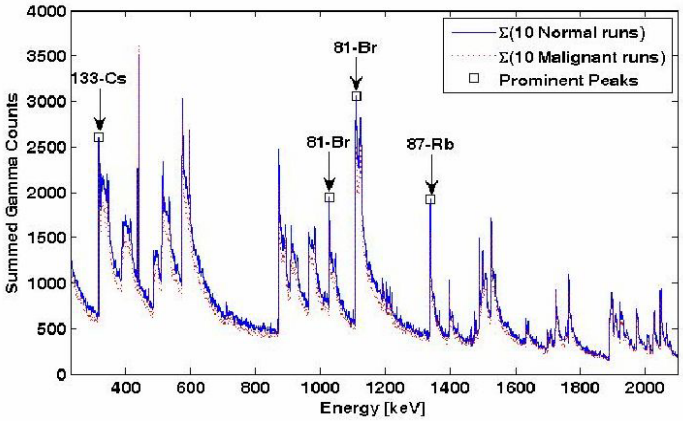


Figure 3. Gamma spectrum obtained from the simulated breast samples, normal and malignant, acquired with 10 million neutron events. Statistically significant differences were observed for three elements – $^{81}$Br, $^{87}$Rb and $^{133}$Cs. While several other elements were also observed in the gamma spectra, these three elements demonstrated maximum statistical detection accuracy. (Figure from [12]).

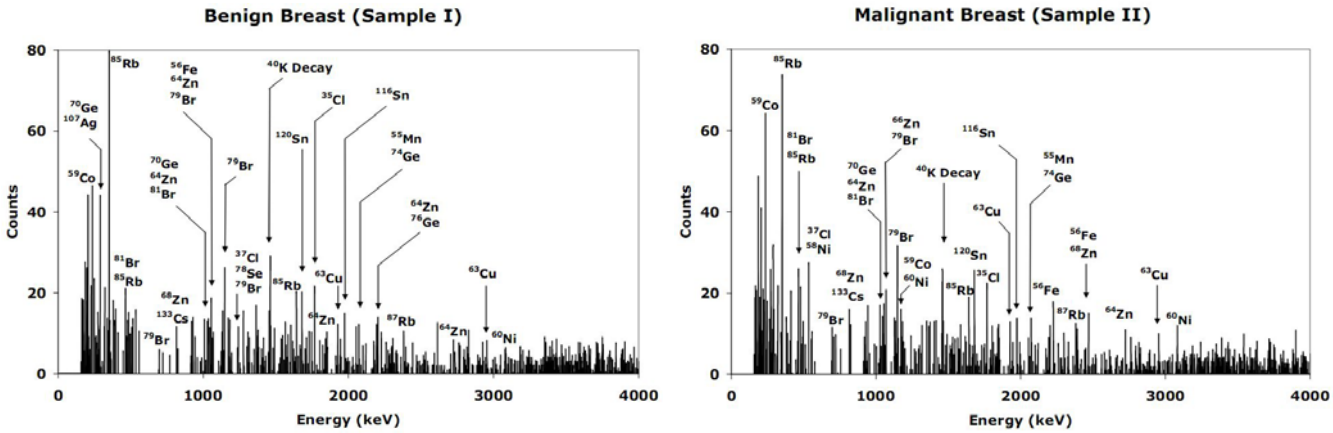


(a) Benign Breast (b) Malignant Breast

Figure 4. Gamma energy spectrum from (a) benign and (b) malignant breast samples showing energy peaks for several potential elements identified. Gamma peaks are seen for $^{72}$Ge and $^{74}$Ge from the germanium detector. Peaks with multiple potential element matches are labeled accordingly. Statistically significant differences are observed for the three elements observed in the simulated results– $^{81}$Br, $^{87}$Rb and $^{133}$Cs. (Figure from [9]).

The concentration differences observed in the breast spectra in Figures 3 and 4 showed variations in microgram quantities, which require an improvement in quantification accuracy for accurate detection of malignant tumors. In order to identify the detection limit and accuracy of NSECT, a single-element disease model was selected to allow the quantification process to be systematically performed by changing only a single variable. The disease model of choice was of iron-overload in the liver, chosen for two main reasons: (a) the disorder is characterized by changes of a single element (iron) in the diseased tissue, and (b) liver tissue has the same organ weighting factor as the breast (i.e. 0.5), thereby allowing the dose-evaluation experiments to be generally translated to the breast.

The liver model was simulated as shown in Figure 5, comprising a torso chamber, liver chamber and high iron-concentration lesions in the liver.

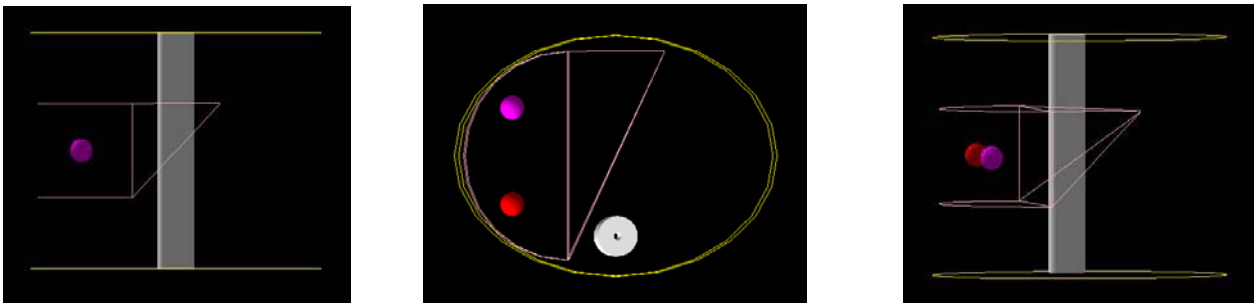

(a) Coronal Plane (b) Transverse Plane (c) Orthogonal view

Figure 5. GEANT4 simulation of the liver iron overload sample. The outline of the torso is marked by the yellow lines. The liver is shown as a pink outline with two high concentration spherical lesions inside. Each lesion contains a different concentration of iron. The spine is visible as a white cylindrical tube. (Figure from [13]).

The phantom was scanned with the simulation developed in Tasks 1-3 to generate a spectrum from iron as shown in Figure 6 below.

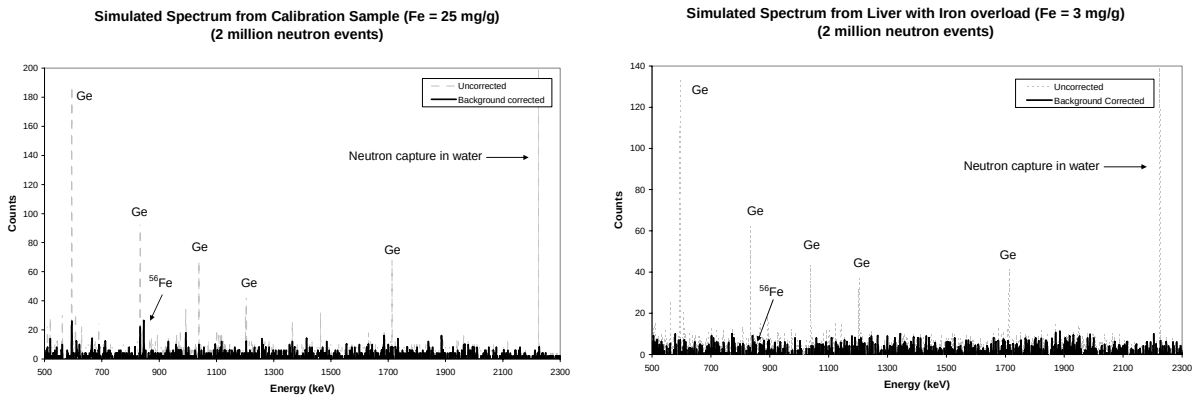


Figure 6. Simulated gamma spectrum from (a) calibration sample (Fe = 25 mg/g) and (b) liver with iron overload (Fe =3 mg/g) with background correction. The background corrected spectrum is shown as a solid black line while the original uncorrected spectrum appears as a gray dotted line. Peaks for germanium and neutron capture on hydrogen are significantly reduced through sample-out subtraction, while the signal peak from iron at 847 keV remains unchanged. (Figure from [13]).

Specialized algorithms were designed for spectral analysis and tested using experimental spectra from nuclear laboratory experiments. These algorithms were used for the following functions in spectral analysis and have been described in the references mentioned: (a) Scatter background Correction [9, 12, 14], (b) Energy peak identification [9, 12, 15], and (c) Compton Background Correction [9, 15].

The experiments performed in this task led to the publication of 4 peer-reviewed manuscripts [9, 12, 14, 16] and 3 conference proceedings [17-19].

**Task 5: Reconstruct tomographic images using MLEM reconstruction algorithms.** (Months 16-20)

**Status:** Completed as proposed.

Tomographic images were generated using the liver iron overload phantom described in Task 4 and reconstructed using a maximum likelihood expectation maximization (MLEM) algorithm for emission tomography with Poisson counting [20]. Reconstructed images are shown in Figure 7 below.

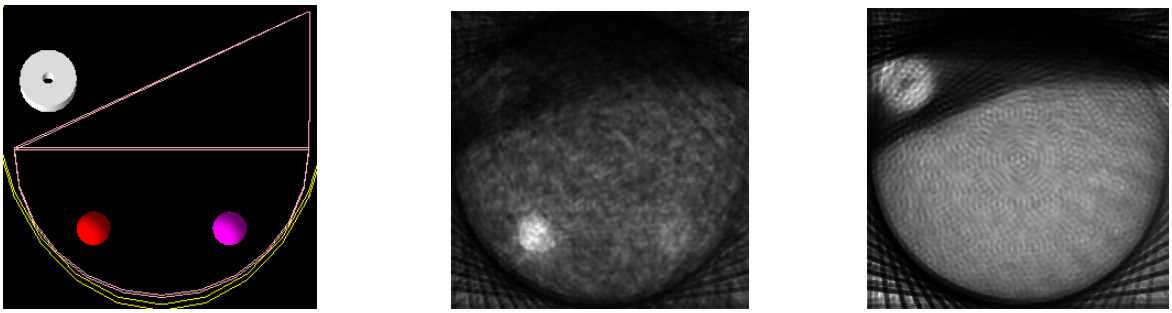

(a) Simulated sample (b) Reconstructed Image (iron) (c) Reconstructed image (carbon)

Figure 7. Comparison of the simulated liver iron overload sample with the corresponding reconstructed image for (b) iron and (c) carbon. The distribution of intensities in the reconstructed image is found to be in agreement with the distribution of iron and carbon in the original sample. (Figure from [13]).

The reconstruction algorithm was tested and validated against experimentally acquired data from a phantom of solid iron and solid copper, shown in Figure 8. The spectral acquisition in GEANT4 is shown in Figure 9.

(a) Physical Sample (b) Simulated Sample

Figure 8. Composite iron-copper tomographic sample used for validation of the MLEM reconstruction algorithm. The sample is made up of copper (outer, vertical bars) and iron (inner, diagonal bars) arranged like the letter N. Each bar measures 6mm in thickness, 60mm in height and 24mm in depth. The sample was simulated in GEANT 4 as shown in (b). (Figure from [13]).

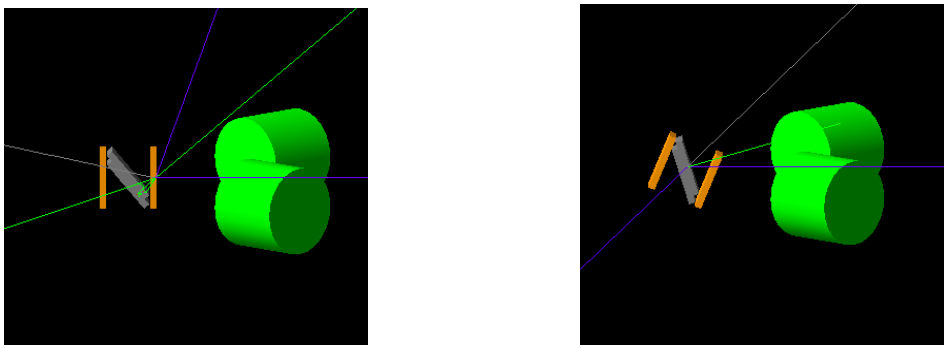

(a) Sample aligned at the initial position of zero degree (b) Sample rotated clockwise through 22.5 degrees

Figure 9. GEANT4 tomography simulation for the composite iron-copper tomographic sample. The two views show the sample rotated through 22.5 degrees. The orange bars correspond to copper, grey bars to iron, and the green cylinders show HPGe detectors. The blue lines correspond to incident and scattered neutrons while green lines correspond to gamma rays created through inelastic scatter. (Figure from [13]).

Figure 10 shows the corresponding images generated for the iron-copper sample. Figure 11 shows a line profile comparing the simulated and experimental data, validating the efficacy of the reconstruction algorithm.

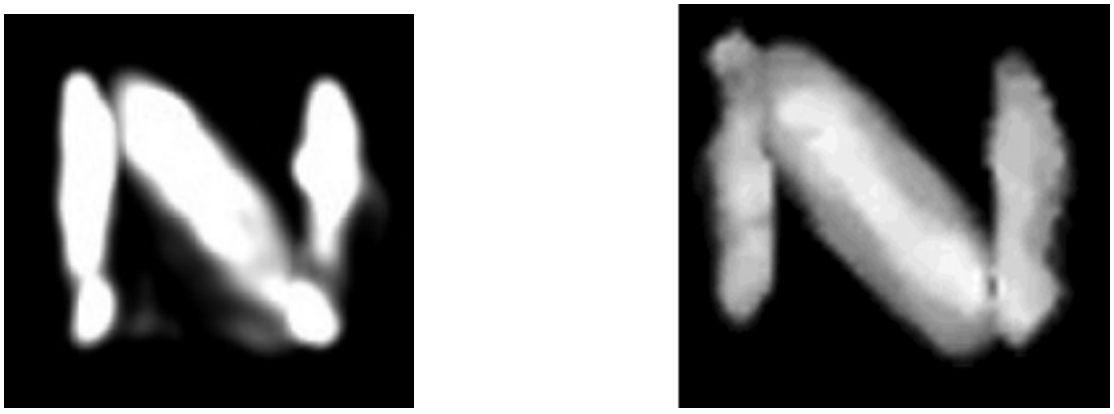

(a) Simulated (b) Experimental

Figure 10. Reconstructed images from simulated and experimental acquisition of the iron-copper sample. (Figures from [16, 21]).

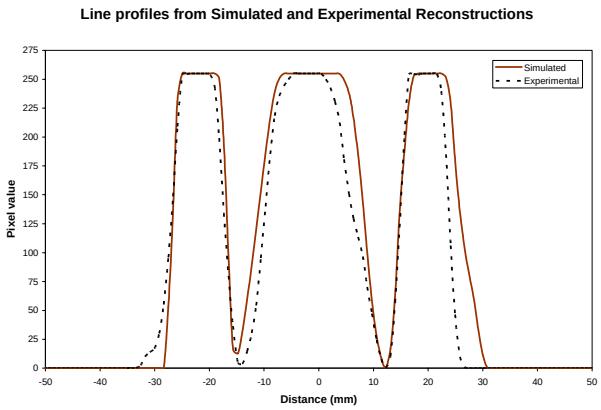


Figure 11. Line profile of the intensity distribution through the simulated and experimentally reconstructed images. At half max, the width of the left and right copper regions is seen to be 10 mm and 9 mm in the simulated image, and 9 mm and 8 mm in the experimental image. The width of iron is seen to be 18.5 mm in the simulated image and 17 mm in the experimental image. (Figure from [13]).

The experiments performed in this task led to the publication of 2 peer reviewed manuscripts [16, 21], a PhD thesis [13] and a book [22].

**Task 6: Evaluate simulation performance by comparing simulated gamma spectrum for multi-element control samples with experimental data from identical real samples.** (Months 21-36)

a) Evaluate and optimize detector performance to match experimental data.
b) Evaluate and optimize beam geometry and flux to match experimental acquisition.

**Status:** Completed as proposed.

The simulation developed and tested in tasks 1-5 was validated against experimentally obtained spectra from several single-element samples and multi-element samples. The different elements and the corresponding spectral images and figure numbers are listed below.

Figure 12: Thin iron sample. Figure 13: Composite sample: Fe + NaCl + KCl + $H_2O$. Figure 14: Mixed iron-copper sample. The experimental spectra for all samples were acquired using the neutron beam scanning facilities at the Triangle Universities Nuclear Laboratory (TUNL). All of the samples demonstrated excellent match between simulated and experimental spectra, with errors ranging from 3% to 15% for different element peaks.

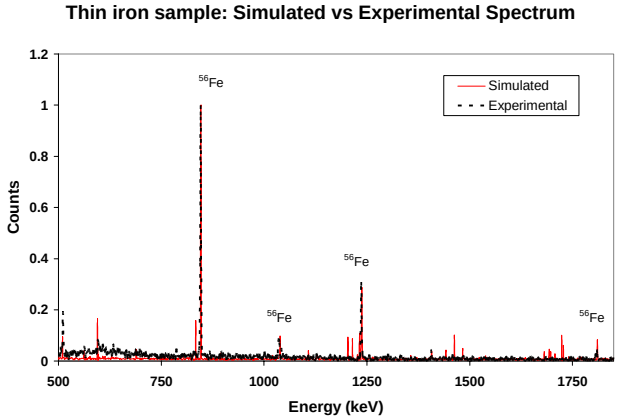


Figure 12. Comparison of simulated and experimental gamma spectra for a natural iron sample in air. The simulated spectrum is shown as a solid red line, while the experimental spectrum is depicted by an overlaid dotted black line. Energy peaks corresponding to the 4 most prominent excited states in $^{56}$Fe can be seen at 847 keV, 1039 keV, 1238 keV and 1811 keV.

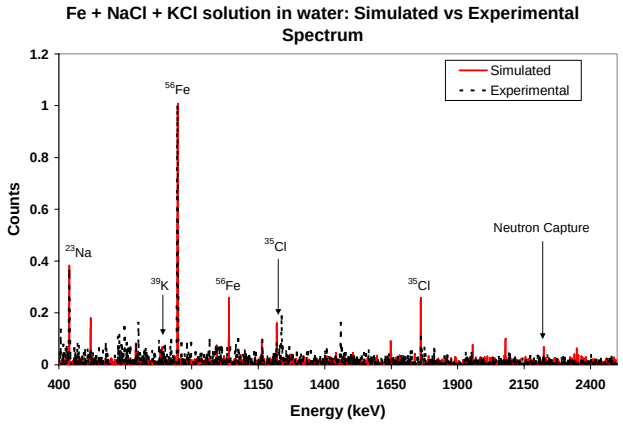


Figure 13. Comparison of simulated and experimental normalized gamma spectra for the Fe, NaCl and KCl composite sample. The simulated spectrum is shown as a solid red line, while the experimental spectrum is depicted by an overlaid dotted black line. Energy peaks corresponding to all 4 elements are seen in the spectra.

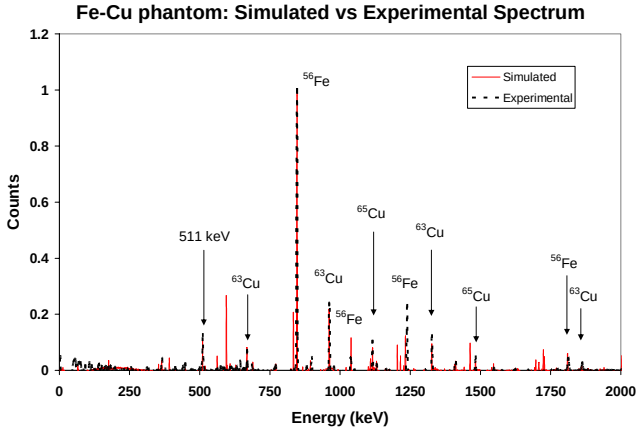


Figure 14. Comparison of simulated and experimental normalized gamma spectra for the iron-copper tomography sample. Gamma spectra from all projections are added to form this composite spectrum. The simulated spectrum is shown as a solid red line, while the experimental spectrum is depicted by an overlaid dotted black line. Energy peaks are identified for several gamma lines in both elements.

The experiments performed in this task led to the publication of 2 conference proceedings papers [17, 19], a PhD thesis [13] and a book [22].

**Task 7: Evaluate patient dose from the NSECT simulation software, considering cumulative neutron and gamma effects with appropriate quality factors for particle type (neutrons/gamma) and weighting factors for tissue type (breast).** (Months 21-36)

**Status:** Completed as proposed.

A dose calculation technique was developed and implemented to calculate the total radiation dose from cumulative neutron and gamma effects. This technique has been described in [16] and has been used to calculate patient dose for breast and liver scans as shown below.

The total energy deposited in the target organ (absorbed energy) was measured using the GEANT4 simulation. The absorbed energy was then converted to absorbed dose by factoring in the volume, mass and density of the organ. The absorbed dose was then converted to an equivalent dose by taking into account the radiation weighting factor for neutrons (10) and the organ weighting factor for the breast and liver (0.5 for both). An example of dose

calculation from [16] is shown in Table 2 below. For each of these experiments, the observed doses for liver and breast scans were well below 1 mSv.

| | Breast | Liver |
|---|---|---|
| **Energy absorbed** = number of neutrons × energy deposited | $1 \times 10^6$ neutrons × 3.74 MeV/ neutron × $1.6 \times 10^{-13}$ J $MeV^{-1}$ = **$5.98 \times 10^{-7}$ J** | $1 \times 10^6$ neutrons × 5.38 MeV/ neutron ∗ $1.6 \times 10^{-13}$ J $MeV^{-1}$ = **$8.61 \times 10^{-7}$ J** |
| Exposure volume | 10 $cm^3$ | 30 $cm^3$ |
| Density | 1.2 g $cm^{-3}$ | 1.2 g $cm^{-3}$ |
| Mass | 0.012 kg | 0.036 kg |
| **Absorbed dose** = energy absorbed per kg of exposed tissue | $5.98 \times 10^{-7}$J/0.012 kg = **$4.98 \times 10^{-5}$** Gray (J $kg^{-1}$) | $8.61 \times 10^{-7}$J/0.036 kg = **$2.39 \times 10^{-5}$** Gray (J $kg^{-1}$) |
| **Equivalent dose** = Absorbed Dose × particle weighting factor | $4.98 \times 10^{-5}$ Gray × 10 = **0.498 mSv** | $2.39 \times 10^{-5}$ Gray × 10 = **0.239 mSv** |

Table 2. Dose calculation for breast and liver scans (from [16]).

**Task 8: Evaluate efficacy of the system in differentiating benign and malignant tissue through ROC analysis.** (Months 24-36)
**Status:** Completed as proposed.

A simulation was developed to model human breast tissue containing tumors with two different disease states: benign (normal) and malignant. Element composition of the tumors was obtained from literature and has been shown above in Table 1. The benign and malignant phantoms were scanned with a simulated 2.5 MeV neutron beam and spectra were generated for each tissue phantom. Spectral analysis was performed to compare the detected differences between concentrations of 10 different gamma lines for 6 different levels of neutron fluence. ROC analysis was used to compare the detection efficacy, with the area under the curve (Az) used as the comparison metric. The results are shown in Table 3 below.

| | Millions of Incident Neutrons | | | | | |
|---|---|---|---|---|---|---|
| keV | 0.5 | 1 | 2 | 3 | 5 | 10 |
| 319 $^{133}Cs$ | 0.68±0.04 | 0.71±0.04 | 0.79±0.03 | 0.81±0.03 | **0.88±0.02** | **0.95±0.01** |
| 439 $^{59}Co$ | 0.54±0.04 | 0.58±0.04 | 0.58±0.04 | 0.64±0.04 | 0.61±0.04 | 0.67±0.04 |
| 1029 $^{81}Br$ | 0.60±0.04 | 0.65±0.04 | 0.79±0.03 | 0.83±0.03 | **0.87±0.02** | **0.97±0.01** |
| 1109 $^{81}Br$ | 0.66±0.04 | 0.81±0.03 | **0.89±0.02** | **0.91±0.02** | **0.95±0.02** | **0.99±0.01** |
| 1124 $^{79}Br$ | 0.63±0.04 | 0.67±0.04 | 0.67±0.04 | 0.67±0.04 | 0.81±0.03 | **0.89±0.02** |
| 1191 $^{79}Br$ | 0.57±0.04 | 0.57±0.04 | 0.58±0.04 | 0.64±0.04 | 0.64±0.04 | 0.74±0.03 |
| 1338 $^{87}Rb$ | 0.64±0.04 | 0.71±0.04 | 0.81±0.03 | **0.87±0.02** | **0.93±0.02** | **1.00** |
| 1476 $^{79}Br$ | 0.60±0.04 | 0.67±0.04 | 0.72±0.04 | 0.75±0.03 | 0.76±0.03 | 0.85±0.03 |
| 1697 $^{41}K$ | 0.52±0.04 | 0.49±0.04 | 0.50±0.04 | 0.56±0.04 | 0.58±0.04 | 0.66±0.04 |
| 2065 $^{67}Zn$ | 0.47±0.04 | 0.54±0.04 | 0.54±0.04 | 0.58±0.04 | 0.60±0.04 | 0.66±0.04 |

Table 3. Elements and corresponding average and standard error for ROC Az values obtained from ROCKIT software. The values in bold are above the significance threshold of Az = 0.85 and are considered statistically significant (from [12]).

The values in bold highlight gamma lines that satisfied the statistical significance condition (Az ≥ 0.85). Four elemental isotopes, $^{133}Cs$, $^{81}Br$, $^{79}Br$, and $^{87}Rb$, were found to have the best discriminatory power to differentiate normal from malignant tissue with neutron fluence values corresponding to clinically relevant dose levels. The study and corresponding results have been reported in [12].

The experiments performed in this task led to the publication of 1 peer reviewed manuscript [12], .

**Task 9: Investigate trade-offs between accuracy and dose.** (Months 26-36)
**Status:** Completed as proposed.

The tradeoffs between accuracy and dose were investigated using the simulated phantom shown in Figure 7. The phantom contained two lesions, each containing a different quantity of the element of interest – in this case $^{56}$Fe (natural iron). The phantom was scanned using 16 different acquisition geometries at 5 levels of neutron fluence, corresponding to a total of 80 different acquisition combinations. An image was reconstructed for each acquisition to obtain the pixel value within each lesion of interest. For each combination, the pixel values within each lesion were compared with the background to obtain an estimate of detection accuracy and compared with each other to obtain an estimate of quantification accuracy. Detection accuracy was analyzed by generating ROC curves for each combination of acquisition parameters, using the area under the curve (Az) as the comparison metric. Tables 4, 5 and 6 show the results from the study. For each combination of acquisition parameters, the patient radiation dose was calculated using the method described in Table 2. The results of dose calculation are shown in Table 7.

| Angular Positions | Spatial Positions | Incident neutrons | | | | |
|---|---|---|---|---|---|---|
| | | 500000 | 250000 | 125000 | 75000 | 25000 |
| 24 | 52 | 1.00 | 1.00 | 0.97 ± 0.03 | 1.00 | 0.97 ± 0.04 |
| | 51 | 1.00 | 1.00 | 1.00 | 1.00 | 0.91 ± 0.05 |
| | 26 | 1.00 | 0.98 ± 0.01 | 0.90 ± 0.04 | 0.91 ± 0.05 | 0.90 ± 0.04 |
| | 13 | 0.97 ± 0.01 | 0.97 ± 0.01 | 0.92 ± 0.03 | 0.90 ± 0.03 | 0.91 ± 0.05 |
| 12 | 52 | 1.00 | 0.95 ± 0.02 | 0.98 ± 0.01 | 0.91 ± 0.04 | 0.98 ± 0.01 |
| | 51 | 1.00 | 0.86 ± 0.04 | 0.97 ± 0.02 | 0.90 ± 0.03 | 0.97 ± 0.03 |
| | 26 | 1.00 | 0.85 ± 0.05 | 0.94 ± 0.04 | 0.92 ± 0.01 | 0.94 ±0.04 |
| | 13 | 0.97 ± 0.01 | 0.87 ± 0.04 | 0.85 ± 0.05 | 0.85 ± 0.03 | 0.86 ± 0.06 |
| 8 | 52 | 0.91 ± 0.03 | 0.95 ± 0.02 | 0.93 ± 0.03 | 0.89 ± 0.05 | 0.93 ± 0.05 |
| | 51 | 0.93 ± 0.02 | 0.88 ± 0.04 | 0.90 ±0.04 | 0.86 ± 0.04 | 0.91 ± 0.05 |
| | 26 | 0.93 ± 0.02 | 0.89 ± 0.06 | 0.88 ± 0.05 | 0.83 ± 0.05 | 0.85 ±0.06 |
| | 13 | 0.97 ± 0.02 | 0.90 ± 0.04 | 0.89 ± 0.03 | 0.84 ± 0.05 | 0.79 ± 0.07 |
| 6 | 52 | 0.90± 0.03 | 0.94 ± 0.01 | 0.86 ± 0.05 | 0.80 ± 0.04 | 0.86 ± 0.05 |
| | 51 | 0.98 ± 0.03 | 0.93 ± 0.03 | 0.80 ± 0.06 | 0.69 ± 0.05 | 0.63 ± 0.04 |
| | 26 | 0.99 ± 0.02 | 0.88 ± 0.04 | 0.77 ±0.05 | 0.62 ± 0.04 | 0.65 ± 0.05 |
| | 13 | 0.82 ± 0.05 | 0.89 ± 0.05 | 0.71 ± 0.04 | 0.60 ± 0.06 | 0.55 ± 0.06 |

Table 4. Results of ROC analysis for the 10 mg/g lesion compared with the background. The ROC values for Az and their standard errors are obtained from LABROC software. Values corresponding to acquisition parameter combinations that are below the detection threshold of Az = 0.85 are shown shaded in gray (from [13]).

| Angular Positions | Spatial Positions | Incident neutrons | | | |
|---|---|---|---|---|---|
| | | 50000 | 25000 | 15000 | 10000 |
| 24 | 26 | 0.91 ± 0.05 | 0.88 ± 0.05 | 0.82 ± 0.04 | 0.81 ± 0.04 |
| | 13 | 0.82 ± 0.04 | 0.83 ± 0.05 | 0.81 ± 0.04 | 0.79 ± 0.04 |
| 12 | 26 | 0.89 ± 0.05 | 0.82 ± 0.05 | 0.83 ± 0.04 | 0.79 ± 0.04 |
| | 13 | 0.81 ± 0.04 | 0.83 ± 0.04 | 0.76 ± 0.04 | 0.61 ± 0.04 |
| 8 | 26 | 0.86 ± 0.04 | 0.79 ± 0.04 | 0.77 ± 0.04 | 0.76 ± 0.05 |
| | 13 | 0.73 ± 0.05 | 0.66 ± 0.05 | 0.65 ± 0.05 | 0.66 ± 0.05 |
| 6 | 26 | 0.81 ± 0.05 | 0.80 ± 0.05 | 0.64 ± 0.05 | 0.51 ± 0.04 |
| | 13 | 0.72 ± 0.05 | 0.68 ± 0.05 | 0.65 ± 0.05 | 0.49 ± 0.04 |

Table 5. Results of ROC analysis for the 5 mg/g lesion compared with the normal liver background. The ROC values for Az and their standard errors are obtained from LABROC software. Values corresponding to acquisition parameter combinations that are below the detection threshold of Az = 0.85 are shown shaded in gray (from [13]).

| Angular Posn. | Spatial Posn. | Incident neutrons | | | | | | | | | |
|---|---|---|---|---|---|---|---|---|---|---|---|
| | | 500000 | | 250000 | | 125000 | | 75000 | | 25000 | |
| | | Value | Error | Value | Error | Value | Error | Value | Error | Value | Error |
| 24 | 52 | 1.86 | 0.07 | 1.77 | 0.12 | 1.92 | 0.04 | 1.81 | 0.10 | 1.46 | 0.27 |
| | 51 | 1.79 | 0.10 | 1.69 | 0.15 | 1.84 | 0.08 | 1.73 | 0.14 | 1.35 | 0.32 |
| | 26 | 1.78 | 0.11 | 1.69 | 0.16 | 1.87 | 0.06 | 1.70 | 0.15 | 1.32 | 0.34 |
| | 13 | 1.67 | 0.16 | 1.74 | 0.13 | 1.97 | 0.01 | 1.74 | 0.13 | 1.63 | 0.18 |
| 12 | 52 | 1.90 | 0.05 | 1.55 | 0.22 | 1.78 | 0.11 | 1.66 | 0.17 | 1.71 | 0.14 |
| | 51 | 1.86 | 0.07 | 1.52 | 0.24 | 1.75 | 0.12 | 1.65 | 0.17 | 1.54 | 0.23 |
| | 26 | 1.84 | 0.08 | 1.49 | 0.25 | 1.69 | 0.15 | 1.59 | 0.20 | 1.51 | 0.25 |
| | 13 | 1.69 | 0.15 | 1.42 | 0.29 | 1.49 | 0.26 | 1.37 | 0.32 | 1.68 | 0.16 |
| 8 | 52 | 1.55 | 0.22 | 1.24 | 0.38 | 1.25 | 0.38 | 0.90 | 0.55 | 0.96 | 0.52 |
| | 51 | 1.50 | 0.25 | 1.18 | 0.41 | 1.18 | 0.41 | 0.87 | 0.57 | 0.83 | 0.59 |
| | 26 | 1.50 | 0.25 | 1.16 | 0.42 | 1.18 | 0.41 | 0.82 | 0.59 | 0.80 | 0.60 |
| | 13 | 1.50 | 0.25 | 1.32 | 0.34 | 1.34 | 0.33 | 0.98 | 0.51 | 1.31 | 0.35 |
| 6 | 52 | 1.68 | 0.16 | 1.36 | 0.32 | 1.59 | 0.20 | 1.48 | 0.26 | 1.49 | 0.26 |
| | 51 | 1.64 | 0.18 | 1.33 | 0.34 | 1.62 | 0.19 | 1.53 | 0.23 | 1.48 | 0.26 |
| | 26 | 1.65 | 0.18 | 1.35 | 0.32 | 1.52 | 0.24 | 1.38 | 0.31 | 1.29 | 0.35 |
| | 13 | 1.52 | 0.24 | 1.27 | 0.37 | 1.34 | 0.33 | 1.47 | 0.26 | 3.41 | 0.70 |

Table 6. Ratio of pixel values within the 10 mg/g and 20 mg/g lesions. The first column shows the ratio of pixel values while the second shaded column shows their difference from the expected value of 2 (from [13]).

| Angular Positions | Spatial Positions | Projections | Neutrons per projection | Total neutron fluence | Dose |
|---|---|---|---|---|---|
| 24 | 26 | 624 | 4.12E+06 | 2.57E+09 | 1.6 mSv |
| 24 | 26 | 624 | 2.06E+06 | 1.29E+09 | 0.84 mSv |
| 12 | 26 | 312 | 4.12E+06 | 1.29E+09 | 0.84 mSv |
| 8 | 26 | 208 | 4.12E+06 | 8.57E+08 | 0.56 mSv |

Table 7. Dose values for different combinations of acquisition parameters (from [13]).

The study highlighted that out of the 90 combinations analyzed through ROC analysis, only four combinations were able to detect a 5 mg/g lesion with Az > 0.85. The combination with 8 angles and 26 projections provided sufficient detection accuracy with minimum dose. Hence it was described as the optimal parameter combination to scan a 5 mg/g lesion inside a normal iron concentration of 0 mg/g iron.

The experiments performed in this task led to the publication of 2 conference proceedings papers [18, 23], a PhD thesis [13] and a book [22].

## KEY RESEARCH ACCOMPLISHMENTS

Through this project we have achieved the following:

- We have developed a simulation of the entire NSECT acquisition system in the GEANT4 environment. The simulation includes gamma detectors, phantoms for benign and malignant breast tissue, phantoms for liver iron overload, as well as a tomographic acquisition gantry. It provides a readily accessible research tool to continue system development and evaluation without the need for a dedicated neutron beam source. The simulation will facilitate easy optimization and customization of future clinical systems catered to specific hospital environments and applications.
- The GEANT4 simulation has been tested and validated against experimental data and is now ready to be used for further breast specimen evaluations.
- A reconstruction algorithm has been designed, tested and verified against experimental spectral data, and has been used to generate tomographic images of phantoms with liver iron-overload.
- Spectral data has been obtained from benign and malignant breast biopsy specimens as well as from several single-element and multi-element control phantoms for validation of the GEANT4 simulations.
- The principles of tomographic reconstruction have been demonstrated through experimental acquisition of a multi-element phantom containing copper and iron. This experiment represents the first of its kind – performing image reconstruction through neutron inelastic-scatter spectroscopy for medical applications.
- An experiment demonstrating clinical application of the device has been performed for iron-overload diagnosis. The experiment, which demonstrates the possibility of detecting clinically relevant quantities of iron in the body at an acceptable level of radiation dose, is the first of its nature.

The work performed in this grant has led to 24 publications in peer-reviewed journals, conference proceedings, books and book chapters (shown below). In addition, it has led to the completion of a Doctoral Thesis for the PI.

## REPORTABLE OUTCOMES

This project has resulted in the following 24 publications (peer reviewed journal papers, conference proceedings, books and book chapters, and a doctoral thesis; in chronological order). The name of the fellow (Kapadia) is boldfaced for emphasis.

1. Floyd CE, Bender JE, Sharma AC, **Kapadia AJ**, Xia JQ, Harrawood BP, Tourassi GD, Lo JY, Crowell AS, and Howell CR, "Introduction to neutron stimulated emission computed tomography," Physics in Medicine and Biology, vol. 51, pp. 3375-3390, 2006. (Featured in "Yearbook of Nuclear Medicine", 2006)
2. Floyd CE, Bender JE, Harrawood BP, Sharma AC, **Kapadia AJ**, Tourassi GD, Lo JY, and Howell CR, "Breast cancer diagnosis using Neutron Stimulated Emission Computed Tomography: Dose and Count requirements," *Proceedings of SPIE Symposium on Medical Imaging*, vol. 6142, pp. 597-603, 2006.
3. Bender JE, Floyd CE, Harrawood BP, **Kapadia AJ**, Sharma AC, and Jesneck JL, "The effect of detector resolution for quantitative analysis of neutron stimulated emission computed tomography," *Proceedings of SPIE Medical Imaging*, vol. 6142, pp. 1597-1605, 2006.
4. **Kapadia AJ**, Sharma AC, Tourassi GD, Bender JE, Howell CR, Crowell AS, Kiser MR, and Floyd CE, "Neutron Spectroscopy of Mouse Using Neutron Stimulated Emission Computed Tomography (NSECT)," *Proceedings of IEEE Nuclear Science Symposium, Medical Imaging Conference*, vol. 6, pp. 3546-3548, 2006.
5. **Kapadia AJ**, Sharma AC, Tourassi GD, Bender JE, Howell CR, Crowell AS, Kiser MR, and Floyd CE, "Neutron Stimulated Emission Computed Tomography (NSECT) for Early Detection of Breast

Cancer," *Proceedings of IEEE Nuclear Science Symposium, Medical Imaging Conference,* vol. 6, pp. 3928-3931, 2006.

6. **Kapadia AJ**, Sharma AC, Tourassi GD, Bender JE, Howell CR, Crowell AS, Kiser MR, and Floyd CE, "Non-Invasive Estimation of Potassium (39K) in Bovine Liver Using Neutron Stimulated Emission Computed Tomography (NSECT)," *Proceedings of IEEE Nuclear Science Symposium, Medical Imaging Conference,* vol. 4, pp. 2076-2078, 2006.
7. Sharma AC, Tourassi GD, **Kapadia AJ**, Harrawood BP, Bender JE, Crowell AS, Kiser MR, Howell CR, and Floyd CE, "Design and Construction of a Prototype Rotation Modulation Collimator for near-Field High-Energy Spectroscopic Gamma Imaging," *Proceedings of IEEE Nuclear Science Symposium, Medical Imaging Conference*, vol. 4, pp. 2021-2024, 2006.
8. Sharma AC, Tourassi GD, **Kapadia AJ**, Bender JE, Xia JQ, Harrawood BP, Crowell AS, Kiser MR, Howell CR, and Floyd CE, "Development of a High-Energy Gamma Camera for Use with NSECT Imaging of the Breast," *Proceedings of IEEE Nuclear Science Symposium, Medical Imaging Conference*, vol. 6, pp. 3925-3927, 2006.
9. Sharma AC, Floyd CE, Harrawood BP, Tourassi GD, **Kapadia AJ**, Bender JE, Lo JY, and Howell CR, "Rotating slat collimator design for high-energy near-field imaging," *Proceedings of SPIE Medical Imaging*, vol. 6142, pp. 405-413, 2006.
10. Floyd CE, Sharma AC, Bender JE, **Kapadia AJ**, Xia JQ, Harrawood BP, Tourassi GD, Lo JY, Kiser MR, Crowell AS, Pedroni RS, Macri RA, Tajima S, and Howell CR, "Neutron Stimulated Emission Computed Tomography: Background Corrections," Nuclear Instruments and Methods in Physics Research Section B, vol. 254, pp. 329-336, 2007.
11. Sharma AC, Tourassi GD, **Kapadia AJ**, Harrawood BP, Crowell AS, Kiser MR, Howell CR, and Floyd CE, "Design and Development of a High-Energy Gamma Camera for use with NSECT Imaging: Feasibility for Breast Imaging," IEEE Transactions on Nuclear Science, vol. 54, pp. 1498-1505, 2007.
12. Sharma AC, Harrawood BP, Bender JE, Tourassi GD, **Kapadia AJ**, "Neutron Stimulated Emission Computed Tomography: a Monte Carlo simulation approach," Physics in Medicine and Biology, vol. 52, pp. 6117-31, 2007. (Featured in Physics in Medicine and Biology Highlights of 2007)
13. Bender JE, **Kapadia AJ**, Sharma AC, Tourassi GD, Harrawood BP, and Floyd CE, "Breast cancer detection using Neutron Stimulated Emission Computed Tomography: prominent elements and dose requirements," Medical Physics, vol. 34, pp. 3866-3871, 2007.
14. Sharma AC, Tourassi GD, **Kapadia AJ**, Crowell AS, Kiser MR, Hutcheson A, Harrawood BP, Howell CR, Floyd CE. "Elemental Spectrum of a Mouse Obtained via Neutron Stimulation." *Proceedings of SPIE Medical Imaging*, vol. 6510, 65100K, 2007.
15. **Kapadia AJ**, Harrawood BP, Tourassi GD, " A GEANT4 Simulation for Iron Overload Detection using NSECT," *Proceedings of IEEE Nuclear Science Symposium, Medical Imaging Conference,* vol. 6, pp 4604-4607, 2007.
16. Sharma AC, **Kapadia AJ**, Harrawood BP, Tourassi GD, "Optimization of a Rotating Modulation Collimator for NSECT imaging," *Proceedings of IEEE Nuclear Science Symposium, Medical Imaging Conference,* vol. 5, pp 3812-3815, 2007.
17. **Kapadia AJ**, Sharma AC, Bender JE, Tourassi GD, Howell CR, Crowell AS, Kiser MR, Harrawood BP, and Floyd CE, "Neutron Stimulated Emission Computed Tomography for Diagnosis of Breast Cancer," IEEE Transactions on Nuclear Science, vol. 55(1), pp .501-509, 2008.
18. Floyd CE, **Kapadia AJ**, Bender JE, Sharma AC, Xia JQ, Harrawood BP, Tourassi GD, Lo JY, Crowell AS, Kiser MR, and Howell CR, "Neutron Stimulated Emission Computed Tomography of a Multi-Element Phantom," Physics in Medicine and Biology, vol. 53, pp 2313-2326, 2008.

19. **Kapadia AJ**, Tourassi GD, Sharma AC, Crowell AS, Kiser MR, Howell CR, "Experimental detection of iron overload in liver through neutron stimulated emission spectroscopy," Physics in Medicine and Biology, vol 53, pp 2633-2649, 2008.
20. **Kapadia AJ**, Harrawood BP, Tourassi GD, "GEANT4 simulation of NSECT for detection of iron overload in the liver," *Proceedings of SPIE Medical Imaging*, vol. 6913, pp. 691309, 2008.
21. **Kapadia AJ**, Harrawood BP, Tourassi GD, "Validation of a GEANT4 simulation of neutron stimulated emission computed tomography," *Proceedings SPIE Medical Imaging*, vol. 6913, pp. 69133H, 2008.
22. **Kapadia AJ**, Gallmeier FX, Iverson EB, Ferguson PD, "Detection of Iron Overload with the ORNL Spallation Neutron Source: an MCNPX Simulation Study", *Proceedings of IEEE Nuclear Science Symposium, Medical Imaging Conference*, pp. 4972-4975, 2008.
23. **Kapadia AJ**, "Evaluation of Accuracy and Patient Dose in Neutron Stimulated Emission Computed Tomography using Simulations in GEANT4", VDM Verlag Publishing, ISBN: 978-3-639-10855-2, 2009.
24. **Kapadia AJ**, Agasthya GA, Tourassi GD, "Detection of Iron Overload through Neutron Stimulated Emission Computed Tomography: A Sensitivity Analysis Study", *Proceedings of SPIE Medical Imaging*, vol. 7258, pp. 725811, 2009.

## CONCLUSION

We have developed a working simulation of the NSECT acquisition system in GEANT4. The simulation was tested and validated against experimental data acquired using a neutron beam generated by a Van-de-Graaff accelerator source. The simulation was then used to demonstrate the efficacy of NSECT for biological applications, specifically, breast cancer detection and detection of iron in the liver. It provides a readily accessible research tool to continue system development and evaluation without the need for a dedicated neutron beam source. Further, the simulation will facilitate easy optimization and customization of NSECT clinical systems that can be catered to specific hospital environments and applications in the future.

We demonstrated the ability of NSECT to generate quantitative tomographic images of individual elements in multi-element phantoms including models of the human body. Results of the simulated iron quantification study showed that it was possible to detect a 5 mg/g lesion in the liver with sufficient detection and quantification accuracy with a radiation dose of less than 2 mSv.

The work performed in this project helped to pinpoint the next immediate research focus to continue development of NSECT for breast cancer diagnosis - the need for improvement in detection sensitivity. We are now focusing on developing methods to improve detection sensitivity as well as developing a portable prototype model of the NSECT device for use in a clinical environment.

Finally, through this grant, the PI was able to complete his PhD as well as a short post-doctoral position, and is now an Assistant Professor at Duke University. He is continuing the development of the NSECT technique for medical applications with an emphasis on early detection of breast cancer.

## REFERENCES


[1] ACS, "Cancer Facts and Figures 2008," American Cancer Society, Atlanta 2008.

[2] A. Garg, V. Singh, et al., "An elemental correlation study in cancerous and normal breast tissue with successive clinical stages by neutron activation analysis," *Biological Trace Element Research,* vol. 46, pp. 185-202, 1994 1994.

[3] H. Mussalo-Rauhamaa, S. Piepponen, J. Lehto, R. Kauppila, and O. Auvinen, "Cu, Zn, Se and Mg concentrations in breast fat of Finnish breast cancer patients and healthy controls," *Trace Elements in Medicine,* vol. 10, pp. 13-15, 1993.

[4] K.-H. Ng, D. Bradley, and L.-M. Looi, "Elevated trace element concentrations in malignant breast tissues," *British Journal of Radiology,* vol. 70, pp. 375-382, 1997.

[5] K.-H. Ng, S.-H. Ong, D. A. Bradley, and L.-M. Looi, "Discriminant analysis of normal and malignant breast tissue based upon INAA investigation of elemental concentration," *Appl. Radiat. Isot.,* vol. 48, pp. 105-109, 1997.

[6] S. Rizk and H. Sky-Peck, "Comparison between concentrations of trace elements in normal and neoplastic human breast tissue," *Cancer Research,* vol. 44, pp. 5390-5394, 1984.

[7] M. Yaman, D. Atici, S. Bakirdere, and I. Akdeniz, "Comparison of trace metal concentrations in malign and benign human prostate," *J. Med. Chem.,* vol. 48, pp. 630-634, 2005.

[8] C. E. Floyd, J. E. Bender, A. C. Sharma, A. J. Kapadia, J. Q. Xia, B. P. Harrawood, G. D. Tourassi, J. Y. Lo, A. S. Crowell, and C. R. Howell, "Introduction to neutron stimulated emission computed tomography," *Physics in Medicine and Biology,* vol. 51, pp. 3375-3390, 2006

[9] A. J. Kapadia, A. C. Sharma, J. E. Bender, G. D. Tourassi, C. R. Howell, A. S. Crowell, M. R. Kiser, B. P. Harrawood, and C. E. Floyd, "Neutron Stimulated Emission Computed Tomography for Diagnosis of Breast Cancer," *IEEE Trans Nuc Sci,* vol. 55, pp. 501 - 509, 2008.

[10] A. J. Kapadia, A. C. Sharma, G. D. Tourassi, J. E. Bender, A. S. Crowell, M. R. Kiser, C. R. Howell, and C. E. Floyd, "Neutron Stimulated Emission Computed Tomography (NSECT) for Early Detection of Breast Cancer," in *IEEE Nuclear Science Symposium, Medical Imaging Conference*, San Diego, CA, 2006, pp. 3928-3931.

[11] A. Schwartz and R. Fink, "Trace Elements in Normal and Malignant Human Breast Tissue," *Surgery,* vol. 76, pp. 325-329, 1974.

[12] J. E. Bender, A. J. Kapadia, A. C. Sharma, G. D. Tourassi, B. P. Harrawood, and C. E. Floyd, "Breast cancer detection using Neutron Stimulated Emission Computed Tomography: prominent elements and dose requirements," *Med Phys,* vol. 34, pp. 3866-3871, 2007.

[13] A. J. Kapadia, "Accuracy and Patient Dose in Neutron Stimulated Emission Computed Tomography for Diagnosis of Liver Iron Overload: Simulations in GEANT4," in *Biomedical Engineering*. vol. PhD Durham, NC: Duke University, 2007.

[14] C. E. Floyd, A. C. Sharma, J. E. Bender, A. J. Kapadia, J. Q. Xia, B. P. Harrawood, G. D. Tourassi, J. Y. Lo, M. R. Kiser, A. S. Crowell, R. S. Pedroni, R. A. Macri, S. Tajima, and C. R. Howell, "Neutron Stimulated Emission Computed Tomography: Background Corrections," *Nuclear Instruments and Methods in Physics Research Section B,* vol. 254, pp. 329 - 336, 2007.

[15] A. J. Kapadia, G. D. Tourassi, A. C. Sharma, A. S. Crowell, M. R. Kiser, and C. R. Howell, "Experimental detection of iron overload in liver through neutron stimulated emission spectroscopy," *Phys Med Biol,* vol. 53, pp. 2633-2649, 2008.

[16] A. C. Sharma, B. P. Harrawood, J. E. Bender, G. D. Tourassi, and A. J. Kapadia, "Neutron stimulated emission computed tomography: a Monte Carlo simulation approach," *Phys Med Biol,* vol. 52, pp. 6117-31, Oct 21 2007.

[17] A. J. Kapadia, B. P. Harrawood, and G. D. Tourassi, "Validation of a GEANT4 simulation of neutron stimulated emission computed tomography," in *SPIE Symposium on Medical Imaging*, San Diego, CA, 2008, p. 69133H.

[18] A. J. Kapadia, B. P. Harrawood, and G. D. Tourassi, "GEANT4 simulation of NSECT for detection of iron overload in the liver," in *SPIE Symposium on Medical Imaging*, San Diego, CA, 2008, p. 691309.

[19] A. J. Kapadia, A. C. Sharma, B. P. Harrawood, and G. D. Tourassi, "GEANT4 simulation of an NSECT system for iron overload detection," in *IEEE Nuclear Science Symposium, Medical Imaging Conference*, Honolulu, HI, 2007, pp. 4604 - 4607.
[20] K. Lange and R. Carson, "EM reconstruction Algorithms for Emission and Transmission Tomography," *Journal of Computer Assisted Tomography*, vol. 8, pp. 306-316, 1984.
[21] C. E. Floyd, A. J. Kapadia, J. E. Bender, A. C. Sharma, J. Q. Xia, B. P. Harrawood, G. D. Tourassi, J. Y. Lo, A. S. Crowell, M. R. Kiser, and C. R. Howell, "Neutron Stimulated Emission Computed Tomography of a Multi-Element Phantom," *Phys Med Biol*, vol. 53, pp. 2313-2326, 2008.
[22] A. J. Kapadia, *Accuracy and Dose in Neutron Stimulated Emission Computed Tomography: Simulations in GEANT4 (Paperback)*: VDM Verlag, 2008.
[23] A. J. Kapadia, G. A. Agasthya, and G. D. Tourassi, "Detection of iron overload through neutron stimulated emission computed tomography: a sensitivity analysis study," in *SPIE Symposium on Medical Imaging*, Orlando, FL, 2009, p. 725811.

## APPENDICES

1. Floyd CE, Bender JE, Sharma AC, **Kapadia AJ**, Xia JQ, Harrawood BP, Tourassi GD, Lo JY, Crowell AS, and Howell CR, "Introduction to neutron stimulated emission computed tomography," Physics in Medicine and Biology, vol. 51, pp. 3375-3390, 2006.
2. Floyd CE, Bender JE, Harrawood BP, Sharma AC, **Kapadia AJ**, Tourassi GD, Lo JY, and Howell CR, "Breast cancer diagnosis using Neutron Stimulated Emission Computed Tomography: Dose and Count requirements," *Proceedings of SPIE Symposium on Medical Imaging*, vol. 6142, pp. 597-603, 2006.
3. Bender JE, Floyd CE, Harrawood BP, **Kapadia AJ**, Sharma AC, and Jesneck JL, "The effect of detector resolution for quantitative analysis of neutron stimulated emission computed tomography," *Proceedings of SPIE Medical Imaging*, vol. 6142, pp. 1597-1605, 2006.
4. **Kapadia AJ**, Sharma AC, Tourassi GD, Bender JE, Howell CR, Crowell AS, Kiser MR, and Floyd CE, "Neutron Spectroscopy of Mouse Using Neutron Stimulated Emission Computed Tomography (NSECT)," *Proceedings of IEEE Nuclear Science Symposium, Medical Imaging Conference*, vol. 6, pp. 3546-3548, 2006.
5. **Kapadia AJ**, Sharma AC, Tourassi GD, Bender JE, Howell CR, Crowell AS, Kiser MR, and Floyd CE, "Neutron Stimulated Emission Computed Tomography (NSECT) for Early Detection of Breast Cancer," *Proceedings of IEEE Nuclear Science Symposium, Medical Imaging Conference*, vol. 6, pp. 3928-3931, 2006.
6. **Kapadia AJ**, Sharma AC, Tourassi GD, Bender JE, Howell CR, Crowell AS, Kiser MR, and Floyd CE, "Non-Invasive Estimation of Potassium (39K) in Bovine Liver Using Neutron Stimulated Emission Computed Tomography (NSECT)," *Proceedings of IEEE Nuclear Science Symposium, Medical Imaging Conference*, vol. 4, pp. 2076-2078, 2006.
7. Sharma AC, Tourassi GD, **Kapadia AJ**, Harrawood BP, Bender JE, Crowell AS, Kiser MR, Howell CR, and Floyd CE, "Design and Construction of a Prototype Rotation Modulation Collimator for near-Field High-Energy Spectroscopic Gamma Imaging," *Proceedings of IEEE Nuclear Science Symposium, Medical Imaging Conference*, vol. 4, pp. 2021-2024, 2006.
8. Sharma AC, Tourassi GD, **Kapadia AJ**, Bender JE, Xia JQ, Harrawood BP, Crowell AS, Kiser MR, Howell CR, and Floyd CE, "Development of a High-Energy Gamma Camera for Use with NSECT Imaging of the Breast," *Proceedings of IEEE Nuclear Science Symposium, Medical Imaging Conference*, vol. 6, pp. 3925-3927, 2006.

9. Sharma AC, Floyd CE, Harrawood BP, Tourassi GD, **Kapadia AJ**, Bender JE, Lo JY, and Howell CR, "Rotating slat collimator design for high-energy near-field imaging," *Proceedings of SPIE Medical Imaging*, vol. 6142, pp. 405-413, 2006.

10. Floyd CE, Sharma AC, Bender JE, **Kapadia AJ**, Xia JQ, Harrawood BP, Tourassi GD, Lo JY, Kiser MR, Crowell AS, Pedroni RS, Macri RA, Tajima S, and Howell CR, "Neutron Stimulated Emission Computed Tomography: Background Corrections," Nuclear Instruments and Methods in Physics Research Section B, vol. 254, pp. 329-336, 2007.

11. Sharma AC, Tourassi GD, **Kapadia AJ**, Harrawood BP, Crowell AS, Kiser MR, Howell CR, and Floyd CE, "Design and Development of a High-Energy Gamma Camera for use with NSECT Imaging: Feasibility for Breast Imaging," IEEE Transactions on Nuclear Science, vol. 54, pp. 1498-1505, 2007.

12. Sharma AC, Harrawood BP, Bender JE, Tourassi GD, **Kapadia AJ**, "Neutron Stimulated Emission Computed Tomography: a Monte Carlo simulation approach," Physics in Medicine and Biology, vol. 52, pp. 6117-31, 2007. (Featured in Physics in Medicine and Biology Highlights of 2007)

13. Bender JE, **Kapadia AJ**, Sharma AC, Tourassi GD, Harrawood BP, and Floyd CE, "Breast cancer detection using Neutron Stimulated Emission Computed Tomography: prominent elements and dose requirements," Medical Physics, vol. 34, pp. 3866-3871, 2007.

14. Sharma AC, Tourassi GD, **Kapadia AJ**, Crowell AS, Kiser MR, Hutcheson A, Harrawood BP, Howell CR, Floyd CE. "Elemental Spectrum of a Mouse Obtained via Neutron Stimulation." *Proceedings of SPIE Medical Imaging*, vol. 6510, 65100K, 2007.

15. **Kapadia AJ**, Harrawood BP, Tourassi GD, " A GEANT4 Simulation for Iron Overload Detection using NSECT," *Proceedings of IEEE Nuclear Science Symposium, Medical Imaging Conference*, vol. 6, pp 4604-4607, 2007.

16. Sharma AC, **Kapadia AJ**, Harrawood BP, Tourassi GD, "Optimization of a Rotating Modulation Collimator for NSECT imaging," *Proceedings of IEEE Nuclear Science Symposium, Medical Imaging Conference*, vol. 5, pp 3812-3815, 2007.

17. **Kapadia AJ**, Sharma AC, Bender JE, Tourassi GD, Howell CR, Crowell AS, Kiser MR, Harrawood BP, and Floyd CE, "Neutron Stimulated Emission Computed Tomography for Diagnosis of Breast Cancer," IEEE Transactions on Nuclear Science, vol. 55(1), pp .501-509, 2008.

18. Floyd CE, **Kapadia AJ**, Bender JE, Sharma AC, Xia JQ, Harrawood BP, Tourassi GD, Lo JY, Crowell AS, Kiser MR, and Howell CR, "Neutron Stimulated Emission Computed Tomography of a Multi-Element Phantom," Physics in Medicine and Biology, vol. 53, pp 2313-2326, 2008.

19. **Kapadia AJ**, Tourassi GD, Sharma AC, Crowell AS, Kiser MR, Howell CR, "Experimental detection of iron overload in liver through neutron stimulated emission spectroscopy," Physics in Medicine and Biology, vol 53, pp 2633-2649, 2008.

20. **Kapadia AJ**, Harrawood BP, Tourassi GD, "GEANT4 simulation of NSECT for detection of iron overload in the liver," *Proceedings of SPIE Medical Imaging*, vol. 6913, pp. 691309, 2008.

21. **Kapadia AJ**, Harrawood BP, Tourassi GD, "Validation of a GEANT4 simulation of neutron stimulated emission computed tomography," *Proceedings SPIE Medical Imaging*, vol. 6913, pp. 69133H, 2008.

22. **Kapadia AJ**, Gallmeier FX, Iverson EB, Ferguson PD, "Detection of Iron Overload with the ORNL Spallation Neutron Source: an MCNPX Simulation Study", *Proceedings of IEEE Nuclear Science Symposium, Medical Imaging Conference*, pp. 4972-4975, 2008.

23. **Kapadia AJ**, Agasthya GA, Tourassi GD, "Detection of Iron Overload through Neutron Stimulated Emission Computed Tomography: A Sensitivity Analysis Study", *Proceedings of SPIE Medical Imaging*, vol. 7258, pp. 725811, 2009.

INSTITUTE OF PHYSICS PUBLISHING PHYSICS IN MEDICINE AND BIOLOGY

Phys. Med. Biol. **51** (2006) 3375–3390 doi:10.1088/0031-9155/51/14/006

# Introduction to neutron stimulated emission computed tomography

**Carey E Floyd Jr[1], Janelle E Bender[1], Amy C Sharma[1], Anuj Kapadia[1], Jessie Xia[1], Brian Harrawood[2], Georgia D Tourassi[2], Joseph Y Lo[2], Alexander Crowell[3] and Calvin Howell[3]**

[1] Department of Biomedical Engineering and Department of Radiology, Duke Advanced Imaging Laboratories Box 2623DUMC, Duke University, Durham, NC 27710, USA
[2] Department of Radiology, Duke Advanced Imaging Laboratories Box 3202DUMC, Duke University, Durham, NC 27710, USA
[3] Department of Physics and Triangle Universities Nuclear Laboratory, Duke University, Durham, NC 27710, USA

E-mail: carey.floyd@duke.edu

Received 25 October 2005, in final form 11 April 2006
Published 23 June 2006
Online at stacks.iop.org/PMB/51/3375

**Abstract**

Neutron stimulated emission computed tomography (NSECT) is presented as a new technique for *in vivo* tomographic spectroscopic imaging. A full implementation of NSECT is intended to provide an elemental spectrum of the body or part of the body being interrogated at each voxel of a three-dimensional computed tomographic image. An external neutron beam illuminates the sample and some of these neutrons scatter inelastically, producing characteristic gamma emission from the scattering nuclei. These characteristic gamma rays are acquired by a gamma spectrometer and the emitting nucleus is identified by the emitted gamma energy. The neutron beam is scanned over the body in a geometry that allows for tomographic reconstruction. Tomographic images of each element in the spectrum can be reconstructed to represent the spatial distribution of elements within the sample. Here we offer proof of concept for the NSECT method, present the first single projection spectra acquired from multi-element phantoms, and discuss potential biomedical applications.

## 1. Introduction

This paper presents feasibility for some of the essential components of a new approach for biological spectroscopy and imaging. Neutron stimulated emission computed tomography (NSECT) is presented as a spectroscopic tomographic technique in which stable nuclei in the sample are stimulated to emit characteristic gamma rays by inelastic scattering of fast neutrons. While a preview of this technique has been presented (Floyd *et al* 2004), here we present the

  

full technique in detail. Section 1 will present both the physical concepts underlying NSECT and will conclude with an overview of the experiments described in the remainder of the paper. Section 2 will describe the specific design of the experiments conducted to acquire the spectra from several elements. Section 3 will present gamma emission spectra for several sample elements. Section 4 will present challenges to be overcome along with three potential practical applications (measurement of iron concentration, diagnosis of breast cancer and small animal spectroscopic imaging) along with a brief radiation dose computation.

### *1.1. Physical concepts*

In concept, NSECT can be thought of as a gamma emission computed tomography (ECT) technique where the gamma emission is from stable isotopes in the sample as they are stimulated by inelastic scattering of neutrons from a collimated external neutron beam. Instead of introducing a radioactive isotope into the sample and imaging its time and spatial distribution as with ECT, we image the naturally existing distribution of stable isotopes along the path of the stimulating neutron beam. While similar in concept, NSECT places significantly different requirements on imaging technology than ECT. For all elements except hydrogen and helium, the gamma energies from the stimulated emissions range from below 100 keV to 6600 keV. All of the stable isotopes (except H and $^4$He) can be detected by their characteristic gamma emission within this energy range. From this range it is obvious that standard nuclear medicine gamma cameras are not well suited to the task of forming projection images. At the higher energies (above 500 keV), the spatial and energy resolution of a standard gamma camera is degraded to the point where it has little value for imaging or spectroscopy. The components of the typical gamma camera that provides spatial localization are the position-sensitive detector crystal (typically NaI(Tl)) combined with the collimator (typically Pb). Neither of these components are suitable for higher energies. Borrowing from experimental nuclear structure physics, a suitable detector for gamma spectroscopy is the high purity germanium (HPGe) detector. While spatially sensitive HPGe detectors have been constructed, the designs that have been successful would not provide adequate energy resolution or stopping power at the high energies ranging up to a few MeV as required by our application. Our solution is to use cylindrical HPGe detectors to provide fine energy resolution and use the neutron beam geometry to provide spatial resolution by defining the projection along which all gamma emission must take place. By scanning the sample with the collimated neutron beam, we avoid the need for the collimator and the position-sensitive detector. This approach does require longer acquisition time and the detection efficiency of the HPGe detector is significantly lower at high energies than the efficiency of the NaI detector at low energies. This longer acquisition time may potentially have a negative impact on image quality due to the possibility of patient motion during the long scan time. A solution to this problem might be to use an imaging detector rather than the simple HPGe detector. This would acquire a two-dimensional projection image at the set projection angle without scanning the neutron beam. For this approach, a broad neutron beam would be used that covered the volume to be imaged. This could be an advantage as it is difficult to collimate the neutron beam into a small size. One detector design that could provide the two-dimensional projection image is the Compton coincidence detector (CCD) that has been developed and evaluated for ECT applications (Singh and Doria 1983, Johnson *et al* 1995, LeBlanc *et al* 1998). One concern in using such a detector is the decreased detection efficiency of the CCD approach due to the multiple coincidence requirement.

In this application, NSECT uses neutron technologies similar to some that recently have been proposed to detect explosives and contraband in cargo containers (Evans *et al* 1999, Gozani 1994, Nunes *et al* 2002). NSECT extends these techniques to a wider range of isotopes

and imaging applications. This novel approach to measuring elemental concentrations in the body is fundamentally different from other approaches that have been developed for biomedical imaging. A low-dose beam of neutrons is scanned over the body and the distribution of nuclei that are stimulated to emit characteristic gamma rays is reconstructed into a tomographic image. A separate image is formed for each element where the image intensity corresponds to the concentration of that element in the sample. To convert the detected gamma yields into concentrations requires correction for the energy-dependent detector efficiency. The results reported here were obtained using the neutron scattering facilities of the Triangle Universities Nuclear Laboratory (TUNL). While the facilities of TUNL are ideal for development and experimentation, a standalone prototype of our first-generation imaging system could be assembled from commercially available components for a single unit cost that is less than the cost of a complete digital chest or digital mammography x-ray system in 2005 (around $300 000).

### *1.2. Overview of experiments*

In this paper, we describe our initial successful experiments leading to NSECT imaging. Here we have acquired spectra from a single projection of a potential tomographic projection set for several phantoms. We describe the techniques for neutron beam production and collimation, sample positioning, gamma detection and spectroscopy, background suppression, and isotope identification. The results of these experiments support the concept for a number of components that are required for the future realization of the potential offered by the NSECT technique.

### *1.3. Relationship to other neutron techniques*

The concept of using neutrons to interrogate an area to determine its content is shared by an assortment of techniques each with its own acronym (Morgan 2000, Cohn 1980). There are subtle differences usually associated with the physical interaction of the neutron with the subject. The most important difference is between techniques where the neutron is captured by the target, transmuting it into an unstable nucleus which then decays by fission or by the release of some particle or photon, and between techniques like NSECT where the neutron scatters from the target and stimulates release of a characteristic photon. Among the techniques that rely on the capture of the neutron are neutron activation analysis (NAA), instrumental neutron activation analysis (INAA), pulsed fast thermal neutron analysis (PFTNA), pulsed gamma activation analysis (PGAA), and sometimes fast neutron analysis (FNA), pulsed fast neutron analysis (PFNA) and fast neutron scattering analysis (FNSA). Techniques that typically use scattering alone include FNSA and NSECT. The most widely used technique is NAA (or INAA) which uses low-energy thermal neutrons produced in a reactor to transmute a wide range of nuclei into unstable isotopes. This irradiation can take many hours and the subsequent measurement of the decay energies and rates of the unstable transmuted isotopes can require days. In comparison, NSECT uses prompt gamma emission at higher neutron energies to provide many of the advantages and accuracy of NAA in a technique that can be implemented for rapid *in vivo* elemental analysis.

## 2. Methods

In this section, we will describe the equipment and techniques used in preliminary NSECT experiments. The equipment for performing NSECT has three required components: (1)

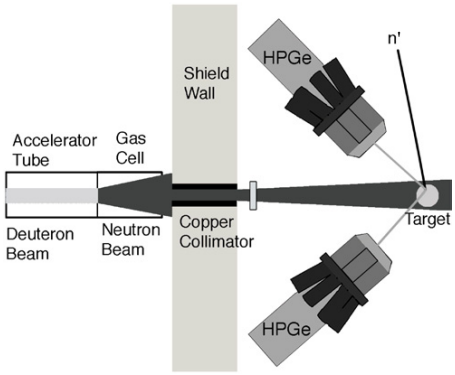


**Figure 1.** Arrangement of equipment for the neutron scattering experiments. The deuteron beam enters from the left from the accelerator and creates neutrons through the d(d,n) reaction, leaving $^3$He in the cell. The neutrons travel through the collimator to the sample where inelastic scattering results in a neutron of reduced energy n′ and a gamma photon which is collected by the Ge detector (HPGe). The pulse height of the detected signal is proportional to the energy of the gamma ray. The placement of the HPGe is intended to minimize neutron interaction (direct or scattered) and background gamma detection. An alternative to the simple HPGe detectors would be to use a two-dimensional imaging detector such as a Compton coincidence detector and to illuminate the entire sample with the neutron beam.

a neutron source, (2) a sample and (3) a gamma spectrometer. The techniques include the following: beam size background suppression and correction both for beam-correlated and beam-uncorrelated backgrounds; the normalization of the detected gamma flux in the spectrometer to the incident neutron beam flux; list-mode data acquisition; identifying specific elements from the acquired spectra. A drawing of the equipment arrangement for this scattering experiment is shown in figure 1.

### *2.1. Neutron source*

The first component of the NSECT system is a neutron source. The source for the neutron beam is the d(d,n)$^3$He fusion reaction. A pulsed deuteron beam is produced by the TUNL accelerator with 2.8 MeV deuteron energy and is focused at the end of the beam line into a gas cell containing 100 psi of deuterium. The deuterons fuse and a neutron beam with 6 MeV energy is emitted. The resulting beam escapes the gas cell and is collimated by a copper channel that passes through a thick shield wall and emerges into the scattering area. This area is thus shielded from the flux of gammas from the neutron production reaction. Copper was chosen for this collimator as a material with reasonable neutron attenuation that had reasonable cost and good machining properties. While tungsten would conceptually make a more effective collimator, the difficulties and expense of obtaining and machining such a large channel would be prohibitive.

### *2.2. Sample*

The second component of the NSECT system is the sample positioning. To achieve the tomographic acquisition geometry, either the neutron source or the sample must be translated and rotated. In this implementation, a narrow neutron beam (square profile 2 cm $\times$ 2 cm)

was produced so that tomographic acquisition would be achieved by translating and rotating the sample on computer controlled stages. Spatial resolution is defined by the size of the collimated neutron beam. The pulsed and collimated neutron beam then strikes the sample. Some of the neutrons scatter inelastically from the nuclei in the sample. The internal energy of these nuclei becomes increased by the energy given up by the neutron. Those excited nuclei then decay rapidly from their excited states and give off gammas whose energy is equal to the difference between the energies of the nuclear states involved in the decay. The energies of these states are unique to the elemental nucleus; consequently, the gamma energies are characteristic of the emitting nucleus.

### *2.3. Gamma spectrometer*

The third component of the NSECT system is the gamma spectrometer. Energy resolution, required for separating gamma events from different elements, is defined by the properties of the gamma spectrometer. For these experiments, a pair of HPGe detectors acquired the emitted gamma flux. HPGe detectors have a nominal energy resolution of 0.1% at 1000 keV with little change over the energy range of interest (500–6500 keV). The advantages of high-energy resolution are somewhat offset by the poor efficiency of the HPGe detectors at high neutron energies. The detectors were positioned at 135° on either side of the incident neutron beam to match the maximum in the quadrupole angular distribution that is typical of most of the transitions creating the gamma emissions from our targets of interest. With the excellent energy resolution of the detectors, there was no overlap of the low-lying energy peaks for any of these states and so identification was straightforward.

At higher energies, it is possible for a gamma to Compton scatter once (or several times) in the detector and then escape leading to an underestimation of the actual gamma energy. To reject a majority of these events, the HPGe section is surrounded by an additional detector called a Compton shield. This is a coaxial cylinder of BGO and NaI coupled to several photomultiplier tubes. When a gamma is detected in the shield within a certain time window of a detection event in the HPGe, the event is rejected.

### *2.4. Background suppression*

In addition to the characteristic gammas from the sample, this experiment acquired other gammas that constituted an unwanted background. Two techniques are practical for removing this background. One is a 'sample-in–sample-out' subtraction. The background is estimated by removing the sample, leaving the beam on, and counting for an equivalent number of incident neutrons. The background measured using this technique includes photons that are emitted from naturally occurring radioactivity in the experimental area as well as photons that are generated by the neutron beam interacting with objects other than the target. Both of these sources of background would be present in a clinical imaging environment. The second approach is to pulse the neutron beam (by pulsing the deuteron beam) and only accepting photons that are detected in a time window that corresponds to the time it would take for the neutron to be produced, travel to the sample, scatter, and the emitted gamma to reach the detector. The time of flight (TOF) is measured between the arrival of a deuteron pulse at the gas cell and the detection of a gamma in the detector. This TOF technique is common in nuclear structure physics experiments. TOF is effective and efficient for laboratory experiments where the experimental geometry and beam energies are often changed. With TOF, the background is acquired simultaneously with the foreground and thus avoids the separate background acquisition. In a clinical system, the sample-out technique might be

preferred to avoid the added complexity in the experimental apparatus required by the TOF technique. This apparatus is readily available in the TUNL facility and so is preferred for our preliminary experiments.

### *2.5. Normalization*

The incident neutron flux varies from run to run due to instabilities in the deuteron source. Two techniques were used to normalize the detected gamma flux to this neutron flux. First, the deuteron flux was monitored by collecting the charge deposited by the deuteron beam onto the electrically isolated deuteron gas target cell. This charge was integrated over each run and the integrated charge was automatically stored as a scalar value for each run. Second, a neutron monitor in the form of a thin plastic scintillator was placed in the neutron beam between the collimator and the sample and was gated by the deuteron beam pulse. The efficiency of this detector was established at this neutron energy by a separate calibration experiment.

To monitor beam integrity the ratio of the neutron monitor to beam current integrator was computed for each run and was displayed in real time at the control console to facilitate identifying difficulties with the pulse beam pickoff system. When the ratio dropped, it meant that beam pulses were being missed. This was usually due to a drop in the beam intensity generated at the deuteron source. When the ratio dropped by 10%, data acquisition was halted and the acquisition for that run was discarded.

### *2.6. List-mode data acquisition*

The data were acquired and recorded in the list mode. For each gamma event in the detector, all parameters were recorded including the following: TOF, pulse height in the detector, and scalar variables associated with the time of the event. From this information, the experiment can be 're-played' in software to allow post-setting of parameters such as detector bias and TOF windows.

### *2.7. Identification of specific elements*

Preliminary experiments were performed on phantoms made from solid C, Ca, Fe, Cu, and a water phantom as a source of O. These samples were chosen for several reasons. C, O and Ca are among the most prevalent elements in living bodies. C and O represent the elements with the highest energies for their first excited states and thus represent the two elements whose spectra are the most difficult to acquire. Fe and Cu appear in small trace quantities in the body. They also have characteristic gamma emission at the lower end of our energy range and were included to test our ability to acquire spectra around 600–800 keV. The form of the samples was as follows: C, Fe, Cu, rectangular solids 6 mm $\times$ 30 mm $\times$ 60 mm; for one spectrum a thin steel sample was used for Fe; Ca, right circular cylinder 12.5 mm radius, 40 mm height; O was a right circular cylinder of water of 500 ml volume.

For these samples, the spectra were analysed by hand and the peaks were identified using the databases of the National Nuclear Data Center (NNDC) at Brookhaven National Labs (NNDC 2005). All isotopes that contribute significantly to each natural element were considered. We chose to ignore any isotope that contributed less than 5% to the natural form of the element. Table 1 shows the stable isotopes examined in this experiment.

For reference, table 2 lists the 16 most prevalent elements that make up the human body along with their percentage contribution by weight. Typically, all but the four most prevalent elements are considered trace elements.

**Table 1.** Stable isotopes and natural abundances for C, O, Ca, Fe and Cu samples.

| Element | Isotope(s) (%) |
|---|---|
| Carbon | $^{12}$C (>98) |
| Oxygen | $^{16}$O (>99) |
| Calcium | $^{40}$Ca (>96) |
| Iron | $^{54}$Fe (6) and $^{56}$Fe (92) |
| Copper | $^{63}$Cu (69) and $^{65}$Cu (31) |

**Table 2.** Composition of the body by weight (per cent values).

| | |
|---|---|
| Oxygen | 61.429 |
| Carbon | 22.857 |
| Hydrogen | 10.000 |
| Nitrogen | 2.571 |
| Calcium | 1.429 |
| Phosphorus | 1.114 |
| Potassium | 0.200 |
| Sulfur | 0.200 |
| Sodium | 0.143 |
| Chlorine | 0.136 |
| Magnesium | 0.027 |
| Iron | 0.006 |
| Fluorine | 0.004 |
| Zinc | 0.003 |
| Silicon | 0.001 |
| Rubidium | 0.001 |

The web interfaces to the NNDC were used to list the gamma emission energies from all of the elements used in the experiments. A match was noted where the expected gamma energy appeared as a peak in the emitted gamma energy spectrum for the appropriate sample. For an unknown sample, the inverse process would be used: peaks noted in the energy spectrum would be matched to the known energy emissions from all elements and those that matched would be candidates. Some careful selection from the possible candidates would identify the likely elements. While commercial software exists for automated spectra analysis of naturally radioactive materials, no such software is available for spectra analysis of stable isotopes whose gamma emission has been stimulated.

The number of target nuclei in the irradiated volume of a sample can be computed from the fact that the emitted gamma flux is proportional to this multiplied by the incident beam flux, taking into account the differential cross sections for each process. We monitor the incident beam flux and measure the emitted gamma flux to solve for the number of targets. Neutron and gamma attenuation will also affect these calculations. These effects are small for biomedical targets.

## 3. Results

Here we present the gamma emission spectra acquired from several elements: carbon, calcium, iron, copper and oxygen (water). Combined spectra for iron with oxygen (water), copper with calcium, and iron with copper are also presented.

**Table 3.** Survey of the literature range of elemental composition within rats (Kollmer *et al* 1972, Carl *et al* 1989, Palm *et al* 1990, Takahashi *et al* 2000) and humans (Persigehl *et al* 1977, Yukawa *et al* 1980, Milman *et al* 1983, Yoshinaga *et al* 1990, Andrasi *et al* 1993, Stedman and Spyrou 1995, Katoh *et al* 2003). All are in $\mu$g g$^{-1}$ dry weight. When values were listed in wet weight a dry/wet weight ratio of 0.3 was assumed for conversion. When a range was given, it was used; otherwise the median values are given.

| Element | Rat or human | Liver | Kidney | Brain | Heart | Method |
|---|---|---|---|---|---|---|
| Al | R | 0.7–7.3 | n/a | n/a | n/a | ICPA, ICPM |
| | H | 8.3–83.3 | 9.8–136.6 | 14.0–75 | 9.0–113.3 | NAA |
| Br | R | n/a | n/a | n/a | n/a | |
| | H | 9.0–13.6 | 49.5–62.5 | 4.9–5.7 | 14.9–17.4 | NAA |
| Ca | R | 53–199 | n/a | 290–334 | n/a | AAS, ICPA, NAA |
| | H | 92.3–460 | 213–3198 | 121–1422 | 129–197 | NAA, PIXE, ICPA |
| Cl | R | n/a | n/a | n/a | n/a | |
| | H | 3110–5720 | 13 400–15 400 | 2480–5460 | 5640–6030 | NAA, PIXE |
| Cu | R | 10.7–29.9 | 34–49 | 7–16 | 11–13 | AAS, ICPA, NAA, ICPM |
| | H | 5–289 | 4.6–63.6 | 1–35.3 | <24.8 | XFS. PIXE, NAA, ICPA |
| Fe | R | 230–1080 | 50–55 | 64–168 | >1 | AAS, fAAS, ICPA, NAA |
| | H | 96.6–4200 | 22–1393 | 39.6–900 | 19.3–850 | NAA, XFS, PIXE, ICPA |
| K | R | 7233–11 900 | n/a | n/a | n/a | AAS, ICPA |
| | H | 9800–1100 | 11 100–12 100 | 5300–13 900 | 14 100–15 200 | NAA, PIXE |
| Mg | R | 570–973 | n/a | n/a | n/a | AAS, ICPA |
| | H | 121–2500 | 176.6–833.3 | 226.6–1266.6 | 276.6–1400 | NAA, ICPA |
| Mn | R | 4.13–9.85 | n/a | ∼1 | 3–4 | AAS, ICPA, NAA, ICPM |
| | H | 3.2–20 | <22.7 | 0.7–5.6 | 0.86–4.6 | NAA |
| Mo | R | 1.47–4 | n/a | <1 | n/a | NAA, ICPM |
| | H | n/a | n/a | n/a | n/a | |
| Na | R | 1519–5266 | n/a | 5399–5941 | n/a | AAS, ICPA |
| | H | 3070–4230 | 10 600–12 800 | 4570–5420 | 5290–5470 | NAA |
| P | R | 9970–12 700 | n/a | n/a | n/a | ICPA |
| | H | 6166–14 800 | 4033–10 483 | 2700–15 000 | 3667–8733 | PIXE, ICPA |
| Rb | R | 24–32.3 | n/a | 14–16 | n/a | ICPM |
| | H | 7–47 | 3.3–44 | 4.5–26 | 4–47 | NAA |
| Zn | R | 63.3–129 | 66–75 | 40–64 | 40–42 | AAS, ICPA, NAA, ICPM |
| | H | 56.6–619 | 30.3–434 | 25.3–130 | 16.3–265 | NAA, XFS, PIXE, ICPA |

AAS: flame atomic absorption spectrophotometry; fAAS: flameless atomic absorption spectrophotometry; ICPA: inductively coupled plasma-atomic emission spectrometry; ICPM: inductively coupled plasma-mass spectrometry; NAA: neutron activation analysis; XRF: x-ray fluorescence spectrometry; PIXE: particle induced x-ray emission analysis.

The acquired gamma energy spectrum from a thin iron (steel) sample is shown in figure 2. For this experiment, the background was removed using the sample-out technique.

While the energy resolution of the HPGe detectors is excellent, the efficiency decreases rapidly with increasing gamma energy. Of the isotopes that have biological interest, $^{16}$O exhibits the highest energy for the first excited state at 6048 keV. Even though the detector

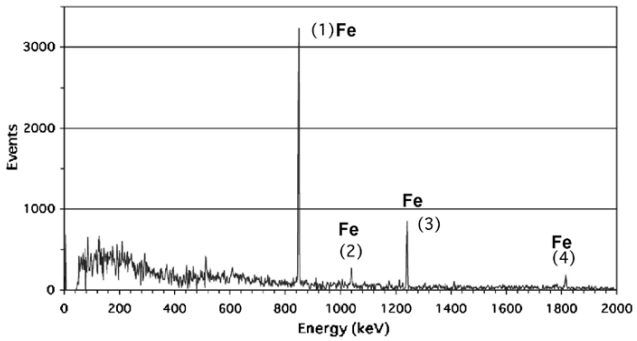


**Figure 2.** Experimental spectrum from a thin iron sample corrected for background by subtracting a spectrum acquired with iron sample removed. Four gamma peaks from $^{56}$Fe are clearly identified: (1) at 847 keV is the gamma from the transition from the first excited state to the ground state; (2) at 1038 keV is the gamma from the transition from the seventh excited state at 3123 keV down to the second excited state at 2085 keV; (3) at 1238 keV is the gamma from the transition from the second excited state at 2085 keV down to the first excited state at 847 keV; (4) at 1811 keV is the gamma for the transition from the third excited state at 2658 keV down to the first excited state at 847 keV.

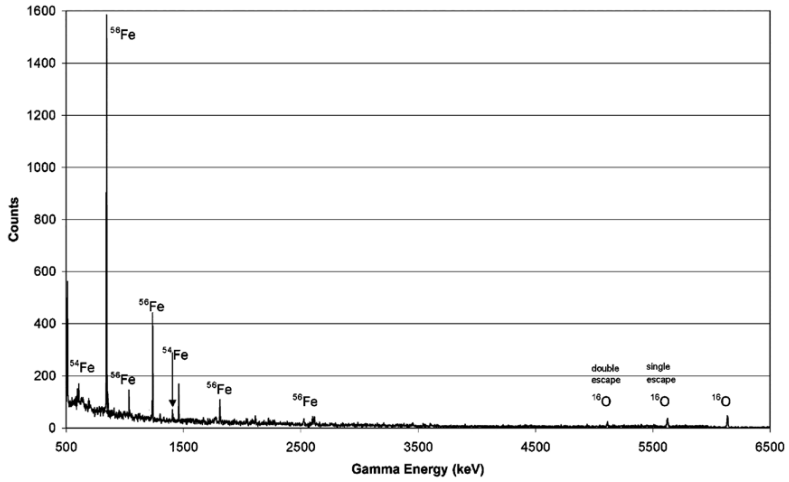


**Figure 3.** Spectrum from iron sample in water. Several states in both $^{54}$Fe and $^{56}$Fe and the first state in $^{16}$O can be recognized. In addition, the single and double escape peaks from $^{16}$O are seen. This demonstrates the full energy range of the NSECT technique when implemented with a HPGe detector.

efficiency is low at this high energy, we were still able to acquire a spectrum from the $^{16}$O in a 500 ml water sample as shown in figure 3.

A spectrum from a graphite carbon sample is shown in figure 4 where the first excited state is seen at 4.4 MeV. The amplitude is moderate for this state due to the low detector efficiency, the low density of the target, and a relatively short acquisition time. In the spectra, the two escape peaks can be seen at 511 and 1022 keV below the primary peak. These are

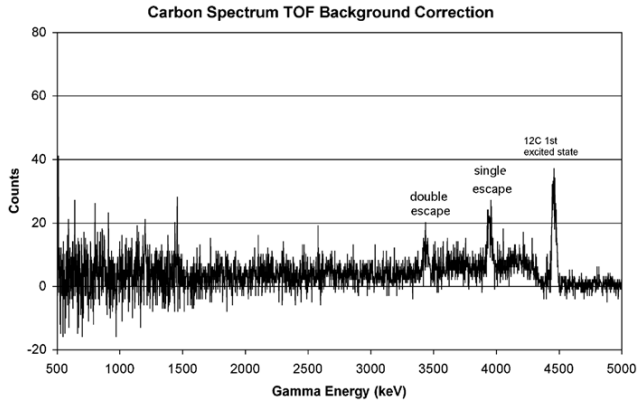


**Figure 4.** Spectrum from carbon sample showing gammas from the first excited state at 4438 keV along with the single and double escape peaks at 511 and 1022 keV below the first excited state.

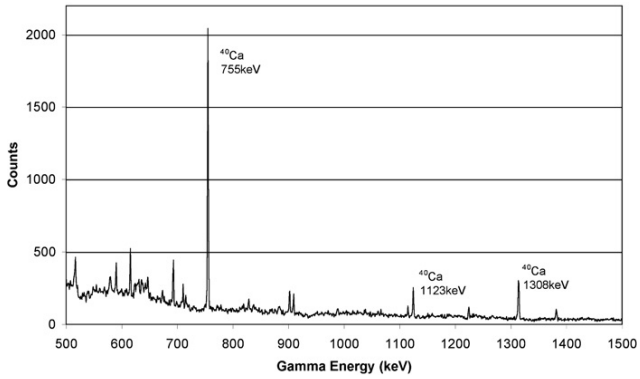


**Figure 5.** Spectrum from $^{40}$Ca showing three characteristic emission peaks.

peaks corresponding to detection events where pair production occurs and either one or both of the products escape from the detector.

In figure 5 the spectrum from a natural calcium sample is shown. The first three gamma energies are easily identifiable in this spectrum.

A spectrum from a mixed sample that contains Cu and C is shown in figure 6. Here the two elements are clearly separated with no overlap. In addition, peaks identified with the two contributing isotopes $^{63}$Cu and $^{65}$Cu are clearly identified.

A spectrum from a mixture of Fe and Cu is shown in figure 7. Here TOF was used to reduce the background. For each of $^{56}$Fe and $^{63}$Cu, several transitions are identified.

## 4. Discussion

We have demonstrated spectroscopic acquisition of neutron stimulated gamma emission projections from several single and multi-element phantoms. In these experiments the elements

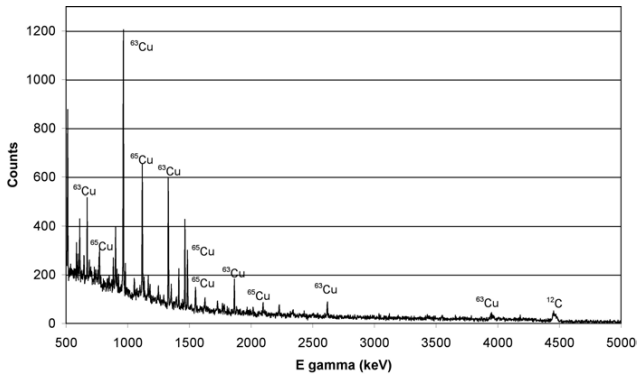


**Figure 6.** Spectrum from mixed copper (Cu) and carbon (C) sample. Multiple states in $^{63}$Cu and $^{65}$Cu are visible.

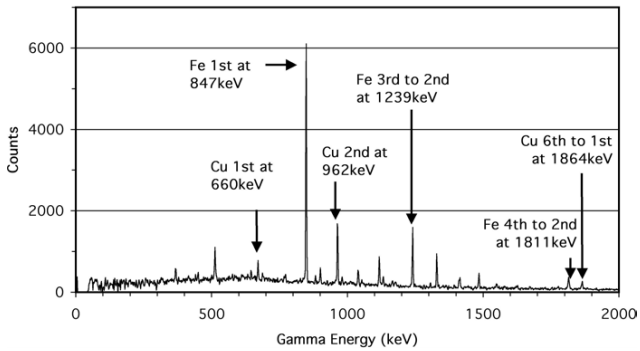


**Figure 7.** Spectrum from iron and copper mixed phantom. Several gamma peaks are identified with transitions between states in $^{56}$Fe and $^{63}$Cu.

were clearly differentiated with no overlap. The background was low as were any obvious contamination gamma acquisitions.

### *4.1. Challenges*

With a biological sample, there would be several primary elements (O, C, H, N, Ca) and a number of trace elements (P, K, S, Na, Cl, Mg, Fe, F, Zn) present. Preliminary analysis (mentioned here but not shown in section 3) of all of the states tabulated in the ENDF files for the 14 most prevalent elements in the body (O, C, H, N, Ca, P, K, S, Na, Cl, Mg, Fe, F, Zn) (633 states in all) indicates that with the energy resolution of HPGe, only 142 of the states would overlap and all 13 elements (omitting H) would be easily and uniquely identified. One potential source of interfering elements could be from pharmaceuticals (stable or radioactive in the case of nuclear medicine examinations). We have not yet undertaken an examination of all of the possible states in the possible elements contained in prescribed pharmaceuticals to identify potential interfering gamma emissions. In section 2 it was mentioned that a 'careful' selection process was used to identify states. In practice this would mean that when a peak is

seen, while there might be many states that are within the energy resolution width of that peak, preference would be given to those states with some likelihood of occurring in the body. As an example, given the 0.1% energy resolution of the HPGe detector, a state seen at 755 keV could have an actual energy between 754.3 and 755.7 keV. While there are 147 state transitions that produce gamma energies in this range (considering all isotopes), only one corresponds to a stable isotope and that is $^{40}$Ca.

### *4.2. Potential applications*

NSECT has potential for a broad range of applications in both medical and biological research. NSECT can provide a three-dimensional map of the spatial distribution of all elements (with the exception of H and He) in a subject from one scan; it also offers the promise of providing isotopic imaging of stable isotopes used as tracers. There may be considerable technological challenges as we strive for high sensitivity at high spatial resolution. The spectral response is already sufficient to resolve any combination of isotopes to be found in the body.

*4.2.1. Cancer diagnosis.* One potential use for NSECT is to detect cancer from the changes in trace elemental composition that occur when a malignancy begins to form. All of the studies referenced below were *in vitro*. Until NSECT, there has not been a technique proposed that can perform these measurements *in vivo*. A difference between trace element concentrations has been measured previously *in vitro* for several different cancers of the breast (Geraki *et al* 2002, Mussalo-Rauhamaa *et al* 1993, Ng *et al* 1997, Rizk and Sky-Peck 1984, Santoliquido *et al* 1976), colon (Margalioth *et al* 1983, Ghadirian *et al* 2000, Kato *et al* 1999, Nelson *et al* 1994, Witkowski *et al* 1993, Xiao and Henderson 1992, Banner *et al* 1984, Gregoriadis *et al* 1983), lung (Rizk and Sky-Peck 1984), prostate (Ogunlewe and Osegbe 1989, Chirulescu *et al* 1987, Bataineh *et al* 2002, Brys *et al* 1997, Zaichick *et al* 1997, Picurelli *et al* 1991, Feustel *et al* 1989, Romics and Katchalova 1983, Feustel *et al* 1982, Habib *et al* 1976, Platz *et al* 2002, Kubo *et al* 1976), kidney (Margalioth *et al* 1983), liver (Margalioth *et al* 1983, Feustel *et al* 1982, Habib *et al* 1976, Platz *et al* 2002, Kubo *et al* 2002) stomach (Margalioth *et al* 1983), urinary bladder (Margalioth *et al* 1983), testis (1983), and female reproductive organs (Margalioth *et al* 1983). Cancer would be identified by measuring the trace element composition of the tissue and analysing this information to identify combinations of elements that have been associated with cancer.

*4.2.2. Non-invasive measurement of iron.* A second potential application of NSECT would be to provide quantitative measurements of the iron concentration in the liver. This measurement is important for thalassemia patients, sickle cell patients at risk for stroke, individuals with haemochromatosis mutations, and for other patients who receive chronic blood transfusions. The mean value for iron concentration in normal human liver is 300 $\mu$g cm$^{-3}$ while for thalassemia patients it has been reported with a mean value of 3 mg cm$^{-3}$ (Angelucci *et al* 2000).

Currently, the definitive measurement of iron burden requires biopsy of the liver. This biopsy has associated morbidity and, for most health care institutions, the biopsy material is evaluated at a remote site with considerable delay (3–7 days) before the results are available (Brittenham and Badman 2003, Kato *et al* 1999). This delay, along with the morbidity associated with repeated biopsy, is an obstacle for following the progress of patients obtaining therapeutic treatments and is thus an obstacle for developing new treatments. NSECT could provide an *in vivo*, non-invasive measurement of the iron concentration in the liver and would pose no morbidity. While there would be some radiation dose associated with this procedure,

preliminary calculations indicate that this dose would be less than that of an abdominal CT exam.

*4.2.3. Small animal spectroscopic imaging.* A third potential area of application for NSECT is to image small animals. With the development of an appropriate sized neutron beam, NSECT could develop adequate spatial and energy resolution to provide a useful tool for spectroscopic imaging of small animals. Table 3 shows previously detected trace element concentrations in rats. As we begin to understand the limits to spatial resolution and noise for NSECT reconstructed images, we will begin to evaluate a number of different roles that NSECT could play in our efforts to understand the mechanisms, both structural and functional, of metabolism and transport of elements in both normal and disease models.

Some of the more speculative but exciting possibilities for this technology include: following the metabolic migration of nutrients in normal and in genetically modified mice (these would likely be described by kinetic parameters); measuring the iron and calcium levels in the cardiac wall; diagnosing cancer *in vivo* at a very early stage when the relative concentrations of trace elements in the tissues begin to change; tagging molecules of interest using stable rather than radioactive isotopes, imaging different proteins and other macromolecules by stoichiometry of the relative concentrations of C, O and N within small imaged volumes. Because of the small concentrations expected in single voxels, the most likely presentation of the imaging data would be as concentrations in reconstructed organs or tumours rather than in the individual voxels themselves.

### *4.3. Neutron radiation dose*

While no studies involving human subjects are described in this paper, the description of potential applications does imply that NSECT would eventually be applied to humans. For this reason, it is appropriate to comment on the radiation dose that would be required to attain a useable signal. Two factors that are beyond the scope of this paper must be estimated to compute the dose to a subject: the fraction of incident neutrons that will deposit energy in the subject and the average fraction of each neutron's energy that will be deposited in the subject. Using a Monte Carlo model of the neutron beam and of a human body (a model we developed using the GEANT4 C++ toolkit), we have calculated these factors for a 2.5 MeV incident neutron beam onto a human abdomen. The fraction of incident neutrons that deposit energy in the abdomen was found to be 0.6 while the average amount of energy deposited by each 2.5 MeV neutron was found to be 1.4 MeV. Note that these are approximate average values. We consider a useable signal to be a peak in the background-corrected spectrum with about 30 counts. Assuming Poisson statistics, the uncertainty on this measurement would be $\pm 5.5$ for a relative error under 20%. This is a realistic, although arbitrary, value for the gamma yield. In a Monte Carlo model of the liver in the abdomen, the element iron will yield a gamma peak of about 30 counts with 10 million incident neutrons in a single projection. The absorbed energy is the average deposited energy per interacting neutron $\times$ number of incident neutrons $\times$ fraction of incident neutrons that interact $= 1.4$ MeV $\times$ $10^7 \times 0.6 = 8.4 \times 10^6$ MeV. For a 1 cm$^2$ beam area over a path through the liver with an average length of 10 cm and for a liver density of 1.1 g cm$^{-3}$, the mass of liver exposed is 0.011 kg. Convert the energy to joules as $8.4 \times 10^6$ MeV $\times$ $1.6 \times 10^{-13}$ (J MeV$^{-1}$) $= 1.34 \times 10^{-6}$ J. The absorbed dose in Gy is then $1.34 \times 10^{-6}$ J/0.011 kg $= 1.22 \times 10^{-4}$ Gy. To get the equivalent dose, multiplying by the quality factor for neutrons (10) and by the weighting factor for the liver (0.05) gives an effective dose of 0.0061 mSv (where 1 Gy = 100 mSv). For comparison, the average effective dose from a chest x-ray examination is 0.02 mSv, so the

neutron dose to the liver would be equivalent to about a third of the dose of a chest radiograph. The chest radiograph is one of the lowest dose radiological examinations that are routinely performed and so this neutron dose is considered acceptable.

## 5. Conclusion

In conclusion, we have demonstrated excellent potential for NSECT as a spectroscopic imaging technique. The sources for gamma backgrounds have been identified and corrections have been implemented. Two isotopes each of Fe and Cu have been clearly detected and identified from spectra obtained with natural samples. Two isotopes, $^{12}$C and $^{16}$O whose acquisition and identification are difficult, were successfully acquired. These are difficult to acquire due to the high gamma energies required (4438 keV for $^{12}$C and 6048 keV for $^{16}$O). Thus we have demonstrated acquisition of characteristic gamma radiation over the entire energy range of interest for biological imaging. The fundamental principles of NSECT have been verified through these experiments. Future work will include acquiring a full set of tomographic projections and reconstructing them into a fully tomographic image of the internal multi-element distribution of a sample.

## Acknowledgments

Duke Advanced Imaging Laboratories (DAILabs), Triangle Universities Nuclear Laboratory (TUNL). This work was supported in part by NIH/NCI grant no 1-R21-CA106873-01.

## References

Agostinelli S *et al* 2003 GEANT4: a simulation toolkit *Nucl. Instrum. Methods* A **506** 250–303

Andrasi E, Suhajda M, Saray I, Bezur L, Ernyei L and Reffy A 1993 Concentration of elements in human brain: glioblastoma multiforme *Sci. Total Environ.* **139/140** 399–402

Angelucci E *et al* 2000 Hepatic iron concentration and total body iron stores in thalassemia major *N. Engl. J. Med.* **343** 327–31

Banner W P, DeCosse J J, Tan Q H and Zedeck M S 1984 Selective distribution of selenium in colon parallels its antitumor activity *Carcinogenesis* **5** 1543–6

Bataineh Z M, Bani Hani I H and Al-Alami J R 2002 Zinc in normal and pathological human prostate gland *Saudi Med. J.* **23** 218–20

Brittenham G M and Badman D G 2003 Noninvasive measurement of iron: report of an NIDDK workshop *Blood* **101** 15–9

Brys M, Nawrocka A D, Miekos E, Zydek C, Foksinski M, Barecki A and Krajewska W M 1997 Zinc and cadmium analysis in human prostate neoplasms *Biol. Trace Elem. Res.* **59** 145–52

Carl G F, Critchfield J W, Thompson J L, McGinnis L S, Wheeler G A, Gallagher B B, Holmes G L, Hurley L S and Keen C L 1989 Effect of kainate-induced seizures on tissue trace element concentrations in the rat *Neuroscience* **33** 223–7

Chirulescu Z, Chiriloiu C, Suciu A, Pirvulescu R and Gh N 1987 Variations of zinc, calcium and magnesium in normal subjects and in patients with neoplasias *Med. Interne* **25** 257–61

Cohn S H 1980 The present state of *in vivo* neutron activation analysis in clinical diagnosis and therapy *At. Energy Rev.* **18** 599–660

ECOTB 2000 *Elemental Concentration of the Body* http://web2.iadfw.net/uthman/elements_of_body.html (posted 14 Feb. 2000, accessed 10 May 2004)

Evans R J, Jupp I D, Lei F and Ramsden D U 1999 Design of a large-area CsI(Tl) photo-diode array for explosives detection by neutron-activation gamma-ray spectroscopy *Nucl. Instrum. Methods Phys. Res.* A **422** 900–5

Feustel A, Wennrich R, Steiniger D and Klauss P 1982 Zinc and cadmium concentration in prostatic carcinoma of different histological grading in comparison to normal prostate tissue and adenofibromyomatosis (BPH) *Urol. Res.* **10** 301–3

Feustel A, Wennrich R and Dittrich H 1989 Investigations of trace elements in metastases and primary carcinoma of the prostate *Urol. Res.* **17** 107–9

Floyd C E Jr *et al* 2004 Neutron stimulated emission computed tomography of stable isotopes *Proc. SPIE* **5368** 248–54

Geraki K, Farquharson M J and Bradley D A 2002 Concentrations of Fe, Cu and Zn in breast tissue: a synchrotron XRF study *Phys. Med. Biol.* **47** 2327–39

Ghadirian P, Maisonneuve P, Perret C, Kennedy G, Boyle P, Krewski D and Lacroix A 2000 A case-control study of toenail selenium and cancer of the breast, colon, and prostate *Cancer Detect. Prev.* **24** 305–13

Gozani T U 1994 Novel applications of fast neutron interrogation methods *Nucl. Instrum. Methods Phys. Res.* A **353** 635–40

Gregoriadis G C, Apostolidis N S, Romanos A N and Paradellis T P 1983 A comparative study of trace elements in normal and cancerous colorectal tissues *Cancer* **52** 508–19

Habib F K, Hammond G L, Lee I R, Dawson J B, Mason M K, Smith P H, Stitch S R Y K, Meade A G, Rack E P and Blotcky A J 1976 Metal-androgen interrelationships in carcinoma and hyperplasia of the human prostate *J. Endocrinol.* **71** 133–41

Johnson W N *et al* 1995 Advanced telescope for high energy nuclear astrophysics (ATHENA) *SPIE Proc. Int. Soc. Opt. Eng.* **2518** 74–84

Kato I, Dnistrian A M, Schwartz M, Toniolo P, Koenig K, Shore R E, Zeleniuch-Jacquotte A, Akhmedkhanov A and Riboli E 1999 Iron intake, body iron stores and colorectal cancer risk in women: a nested case-control study *Int. J. Cancer* **80** 693–8

Katoh Y, Sato T and Yamamoto Y 2003 Use of instrumental neutron activation analysis to determine concentrations of multiple trace elements in human organs *Arch. Environ. Health* **58** 655–61

Kollmer W E, Schramel P and Samsal K 1972 Simultaneous determination of nine elements in some tissues of the rat using neutron activation analysis *Phys. Med. Biol.* **17** 555–62

Kubo H, Hashimoto S and Ishibashi A 1976 Simultaneous determinations of Fe, Cu, Zn, and Br concentrations in human tissue sections *Med. Phys.* **3** 204–9

LeBlanc J W, Clinthorne N H, Hua C H, NygŒrd E, Rogers W L, Wehe D K, Weilhammer P and Wilderman S J 1998 C-SPRINT: a prototype Compton camera system for low energy gamma ray imaging *IEEE Trans. Nucl. Sci.* **45** 943–9

Margalioth E J, Schenker J G and Chevion M 1983 Copper and zinc levels in normal and malignant tissues *Cancer* **52** 868–72

Milman N, Laursen J, Podenphant J and Staun-Olsen P 1983 Iron, copper, zinc, and selenium in lumen liver tissue measured by X-ray fluorescence spectrometry *Scand. J. Clin. Lab. Invest.* **43** 691–7

Morgan W D 2000 Of mermaids and mountains. Three decades of prompt activation *in vivo Ann. N. Y. Acad. Sci.* **904** 128–33

Mussalo-Rauhamaa H, Piepponen S, Lehto J, Kauppila R and Auvinen O 1993 Cu, Zn, Se and Mg concentrations in breast fat of Finnish breast cancer patients and healthy controls *Trace Elem. Med.* **10** 13–5

Nelson R L, Davis F G, Sutter E, Sobin L H, Kikendall J W and Bowen P 1994 Body iron stores and risk of colonic neoplasia *J. Natl Cancer Inst.* **86** 455–60

Ng K-H, Bradley D and Looi L-M 1997 Elevated trace element concentrations in malignant breast tissues *Br. J. Radiol.* 375–82

NNDC (National Nuclear Data Center) 2005 *Brookhaven National Laboratory* http://www.nndc.bnl.gov (date of access 14 Sept. 2005)

Nunes W, da Silva A, Crispim V and Schirru R 2002 Explosives detection using prompt-gamma neutron activation and neural networks *Appl. Radiat. Isot.* **56** 937–43

Ogunlewe J O and Osegbe D N 1989 Zinc and cadmium concentrations in indigenous blacks with normal, hypertrophic, and malignant prostate *Cancer* **63** 1388–92

Palm R, Wahlstrom G and Hallmans G 1990 Age related changes in weight and concentrations of zinc and copper in the brain of the adult rat *Lab. Anim.* **24** 240–5

Persigehl M, Schicha H, Kasperek K and Klein H J 1977 Trace element concentration in human organs in dependence of age *Beitr. Pathol.* **161** 209–20

Picurelli L, Olcina P V, Roig M D and Ferrer J 1991 Determination of Fe, Mg, Cu, and Zn in normal and pathological prostatic tissue *Actas Urol. Esp.* **15** 344–50

Platz E A, Helzlsouer K J, Hoffman S C, Morris J S, Baskett C K and Comstock G W 2002 Prediagnostic toenail cadmium and zinc and subsequent prostate cancer risk *Prostate* **52** 288–96

Rizk S and Sky-Peck H 1984 Comparison between concentrations of trace elements in normal and neoplastic human breast tissue *Cancer Res.* **44** 5390–9

Romics I and Katchalova L 1983 Spectrographic determination of zinc in the tissues of adenoma and carcinoma of the prostate *Int. Urol. Nephrol.* **15** 171–6

Santoliquido P, Southwick H and Olwin J 1976 Trace metal levels in cancer of the breast *Surg. Gynecol. Obstet.* **142** 65–70

Singh M and Doria D 1983 An electronically collimated gamma camera for single photon emission computed tomography: II. Image reconstruction and preliminary experimental measurements *Med. Phys.* **10** 428–35

Stedman J D and Spyrou N M 1995 Major and trace element concentration differences between right and left hemispheres of the 'normal' human brain *Nutrition* **11** 542–5

Takahashi S, Hatashita S, Taba Y, Sun X Z, Kubota Y and Yoshida S 2000 Determination of the spatial distribution of major elements in the rat brain with x-ray fluorescence analysis *J. Neurosci. Methods* **100** 53–63

Witkowski K, Kozlowski A, Pardela M, Piecuch J and Walichiewicz P 1993 Level of copper in plasma and tissue of patients with esophageal and large bowel cancer *Wiad. Lek.* **46** 586–8 (article in Polish: from translated abstract)

Xiao K Q and Henderson W J 1992 Electron microscopy microanalysis and quantitative detection of trace elements in carcinoma of the colon *Zhonghua Bing Li Xue Za Zhi* **21** 142–5 (article in Chinese: from translated abstract)

Yoshinaga J, Imai H, Nakazawa M and Suzuki T 1990 Lack of significantly positive correlations between elemental concentrations in hair and organs *Sci. Total Environ.* **99** 125–35

Yukawa M, Suzuki-Yasumoto M, Amano K and Terai M 1980 Distribution of trace elements in the human body determined by neutron activation analysis *Arch. Environ. Health* **35** 36–44

Zaichick V Ye, Sviridova T V and Zaichick S V 1997 Zinc in the human prostate gland: normal, hyperplastic and cancerous *Int. Urol. Nephrol.* **29** 565–74

# Breast Cancer Diagnosis using Neutron Stimulated Emission Computed Tomography: Dose and Count Requirements

Carey E. Floyd Jr.[*a,b,c] , Janelle E. Bender[a,b], Brian Harrawood[b], Amy C. Sharma[a,b], Anuj Kapadia[a,b], Georgia D. Tourassi[b], Joseph Y. Lo[a,b,c], Calvin Howell[d]

[a]Department of Biomedical Engineering
[b]Department of Radiology, Duke Advanced Imaging Laboratories
[c]Medical Physics Graduate Program
[d]Department of Physics and Triangle Universities Nuclear Laboratory
Duke University, Durham NC 27710 Tel: (919) 684-4138, Fax: (919) 684-3934
Email: carey.floyd@duke.edu

## ABSTRACT

Neutron Stimulated Emission Computed Tomography (NSECT) was evaluated as a potential technique for breast cancer diagnosis. NSECT can form a 3D tomographic image with an elemental (isotopic) spectrum provided at each reconstructed voxel. The target is illuminated (in vivo) by a neutron beam that scatters in-elastically producing characteristic gamma emission that is acquired tomographically with a spectrograph. Images are reconstructed of each element in the acquired spectrum. NSECT imaging was simulated for benign and malignant breast masses. A range of the number of incident neutrons was simulated from 19 million to 500k neutrons. Simulation included all known primary and secondary physical interactions in both the breast as well as in the spectrometer. Characteristic energy spectra were acquired by simulation and were analyzed for statistically significant differences between benign and malignant breasts. For 1 million incident neutrons, there were 61 differences in the spectra that were statistically significant ($p < 0.05$). Of these, 23 matched known characteristic emission from 6 elements that have been found in the breast (Br, Cs, K, Mn, Rb, Zn). The dose to two breasts was less than 3% of the dose of a 4 view screening mammogram. Increasing the dose to 52% of the mammogram (19 million neutrons) provided 89 significant spectral differences that matched 30 known emissions from 7 elements that have been found in the breast (Br, Co, Cs, K, Mn, Rb, Zn). Decreasing the dose to 1.4% (500K neutrons) eliminated all statistically significant matches to known elements. This study suggests that NSECT may be a viable technique for detecting human breast cancer in vivo at a reduced dose compared to 4 view screening mammography.

**KEYWORDS:** Novel Methods (OT), Simulation (SIM), Neutrons in Imaging

## 1. INTRODUCTION

This study evaluates the neutron flux and resulting dose required to diagnose breast cancer using Neutron Stimulated Emission Computed Tomography (NSECT). Previous studies using neutron activation analysis (NNA) have demonstrated statistically significant elevation of the concentration of up to 12 elements in malignant breast tissue samples when compared to benign samples[1]. While NAA cannot be adapted to an in-vivo diagnostic examination, NSECT can. In previous studies we have introduced experimental NSECT [2-6] and demonstrated tomographic spectroscopy from multi-element phantoms [7]. In this current study we have evaluated the minimum number of incident neutrons (in a tomographic geometry) required to reject the null hypothesis that benign and malignant breast tissues have the same concentration of Al, Br, Ca, Cl, Co, Cs, Fe, K, Mn, Na, Rb, or Zn. We present the effective dose for exposure of both breasts to these numbers of neutrons to help evaluate the clinical feasibility of the NSECT technique.

No other technique has been proposed to use neutrons in this manner for breast cancer diagnosis. While other neutron-based approaches have been suggested for identification of explosives and contraband, these approaches typically involve relatively large neutron exposures and/or long counting times and thus are unsuitable for in-vivo diagnosis.

The imaging technique described here and named NSECT represents the natural evolution of a previous technique known as PFNA for Pulsed Fast Neutron Analysis. The primary differences are in the use of tomography and statistical classifiers for breast cancer disease detection with NSECT.

Medical Imaging 2006: Physics of Medical Imaging, edited by Michael J. Flynn, Jiang Hsieh,
Proceedings of SPIE Vol. 6142, 61421O, (2006) · 1605-7422/06/$15 · doi: 10.1117/12.656045

## 2. METHODS:

NSECT forms a 3D tomographic image with an elemental (isotopic) spectrum provided at each reconstructed voxel. The target is illuminated (in vivo) by a neutron beam that scatters in-elastically producing characteristic gamma emission that is acquired tomographically with a spectrograph. Images are reconstructed of each element in the target. While a majority of our neutron scattering experiments have been conducted at 6 to 7.5 MeV neutron energy in a nuclear structure accelerator laboratory (Triangle Universities nuclear Laboratory: TUNL, www.tunl.edu), our proposed clinical implementation of NSECT would be at a neutron energy of 2.5 MeV using commercially available "neutron tube". The commercial neutron tube forms a neutron beam via the deuteron + deuteron -> $^{3}$He + neutron reaction in a sealed tube. This is the same reaction that we use as a neutron source at TUNL. These tubes are used commercially to log petroleum wells. For the current study, NSECT of the breast was simulated at 2.5 MeV by a Monte Carlo model that we built from the GEANT4 C++ toolkit [8].

GEANT4 simulates materials by allowing the user to specify the percent contribution of each element and isotope in the material. A variety of geometric shapes are available for simulating the objects with which the neutrons and gammas interact. We modeled the uncompressed pendent breast as a cylinder of tissue with diameter 14 cm and length 10 cm. Table 1 shows the composition of normal and malignant breast tissue. The density of benign breast tissue was modeled as 1.01 g/cm$^3$ while that of malignant tissue was 1.03 g/cm$^3$ [9]. The percentage for each element was computed as follows. The percentage for O, C, and H were taken from the IRCU report. For the trace elements, the dry weight composition values for benign and malignant were taken from reference [1] They were converted to wet weights using the dry/wet ratio from [1] and the densities. The total density for benign and malignant tissue was used to normalize each trace element contribution and the percent contribution was calculated.

Table 1: Elemental composition of model of benign and malignant breast tissue.

| Number | Element | Symbol | Benign Composition | Malignant Composition |
|---|---|---|---|---|
| 1 | Nitrogen | N | 2.571 | 2.456 |
| 2 | Oxygen | O | 61.43 | 58.67 |
| 3 | Carbon | C | 22.86 | 21.83 |
| 4 | Hydrogen | H | 9.878 | 9.434 |
| 5 | Aluminum | Al | 0.0044 | 0.0068 |
| 6 | Bromine | Br | 0.0047 | 0.0079 |
| 7 | Calcium | Ca | 0.0548 | 0.1354 |
| 8 | Clorine | Cl | 1.306 | 2.583 |
| 9 | Cobalt | Co | 0.00014 | 0.00024 |
| 10 | Cesium | Cs | 0.000002 | 0.000004 |
| 11 | Iron | Fe | 0.0648 | 0.0943 |
| 12 | Potasium | K | 0.5912 | 2.357 |
| 13 | Manganese | Mn | 0.00026 | 0.00038 |
| 14 | Sodium | Na | 1.227 | 2.403 |
| 15 | Rubidium | Rb | 0.0040 | 0.0070 |
| 16 | Zinc | Zn | 0.0077 | 0.0137 |

A neutron beam of 1 cm$^2$ area was simulated incident on the breast model centered at the level of the malignancy.

The gamma spectrometer was modeled as a cylinder of Germanium with density 5.32 g/cm3, radius 3.5 cm and height 9 cm. This cylinder was oriented in the plane of the neutron beam and normal to the breast cylinder axis. A majority of the energy state transitions expected from in-elastic scattering of neutrons from the materials that comprise the breast will be electric quadrupole transitions and thus have peaks in the gamma emission cross section at 45,135, 225, and 315 degrees relative to the incident neutron beam and azimuthally symmetric about the axis of the beam. Because the neutron beam scatters primarily in the forward direction and we wished to avoid scattered neutrons striking the detector, we placed the Ge detector at 135 degrees, at a radial distance of 20 cm with its central axis pointing at the origin. This arrangement replicates that of our laboratory experiments.

Spectra acquisition was simulated by recording every event where energy was deposited in the volume of the Ge cylinder. Since each particle event is tracked and reported separately, this simulation was sensitive to gammas emitted by the neutron stimulated breast, scattered neutrons themselves, and all subsequent interactions within the detector. This approach implicitly includes pair production product escape and Compton escape effects in the Ge detector. No Compton shield was included in the simulation. All interaction events were reported as a list mode output. After running the GEANT4 simulation for the respective number of incident neutrons for the selected breast model, spectra were computed by summing all energy deposited in the detector for each incident neutron. These energies were rounded to 0.1% of their value in keeping with the appropriate energy resolution of a High Purity Germanium (HPGe) detector and a histogram was formed with bin width of 1 keV and range from 0 to 3000 keV. This range is adequate for simulating the gamma emission from inelastically scattered neutrons having 2.5 MeV energy. This will not record the infrequent higher energy gammas emitted as a result of slow neutron capture on some target nuclei. Exploratory simulations demonstrated these events to occur for fewer than 1 out 200,000 incident neutrons and that they contribute a negligible amount of energy to the total spectrum or to the absorbed dose.

To identify elements that could signal a difference between malignant and benign, we formed a difference spectrum by subtracting the spectrum from the benign breast model and the malignant breast model and then looked for peaks that were statistically significantly different from zero. The resulting difference spectrum for the simulation was analyzed by comparing the energies of those peaks that were different from zero with a list of all gamma energies emitted by level transitions in isotopes included in our breast model. These spectrum values are Poisson distributed and so their variance is equal to their mean value. The peak values were subtracted (malignant - benign) to form a difference peak value. The variances were added to form the variance in the difference peak value. The significance of each peak was determined from a two-tailed t-test of the hypothesis that the difference peak value was zero. The t-test was performed using the difference peak value and its standard deviation as calculated above. For the t-test, an arbitrary but customary cut off value of 0.05 was accepted for the probability that the difference peak value was zero. For each number of incident neutrons, we examined the number of peaks for which the null hypothesis was rejected.

For each of these peaks for which the null hypothesis was rejected, we attempted to identify the element that generated the peak. We compared the energy of the peaks to the emission energy for transitions between states in the target nuclei. These energies were obtained from a database that we assembled from the National Nuclear Database at Brookhaven National Laboratories (www.bnl.gov). Our database is as fully comprehensive as the one at Brookhaven and includes only the stable isotopes of those elements listed in table 1 and includes all of the excited state transitions that are included in the BNL database. In this study we considered only states that could be excited by our neutron beam energy of 2.5 MeV. For each number of incident neutrons, we recorded the number of peaks that were statistically significantly different from zero, the number of these peaks that corresponded to emission gamma energies from elements in our breast model, the number of isotopes represented by this set, the number of elements that were represented by this set, and the identity of these elements. These are shown below in Table 2.

The equivalent dose to a patient for each number of incident neutrons was calculated. A separate simulation was performed to estimate the total energy deposited in the breast for incident 2.5 MeV neutrons. The value was found to be 1.4 MeV per incident (2.5 MeV) neutron on average. So the total number of neutrons was multiplied by this factor to compute the total energy deposited in the breast. This value was converted to units of Gy by converting MeV to Joules (1.4 MeVconverted to Joules is $2.24 \times 10^{-13}$ J/neutron) and dividing by the mass in kg of the breast that was illuminated to acquire the spectrum. This provides the absorbed dose. To compute the equivalent dose, this absorbed dose was multiplied by the neutron weighting factor which is 10 and by the breast weighting factor which is 0.05. The result is in units of Sv. The mass of the breast that is illuminated is computed by multiplying the volume of the beam that intersects the breast by the density of the appropriate breast model (benign, malignant). For the non-tomographic use of NSECT, the central portion of the breast is illuminated which is a volume denoted by V = 10 $cm^3$. The increased density of the malignant region does not appreciably change the density of the breast from 1.01 $g/cm^3$ and so the mass of the region that is illuminated is $1.01 \times 10^{-2}$ kg. Divided by the mass gives $2.22 \times 10^{-11}$ Gy/neutron. Multiply by the weighting factors equals $1.11 \times 10^{-11}$ Sv/neutron or $1.11 \times 10^{-8}$ mSv/neutron.

## 3. RESULTS:

We will begin this section by showing an individual spectrum in Fig. 1 in which peaks corresponding to elements in the breast models are evident.

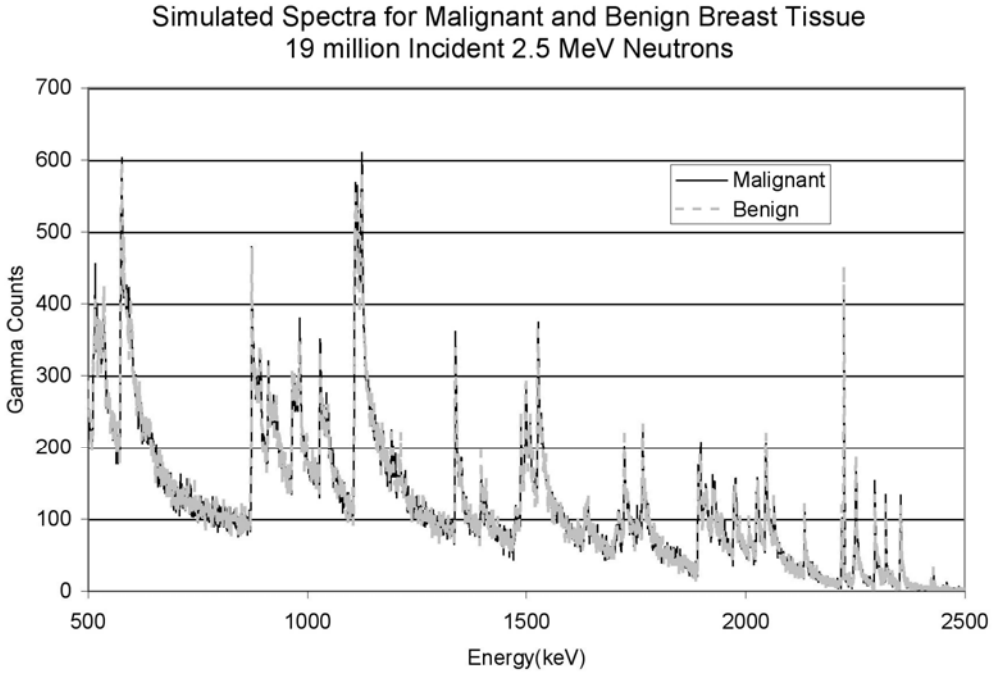


Figure 1 Simulated NSECT spectra for malignant and benign breast tissue. There were 19 million incident neutrons each with 2.5 MeV energy. The solid curve in the background is the spectrum for the malignant tissue, The grey dashed curve in the foreground is for the benign tissue.

Fig. 2 shows the difference spectrum obtained by subtracting the two spectra shown in Fig. 1.

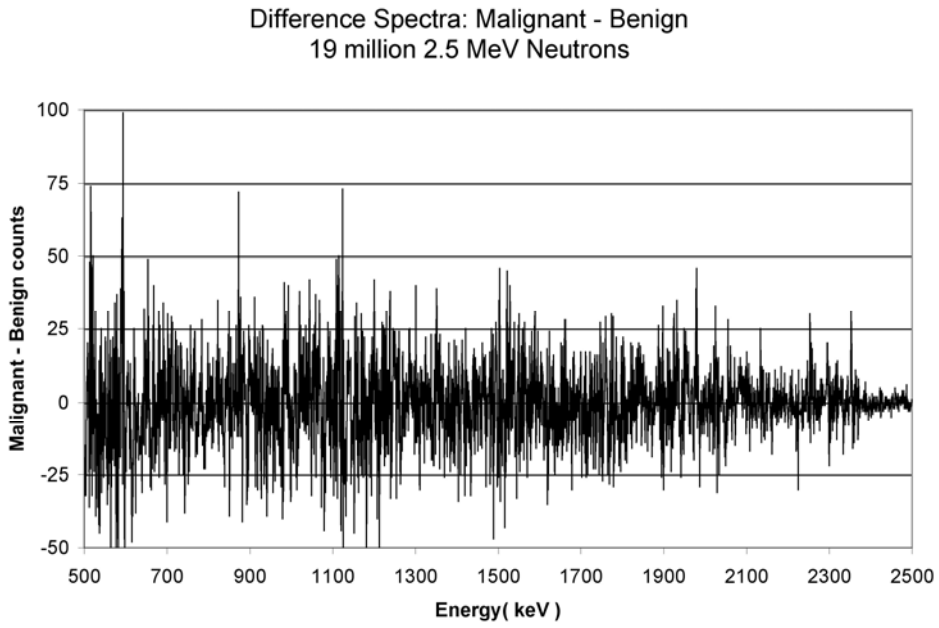


Figure 2 This spectrum shows the difference between the malignant breast tissue spectrum and the benign breast tissue spectrum for 19 million incident 2.5 MeV neutrons.

Fig.3 shows the magnitude and matching element for some of the significant difference peaks.

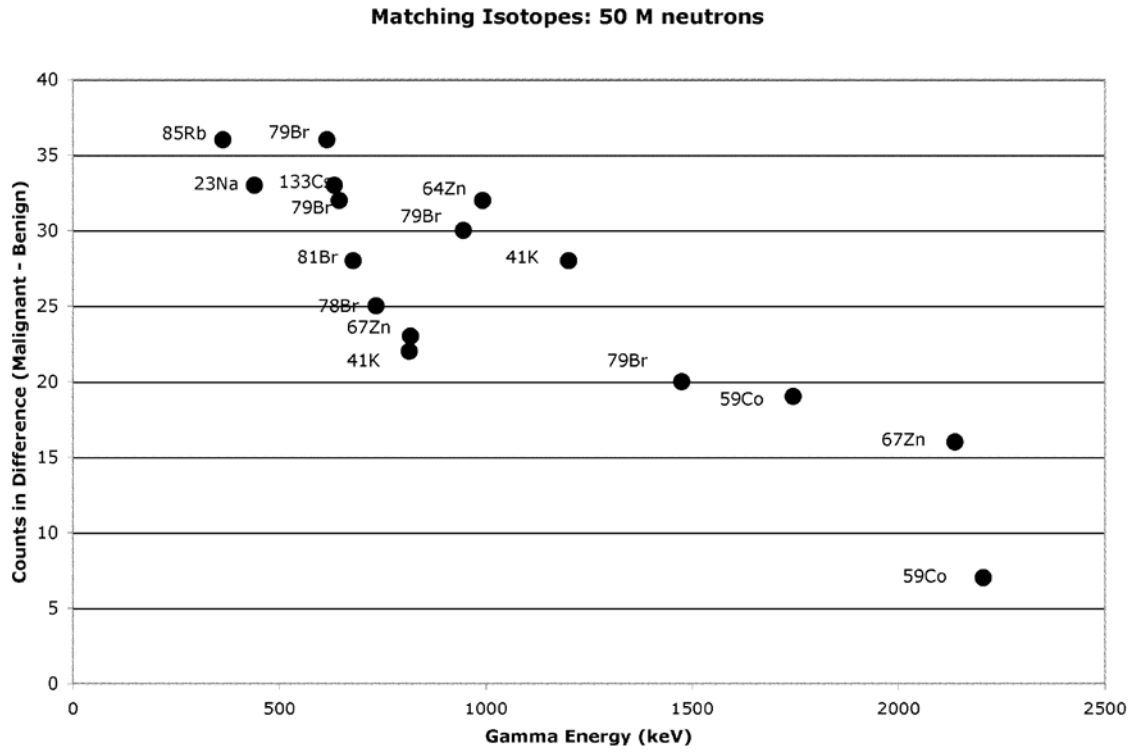


Figure 3 Plot of some energy channels for which the difference between malignant and benign yields was significant and for which there was a match to a characteristic gamma emission from a unique element.

**Table 2**

| Number of Neutrons (millions)[a] | 50 | 40 | 20 | 10 | 1 | 0.5 |
|---|---|---|---|---|---|---|
| Number of spectral channels with significant difference [b] | 63 | 40 | 35 | 64 | 42 | 0 |
| Number with matches [c] | 16 | 12 | 6 | 10 | 11 | 0 |
| Number of matching isotopes[d] | 9 | 7 | 5 | 5 | 9 | 0 |
| Number of matching elements[e] | 7 | 5 | 4 | 3 | 7 | 0 |
| Elements uniquely corresponding to significant differences [f] | Br, Co, Cs, K, Na, Rb, Zn | Br, Co, Cs, K, Zn | Br, Co, K, Zn | Br, Co, Zn | Al, Br, Co, K, Mn, Rb, Zn | |
| Dose to two breasts (mSv) [g] | 0.0090 | 0.0072 | 0.0036 | 0.0018 | 0.0002 | 0.00009 |
| Percent of dose of a 4 view mammogram [h] | 14% | 11.2% | 5.6% | 2.8% | 0.28% | 0.14% |

Table 2 As a function of (a)the number of incident neutrons, this table shows: (b)the number of spectral channels (1 keV/channel) with a statistically significant difference between benign and malignant (note: none of these channels were adjacent), (c)the number of these for which at least one element in our breast model had a characteristic gamma emission that matched in energy, (d)the number distinct matches between isotope and spectral difference, (e)the number of elements for which there was a unique matching between element and spectral difference, (f)the elements for which there was a unique matching between element and spectral difference, (g)the dose to both breasts, (h)the percentage of the dose of a standard 4 view mammographic examination that this dose represents.

As the number of incident neutrons was decreased, the dose decreased as did the number spectral channels with significant differences and the number of matches to known elements in the breast. For 1 million neutrons, the dose to both breasts was less than 0.3% of a 4 view screening mammogram and 61 independent energy channels had significant differences with 11 of these matching known characteristic emissions from 9 stable isotopes of elements: Br, Cs, K, Na, Rb, and Zn. For 500K neutrons, there were no matches. For 50 million neutrons, (14% of the dose of the 4 view screening mammogram), there were 63 channels with significant differences and 16 of these had matches with 7 elements.

## 5. CONCLUSION

In these simulations, NSECT provided statistically significant differentiation between benign and malignant breasts at only 0.3% of the dose of a 4 view screening mammogram. The differentiation was based on 11 significant spectral differences ($p<0.05$) that matched 9 stable isotopes of 7 known elements. Increasing the dose by a factor of 50 did not appreciably improve the diagnostic power while decreasing the dose by a factor of 2 eliminated all significant differences. This is the first demonstration of the potential for breast cancer diagnosis using neutrons.


## ACKNOWLEDGEMENT

Supported in part by: NIH Training Grant EB001040 and Innovative Research Grant R21CA106873.


## REFERENCES


1. Ng, K.-H., D. Bradley, and L.-M. Looi, *Elevated trace element concentrations in malignant breast tissues.* British Journal of Radiology, 1997. **70**(April): p. 375-382.
2. Floyd, C.E., et al., *Introduction to Neutron Stimulated Emission Computed Tomography*, submitted to *Physics in Medicine and Biology*. 2005.
3. Floyd, C.E., et al. *Neutron stimulated emission computed tomography of stable isotopes*. in *SPIE 5368, 248-254*. 2004.
4. Floyd, C.E.J., et al., *Neutron Stimulated Emission Computed Tomography: Background Corrections.* Submitted to Medical Physics, 2005.
5. Kapadia, A. and C. Floyd, Jr. *An attenuation correction technique to correct for neutron and gamma attenuation in the reconstructed image of a neutron stimulated emission computed tomography (NSECT) system*. in *Medical Imaging 2005: Visualization, Image-Guided Procedures, and Display, SPIE*. 5745; 737-743, 2005..
6. Kapadia, A., et al., *Experimental Implementation of Neutron Stimulated Emission Computed Tomography (NSECT).* Nuclear Instruments and Methods Research Section A, Submitted 2005.
7. Floyd, C., et al., *Neutron Stimulated Emission Computed Tomography of a Multi-element Phantom.* Submitted to IEEE Transactions on Medical Imaging, 2005.
8. Agostinelli, S. and G. Collaboration, *GEANT4: A Simulation Toolkit.* Nuclear Instruments and Methods in Physics Research NIM A, 2003. **506**: p. 250-303.
9. ICRU, *Tissue Substitutes in Radiation Dosimetry and Measurement*. 1988, ICRU.

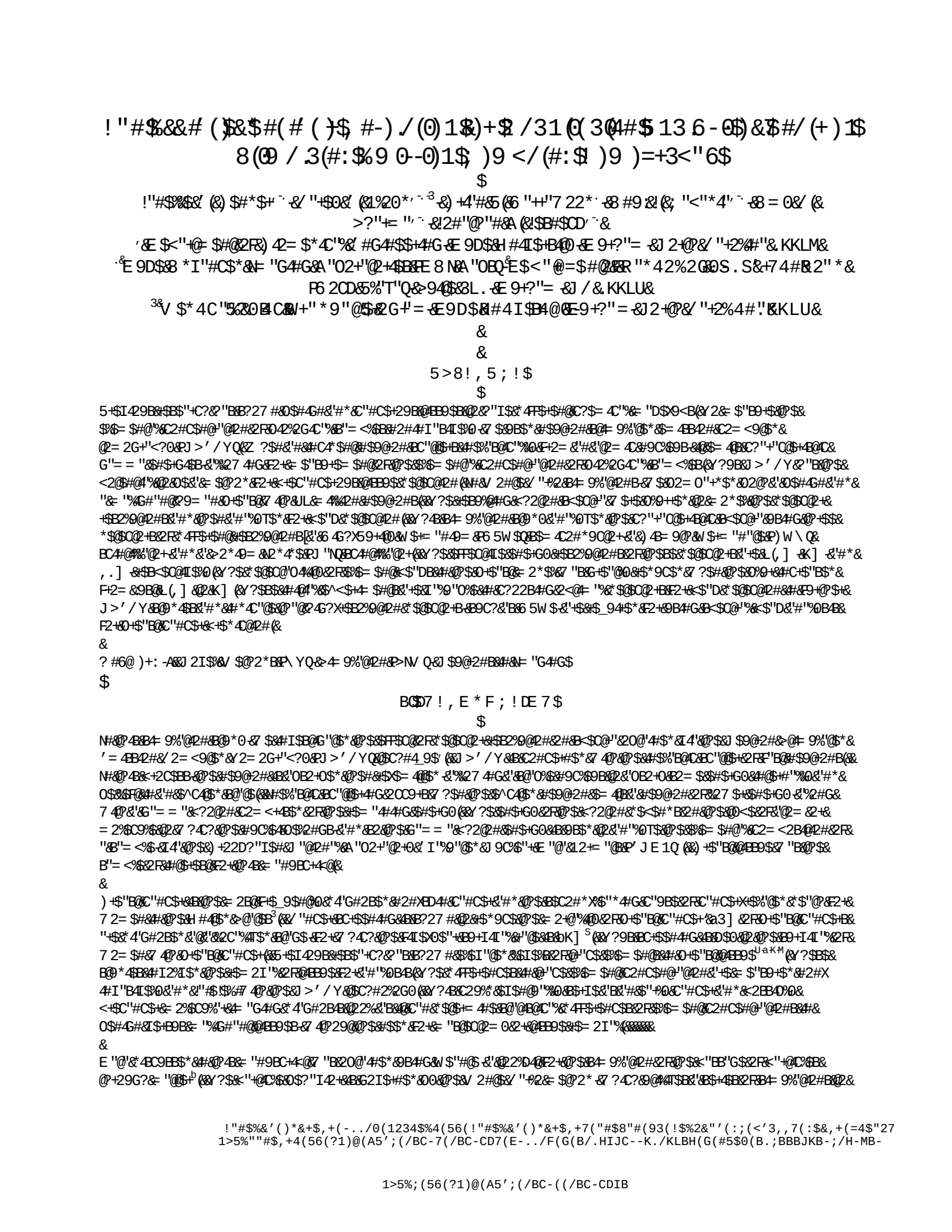

!"#$%&&#'(#)$&$#(#'(*)+$,#-).//(0)1$&)+$2/31(0(3(4#$5136-0$)&7$#/(+)1$
8(09/.3(#:$%90-0)1$,)9</(#:$1)9)=+3<"6$
$
!"#$%&$'(&)$#*$+,-.&/"+$0&'(&1%20*',-3.&)+4'#&5(&6"++"7 22*'-&8#9:&1(&;"<"*4',-.&8=0&/(&
>?"+=",-.&12#"@?"#&A(&1$B#$CD',-&
'&E$<"+@=$#@&2FR&)42=$*4C'"%&'#G4#$$+4#G-&E9D$&H#4I$+B4@0-&E9+?"=-&J2+@?&/"+2%4#"&.KKLM&
.&E9D$&8*I"#C$*&N=''G4#G&A"O2+"@2+4$B&RE8N&A"OBQ&E$<"@=$#@&&R"*42%2G&0S.S&+74#&2"*&
P62CD&5%'T"Q&-94@$&3L.-&E9+?"=-&J/&.KKLU&
3&V$*4C"%&0B4C&W+"*9"@5&2G+'=-&E9D$&#4I$B4@&E9+?"=-&J2+@?&/"+2%4#".&KLU&
&
&
5>8!,5;!$
$
5+$I429B&$B$"+C?&"B&B?27#&0$#4G#&'#*&C"#C$+29B&@&B9$B&@&&"I$&'4F$+$#@&C?$=4C'"%&="D$X9<B(&Y2&=$"B9+$&@?$&
$%&=$#@'%&C2#C$#@"@2#&2FR042%2G4C'"%&B'=<%&B&#2#4#I"B4I$%0-&7$9B$*&#$9@2#&B@4=9%'@$*&$=4BB42#&C2=<9@$*&
@2=2G+'"<?0&PJ>'/YQ(&Z?$#&'#&#C4*$#@&#$9@2#&BC"@@+B&4#$%'B@C'%0&4+2=&'#&'@2=4C&#9C%$9B-&@$=4B&C?"+"C@$+4@C&
G'"==''&$#$+G4$B-&'%&27 4#G&F2+&=$"B9+$=$#@&2FR@?$&$%=$#@'%&C2#C$#@"@2#&2FR042%2G4C'"%&B'=<%&B(&Y?9B&J>'/Y&?"B&@?$&
<2@$#@4'%&@&0$&'&=$@?2*&F2+&<+$C'"#C$+29B&@&B9$&'$@$C@2#(&N#&V 2#@$&/"+%&B4=9%'@2#B-&7$&O2=O"+*$*&O2@?&'&O$#4G#&'#*&
"&='%&G#"#@&?9="#&O+$"B@&7 4@?&JL&=4%&2#&#$9@2#B(&Y?$&$B9%@#G&<?2@2#&B<$C@"'&7$+$&O9+$*&@2&=2*$%@?$&'$@$C@2+&
+$B2%9@2#B&'#*&@?$#&'#"%0T$*&F2+&<$"D&'$@$C@2#(&Y?4B&B4=9%'@2#&@9*0&'#"%0T$*&@?$&C?"+"C@$+4@C&B<$C@"&9B4#G&@?+$$&
*$@$C@2+B&2F&'4F$+$#@&$B2%9@2#B[&'&64G?X59+4@&W$+="#49=&F65W$Q&B$=4C2#*9C@2+&'&)4B=9@?&W$+="#"(@$P)W\Q&
BC4#@4%'@2+&'#*&'&>2*49=&N2*4*$&PJ"NQ&BC4#@4%'@2+(&Y?$&$FF$C@4I$&#$+G0&$B2%9@2#B&2F&@?$B$&'$@$C@2+B&'+$L(,]-&K]-&'#*&
,.]-&$B<$C@4I$%0(&Y?$&'$@$C@'O4%&@&2F&$%=$#@&$"DB&4#@?$&O+$"B@&=2*$%&7"B&G+$"@%0&$*9C$*&7?$#@?$&O%0+&4#C+$"B$*&
F+2=&9B@&L(,]&@2&K](&Y?$B$&4#4@'%&$\<$+4=$#@B&'+$I"%0"O%&4#&C?22B4#G&2<@4="%&'$@$C@2+B&F2+&<$"D&'$@$C@2#&4#&F9+@?$+&
J>'/Y&B@*4$B&'#*&#*4C'"@$&@"@&2G?X$B2%9@2#&'$@$C@2+B&B9C?&'B&65W$&'+$&$_94$*&F2+&9B4#G&B<$C@"%&$"D&'#"%0B4B&
F2+&O+$"B@&C"#C$+&<+$*4C@2#(&
&
?#6@)+:-A&J2I$%&V$@?2*B&P\YQ&=4=9%'@2#&P>NVQ&J$9@2#B&4#&N="G4#G$
$
B($D7!,E*F;!DE7$
$
N#&@?4B&B4=9%'@2#&B@9*0&7$&#I$B@G"@$*&@?$&$FF$C@&2F&'$@$C@2+&+$B2%9@2#&2#&B<$C@"&2O@'4#$*&I4'&@?$&J$9@2#&=&@4=9%'@$*&
'=4BB42#&/2=<9@$*&Y2=2G+'"<?0&PJ>'/YQ&@C?#4_9$'(&J>'/Y&4B&C2#C$+#$*&7 4@?&@?$4#$%'B@C&BC"'@$+&2F&'B@&#$9@2#B(&&
N#&@?4&=+2C$BB+&@?$&#$9@2#&B&'OB2+O$*&@?$+&#$X$=4@$*&'%&27 4#G&'B@'O$&#9C%$9B@2&'OB2+O&B2=$&$#$+G0&4#@$+#'%0&'#*&
O$&$F@4#&'#&$^C4@$*&B@'@$(&N#$%'B@C&BC"'@$+4#G&2CC9+B&7?$#@?$&$^C4@$*&$9@2#&$=4B&'&$9@2#&2F&27 $+&$+G0&'%2#G&&
7 4@?&'&G"=''&<?2@2#&C2=<+4B$*&2F&@?$&$=''4#4#G&$#+G0(&Y?$&$#+G0&2F&@?$&<?2@2#&'$<$#*B&2#&@?$&@<$&2F&'@2=&2+&
=2%&C9%&@2&7?4C?&@?$&#9C%&O$%2#GB-&'#*&B2&@?$&G"=''&<?2@2#&$+G0&B9B$*&@2&'#"%0T$&@?$&$%=$#@'%&C2=<2B4@2#&2F&
"&B"=<%&-&14'&@?$&)+22D?"I$#&J"@2#'"%&A"O2+"@2+O&'I"%0"@$*&J9C%$"+&E"@'&12+="@&P'JE1Q(&)+$"B@&EB9$&7"B@?$&
B'=<%&2F&4#@$+#$B@&F2+&@?4B&="#9BC+4<@&
&
)+$"B@&C"#C$+&B@?$&=2B@F+$_9$#@%0&*4'G#2B$*&#2#XBD4#&C"#C$+&'#*&@?$&B$C2#*X%&"*4#G&C"9B$2F&C"#C$+X+$%'@$*&'$@?&F2+&
7 2=$#&#@?$%&#4@$*&-@'@B3(&Y"#C$+&BC+$$#4G&B&B?27 #&@2&$*9C$@?$&=2+@'%0&2F0+$"B@&C"#C$+'&a3]&2F0+$"B@&C"#C$+B&
"+$&*4'G#2B$*&'@'&2C'%4T$*&B@'G$&F2+&7?4C?&@?$&F4I$X0$"+&B9+I4I"%&"@$&B&K]S(&Y?9B&BC+$$#4G&B&D$0&@?@?$&B9+I4I"%2F&
7 2=$#&7 4@?&O+$"B@&C"#C$+(&5+$I429B&$B$"+C?&"B&B?27 #&@$&I"@$*&&I$%&B2F&@"C$&@$=$#@&4&O+$"B@&B9$U-aK<M(&Y?$B$&
B@*4B&4I2%I$*&@?$&$=2I"%2F&@&B9$&2+&'#"%0B4B(&Y?$*4FB+$#C$B&4@"C$&@$=$#@&C2#C$#@"@2#&'+$&=$"B9+$*&#2#X
4#I"B4I$%0&'#*&'#$%#74@?&@?$&J>'/Y&@C?#2%2G0(&Y?4B&C29%&$I$#@)"%0&B$+I$&'B&'#$&"+%0&C"#C$+&'#*&<2B4O%0&
<+$C"#C$+&=2%C9%'+&4=''G4#G&'4'G#2B4B@2%&'B&@C"#&'$@=4#$B@'@2#@C"%&4FB+$#C$B2F&@%$=$#@&C2#C$#@"@2#B&4#&
O$#4G#&I$+B9B&="%G#"#@&@EB9$B-&7 4@29&@$&$*&F2+&="B@&C@2=0&2+&@EB9$&=2I"%(&&&&&
&
E"@'&4BC9BB$*&#&@?4B&="#9BC+4<@&"B&2O@'4#$*&9B4#G&W$"#@&'&@2%D4F2+&@?$B4=9%'@2#&2F&@?$&"BB'G$&2F&"+&C%$B&
@?+29G?&="@$+b(&Y?$&"+&C%&O$?"I42+&B&G2I$#*&O0&@?$&V 2#@$&/"+%&=$@2*&7?4C?&@4%T$B&'B$&+$B&2F&B4=9%'@2#B&@2&

!"#$%&'()*&+$,+(-../0(1234$%4(56(!"#$%&'()*&+$,+7("#$8"#(93(!$%2&"'(:;(<'3,,7(:$&,+(=4$"27
1>5%""#$,+4(56(?1)@(A5';(/BC-7(/BC-CD7(E-../F(G(B/.HIJC--K./KLBH(G(#5$0(B.;BBBJKB-;/H-MB-

1>5%;(56(?1)@(A5';(/BC-(((/BC-CDIB

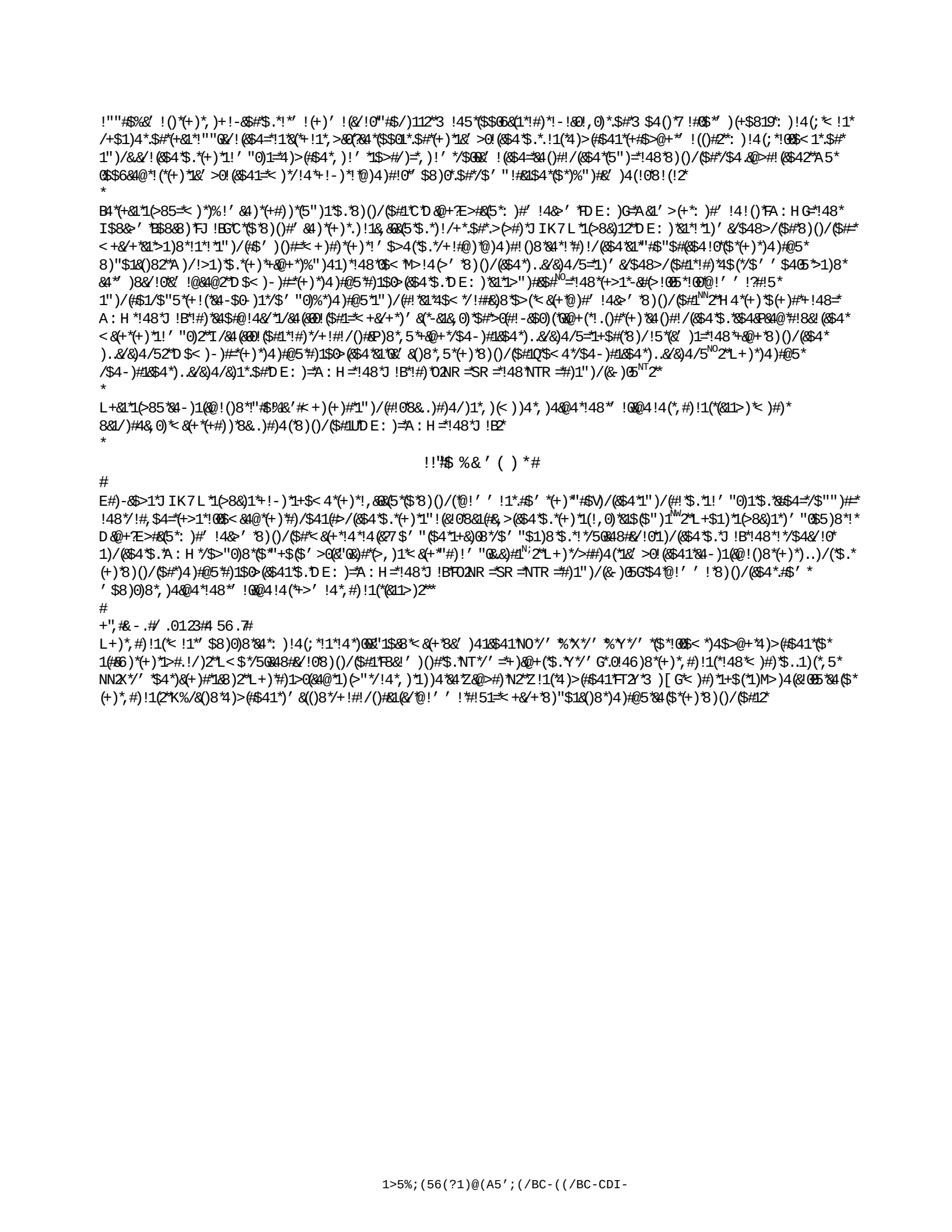

!

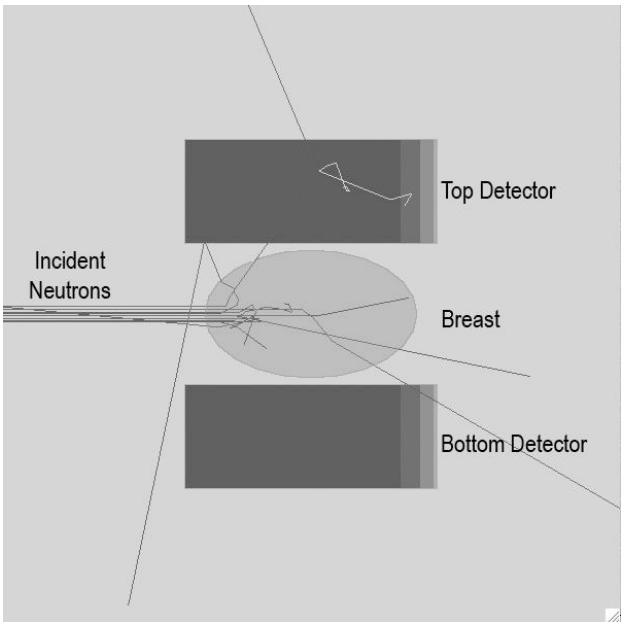


!

! "#$%&'()'* +,&-'.&/$01"23'/4&'/+0',&/&5/+%67'#78 8 7'&9&3/"'.9".": -&7.'7'-'!#4/'-'!3&.'%&0%&.&3/'#78 8 7'%7=.1'

!

"#$!%&'(!)(%!*%+,-+!&+.!/'&0,-+&+)!/'#.%01!)(%$%!2%$%!34!$5+6!#7!34!/',0,#+!+%5)$#+6!%&'(1!8,%0.,+-!344!/',0,#+!,+',.%+)!
+%5)$#+6!)#)&07#$!%,)(%$!'&0%9!!:&*0%!3!6(#2 6!)(%!.,7'%$%+'%6!,+!)(%!)$&'%!%0%/ %+)!'#+'%+)$&),#+!,+!)(%!*%+,-+!;%$66 6!
/ &0,-+&+)!*$%&6)9!!<$8!2%,-()62%$%!'#+;%$)%.!)#!2%)2%,-()656,+-!&!2%)=)#=.$8!$&),#'9!?)6(#50.!*%!+#)%.!)(&)!)($%%#7!
)(%!/ &0#$!%0%/ %+)6!A!#B8-%+1!'&$*#+1!&+.!+,)$#-%+!A!'#/ C$,6%.!)(%6&/ %!C$#C#$),#+!#7!)(%!*%+,-+!&+.!/ &0,-+&+)!),665%9!!
:(%!C%$'%+)&-%!#7!(8.$#-%+!;&$%.!60,-()8!)#!&''#5+)!7#$!)(%!.,7'%$%+'%!,+!)(%!)#)&0&/ #5+)!#7!)$&'%!%0%/ %+)6!,+!)(%!
),665%!)8C%69!D)!)(%!+%5)$#+%+%$8!56%.!(%$%!EF9>!G%H I1!C%&J6!7$#/ #B8-%+1!'&$*#+1!(8.$#-%+!&+.!+,)$#-%+!2,0!+#)!
6(#2 !5C9!!:(%!)$&'%%0%/ %+)6!&0$%!)(56!)(%!/ &0#$!%C%&J6!)(&)!2%$%!.%%'&*0%!7#$!)(%6%6)5.8!C&$&/ %)$&69!K%'&56%!)(%!
/ &0,-+&+)#!*%+,-+!$&),#!7#$!%#7!)(%!$&'%%0%/ %+)6!2&6!0%66!)(&+!#+%1!C%'&$J&+&$86,62&6!C%$7#$/ %.!#+!
+%-&),;%!&62%0!&6!C#6,),;%!C%&J69!!!

!

>7:-&'()'?&%5&3/'5+8 0+.'/'+3'+@':&3'#3'73,'8 7-'#373/':%&7./A'B&/'B&'#4/.1'C&57$.&'/4&'* 7-'#373/'/+'C&3'#3%7/'+'B7.'3+/'
7-B7=.'#%&7/&%'/473'(6B&'-++<&,'@+%'3&#7/'9&'7.'B&–'7.'0+.'/'9&'0&7<.1'

| ! | CDE2FE'GH I' | * JK2FEJE>'GH I' | * LC'MJ>2N' |
|---|---|---|---|
| NO=#&3' | L39MFN! | L39MFN! | 3! |
| P7%:+3' | FF9O>P! | FF9O>P! | 3! |
| Q=,%+#&3' | 3F9LMN! | 3F9>34! | 49NON! |
| E'/%+#&3' | F9>P3! | F9>P3! | 3! |
| J-$8'3$8' | 49444LLP! | 49444>P4! | 49O>>! |
| C%+8'3&' | 49444P4P! | 49444L>>! | 49NFL! |
| P7-5'$8' | 4944OFN! | 4943 3Q! | 39QLQ! |
| P4-+%'3&' | 493NO! | 49F3>! | 394OL! |
| P+:7-/' | 494444F4L! | 4944443NO! | 49NL3! |
| P&.'$8' | 49444444QFP! | 494444 4QL4! | 393 43! |
| 2%+3' | 4944NO4! | 4944PO>! | 4904 3! |
| ?+/7..$'8' | 494ONM! | 493NL! | F93NF! |
| * 73#73&.&' | 4944440OO! | 4944443L! | 4903M! |
| R+,'$8' | 493O>! | 49F44! | 394O3! |
| M$:",'$8' | 49444>NO! | 49444>OM! | 49NPP! |
| S'35' | 494433P! | 494433M! | 49NPM! |

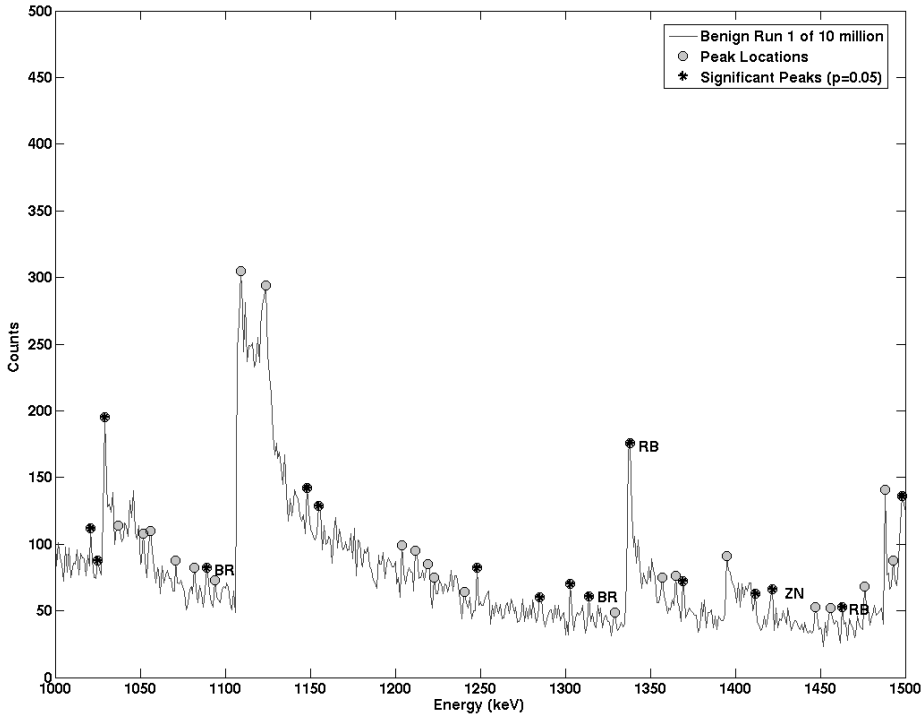
Benign Run 1 of 10 million
Peak Locations
Significant Peaks (p=0.05)
Counts
Energy (keV)
RB
BR
BR
ZN
RB

!

!"#$%&'()*+&,-''./0$/$(1-$2 3 4 $5/6$7 58$9 &6-:'$

"#$!%&' !(&)&!*&)#$%$( !+%,- !. $&/)0!123/*!)#$!4 5. $!($)$6),%!' &2!12$( !+,%!)#$!7&2$8 3/$!+,%!)#$!9 . : !&/( !; &<!(&)&=!"#$! (&)&!' &2!6%,>>$( !3/ !)#$!2&- $!' &? !&2!+,%!4 5. $@&/( !)#$/ !)#$!2>$6)%&!' $%$!781%%$(=!</ !,%($%!), !781%!)#$!%&' !(&)&@&! . &1223&/ !6,/A,81)3,/ !B$%/$8!' &2!3- >8$- $/)$( !&)!$&6# !B$C !2)$> !3/ !)#$!2>$6)%&=!"#$!+188D' 3( )# !#&8+D- &E !' &2!($+3/$( !&2! +,8B,' 2@!' #$%$!%$2,81)3,/ !' &2!FG !&/( !HIG !+,%!9 . : !&/( !; &<@%$2>$6)3A$8?J!

!

!"#$ %&'()*+,-(./0123/!&,'4(5)6*+,47(!8!6!!!!!!!!!!!!!!!!!!!!!!!!!!!!!!!!!!!!!!!!!!!!!!!!!!!!!!!!!!!!!!!!!!!!!!!!!!!!!!!!!!!!!!!KIL!

!

"#$!A&%3&/6$!' &2!($+3/$( !&2J!

!

$$/ \; ! \; " \; \frac{\#\$\%\&}{\sqrt{'\;"()*+!,}} \; !!!!!!!!!!!!!! \; ! \qquad ! \qquad ! \qquad ! \qquad ! \qquad ! \qquad ! \qquad ! \qquad ! \qquad ! \qquad !KML!$$

!

"#$!$/$%*?!' 3/(,' !' &2!,+!)#$!23N$J!0/$%*?!K>$%B$C L!! !IP! $^{I}$=!"#$!/,%- &8!>%,7&738)?!($/23)?!+1/6)3,/ !($+3/$( !3/ !)#$! Q &)8&7" !F=R=!S )&)3)362!),,87,E!' &2!$A&81&)$( !)#%,1*#,1)!)#$!$/$%*?!2>$6)%1- !&)!)#$!*3A$/ !$/$%*?!' 3/(,' !&/( !12$( !&2! )#$!. &1223&/ !B$%/$8=!"#$!%$218)3/*!/,%- &8!61%A$!' &2!)#$/ !6,/A,8A$( !' 3)# !)#$!6,1/)2!,+!)#$!2>$6)%&!&)!)#$!2&- $!$/$%*?! ' 3/(,' =!"#$!2$!2)$>2!&%$!21- - &%3N$( !3/ !T3*1%$!M=!

!

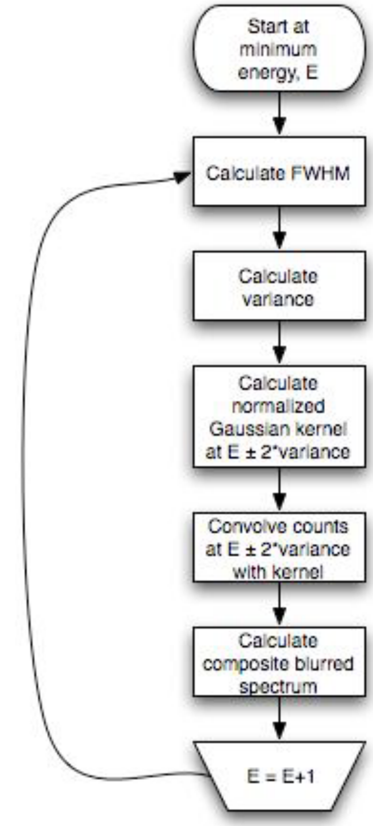

!

; .0<+-$#=$2 :<++./0$&>$(1-$? %3 -$@*-,(+<9 $

!

U +)$%!)#$!781%%3/*!' &2!6,- >8$)$(@>$&B!($)$6)3,/ !' &2!>$%+,%- $( !3/ !)#$!2&- $!- &//$%!&2!+,%!4 5. $@' 3)# !)#$!$E6$>)3,/ !,+! (3+$%$/ )!- 3/3- 1- !>$&B!#$3*#)!&/( !' 3/(,' !' 3( )#=!"#$!- 3/3- 1- !>$&B!#$3*#)!' &2!($+3/$( !), !7$!V !6,1/)2@&2!)#$!2>$6)%&!

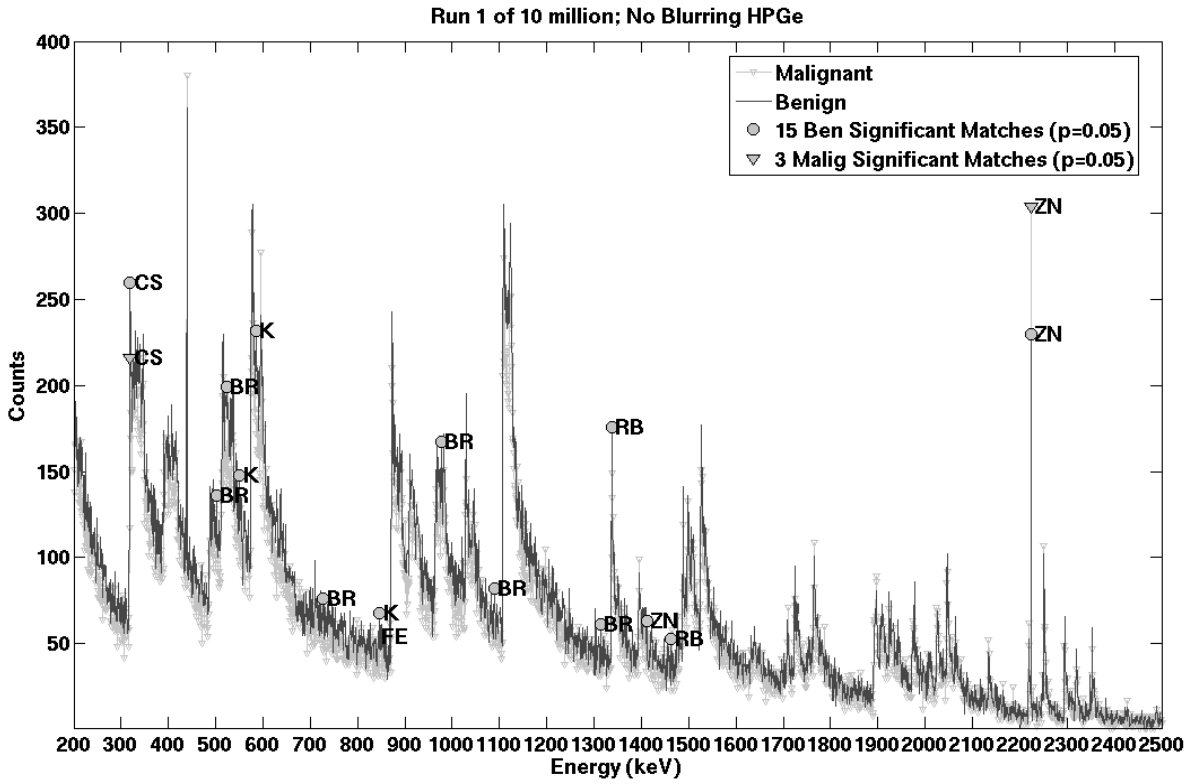
Run 1 of 10 million; No Blurring HPGe
Malignant
Benign
15 Ben Significant Matches (p=0.05)
3 Malig Significant Matches (p=0.05)
Counts
Energy (keV)
CS
CS
K
BR
K
BR
BR
K
FE
BR
BR
RB
BR
ZN
RB
ZN
ZN

!"#$%&'(&)*%+,%-./&0122"3.4%5&10*&#%-67-&'-8&2"$67-"-3&9%.3*"&&;03%&4%*%&<%*%&-%"*$/&'==&#%-67-&9%">5&'-8&0-$/&?=&
2"$67-"-3&9%">5&

| @$%2%-3& | A503 09%& | B%-67-&)*%+,%-./& | C"$67-"-3&)*%+,%-./& |
|---|---|---|---|
| !'# | $%# | &# | '# |
| ('# | )*# | &# | '# |
| +# | ,&# | -# | '# |
| ./# | **# | $# | '# |
| 01# | *2# | $# | '# |
| (3# | *-# | &&# | )# |
| 4/# | 2,# | )# | '# |
| 4/# | 22# | *# | '# |
| 4/# | 2%# | )$# | &&# |
| 4/# | 25# | &# | '# |
| 67# | %-# | ,2# | *# |
| 67# | 5&# | )*# | %# |
| 89# | 5*# | &2# | '# |
| 89# | 5%# | 2# | &# |
| (:# | &))# | $*# | ,# |
| !03'$& | & | DEF& | ?D& |

#
&
?:'&BGH&'-8&;"A&
;<171#=171#/3#:>?/>@?AB/GD BCA<1:#@87#1<6<17#6<1#6EF#87#6<1#GBH#IBCB#JK11#0>?L71#'M#;<1#1/17?O#71:3'LC<8/#=B:#C33#
'B7?1P#:3#6<1#Q1BR#<1>?<C:#=171#/3G#71Q71:1/GBCS1#8@#1"1D 1/C:#>/#6<1#D 3I1'N##
#

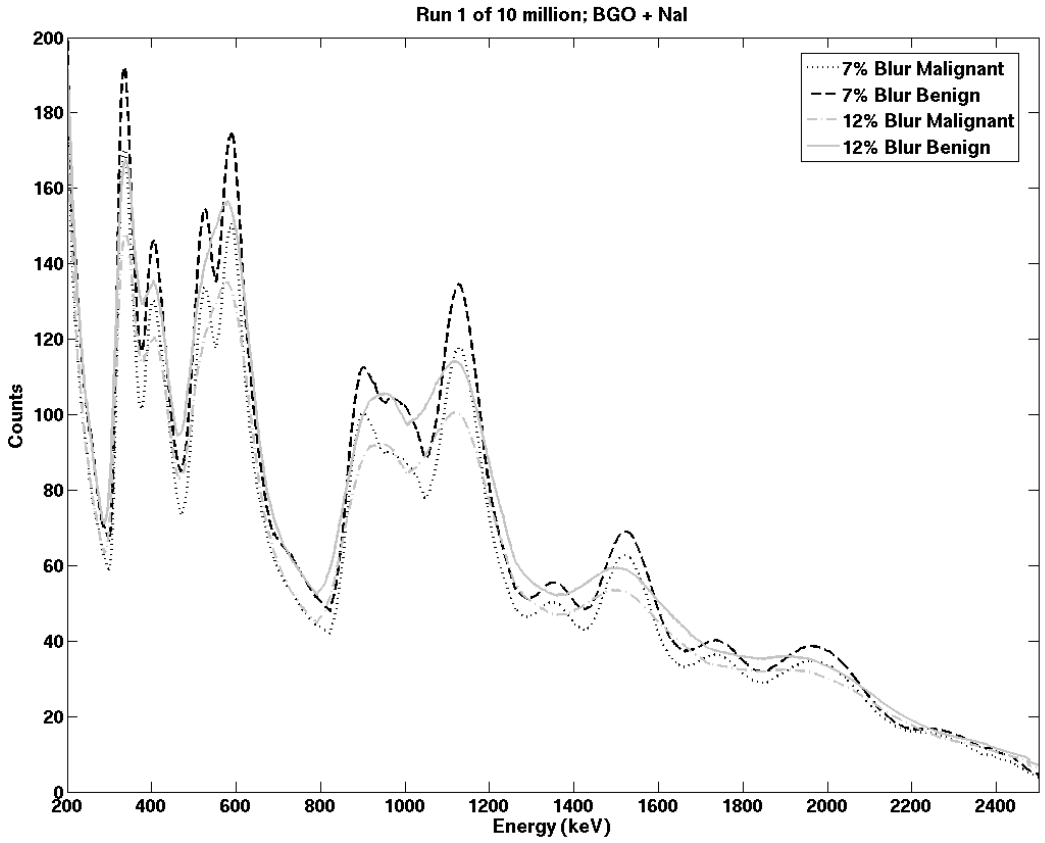


!

! '#$%&'()*+&%&', &%&'-./ 012+&3"-'1+&'4&-'#-'.%'5 06'#-0-1'37&21%0'8.%'49:'.%'; 0<=>$&'1.'1+&'0?&%0#'-#'.8'7&0@'+&'#+13'
.?&%'06&-&%#'&3A

!

<BACD<DEFDD<:;'
'

" #$%&#!'#( )*+,-%,#'!,$#!.'#*,/.0%,.)*!)/!+,%,.+,.0%112!+.3*/.0%*,!'//#-#*0#+!.*14#*.3*%*'!( %13*%*,14-#%+,!,.+15#!
5+.*3%16.3$785-.,219#-( %*.5( !#( .0)*'50,)-:!!;$#<#%=7'#,#0,.*3<#-/)-( %*0#!)/!,$#16891#!'#,#0,)-1%-!+5-<%+#'!,$#!
<#-/)-( %*0#!)/14),$!,$#>.+( 5,$!91#-( %*%,#%*'!?)'.5( !@)'.'#!'#,#0,)-:!!;$#!#*#-321#//.0#*021/)->91A %*'B%@!.+!,)))!
4-)%'!,)!.'#*,/2<#%=+!,$%,!( %,0$!,$#!CBDE!'%,%4%#:!" $.1#!,$#-#F#-#!.'#*,/%41#<#%=!1)0%,.)*+G!,$#!0)5*,+%,!,$)+#!
#*#-3.#+F#-#!*),!-#<-#+#*,%,&#!)/!,$#!.*'&.'5%1#1#( #*,+!.*!,$#14-#%+,!,.+15#:!@*!)-'#-!,)!'#,#-( .*#+.3*/.0%*,!( %,0$#+!
/-)( B?CH;!+<#0,-%G%!$.3$7<5-.,219#-( %*.5( !'#,#0,)-!)-!)*#F.,$!+.( .1%-!+5<#-.)-!#*#-321-#+)15,.)*!( 5+,14#!5+#':!!!
'
'
'

GEH;:I JKC9K5K;*D'
'

;$.+F)=F%+!+5<<)-,#'!.*!<%-,42!B@6!9-%*,!C>IIJIKI7IJ:!
!
!
!
!
'

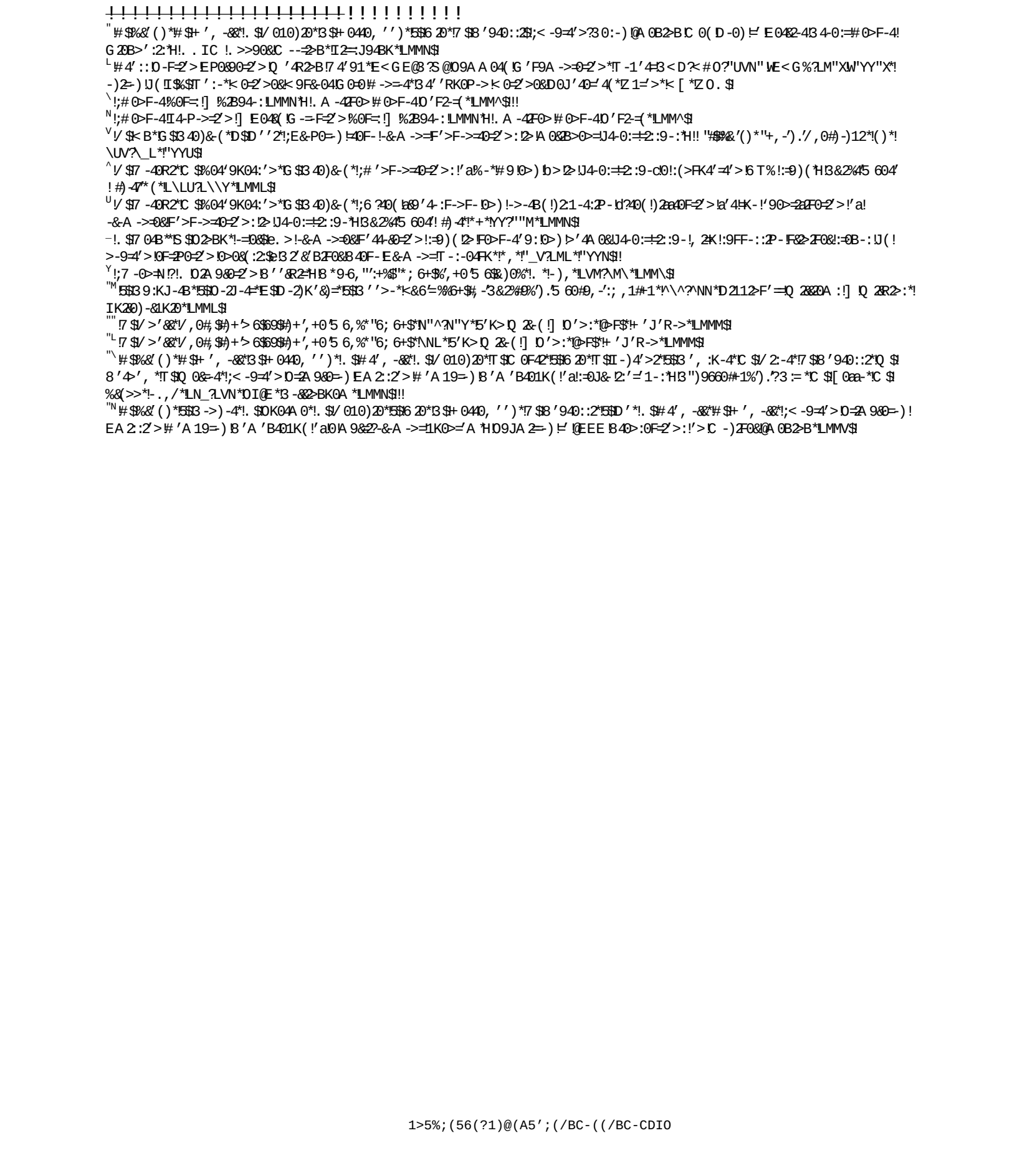

# Neutron Spectroscopy of Mouse Using Neutron Stimulated Emission Computed Tomography (NSECT)

Anuj J. Kapadia, Amy C. Sharma, Georgia D. Tourassi, Janelle E. Bender, Alexander S. Crowell, Matthew R. Kiser, Calvin R. Howell, Carey E. Floyd Jr.

***Abstract*– Neutron spectroscopy is evolving as a non-invasive technique to measure element concentration in biological tissue. We have developed a neutron stimulated emission computed tomography (NSECT) system that maps the elemental composition of a body through a non-invasive scan. A neutron beam incident on a sample energizes the sample's atomic nuclei through inelastic scatter interactions. These energized nuclei then spontaneously return to their ground energy states emitting the extra energy as a characteristic gamma photon. An energy-sensitive gamma detector is used to detect this energy and hence identify the emitting atom. Such a technique has several applications in both humans and small animals. Here we demonstrate NSECT's feasibility in scanning small animals, and show results from a spectroscopic examination of a fixed mouse specimen. The mouse was flushed with saline and fixed using a gadolinium/formalin solution. Scanning was performed using a 5 MeV monochromatic neutron beam. Background was corrected using time-of-flight correction to reduce time-uncorrelated noise and polynomial curve-fit subtraction to remove the residual underlying background. The emitted gammas were measured using a high purity germanium (HPGe) clover detector. The resulting spectrum shows various peaks corresponding to elements expected in this specimen such as C, Ca and Gd, several other potential matches such as K and Zn, as well as some system related elements such as Fe, Al and Ge from the detector. This experiment demonstrates the ability of NSECT to obtain element information from an intact small animal specimen through a single non-invasive scan.**

Manuscript received November 13, 2006. This work was supported by the NIH/NCI grant 1-R21-CA106873-01 and in part by Department of Defense (Breast Cancer Research Program) under award number W81XWH-06-1-0484.

A. J. Kapadia is with the Department of Biomedical Engineering and the Duke Advanced Imaging Laboratories (DAILabs) of the Department of Radiology, Duke University, Durham, NC 27710, USA (phone: 919-684-1470; fax: 919-684-1491; email: anuj.kapadia@duke.edu).

A.C. Sharma is with the Department of Biomedical Engineering and the DAILabs of the Department of Radiology, Duke University, Durham, NC 27710, USA (phone: 919-684-1471; fax: 919-684-1491; email: anc4@duke.edu).

G.D. Tourassi is with the DAILabs of the Department of Radiology, Duke University, Durham, NC 27710, USA (phone: 919-684-1447; fax: 919-684-1491; email: gt@deckard.duhs.duke.edu).

J. E. Bender is with the Department of Biomedical Engineering, Duke University, Durham, NC 27710, USA (email: janelle.bender@duke.edu).

A. S. Crowell is with the Department of Physics, Duke University and the Triangle Universities Nuclear Laboratory, Durham, NC 27708, USA (phone: 919-660-2639; fax: 919-660-2634; email: crowell@tunl.duke.edu).

M. R. Kiser is with the Department of Physics, Duke University and the Triangle Universities Nuclear Laboratory, Durham, NC 27708, USA (phone: 919-660-2639; fax: 919-660-2634; email: kiser@tunl.duke.edu).

C. R. Howell is with the Department of Physics, Duke University and the Triangle Universities Nuclear Laboratory, Durham, NC 27708, USA (phone: 919-660-2632; fax: 919-660-2634; email: howell@tunl.duke.edu).

C. E. Floyd Jr. is with the DAILabs of the Department of Radiology, Duke University Medical Center and the Department of Biomedical Engineering Duke University, Durham, NC 27710.

## I. Introduction

NEUTRON spectroscopy is evolving as a non-invasive technique to determine element concentrations in biological tissue. We have developed a neutron stimulated emission computed tomography system (NSECT) to identify element concentrations of in-vivo tissue using inelastic scattering of fast neutrons by target nuclei [1, 2]. A neutron incident on a target atom often scatters inelastically with the target atomic nucleus, exciting it to a higher unstable energy state. The unstable nucleus then rapidly decays to its ground state, emitting the excess energy as a characteristic gamma photon. The energy of the gamma photon is equal to the energy difference between the ground state and the excited state. These energy states are well-known and quantified for most known elements and isotopes and their energy difference therefore serves as a signature of the emitting atom. Thus, measuring the energy of the emitted gamma photon identifies the emitting atom and its concentration in the tissue sample.

## II. Relevance

Such a technique for spectroscopic evaluation of elements in tissue has several applications in both humans and small animals.

First, there are several disorders in humans which are associated with an increase in element concentration within the affected organ. For example, hemochromatosis which is an iron overload disorder associated with thalassemia and sickle cell anemia, is characterized by an increase in iron concentration in the liver [3, 4]. Wilson's disease shows an increase in the concentration of copper in the liver. These disorders both require element quantification for diagnosis, which is currently done through a liver biopsy [5, 6]. Biopsy is an unpleasant procedure which also has several potential complications associated with it. Despite being the current preferred diagnostic technique for these disorders, it has limitations in being used widely in patients suffering from these disorders due to its invasive nature. NSECT has the ability to diagnose iron and copper concentration changes in

the liver through a non-invasive scan, which could significantly reduce the need for liver biopsies.

Second, various experiments conducted on trace elements in humans and animals have shown that changes in concentration of trace elements are often associated with cancer in very early stages of development [7-10]. These concentration changes are seen in elements such as aluminum, iron, zinc, copper, rubidium, gold, silver and antimony, and have been observed as a pre-cursor to malignancy. Identifying the concentrations of these elements could potentially enable diagnosis of cancer very early, much before the tumor grows large enough to be detected through other conventional imaging techniques such as CT or mammography.

Finally, in small animals, NSECT's ability to detect element concentrations can be used to follow metabolic migration of nutrients or in normal and genetically modified mice or drug delivery in normal and modified tissue all without the need to tag molecules of interest with radioactive isotope tracers. NSECT has the ability to detect stable isotopes which occur naturally in these molecules which eliminates the need for radioactive tracers. It can also be used to measure iron and calcium levels in the cardiac wall.

## III. Motivation

The first step towards imaging small animals through NSECT is to demonstrate its feasibility in small animal imaging. Small animals have lower concentrations of elements such as carbon and calcium, which are otherwise found in greater quantities in humans. Low concentrations pose a challenge in detection due to the several reasons. The signal from low concentrations is low, which then requires a longer scan time to obtain adequate statistical accuracy. The increased scan time in turn increases the background noise and reduces the signal to noise ratio further. To demonstrate feasibility of small animal imaging, we have scanned and obtained a gamma spectrum from an intact biological specimen of a fixed mouse. Here we show results from the spectroscopic examination of the mouse and comment about NSECT's feasibility in imaging small animals.

## IV. Methods

This experiment was performed at the Triangle Universities Nuclear Laboratory (TUNL) accelerator lab, on Duke University's campus. Since the experimental setup has been described in detail elsewhere [1], only a brief description is included here.

A 5 MeV monochromatic neutron beam was produced through a $^{2}H(d,n)^{3}He$ reaction by using a Van-de-Graaf accelerator to bombard a deuterium gas target with accelerated deuterons. The emerging neutrons were then collimated using copper collimators, and focused on the target mouse specimen. A neutron flux monitor made up of a scintillator attached to a photo-multiplier tube counted the number of neutrons incident on the target. Two high purity germanium (HPGe) clover detectors were used to count the gamma photons emitted by the sample. Lead and paraffin wax blocks were used to shield the detector from unwanted neutrons and gammas. The detectors were calibrated against known energy peaks from a radioactive $^{22}Na$ source. The neutron beam profile was measured to be cylindrical with a 6cm diameter, corresponding to a beam area of $28.26cm^2$.

The mouse specimen was prepared for scanning as follows. A freshly sacrificed mouse was flushed with saline and then fixed for one week using a 1:10 gadolinium/formalin solution. After flushing the fixed mouse with saline once again, it was enclosed in a glass tube along with diluted formalin solution and sealed. This enclosed specimen was scanned for 95 minutes with the 5 MeV monochromatic neutron beam.

A second sample of 40g $H_2O$ was then scanned to provide a background spectrum to correct for sample-dependent background. Hydrogen atoms in water (which forms a large part of tissue) have the same mass as neutrons, and hence generate a lot of neutron scatter which adds to sample-related noise. Neutrons that scatter elastically off of the hydrogen atoms still carry a large part of their original energy, and can interact and generate inelastic scatter gamma photons from other materials present in the room, such as the detectors and sample mounting hardware. The spectrum from this water sample was normalized to incident neutron flux and used as background which was subtracted from the mouse spectrum.

Each spectrum was background corrected using three correction techniques. First, time-of-flight correction was used to reduce time-uncorrelated background noise from random sources of activity in the beam room. Second, sample-related scatter background was reduced by subtracting the normalized water spectrum from the mouse spectrum. Finally, a polynomial curve fit was used to model and subtract the residual underlying background, which is an effect of the detector efficiency. A photon entering the detector may not deposit all its energy at once, but instead do so in stages, leading to a greater energy spread over the lower energy channels of the detector.

As this was an experiment to demonstrate feasibility, no quantitative analysis was performed on the detected elements. Quantitative analysis would require obtaining calibration spectra from known quantities of element samples under conditions similar to those of the unknown specimen (fixed mouse in this case). Quantitative analysis has been performed in other experiments and described elsewhere [11].

## V. Results

The background corrected spectrum from the fixed mouse specimen is shown in Fig 1. Gamma peaks were observed for various elements expected from the mouse specimen as well as from materials expected in the system. Energy peaks were identified for $^{12}C$ from tissue, $^{40}Ca$ from bone, and elements $^{39}K$, $^{27}Al$, $^{37}Cl$, $^{56}Fe$, $^{68}Zn$ and $^{25}Mg$ which could potentially be present in the specimen. The elements $^{27}Al$ and $^{56}Fe$ could also be system dependent as many components used to mount the detectors and other hardware were made of aluminum and iron. Energy peaks were identified for $^{158}Gd$ and $^{160}Gd$ from the 1:10 gadolinium/formalin fixing solution in the sample,

along with energy peaks from several naturally occurring states in germanium from the HPGe detectors.

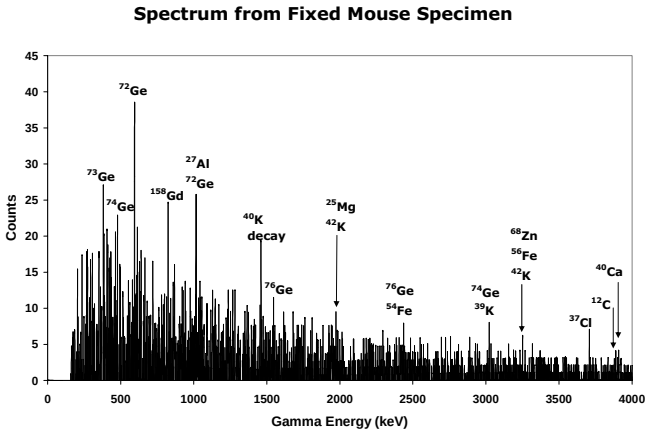


Fig.1. Gamma spectrum from a formalin fixed mouse specimen showing peaks corresponding to excited states in various elements. Gamma peaks are seen for $^{12}$C (escape peaks), $^{40}$Ca, $^{39}$K, $^{27}$Al, $^{37}$Cl, $^{56}$Fe, $^{68}$Zn and $^{25}$Mg. Gamma peaks are also seen for $^{72}$Ge and $^{74}$Ge from the germanium detector, and $^{158}$Gd and $^{160}$Gd from the fixing solution. Peaks with multiple potential element matches are labeled accordingly. These spectra are shown without neutron or gamma attenuation correction.

## VI. Conclusion

This experiment demonstrates the ability of NSECT to obtain an elemental map of an intact small-animal specimen through a non-invasive scan. To cross-check the presence of potential elements, the mouse specimen will be sent for Neutron Activation Analysis (NAA) which will return quantitative analyses of elements present in this individual specimen. While a few of the dominant element peaks are system related, peaks corresponding to elements known to be present in the mouse specimen are also seen.

Sources of error in the system currently include high scan time, low detection efficiency and high background noise, all of which reduce the sensitivity of the system. Efforts are being made to improve the overall sensitivity of the system to be able to detect low concentration elements in the specimen. Scan time can be reduced greatly by using commercial neutron sources with high neutron flux, and using multiple detectors to acquire data. These two factors will greatly reduce the overall scan time, which in turn will reduce time-related background noise and improve the signal to noise ratio. Shorter scans with multiple detectors will also improve detection efficiency and reduce patient dose.

## Acknowledgment

We thank all the members of the Triangle Universities Nuclear Laboratory for their help with data acquisition and the members of Duke Advanced Imaging Laboratories for their help with data analysis. We thank the Center for In-vivo Microscopy at Duke University for providing the fixed mouse specimen.

## References

[1] C. E. Floyd, J. E. Bender, A. C. Sharma, A. J. Kapadia, J. Q. Xia, B. P. Harrawood, G. D. Tourassi, J. Y. Lo, A. S. Crowell, and C. R. Howell, "Introduction to neutron stimulated emission computed tomography," *Physics in Medicine and Biology*, vol. 51, pp. 3375-3390, 2006.

[2] C. E. Floyd, C. R. Howell, B. P. Harrawood, A. S. Crowell, A. J. Kapadia, R. Macri, J. Q. Xia, R. Pedroni, J. Bowsher, M. R. Kiser, G. D. Tourassi, W. Tornow, and R. Walter, "Neutron Stimulated Emission Computed Tomography of Stable Isotopes," presented at SPIE Medical Imaging, San Diego, CA, 2004.

[3] N. C. Andrews, "Disorders of iron metabolism," *N Engl J Med*, vol. 341, pp. 1986-95, 1999.

[4] L. W. Powell and K. J. Isselbacher, "Hemochromatosis," in *Harrison's Principles of Internal Medicine*: McGraw-Hill.

[5] L. W. Powell, "Diagnosis of hemochromatosis," *Semin Gastrointest Dis*, vol. 13, pp. 80-8, 2002.

[6] L. W. Powell, D. K. George, S. M. McDonnell, and K. V. Kowdley, "Diagnosis of hemochromatosis," *Ann Intern Med*, vol. 129, pp. 925-31, 1998.

[7] A. Danielsen and E. Steinnes, "A study of some selected trace elements in normal and cancerous tissue by neutron activation analysis," *J Nuclear Medicine*, vol. 11, pp. 260-264, 1970.

[8] A. Garg, V. Singh, et al., "An elemental correlation study in cancerous and normal breast tissue with successive clinical stages by neutron activation analysis," *Biological Trace Element Research*, vol. 46, pp. 185-202, 1994.

[9] H. Mussalo-Rauhamaa, S. Piepponen, J. Lehto, R. Kauppila, and O. Auvinen, "Cu, Zn, Se and Mg concentrations in breast fat of Finnish breast cancer patients and healthy controls," *Trace Elements in Medicine*, vol. 10, pp. 13-15, 1993.

[10] S. Rizk and H. Sky-Peck, "Comparison between concentrations of trace elements in normal and neoplastic human breast tissue," *Cancer Research*, vol. 44, pp. 5390-5394, 1984.

[11] A. J. Kapadia, C. E. Floyd, J. E. Bender, C. R. Howell, A. S. Crowell, and M. R. Kiser, "Non-invasive quantification of iron 56-Fe in beef liver using neutron stimulated emission computed tomography," presented at IEEE Nuclear Science Symposium Conference, Puerto Rico, 2005.

# Neutron Stimulated Emission Computed Tomography (NSECT) for Early Detection of Breast Cancer

Anuj J. Kapadia, Amy C. Sharma, Georgia D. Tourassi, Janelle E. Bender, Alexander S. Crowell, Matthew R. Kiser, Calvin R. Howell, Carey E. Floyd Jr.

***Abstract*– Neutron stimulated emission computed tomography (NSECT) is being developed as a non-invasive spectroscopic technique to determine element concentrations in the human body. We have implemented an NSECT system that uses a beam of high-energy neutrons to identify element concentrations in tissue and create 2-dimensional maps of elemental distribution through a single non-invasive tomographic scan. Neutrons scatter inelastically with atomic nuclei in tissue, causing them to emit characteristic gamma photons. These gamma photons are detected and identified using an energy-sensitive gamma detector. By measuring the energy and number of emitted gamma photons, the system can determine the elemental composition of the target tissue. NSECT has the advantage of being able to detect breast cancer at very early stages compared to anatomic screening techniques, as it detects changes in trace element concentrations in the breast, which usually occur before anatomical features such as tumors and micro-calcifications appear. The tomographic scanning system eliminates the need for breast compression and patient disrobing. The system design can be made portable by using a commercially available portable neutron source with a gamma detector. From our preliminary results, NSECT shows significant promise in early diagnosis of breast cancer. It has the potential to evolve into an easily accessible screening modality and diagnostic technique for breast cancer, which can detect and identify malignant tissue in the breast and generate a two-dimensional image through a single non-invasive tomographic scan. Patient dose levels from NSECT are comparable to those of screening mammography. Efforts are under way to achieve the micro-gram sensitivity required for in-vivo trace element detection in the breast at the lowest possible patient dose levels. Our final goal is to implement a portable, low-dose tomographic screening system for breast cancer which does not require breast compression or invasive biopsies.**

Manuscript received November 13, 2006. This work was supported by the NIH/NCI grant 1-R21-CA106873-01 and in part by Department of Defense (Breast Cancer Research Program) under award number W81XWH-06-1-0484.

A. J. Kapadia is with the Department of Biomedical Engineering and the Duke Advanced Imaging Laboratories (DAILabs) of the Department of Radiology, Duke University, Durham, NC 27710, USA (phone: 919-684-1470; fax: 919-684-1491; email: anuj.kapadia@duke.edu).

A.C. Sharma is with the Department of Biomedical Engineering and the DAILabs of the Department of Radiology, Duke University, Durham, NC 27710, USA (phone: 919-684-1471; fax: 919-684-1491; email: anc4@duke.edu).

G.D. Tourassi is with the DAILabs of the Department of Radiology, Duke University, Durham, NC 27710, USA (phone: 919-684-1447; fax: 919-684-1491; email: gt@deckard.duhs.duke.edu).

J. E. Bender is with the Department of Biomedical Engineering, Duke University, Durham, NC 27710, USA (email: janelle.bender@duke.edu).

A. S. Crowell is with the Department of Physics, Duke University and the Triangle Universities Nuclear Laboratory, Durham, NC 27708, USA (phone: 919-660-2639; fax: 919-660-2634; email: crowell@tunl.duke.edu).

M. R. Kiser is with the Department of Physics, Duke University and the Triangle Universities Nuclear Laboratory, Durham, NC 27708, USA (phone: 919-660-2639; fax: 919-660-2634; email: kiser@tunl.duke.edu).

C. R. Howell is with the Department of Physics, Duke University and the Triangle Universities Nuclear Laboratory, Durham, NC 27708, USA (phone: 919-660-2632; fax: 919-660-2634; email: howell@tunl.duke.edu).

C. E. Floyd Jr. is with the DAILabs of the Department of Radiology, Duke University Medical Center and the Department of Biomedical Engineering Duke University, Durham, NC 27710.

## I. Introduction

Neutron stimulated emission computed tomography (NSECT) is being developed as a non-invasive spectroscopic technique to determine element concentrations in the human body. We have implemented and demonstrated the feasibility of an NSECT system that uses a beam of high-energy fast neutrons to identify element concentrations in tissue and create 2-dimensional maps of elemental distribution in the tissue, all through a single non-invasive tomographic scan [1, 2]. NSECT relies on inelastic scattering interactions between neutrons and target atomic nuclei to obtain this information. If a neutron incident on tissue scatters inelastically with an atomic nucleus in the target tissue, it excites the nucleus to a higher energy state that is often unstable and short-lived. The unstable nucleus then rapidly decays to its ground state from the higher energy state, emitting the excess energy as a gamma photon. The energy of the emitted photon is equal to the energy difference between the two states, and can be measured by an energy-sensitive gamma detector. As these energy states and transitions are mostly unique to each element and isotope, an atom can be identified by measuring the energy of the emitted gamma photon.

## II. Relevance

Non-invasive quantification of elements in the body shows great potential in diagnosis of several disorders that are characterized by changes in element concentration in the affected organ or tissue. One of these disorders is breast cancer. Several studies have shown that a change in trace element concentration is often associated with cancer, specifically in the breast [3-10], prostate [11] and brain [12, 13]. Breast cancer has been associated with changes in Al, Br, Ca, Cl, Co, Cs, Cu, Fe, K, Mn, Na, Rb, Sb, Se, Zn; prostate cancer with Ca, Cu, Fe, Mg, Ni, Zn; and brain cancer with B, Ba, Sr, Zn. In many cancers, these element concentration changes are seen much before morphologic changes such as

tumors and micro-calcifications develop to a point where they can be detected by current imaging modalities. Quantifying these element concentrations could enable in-vivo cancer diagnosis earlier than is possible with conventional imaging techniques, potentially increasing survival rates of patients through early diagnosis.

Additionally, disorders such as hemochromatosis (liver iron overload associated with thalassemia and sickle cell anemia) and Wilson's disease (liver copper overload), are characterized by increased iron and copper concentration respectively in the liver [14, 15]. These are currently diagnosed through liver biopsy, which is an unpleasant procedure that has several complications associated with it [16, 17]. NSECT has the potential to diagnose liver overload disorders through a non-invasive scan with a dose level equivalent to that of a single abdominal CT scan.

## III. Methods

NSECT experiments are performed at the Triangle Universities Nuclear Laboratory (TUNL) accelerator lab, on Duke University's campus. Their shielded neutron source is an excellent source of fast neutrons (energy in MeV range) with adequate high-flux beams, which can be collimated to desired size and shape using swappable collimator inserts. A brief description of the experimental setup follows.

### A. Experimental Setup

A 5 MeV neutron beam is produced through a $^{2}H(d,n)^{3}He$ reaction, by bombarding a deuterium gas target with a deuteron beam accelerated by a Van de Graaf accelerator. This beam is collimated to a desired profile and size using appropriate copper collimators, and focused onto the target tissue sample. Neutron flux at the target is monitored by a plastic scintillator attached to a photo-multiplier tube placed between the collimator and the target. The target tissue sample is placed on a translation-rotation stage, which enables tomography through a first generation CT scanning technique. The sample is first translated through a fixed number of steps, then rotated through a fixed angular rotation and translated again. This process is repeated for the required number of angles. Gamma photons emitted by the sample are counted by high purity germanium detectors (HPGe) hooked up to a data acquisition system. These detectors are shielded from unwanted neutrons and gammas using lead and borated paraffin wax shielding.

### B. Patient Dose

Using neutrons as the incident radiation leads to significant concerns about patient dose. At the energies we propose, neutrons are known to damage the body 10 times more than x-rays. However, as it takes an immensely smaller number of neutrons to create an NSECT image than x-rays required to create a mammogram, it is possible to achieve dose levels comparable to other ionizing radiation modalities. Our preliminary experiments suggest that for breast cancer detection, it may be possible to achieve effective patient dose levels of approximately 15 mSv. By increasing the number of detectors and using high-flux neutron sources to reduce scan time, dose levels can potentially be brought down to values comparable to screening mammography.

Dose measurements are currently done through a Geant4 simulation which models the acquisition geometry, neutron beam characteristics and sample data. The energy deposited in the sample is counted and used to calculate an effective dose equivalent for the organ.

### C. Current Status

Several samples have been scanned to date, ranging from solid metals for calibration and sensitivity studies, to biological samples such as excised breast tissue, bovine liver and a fixed mouse specimen. These spectra have been shown below. We have also successfully reconstructed a 2-dimensional image from a tomographic scan of a mixed iron and copper sample and separately identified and reconstructed each element in the sample [18].

### D. Background Correction

Background correction is generally performed using three techniques. First, time-of-flight correction is used to reduce time-uncorrelated background noise from random sources of activity in the beam room. Using a pulsed deuteron beam, it is possible to calculate the expected arrival time of gamma photons originating from the sample through neutron inelastic scatter. Events that occur outside this expected arrival time window are discarded as noise events and suppressed.

Second, sample-related background is reduced by acquiring and subtracting a sample out scan from the sample spectrum. For solid metal samples, the sample-out scan is generally acquired with room air in place of the metal. For biological tissue, a sample of distilled water of equal mass as the scanned tissue is used to generate elastic neutron scatter comparable to that of the original tissue. Hydrogen nuclei in water (which is a large component of biological tissue) have the same mass as neutrons. Hence, a lot of neutron scatter is generated while scanning a tissue sample. Scattered neutrons can interact with other materials in the room and generate inelastic scatter gamma photons from them. The sample-out scan is used to estimate this background and subtract it from the sample in spectrum.

Finally, the residual underlying background, which is an effect of the detector efficiency, is modeled and subtracted using a polynomial curve fit. A detected photon may not deposit all of its energy in a single step. Instead it may do so in several steps in the detector crystal, causing an energy spread over the lower channels of the detector. As a result, there is a gradual increase in photon counts over the lower detector channels. This extra-count trend is fitted using a polynomial curve fit and subtracted from the spectrum.

## IV. Results

Background corrected spectrums obtained from several samples are shown here. Fig. 1 shows a spectrum from a

mixture of iron, potassium, sodium and chlorine in water. As can be seen from the spectrum, peaks corresponding to Fe, Cl, Na and K are easily distinguished from each other.

Fig. 2 shows a spectrum from bovine liver. Several elements present in the liver were identified and their concentrations were determined. The presence of some elements was cross-validated through a quantitative neutron activation analysis scan of the liver sample. The concentrations predicted by NSECT differed from the NAA values by 15-50% for different elements.

Fig. 3 shows a spectrum from a fixed mouse specimen. Peaks can be seen for carbon and calcium from bone and tissue respectively. Also seen are peaks for germanium from the detectors and gadolinium from the fixing solution.

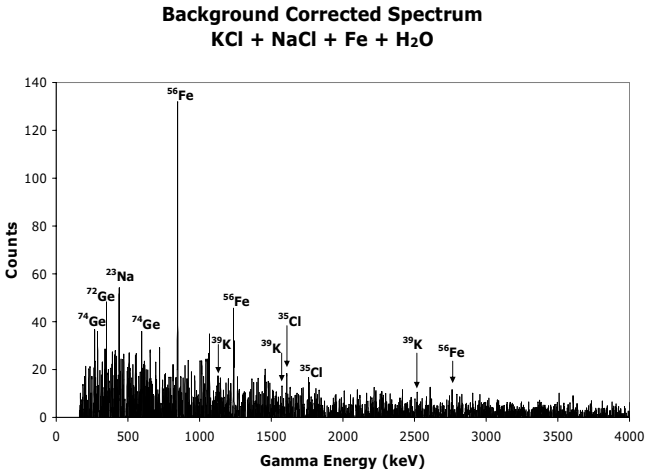


Fig.1. Gamma spectrum from a KCl, NaCl and Fe solution in water showing peaks corresponding to excited states in $^{39}$K, $^{23}$Na, $^{35}$Cl, $^{37}$Cl, $^{56}$Fe, $^{70}$Ge, and $^{74}$Ge. These spectra are shown without neutron or gamma attenuation correction.

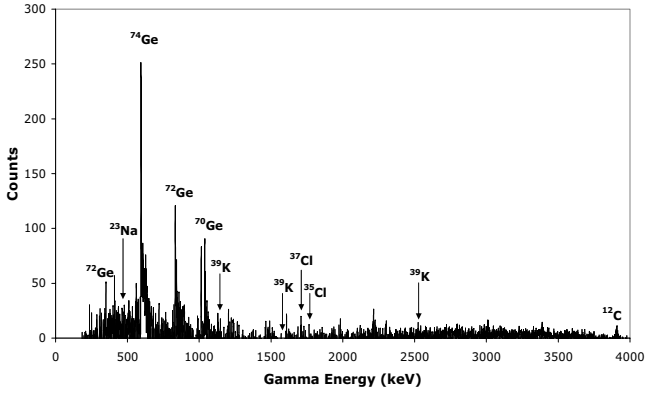


Fig.2. Gamma spectrum from a bovine liver specimen showing peaks corresponding to excited states in $^{39}$K, $^{23}$Na, $^{35}$Cl, $^{37}$Cl, $^{56}$Fe, $^{70}$Ge, and $^{74}$Ge Gamma peaks are also seen for $^{12}$C (escape peaks) from tissue. These spectra are shown without neutron or gamma attenuation correction.

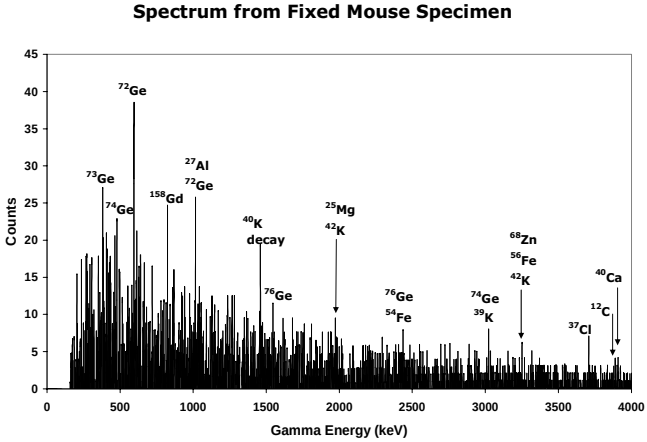


Fig.3. Gamma spectrum from a formalin fixed mouse specimen showing peaks corresponding to excited states in various elements. Gamma peaks are seen for $^{12}$C (escape peaks), $^{40}$Ca, $^{39}$K, $^{27}$Al, $^{37}$Cl, $^{56}$Fe, $^{68}$Zn and $^{25}$Mg. Gamma peaks are also seen for $^{72}$Ge and $^{74}$Ge from the germanium detector, and $^{158}$Gd and $^{160}$Gd from the fixing solution. Peaks with multiple potential element matches are labeled accordingly. These spectra are shown without neutron or gamma attenuation correction.

## V. Conclusion and Future Work

NSECT shows significant promise in early diagnosis for patients suffering from breast cancer and several other disorders. It has the potential to evolve into an easily accessible screening modality and diagnostic technique for breast cancer through the use of portable neutron sources and portable gamma detectors. It can detect and identify malignant tissue in the breast and generate a two-dimensional image through a single non-invasive tomographic scan without the need for breast compression or biopsies. TO be able to detect concentrations of elements that are markers of cancer, significant improvements in sensitivity are required. Efforts are under way to achieve the micro-gram sensitivity while maintaining the lowest possible dose level delivered to the patient. Using high-flux sources and multiple detectors will increase detection efficiency and reduce scan time, which will both in turn reduce the time-dependent background and hence increase signal to noise ratio. Increased detection efficiency will also reduce patient dose. Our final goal is to implement a portable, low-dose breast cancer screening system to detect breast cancer without the need for breast compression or invasive biopsies.

## Acknowledgment

We thank all the members of the Triangle Universities Nuclear Laboratory for their help with data acquisition and the members of Duke Advanced Imaging Laboratories for their help with data analysis. We thank the Center for In-vivo Microscopy at Duke University for providing the fixed mouse specimen.

## REFERENCES


[1] C. E. Floyd, J. E. Bender, A. C. Sharma, A. J. Kapadia, J. Q. Xia, B. P. Harrawood, G. D. Tourassi, J. Y. Lo, A. S. Crowell, and C. R. Howell, "Introduction to neutron stimulated emission computed tomography," *Physics in Medicine and Biology*, vol. 51, pp. 3375-3390, 2006.

[2] C. E. Floyd, C. R. Howell, B. P. Harrawood, A. S. Crowell, A. J. Kapadia, R. Macri, J. Q. Xia, R. Pedroni, J. Bowsher, M. R. Kiser, G. D. Tourassi, W. Tornow, and R. Walter, "Neutron Stimulated Emission Computed Tomography of Stable Isotopes," presented at SPIE Medical Imaging, San Diego, CA, 2004.

[3] A. Garg, V. Singh, et al., "An elemental correlation study in cancerous and normal breast tissue with successive clinical stages by neutron activation analysis," *Biological Trace Element Research*, vol. 46, pp. 185-202, 1994.

[4] K. Geraki and M. Farquharson, "Concentrations of Fe, Cu and Zn in breast tissue: a synchrotron XRF study," *Phys. Med. Biol*, vol. 47, pp. 2327-2339, 2002.

[5] K. Geraki, M. J. Farquharson, and D. A. Bradley, "X-ray fluorescence and energy dispersive x-ray diffraction for the quantification of elemental concentrations in breast tissue," *Phys. Med. Biol*, vol. 49, pp. 99-110, 2004.

[6] H. Mussalo-Rauhamaa, S. Piepponen, J. Lehto, R. Kauppila, and O. Auvinen, "Cu, Zn, Se and Mg concentrations in breast fat of Finnish breast cancer patients and healthy controls," *Trace Elements in Medicine*, vol. 10, pp. 13-15, 1993.

[7] K.-H. Ng, D. Bradley, and L.-M. Looi, "Elevated trace element concentrations in malignant breast tissues," *British Journal of Radiology*, vol. 70, pp. 375-382, 1997.

[8] K.-H. Ng, S.-H. Ong, D. A. Bradley, and L.-M. Looi, "Discriminant analysis of normal and malignant breast tissue based upon INAA investigation of elemental concentration," *Appl. Radiat. Isot.*, vol. 48, pp. 105-109, 1997.

[9] S. Rizk and H. Sky-Peck, "Comparison between concentrations of trace elements in normal and neoplastic human breast tissue," *Cancer Research*, vol. 44, pp. 5390-5394, 1984.

[10] A. Schwartz and R. Fink, "Trace Elements in Normal and Malignant Human Breast Tissue," *Surgery*, vol. 76, pp. 325-329, 1974.

[11] M. Yaman, D. Atici, S. Bakirdere, and I. Akdeniz, "Comparison of trace metal concentrations in malign and benign human prostate," *J. Med. Chem.*, vol. 48, pp. 630-634, 2005.

[12] E. Andrasi, M. Suhajda, I. Saray, L. Bezur, L. Ernyei, and A. Reffy, "Concentration of elements in human brain: *glioblastoma multiforme*," *Sci Total Env*, vol. 139-140, pp. 399-402, 1993.

[13] J. D. Stedman and N. M. Spyrou, "Major and trace element concentration differences between right and left hemispheres of the 'normal' human brain," *Nutrition*, vol. 11, pp. 542-545, 1995.

[14] S. R. Hollan, "Transfusion-associated iron overload," *Curr Opin Hematol*, vol. 4, pp. 436-41, 1997.

[15] L. W. Powell and K. J. Isselbacher, "Hemochromatosis," in *Harrison's Principles of Internal Medicine*: McGraw-Hill.

[16] L. W. Powell, "Diagnosis of hemochromatosis," *Semin Gastrointest Dis*, vol. 13, pp. 80-8, 2002.

[17] L. W. Powell, D. K. George, S. M. McDonnell, and K. V. Kowdley, "Diagnosis of hemochromatosis," *Ann Intern Med*, vol. 129, pp. 925-31, 1998.

[18] C. E. Floyd, J. E. Bender, A. C. Sharma, A. J. Kapadia, J. Q. Xia, B. P. Harrawood, G. D. Tourassi, J. Y. Lo, and A. S. C. C. R. Howell, "Neutron Stimulated Emission Computed Tomography of a Multi-Element Phantom," *IEEE Trans Med Imag*, vol. submitted (2006), 2006.

# Non-Invasive Estimation of Potassium (39K) in Bovine Liver Using Neutron Stimulated Emission Computed Tomography (NSECT)

Anuj J. Kapadia, Amy C. Sharma, Georgia D. Tourassi, Janelle E. Bender, Alexander S. Crowell, Matthew R. Kiser, Calvin R. Howell, Carey E. Floyd Jr.

***Abstract*– Neutron stimulated emission computed tomography (NSECT) is being developed as a non-invasive technique to measure element concentration in in-vivo tissue at molecular levels. We have developed a system that performs this task using an incident neutron beam that scatters inelastically with an atomic nucleus causing it to emit a characteristic gamma photon. An energy-sensitive gamma detector is used to detect this energy and identify the target atom. Here we describe an experiment to determine the concentration of natural potassium (39K) in bovine liver without the need for a biopsy. A 5 MeV neutron beam was used to scan a known quantity of bovine liver to obtain a gamma spectrum showing element concentration in the liver. An aqueous KCl solution calibration sample was then scanned to establish a ratio of potassium concentration to gamma counts for the experimental setup. Counts from gamma peaks corresponding to excited states in 39K were summed and compared with counts from the known calibration sample, to give the concentration of 39K in the liver. A high purity germanium (HPGe) clover detector was used to measure the emitted gamma energy. The results were validated through neutron activation analysis (NAA) of the liver sample. The concentration of 39K reported by NSECT was found to be within 13% of the NAA result, clearly demonstrating the ability of NSECT for non-invasive quantification of element concentration in tissue.**

Manuscript received November 13, 2006. This work was supported by the NIH/NCI grant 1-R21-CA106873-01 and in part by Department of Defense (Breast Cancer Research Program) under award number W81XWH-06-1-0484.

A. J. Kapadia is with the Department of Biomedical Engineering and the Duke Advanced Imaging Laboratories (DAILabs) of the Department of Radiology, Duke University, Durham, NC 27710, USA (phone: 919-684-1470; fax: 919-684-1491; email: anuj.kapadia@duke.edu).

A.C. Sharma is with the Department of Biomedical Engineering and the DAILabs of the Department of Radiology, Duke University, Durham, NC 27710, USA (phone: 919-684-1471; fax: 919-684-1491; email: anc4@duke.edu).

G.D. Tourassi is with the DAILabs of the Department of Radiology, Duke University, Durham, NC 27710, USA (phone: 919-684-1447; fax: 919-684-1491; email: gt@deckard.duhs.duke.edu).

J. E. Bender is with the Department of Biomedical Engineering, Duke University, Durham, NC 27710, USA (email: janelle.bender@duke.edu).

A. S. Crowell is with the Department of Physics, Duke University and the Triangle Universities Nuclear Laboratory, Durham, NC 27708, USA (phone: 919-660-2639; fax: 919-660-2634; email: crowell@tunl.duke.edu).

M. R. Kiser is with the Department of Physics, Duke University and the Triangle Universities Nuclear Laboratory, Durham, NC 27708, USA (phone: 919-660-2639; fax: 919-660-2634; email: kiser@tunl.duke.edu).

C. R. Howell is with the Department of Physics, Duke University and the Triangle Universities Nuclear Laboratory, Durham, NC 27708, USA (phone: 919-660-2632; fax: 919-660-2634; email: howell@tunl.duke.edu).

C. E. Floyd Jr. is with the DAILabs of the Department of Radiology, Duke University Medical Center and the Department of Biomedical Engineering Duke University, Durham, NC 27710.

## I. Introduction

NEUTRON stimulated emission computed tomography (NSECT) is being developed as a non-invasive technique to measure element concentration in the human body. We have developed an NSECT system that identifies element concentrations in in-vivo biological tissue using a beam of fast neutrons [1-3]. The basic principle of NSECT is as follows: An incident neutron interacts with target atomic nuclei mainly through scattering. If the scattering is inelastic, the target nucleus gets excited to a higher energy state which is often unstable. The unstable nucleus then rapidly decays to its ground state, emitting the excess energy as a characteristic gamma photon. The energy of the emitted photon is equal to the difference between the two energy states, and is well known and unique to most elements and isotopes. Hence, it serves as a signature of the emitting atom and can be measured by an energy-sensitive gamma detector to identify the atom.

## II. Relevance and Motivation

Such non-invasive quantification of elements in the body shows great potential in diagnostic procedures associated with several disorders in humans. For example, hemochromatosis (liver iron overload associated with thalassemia and sickle cell anemia) and Wilson's disease (liver copper overload) are both characterized by increased element concentration in the liver [4]. Patients suffering from thalassemia and sickle cell anemia often require weekly blood transfusions. With each transfusion fresh iron enters the body while the old iron remains in it. Since the body does not have an effective method to get rid of excess iron, it starts accumulating in various organs, especially the liver. The preferred diagnostic procedure for liver overload disorders is liver biopsy [5, 6]. This is an unpleasant procedure that can have several potential complications in patients. Quantification results from biopsy suffer from a 20% margin of error in determining element concentration in tissue. There is a need for an alternative technique to measure hepatic element concentration non-invasively. Here we describe an experiment to non-invasively determine the concentration of an element in the liver.

## III. METHODS

This experiment was performed at the Triangle Universities Nuclear Laboratory (TUNL) accelerator lab, on Duke University's campus. The experimental setup has been described in detail elsewhere [1]. A brief description follows.

### A. Experimental Setup

A 5 MeV neutron beam was produced by a Van-de-Graaf accelerator through a $^{2}H(d,n)^{3}He$ reaction, by bombarding a deuterium gas target with a deuteron beam. This beam was then collimated to a cylindrical profile using copper collimators, and focused on the target bovine liver sample. A neutron flux monitor made up of a scintillator attached to a photo-multiplier tube counted the number of neutron particles reaching the target. The gamma photons emitted by the sample were counted by two high purity germanium (HPGe) clover detectors hooked up to a data acquisition system. Lead and borated paraffin wax shielding was used to shield the detector from scattered neutrons and gammas. The detectors were calibrated against known energy peaks from a radioactive $^{22}Na$ source. The neutron beam profile was measured to be cylindrical with a 6cm diameter corresponding to a beam area of $28.26cm^2$.

### B. Samples

Three samples were prepared and scanned using this experimental setup.

A calibration sample was prepared using an aqueous solution of 2.5g KCl and 2.5g NaCl in 40g $H_2O$, along with 5g of iron powder. It was determined that 1.22g of $^{39}K$ was present in the sample. This sample was scanned with the 6cm beam to determine a ratio of potassium concentration to gamma counts for this experimental setup.

The second sample comprised a bovine liver (392.5g) with an unknown concentration of $^{39}K$, placed inside a plastic container. The cylindrical plastic container measured 9cm in diameter and 7cm in height. Calculations showed that 177.7g of liver lay in the neutron beam path. This unknown sample was scanned using the same experimental setup to determine its elemental concentration.

A third sample comprising 40g $H_2O$ was scanned to provide a background spectrum to correct for sample-dependent background. Hydrogen atoms in water have the same mass as neutrons, and hence generate a lot of neutron scatter adding to sample-related noise. The normalized spectrum from this sample was used as the background which was subtracted from the other two spectrums.

### C. Background Correction

Each spectrum was background corrected using 3 techniques. First, time-of-flight correction was used to reduce time-uncorrelated background noise from random sources of activity in the beam room. Second, sample-related background was reduced by subtracting the normalized water spectrum from each of the other two spectrums. Finally, a polynomial curve fit was used to model and subtract the residual underlying background, which is an effect of the detector efficiency. A photon entering the detector may not deposit all its energy at once, but do so in stages instead, leading to an energy spread over the low energy channels in the detector.

Background corrected spectrums obtained from the calibration sample and bovine liver sample are shown in Fig. 1 and Fig. 2 respectively.

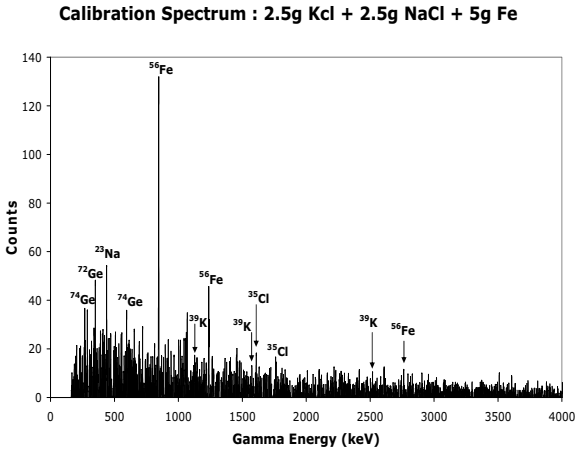


Fig.1. Gamma spectra showing peaks corresponding to excited states in various elements detected in the calibration sample. Gamma peaks are seen for $^{39}K$, $^{23}Na$, $^{35}Cl$, $^{37}Cl$, $^{56}Fe$, $^{70}Ge$, and $^{74}Ge$. These spectra are shown without neutron or gamma attenuation correction.

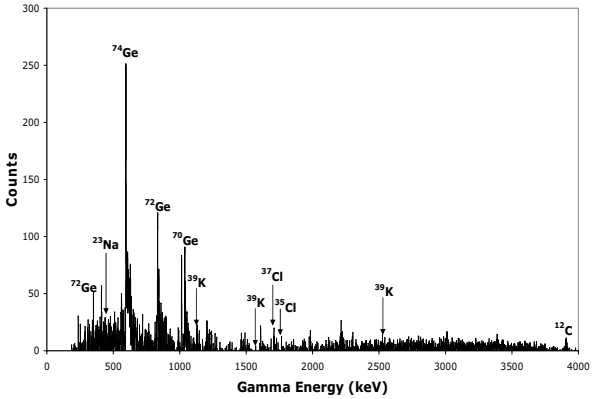


Fig.2. Gamma spectra showing peaks corresponding to excited states in various elements detected in the liver sample. Gamma peaks are identified for all the elements seen in the calibration sample, i.e.$^{39}K$, $^{23}Na$, $^{35}Cl$, $^{37}Cl$, $^{56}Fe$, $^{70}Ge$, and $^{74}Ge$. Peaks from $^{39}K$ are relatively isolated from neighboring peaks and can be used for quantification studies. These spectra are shown without neutron or gamma attenuation correction.

The calibration sample shows peaks from energy states in potassium ($^{39}K$), sodium ($^{23}Na$), chlorine ($^{35}Cl$, $^{37}Cl$), and iron ($^{56}Fe$). Peaks corresponding to natural states in germanium are seen from the HPGe detectors. Peaks from $^{39}K$ were seen to be relatively isolated from neighboring peaks and were hence used in this quantification study. The concentration of other

elements in the liver was too low to be detected accurately by this system.

To calculate the concentration of potassium in the liver, counts from energy peaks at 1130 keV and 1573 keV corresponding to excited states in $^{39}$K were summed and normalized against neutron flux monitor counts to get a normalized gamma count yield for both samples. Comparison of the gamma count yield from the unknown bovine liver to that of the calibration sample determined the concentration of $^{39}$K seen by the neutron beam in the bovine liver.

The bovine liver sample was sent for neutron activation analysis (NAA) to determine its elemental composition and provide an estimate of the potassium content to validate the results of this experiment. As expected, NAA showed that the other elements seen in the calibration sample, i.e. $^{39}$K, $^{23}$Na, $^{35}$Cl, $^{37}$Cl and $^{56}$Fe were present in extremely low concentrations in the liver sample. NAA scanning was performed on a wet sample.

## IV. Results and Conclusion

Using the ratio of potassium concentration to gamma counts determined for the calibration sample, the liver potassium concentration was estimated to be 3.37 mg/g wet liver. The NAA results estimated the potassium concentration to be 3.0 mg/g wet liver. The result obtained through NSECT was within 13% of that reported by NAA, an accepted standard element analysis technique. This experiment clearly demonstrates NSECT's ability to non-invasively estimate element concentration in biological tissue. Efforts are being made to improve the sensitivity of the system and detect elements present in low concentrations. Some of the errors in this system can be attributed to a low detection efficiency, high noise background, neutron and gamma attenuation by the samples, and loss of statistical accuracy due to overlapping peaks. Detection efficiency can be improved by using multiple detectors and high flux neutron sources, both of which will also reduce overall scan time. While patient dose for this experiment was calculated to be approximately 15 mSv, increasing detection efficiency will help reduce patient dose even further. Future work includes implementing attenuation correction techniques for both neutron and gamma attenuation in the sample and implementing mathematical peak-fitting algorithms to separate overlapping energy peaks.

## Acknowledgment

We thank all the members of the Triangle Universities Nuclear Laboratory for their help with data acquisition and the members of Duke Advanced Imaging Laboratories for their help with data analysis.

## References

[1] C. E. Floyd, J. E. Bender, A. C. Sharma, A. J. Kapadia, J. Q. Xia, B. P. Harrawood, G. D. Tourassi, J. Y. Lo, A. S. Crowell, and C. R. Howell, "Introduction to neutron stimulated emission computed tomography," *Physics in Medicine and Biology*, vol. 51, pp. 3375-3390, 2006.

[2] C. E. Floyd, J. E. Bender, A. C. Sharma, A. J. Kapadia, J. Q. Xia, B. P. Harrawood, G. D. Tourassi, J. Y. Lo, and A. S. C. C. R. Howell, "Neutron Stimulated Emission Computed Tomography of a Multi-Element Phantom," *IEEE Trans Med Imag*, vol. submitted (2006), 2006.

[3] C. E. Floyd, C. R. Howell, B. P. Harrawood, A. S. Crowell, A. J. Kapadia, R. Macri, J. Q. Xia, R. Pedroni, J. Bowsher, M. R. Kiser, G. D. Tourassi, W. Tornow, and R. Walter, "Neutron Stimulated Emission Computed Tomography of Stable Isotopes," presented at SPIE Medical Imaging, San Diego, CA, 2004.

[4] L. W. Powell and K. J. Isselbacher, "Hemochromatosis," in *Harrison's Principles of Internal Medicine*: McGraw-Hill.

[5] L. W. Powell, "Diagnosis of hemochromatosis," *Semin Gastrointest Dis*, vol. 13, pp. 80-8, 2002.

[6] L. W. Powell, D. K. George, S. M. McDonnell, and K. V. Kowdley, "Diagnosis of hemochromatosis," *Ann Intern Med*, vol. 129, pp. 925-31, 1998.

# Design and Construction of a Prototype Rotation Modulation Collimator for Near-Field High-Energy Spectroscopic Gamma Imaging

Amy C. Sharma, Georgia D. Tourassi, Anuj J. Kapadia, Brian P. Harrawood, Janelle E. Bender, Alexander S. Crowell, Mathew R. Kiser, Calvin R. Howell, Carey E. Floyd, Jr

***Abstract*– Neutron Stimulated Emission Computed Tomography (NSECT) is being developed for *in vivo* measurement of the concentration and location of biologically relevant elements. NSECT is a spectroscopic imaging technique whereby the body is illuminated via high-energy neutrons that excite elemental nuclei that then relax through characteristic gamma radiation. This imaging technique requires high-resolution spectroscopy, thereby eliminating the use conventional scintillation gamma cameras. Consequently, high-purity germanium (HPGe) semi-conductor detectors are utilized, providing no spatial information. To obtain 2D elemental concentration images, we are adapting high-energy solar spectroscopy technology. A rotating modulation collimator (RMC) consisting of two parallel-slat collimators is placed in front of the detector to modulate the incoming signal in a manner predicted by its geometry. Reconstruction of 2D images is feasible by counting the number of incident gammas at each rotation angle. The challenge is to identify a RMC geometry that allows this method to work in the near-field environment, which has far fewer assumptions and simplifications than the infinite focus of solar imaging. Herein we describe construction of a prototype RMC and experiments conducted with a radioactive $^{22}$Na point source. These experiments verified that the RMC modulates the signal in manner consistent with its geometric and physical properties.**

A. C. Sharma is with the Department of Biomedical Engineering and the DAILabs of the Department of Radiology, 2424 Erwin Rd, Suite 302, Duke University, Durham, NC, 27705 USA (phone: 919-684-1440; fax: 919-684-1491; email: anc4@duke.edu).

G. D. Tourassi is with the DAILabs of the Department of Radiology, Duke University, Durham, NC, 27710 USA (phone: 919-684-1447; fax: 919-684-1491; email: gt@deckard.duhs.duke.edu).

A. J. Kapadia is with the Department of Biomedical Engineering and the DAILabs of the Department of Radiology, Duke University, Durham, NC, 27710 USA (phone: 919-684-1470; fax: 919-684-1491; email: anuj,kapadia@duke.edu).

B. P. Harrawood is with the DAILabs of the Department of Radiology, Duke University, Durham, NC, 27710 USA (phone: 919-684-7782; fax: 919-684-1491; email: brian.harrawood@duke.edu).

J. E. Bender is with the Department of Biomedical Engineering, Duke University, Durham, NC, 27710 USA (email: jeb9@duke.edu).

A. S. Crowell is with the Department of Physics Duke University and the Triangle Universities Nuclear Laboratory, Durham, NC, 27708 USA (phone: 919-660-2639; fax: 919-660-2634; email: crowell@tunl.duke.edu).

M. R. Kiser is with the Department of Physics Duke University and the Triangle Universities Nuclear Laboratory, Durham, NC, 27708 USA (phone: 919-660-2639; fax: 919-660-2634; email: kiser@tunl.duke.edu).

C. R. Howell is with the Department of Physics Duke University and the Triangle Universities Nuclear Laboratory, Durham, NC, 27708 USA (phone: 919-660-2632; fax: 919-660-2634; email: howell@need4speed.duke.edu).

C. E. Floyd Jr. is with the Digital Advanced Imaging Laboratories (DAILabs) of the Department of Radiology, Duke University Medical Center and the Department of Biomedical Engineering Duke University, Durham, NC, 27710 USA

## I. Introduction

Certain elements are vital to the body and an elemental imbalance can be a symptom or cause of certain pathologies. Several studies have shown trace element concentration may be able to distinguish between malignant and benign tumors [1-7] and certain liver diseases are also distinguished by an imbalance of copper and/or iron [2, 8].

Neutron Stimulated Emission Computed Tomography (NSECT) is a spectroscopic imaging technique whereby the body is illuminated via a beam of neutrons causing elemental nuclei to become excited and emit characteristic gamma radiation as they relax. The gamma energy spectra are acquired in a tomographic geometry allowing reconstruction of elemental concentration images [9].

Previously we have demonstrated the feasibility of NSECT using first generation CT approaches by scanning phantoms via a thin neutron beam at many different angles [10]. While successful, the approach does not scale well and limits resolution to the size of the neutron beam. Current gamma cameras operate in an energy range too low for NSECT imaging and are limited by both crystal size and collimation [11]. Another approach would be to adapt technology used in high-energy solar spectroscopy. A rotating modulation collimator (RMC), consisting of two parallel-slat collimators offset from one another, is placed in front of the detector and modulates the incoming signal by rotating about the z-axis. Reconstruction of 2D images is possible by counting the number incident gammas at each collimator rotation angle, as these modulation profiles are unique to a gamma source's location in space. Currently, this method is being employed to successfully image the sun in the Reuven Ramaty High Energy Solar Spectroscopic Imager (RHESSI) [12-15].

We previously reported on geometric modeling of the collimator behavior based on a model developed by Schnopper, et al [16] and Hurford, et al [12]. While this model allowed for excellent simulation and reconstruction [17], it does not accurately reflect the behavior of the RMC in the near-field environment. The challenge is to identify a RMC geometry that allows this method to work in the near-field environment, which has far fewer assumptions and simplifications than the infinite focus of solar imaging. To that

end we have designed and developed a prototype RMC for testing in the near field environment.

The methods section will describe the design and construction of a prototype RMC, experimental validation using a radioactive point source to obtain modulation profiles and a Monte Carlo scheme developed in Matlab to confirm the behavior of the RMC. Results will show that adequate modulation profiles were obtained experimentally and that modulation behaves as predicted by the Monte Carlo simulation. We will then discuss implications for future research.

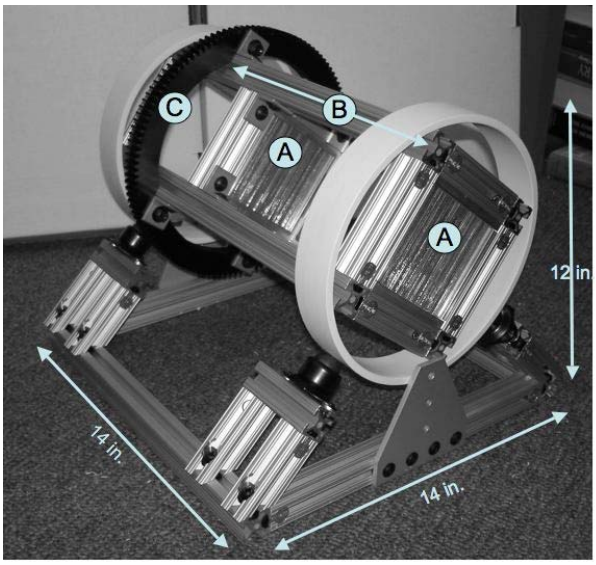


Figure 1. Prototype RMC, designed for flexibility. The slats and slots (A) are made of lead and plastic respectively, and can be switched out to test different slat and slot widths. The far bank of slats and slots can be moved along the rails (B) to test different separation heights. The gear (C) is used to provide rotation of the unit.

## II. Methods

### A. Prototype Construction

A prototype RMC was constructed. Aluminum extrusion was used to build a rectangular frame. This frame contained the two collimators, which consisted of lead slots separated by plastic slots. A piece of plastic PVC pipe was fitted around each end of the rectangle, and the entire unit then rested on rollers. To rotate the RMC, a steel ring gear was fitted around the frame and coupled to a gear fixed to a computer controlled rotational stage. The axis of rotation of the RMC intersects the center of the detector face.

The prototype RMC was designed for flexibility, as the distance between the collimators can be varied, and the collimator slats and slots can be exchanged for ones with different thicknesses and widths (see Figure 1).

The RMC parameters chosen for this experiment were: slat width: 0.5mm, slot width: 1.0mm, and slat height: 1.5cm. The distance between collimators was varied (see Table I).

### B. Radioactive Point Source Testing

A 17.9μCi point source of $^{22}$Na (which emits both 511keV and 1274keV gamma rays) was positioned at various locations on the imaging plane (located orthogonal to the face of the detector and centered about the axis of rotation of the detector). It was always located on the y-axis, so that the radial distance on the image plane was equal to its y location. This also centered the peak of the modulation profile. An HPGe detector was placed directly behind the rear collimator of the RMC (see Figure 2). This was connected to a multi-channel analyzer (MCA), which counted the number of energy events recorded at both 511 keV and 1.2 MeV. The RMC and point source geometries are listed in Table I. For each setup, modulation profiles were obtained by recording the number of gammas detected in a two-minute interval at 10° intervals between 0° and 180°, resulting in 19 measurements per setup.

TABLE I
EXPERIMENTAL SETUPS

| Distance Between Source and Detector | Distance Between Collimators | Point Source Location (radius, cm) |
|---|---|---|
| 40 cm | 10 cm | 0, 4, 5 and 6 cm |
| 40 cm | 20 cm | 0, 3, 4 and 5 cm |
| 50 cm | 10 cm | 0, 5, 6 and 7 cm |
| 50 cm | 20 cm | 0, 4, 5 and 6 cm |

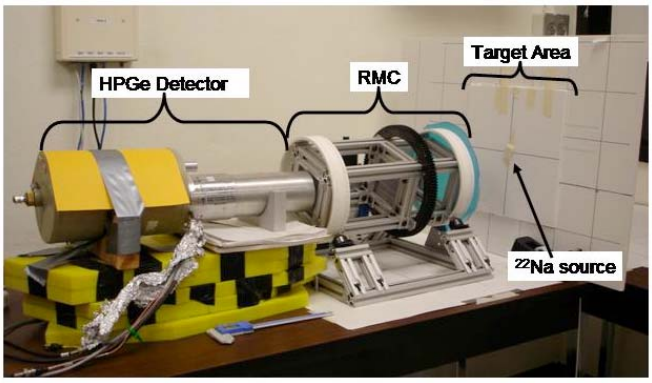


Figure 2. Experimental setup including HPGe detector, RMC and point source on an imaging plane (the poster board).

### C. Monte Carlo Simulation

A Monte Carlo environment was developed in Matlab to model the behavior of the RMC and detector. The collimators were defined as four planes parallel to the x,y plane. Located within each place were the collimator slates, with known locations. A line was drawn from the point source (located at a certain radius and angle on the imaging plane) to a position on the detector face and its points of intersection with each plane were calculated. If the intersection points coincided with a slat or crossed a slat, the gamma ray was considered blocked and did not reach the detector (see Figure 3). This process was repeated for paths from the source to many points on the detector face, assigning a value of 1 to a complete path and 0 to a blocked path. The sum of all paths was calculated for many different collimator angles, which resulted in a modulation profile for that point source's location in space.

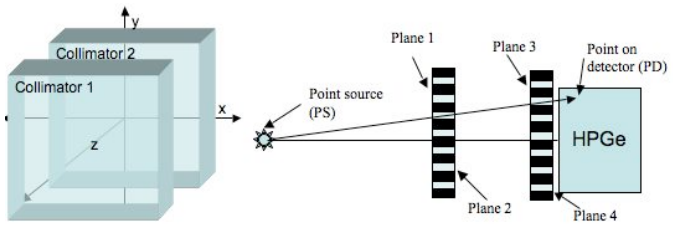


Figure 3. Left: Collimator geometry in the x,y,z plane. Right, view along the z axis of point source, collimators, and detector. The front and back of each collimator face define four planes. The gamma ray traveling on the line between the point source (PS) and a point on the detector (PD) must navigate through each plane in order to be seen by the detector.

## III. Results / Discussion

In order to reconstruct images, the RMC must collimate the gammas in a manner unique to their location. The more unique this modulation profile is, the better resolution that is obtained. Of note: the collimators do not have to attenuate all incoming gamma rays, but rather only modulate them in a predictable and unique manner.

Adequate modulation profiles were obtained for all RMC configurations with the 511 keV gamma rays. $^{22}$Na produces twice as many 511 keV annihilation gammas as 1.2 MeV relaxation gammas; therefore, the lower number of counts and increased collimator penetration by the higher energy gamma rays resulted in less distinct modulation profiles for the 1.2 MeV gamma rays (see Figure 4).

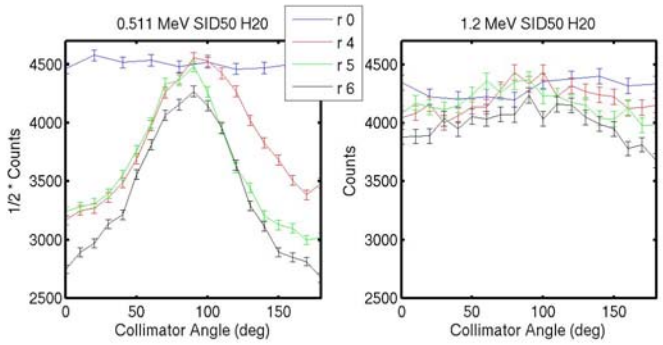


Figure 4. Modulation profiles obtained by the collimator with collimator separation of 20cm and axial distance to source of 50 cm. Left: number of 511 keV gamma events (divided by two for comparison to the 1.2 MeV). Right: number of 1.2 MeV gamma events. Note that while the "peak" in the profile occurs in the same place, the 511 keV profiles are more distinct. Also, the profiles become thinner as the radial distance from the axis of rotation increases.

The Monte Carlo simulation provided similar results, with the same modulation profile pattern (see Figure 5). But, the model did not account for gamma ray penetration, so the modulation profiles were “ideal” and could not vary based on gamma strength. Regardless, the Monte Carlo results verify the basic shape of the modulation profiles obtained.

The radial and angular locations of the point source affect the modulation profile. As the point source’s radial distance from the axis of rotation increases, the modulation profiles become thinner. As the collimator rotates the area of the detector face that the point source can “see” varies. This area will be a maximum when the slits of the collimator are aligned with the angular location of the point source (Figure 5).

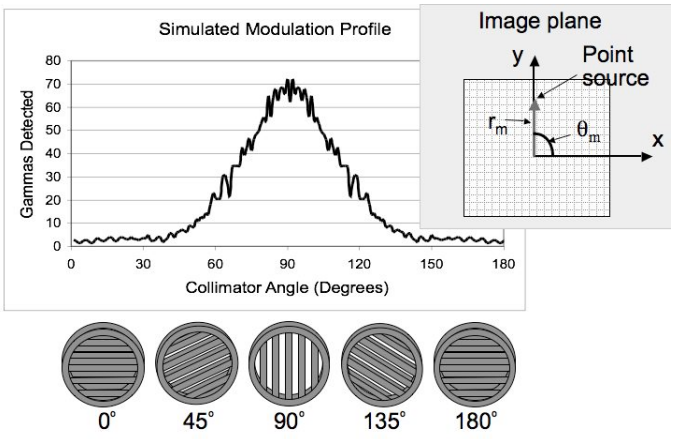


Figure 5. Simulated modulation profile. Beneath the profile are the corresponding collimator views as seen from the perspective of a point source located on the y-axis of the imaging plane (the point source that created this profile). The top inset depicts the location of the point source in the imaging plane. The z-axis is pointed out of the page.

Overall, there are many lessons to be learned from the prototype camera. The RMC geometries used in this setup were less then ideal. The modulation profiles were wide, and barely existent for the 1.2 MeV gamma rays. The aluminum frame was too bulky and attenuated the gamma rays. The small area of the first collimator limited the field-of-view. The large steel ring gear will also interfere with measurements. All of these limitations can be addressed in a new RMC design including: a less bulky, less attenuating frame, a larger first collimator and a less attenuating drive mechanism.

## IV. Conclusions

Herein, we described the design and construction of a prototype RMC and its subsequent testing with a radioactive point source and confirmation of the results via a Monte Carlo simulation. To our knowledge this is the first experimental demonstration of RMC modulation of gamma rays in the near field. Our study provides evidence that modulation of incoming gamma rays is feasible and does vary based on gamma ray source location. Future work will be focused on using this modulation knowledge to develop a model of the RMC. This model will be used to develop and design a RMC that adequately modulates the incoming signal in a manner that allows reconstruction of images with reasonable resolution. The resolution necessary depends on the final imaging goal of the camera and NSECT has potential uses in small animal imaging, cancer screening and liver disease monitoring.

The design of a near field, high energy, gamma camera is a necessary step in furthering NSECT development. In order for NSECT to become a feasible modality a reasonably quick imaging method must be identified. The proposed high-energy resolution gamma camera also has other possible nuclear medicine uses including dual-isotope imaging.

## ACKNOWLEDGMENTS

The authors wish to thank Triangle Universities Nuclear Laboratory for the use of their expertise, spectroscopy equipment and laboratory space. They also wish to thank Joe Owen for his help in machining several collimator parts.

This work was supported in part by:
- NIH/NCI grant no. 1-R21-CA106873-01
- NIH Training grant no. 1-T32-EB001040

## REFERENCES

[1] E. Andrasi, Suhajda, M., Saray, I., Bezur, L., Ernyei, L., Reffy, A. , "Concentration of elements in human brain: glioblastoma multiforme," *Sci. Total Env.*, vol. 139/140, pp. 399-402, 1993.

[2] A. Danielsen, Steinnes, E., "A study of some selected trace elements in normal and cancerous tissue by neutron activation analysis," *J. Nuclear Med.*, vol. 11, pp. 260-264, 1970.

[3] A. N. Garg, Weginwar, R.G., Chutke, N.L. , "Radiochemical neutron activation analysis of Fe, Co, Zn, Sb, and Se in biomedical and environmental samples," *Sci. Total Env.* , vol. 139/140, pp. 421-430, 1993.

[4] K. Geraki, Farquharson, M.J., Bradley, D.A. , "X-ray fluorescence and energy dispersive x-ray diffraction for the quantification of elemental concentrations in breast tissue," *Phys. Med. Biol.*, vol. 49, pp. 99-110, 2004.

[5] K. H. Ng, Bradley, D.A., Looi, L.M., Seman Mahmood, C., Khalik Wood, A., "Differentiation of elemental composition of normal and malignant breast tissue by instrumental neutron activation analysis," *Appl. Radiat. Isot.*, vol. 44, pp. 511-516, 1993.

[6] K. H. Ng, Bradley, D.A., Looi, L.M. , "Elevated trace element concentrations in malignant breast tissues," *British J. Rad.*, vol. 70, pp. 375-382, 1997.

[7] M. Yaman, Atici, D., Bakirdere, S., Akdeniz, I. , "Comparison of Trace Metal Concentration in malign and Benign Human Prostate," *J. Med. Chem.*, vol. 48, pp. 630-634, 2005.

[8] N. Milman, Laursen, J., Podenphant, J., Staun-Olsen, P. , "Iron, copper, zinc, and selenium in lumen liver tissue measured by X-ray fluorescence spectrometry," *Scand. J. Clin. Lab. Invest.*, vol. 43, pp. 691-697, 1983.

[9] C. Floyd, Bender, JE, Sharma, AC, Kapadia, AJ, Xia, JQ, Harrawood, BP, Tourassi, GD, Lo, JY, Crowell, AS, Howell, CR. , "Introduction to Neutron Stimulated Emission Computed Tomography," *Phys Med Biol*, vol. 51, pp. 3375-3390, 2006.

[10] C. Floyd, Bender, JE, Sharma, AC, Kapadia, AJ, Xia, J, Harrawood, BP, Tourassi, GD, Lo, JY, Crowell, A, Howell, CR. , "Neutron Stimulated Emission Computed Tomography of a Multi-Element Phantom," *IEEE TMI*, vol. (submitted Sept 2006), 2006.

[11] J. Bushberg, Seibert, JA, Leidholdt Jr, EM, Boone, JM, *The Essential Physics of Medical Imaging*, 2 ed. Philadelphia, PA: Lippincott Williams & Wilkins, 2002.

[12] G. J. Hurford, Schmahl, E.J., Schwartz, R.A., Conway, A.J., Aschwanden, M.J., Csillaghy, A., Dennis, B.R., Johns-Krull, C., Krucker, S., Lin, R.P., McTiernen, J., Metcalf, T.R., Sato, J., Smith, D.M., "The RHESSI Imaging Concept," *Solar Physics*, vol. 210, pp. 61-86, 2002.

[13] R. P. Lin, Dennis, B.R., Hurford, G.J., et. al., "The Reuven Ramety High-Energy Solar Spectroscopic Imager (RHESSI)," *Solar Physics*, vol. 210, pp. 3-32, 2002.

[14] R. P. Lin, Krucker, S., Hurford, G.J., Smith, D.M., Hudson, H.S., Holman, G.D., Schwartz, R.A., Dennis, B.R., Share, G.H., Murphy, R.J., Emslie, A.G., Johns-Krull, C., Vilmer, N., "REHSSI observations of particle acceleration and energy release in an intense solar gamma-ray line flare," *Astrophysical J*, vol. 595, pp. L69-L76, 2003.

[15] R. P. P. I. Lin, "HESSI-SMEX Proposal," vol. 2005. Berkeley, CA, 1997.

[16] H. Schnopper, Bradt, HV, Rappaport, S, Boughan, E, Burnett, B, Doxsey, R, Mayer, W, Watt, S., "Percise Location of Sagittarius X-ray sources with a Rocket-Borne Rotating Modulation Collimator," *Astrophysical J.*, vol. 161, pp. L161-L167, 1970.

[17] A. Sharma, Floyd, CE, Harrawood, B, Tourassi, G, Kapadia, A, Bender, J, Lo, J, Howell, C., "Rotating slat collimator design for high-energy near-field imaging," presented at Proceedings of the 2006 SPIE Symposium on Medical Imaging, San Diego, 2006.

# Development of a High-Energy Gamma Camera for use with NSECT Imaging of the Breast

Amy C. Sharma, Georgia D. Tourassi, Anuj J. Kapadia, Janelle E. Bender, Jessie Q. Xia, Brian P. Harrawood, Alexander S. Crowell, Mathew R. Kiser, Calvin R. Howell, Carey E. Floyd, Jr

***Abstract*– A new imaging technique, Neutron Stimulated Emission Computed Tomography (NSECT), is being developed that has potential for utilization in breast cancer imaging. NSECT is a spectroscopic imaging technique that is able to produce elemental concentration images and previous studies have identified differences in trace element concentrations between malignant and benign tissues. NSECT illuminates the body via a beam of neutrons causing elemental nuclei to become excited and emit characteristic gamma radiation. By imaging the gamma rays in a tomographic manner it is possible to reconstruct elemental composition images. This method requires high-resolution spectroscopy, thereby eliminating the use conventional scintillation gamma cameras; in this case, spectral information is obtained from high-purity germanium (HPGe) semi-conductor detectors, providing only 1D spatial information. To obtain 2D elemental concentration images, we are adapting high-energy solar spectroscopy technology. A rotating modulation collimator (RMC) consisting of two parallel-slat collimators is placed in front of the detector and modulates the incoming signal in a manner predicted by its geometry. Reconstruction of 2D images is possible by counting the number incident gammas at each rotation angle. A significant challenge is presented when attempting to modify the RMC for use in the near field and a prototype camera has been constructed to verify the geometric validity of a RMC for this use. Herein we present the progress to date in the design and development of a high-energy spectroscopic gamma camera for use with NSECT imaging of the breast.**

This work was supported in part by: NIH/NCI grant no. 1-R21-CA106873-01 and NIH Training grant no. 1-T32-EB001040

A. C. Sharma is with the Department of Biomedical Engineering and the DAILabs of the Department of Radiology, 2424 Erwin Rd, Suite 302, Duke University, Durham, NC, 27705 USA (phone: 919-684-1440; fax: 919-684-1491; email: anc4@duke.edu).

G. D. Tourassi is with the DAILabs of the Department of Radiology, Duke University, Durham, NC, 27710 USA (phone: 919-684-1447; fax: 919-684-1491; email: gt@deckard.duhs.duke.edu).

A. J. Kapadia is with the Department of Biomedical Engineering and the DAILabs of the Department of Radiology, Duke University, Durham, NC, 27710 USA (phone: 919-684-1470; fax: 919-684-1491; email: anuj,kapadia@duke.edu).

J. E. Bender is with the Department of Biomedical Engineering, Duke University, Durham, NC, 27710 USA (email: jeb9@duke.edu).

J. Q. Xia is with the Department of Biomedical Engineering and the DAILabs of the Department of Radiology, Duke Univsersity, Durham, NC, 27710 USA (phone: 919-684-1667; fax: 919-684-1491; email: xq1977@duke.edu).

B. P. Harrawood is with the DAILabs of the Department of Radiology, Duke University, Durham, NC, 27710 USA (phone: 919-684-7782; fax: 919-684-1491; email: brian.harrawood@duke.edu).

A. S. Crowell is with the Department of Physics Duke University and the Triangle Universities Nuclear Laboratory, Durham, NC, 27708 USA (phone: 919-660-2639; fax: 919-660-2634; email: crowell@tunl.duke.edu).

M. R. Kiser is with the Department of Physics Duke University and the Triangle Universities Nuclear Laboratory, Durham, NC, 27708 USA (phone: 919-660-2639; fax: 919-660-2634; email: kiser@tunl.duke.edu).

C. R. Howell is with the Department of Physics Duke University and the Triangle Universities Nuclear Laboratory, Durham, NC, 27708 USA (phone: 919-660-2632; fax: 919-660-2634; email: howell@need4speed.duke.edu).

C. E. Floyd Jr. is with the Digital Advanced Imaging Laboratories (DAILabs) of the Department of Radiology, Duke University Medical Center and the Department of Biomedical Engineering Duke University, Durham, NC, 27710 USA

## I. Introduction

A new imaging technique – Neutron Stimulated Emission Computed Tomography (NSECT) – is being developed to provide elemental concentration images of the body being interrogated. NSECT has the potential to be utilized in breast cancer imaging in both the detection and classification of suspicious lesions.

An NSECT image is obtained by illuminating the region of interest via a beam of high-energy (3-5 MeV) neutrons. These neutrons scatter inelastically off of elemental nuclei, causing the nuclei to become excited and emit characteristic gamma radiation. Imaging these gammas in a tomographic manner allows for the reconstruction of elemental composition images [1].

### *A. Breast Cancer Application & Innovation*

Several studies have identified elemental composition differences between malignant and benign tumors in the breast [2-6]. NSECT has the ability to non-invasively measure and image elemental concentrations. In the future, NSECT has the potential to identify and map regions of the breast containing elemental abnormalities. This could lead to one non-invasive scan where suspicious lesions could be detected and the tissue classified as malignant, benign or normal.

There are several advantages to NSECT imaging. Neutrons are highly penetrating and may be more effective on dense breasts. Imaging could be preformed in the more comfortable "pendant breast" position. By identifying and classifying suspicious lesions in one step, a large majority of biopsy follow-ups could be eliminated, thereby simplifying and speeding diagnosis and treatment.

### *B. Proposed Imaging System*

NSECT requires high-resolution, high-energy (up to several MeV) spectroscopy that cannot be accomplished using conventional nuclear medicine scintillation cameras. Instead spectral information is obtained from a large volume (7cm diameter), single-crystal, high purity germanium (HPGe) semi-conductor detector. These detectors provide approximately 1% FWHM resolution over the energy range of

interest (300 keV – 2 MeV) [7], but provide no spatial information. To obtain images we are adapting high-energy space-based spectroscopic imaging technology for use in the near field. A rotating modulation collimator (RMC) consisting of two parallel-slat collimators is placed in front of the HPGe detector and modulated the incident gamma flux in a manner predicted by its geometry. Counting the number of incident gammas at each collimator rotation angle results in a modulation profile. Each point in the imaging plane has a modulation profile unique to its location in space. Using the observed gamma flux, 2D planar images can be reconstructed [8-13]. By placing several RMC cameras at different locations around the breast and the rotating the entire assembly, it is possible to generate 3D volumetric elemental composition images (see Fig. 1).

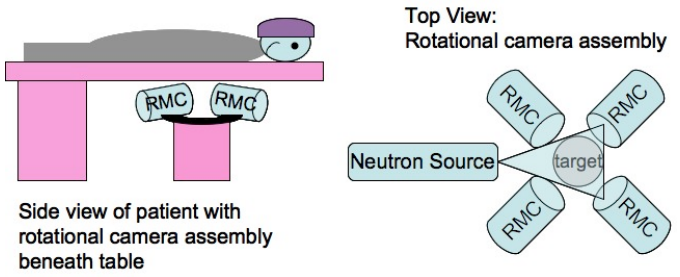


Figure 1: Proposed breast imaging system.

Herein we will describe the progress to date in the development of this RMC imaging system including prototype construction and testing, Monte Carlo simulation, and reconstruction with multiple camera views.

## II. Progress to Date

### A. Prototype RMC

A prototype RMC was built using aluminum extrusion for the frame, lead "slats" and plastic "slots." Rotational motion was provided by a gear mounted on a rotational stage coupled to a steel ring gear mounted on the frame (see Fig. 2).

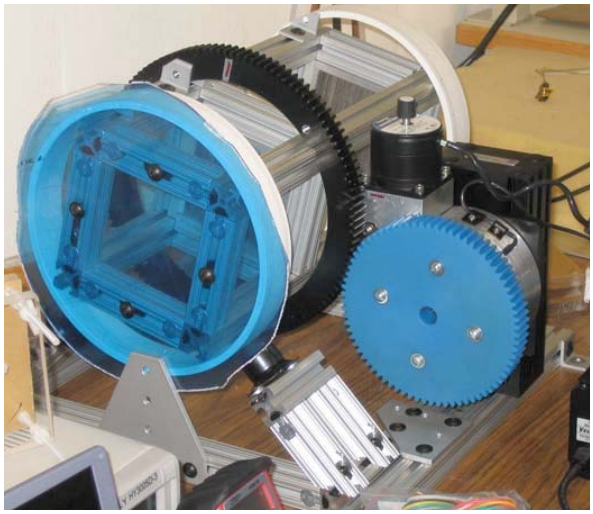

Figure 2: Prototype RMC. The two parallel slat collimators are the striped squares. The ring gear is coupled to a gear mounted on the rotational stage.

The RMC was placed in front of a HPGe detector and then tested with a 17.9μCi $^{22}$Na point source. Modulation profiles were obtained with the source and the RMC placed in various configurations. Results are depicted in Fig. 3. For more information on this experiment and the RMC please see [14]. Of note: in order to obtain spatial information the collimators only have to modulate the incoming gamma rays and provide a distinct modulation profile, they do not have to provide complete gamma attenuation.

### B. Monte Carlo Simulation

A Monte Carlo simulation environment consisting of a gamma ray point source, the two collimators and an HPGe detector was developed in GEANT4. The same RMC and point source configurations as those tested with the prototype were simulated. Similar modulation profiles were obtained for both the simulated and experimental results (see Fig. 3).

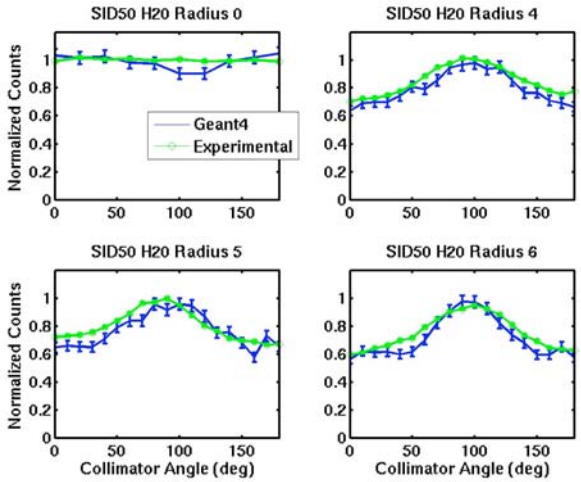


Figure 3: Normalized experimental (green) and simulated (blue) results for a 511 keV source located 50 cm from the detector at various distances from the axis of rotation.

### C. Reconstruction with Multiple Camera Views

We have conducted several simulations of the system geometry in Matlab and used this data to reconstruct 2D images with the MLEM algorithm [15]. Due to the simple modulation profiles provided by the system, multiple camera views of the same object are necessary in order to adequately visualize point and extended sources. Successful reconstruction of point and extended sources was achieved by simulating imaging the same object from several different locations (see Fig. 4). For further information the reader is referred to [8, 16].

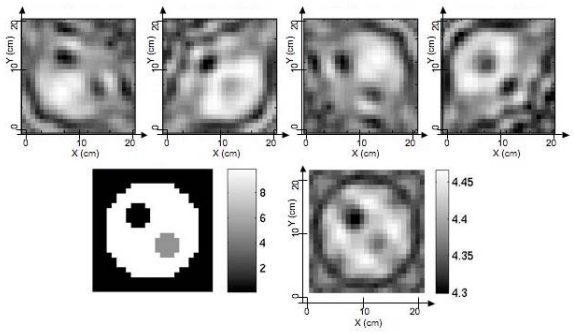


Figure 4: Top: Reconstructed images of a simulated extended source as seen from four different camera positions. Bottom: Original Image and image obtained by reconstructing all four data sets simultaneously.

## III. Conclusions / Future Work

NSECT is a novel imaging method with the potential to distinguish between malignant and benign tissue in one non-invasive step. Development of a high-energy high-energy-resolution gamma camera is an essential step in the development of NSECT. Herein, we presented out progress to date on the development of such a camera.

The prototype camera modulated the incident gamma rays in a manner predicted by its geometry. A Monte Carlo simulation environment produced similar modulation results. Development of this simulation environment allows for the identification of suitable camera designs. In order to successfully image the breast a camera with at least 1cm resolution in a 15cm$^2$ field-of-view must be developed. Future work will focus on identifying suitable camera designs that can provide adequate images with a minimal dose.

Simulated modulation of the incident gamma rays shows that the modulation is distinct enough to reconstruct images. However, due to the simplistic nature of the modulation profiles, multiple camera views are necessary. The use of multiple cameras should also serve to reduce scanning time and therefore reduce the dose.

## Acknowledgment

We thank Joe Owen for his machining help. We also thank the people at Triangle Universities Nuclear Laboratory for their equipment, space, supplies and support.

## References

[1] C.E. Floyd, J.E. Bender, A.C. Sharma, A.J. Kapadia, J. Q. Xia, B.P. Harrawood, G.D. Tourassi, J.Y. Lo, A.S Crowell, C.R. Howell. "Introduction to Neutron Stimulated Emission Computed Tomography," *Phys Med Biol*, vol. 51, pp. 3375-3390, 2006.

[2] A. Danielsen, E. Steinnes. "A study of some selected trace elements in normal and cancerous tissue by neutron activation analysis," *J. Nuclear Med.*, vol. 11, pp. 260-264, 1970.

[3] A. N. Garg, R.G. Weginwar, N.L. Chutke. "Radiochemical neutron activation analysis of Fe, Co, Zn, Sb, and Se in biomedical and environmental samples," *Sci. Total Env.* , vol. 139/140, pp. 421-430, 1993.

[4] K. Geraki, M. J. Farquharson, D.A. Bradley, "X-ray fluorescence and energy dispersive x-ray diffraction for the quantification of elemental concentrations in breast tissue," *Phys. Med. Biol.*, vol. 49, pp. 99-110, 2004.

[5] K. H. Ng, D.A. Bradley, L.M. Looi, C. Seman Mahmood, A. Khalik Wood, "Differentiation of elemental composition of normal and malignant breast tissue by instrumental neutron activation analysis," *Appl. Radiat. Isot.*, vol. 44, pp. 511-516, 1993.

[6] K. H. Ng, D.A. Bradley, L.M. Looi, "Elevated trace element concentrations in malignant breast tissues," *British J. Rad.*, vol. 70, pp. 375-382, 1997.

[7] G. F. Knoll, *Radiation Detection and Measurement*, 3 ed. Hoboken, NJ: Wiley, 2000.

[8] A.C. Sharma, T.G. Turkington, G.D. Tourassi, C.E. Floyd, "Near-Field High-Energy Spectroscopic Gamma Imaging Using a Rotation Modulation Collimator," *IEEE TNS*, vol. Submitted Nov 2006, 2006.

[9] G. J. Hurford, E.J. Schmahl, R.A. Schwartz, A.J. Conway, M.J. Aschwanden, A. Csillaghy, B.R. Dennis, C. Johns-Krull, S. Krucker, R.P. Lin, J. McTiernen, T.R. Metcalf, J. Sato, D.M. Smith, "The RHESSI Imaging Concept," *Solar Physics*, vol. 210, pp. 61-86, 2002.

[10] R. P. Lin, B.R. Dennis, G.J. Hurford, et. al., "The Reuven Ramety High-Energy Solar Spectroscopic Imager (RHESSI)," *Solar Physics*, vol. 210, pp. 3-32, 2002.

[11] R. P. Lin, S. Krucker, G.J. Hurford, D.M. Smith, H.S. Hudson, G.D. Holman, R.A. Schwartz, B.R Dennis, G.H. Share, R.J. Murphy, A.G. Emslie, C. Johns-Krull, N. Vilmer, "REHSSI observations of particle acceleration and energy release in an intense solar gamma-ray line flare," *Astrophysical J*, vol. 595, pp. L69-L76, 2003.

[12] R. P. Lin, "HESSI-SMEX Proposal," vol. 2005. Berkeley, CA, 1997.

[13] H. Schnopper, H.V. Bradt, S. Rappaport, E. Boughan, B. Burnett, R. Doxsey, W. Mayer, S. Watt, "Percise Location of Sagittarius X-ray sources with a Rocket-Borne Rotating Modulation Collimator," *Astrophysical J.*, vol. 161, pp. L161-L167, 1970.

[14] A.C. Sharma, G.D. Tourassi, A.J. Kapadia, B.P. Harrawood, J.E. Bender, A.S. Crowell, M.R. Kiser, C.R. Howell, C.E. Floyd, "Design and Construction of a Prototype Rotation Modulation Collimator for Near-Field High-Energy Spectroscopic Gamma Imaging," presented at IEEE NSS & MIC, San Diego, CA, 2006.

[15] K. Lange, R. Carson, "EM reconstruction algorithms for emission and transmission tomography," *J. Comp. Assist. Tomo.*, vol. 8, pp. 306-316, 1984.

[16] A.C. Sharma, C.E. Floyd, B.P. Harrawood, G.D. Tourassi, A.J. Kapadia, J.E. Bender, J.Y. Lo, C.R. Howell, "Rotating slat collimator design for high-energy near-field imaging," *Proceedings of the 2006 SPIE Symposium on Medical Imaging*, vol. 6142, pp. 405-413, 2006.

# Rotating Slat Collimator design for high-energy near-field imaging

Amy Sharma[a], Carey Floyd[a,b], Brian Harrawood[b], Georgia Tourassi[b], Anuj Kapadia[a], Janelle Bender[a], Joseph Lo[a,b], Calvin Howell[c]
[a]Dept. of Biomedical Engineering, Duke University, 136 Hudson Hall, Durham, NC 27708,
[b]Dept. of Radiology, Duke University Medical Center, Durham, NC 27710
[c]Dept. of Physics, Triangle Universities Nuclear Laboratory, Duke University, Durham, NC 27706

## ABSTRACT

Certain elements (such as Fe, Cu, Zn, etc.) are vital to the body and an imbalance of such elements can either be a symptom or cause of certain pathologies. Neutron Stimulated Emission Computed Tomography (NSECT) is a spectroscopic imaging technique whereby the body is illuminated via a beam of neutrons causing elemental nuclei to become excited and emit characteristic gamma radiation. Acquiring the gamma energy spectra in a tomographic geometry allows reconstruction of elemental concentration images. Previously we have demonstrated the feasibility of NSECT using first generation CT approaches; while successful, the approach does not scale well and has limited resolution. Additionally, current gamma cameras operate in an energy range too low for NSECT imaging. However, the orbiting Reuven Ramaty High Energy Solar Spectroscopic Imager (RHESSI) captures and images gamma rays over the high-energy range equivalent to NSECT's (3 keV to 17 MeV) by utilizing Collimator-based Fourier transform imaging. A High Purity Germanium (HPGe) detector counts the number of energy events per unit of time, providing spectroscopic data. While a pair of rotating collimators placed in front of the detector modulates the number of gamma events, providing spatial information. Knowledge of the number of energy events at each discrete collimator angle allows for 2D image reconstruction. This method has proven successful at a focus of infinity in the RHESSI application. Our goal is to achieve similar results at a reasonable near-field focus. Here we describe the results of our simulations to implement a rotating modulation collimator (RMC) gamma imager for use in NSECT using simulations in Matlab. To determine feasible collimator setups and the stability of the inverse problem a Matlab environment was created that uses the geometry of the system to generate 1D observation data from 2D images and then to reconstruct 2D images using the MLEM algorithm. Reasonable collimator geometries were determined, successful reconstruction was achieved and the inverse problem was found to be stable.

**Keywords:** imaging, neutrons, tomography, spectroscopy, image reconstruction

## 1. INTRODUCTION

Certain elements are vital to the body and an elemental imbalance can be a symptom or cause of certain pathologies. Several studies have shown trace element concentration may be able to distinguish between malignant and benign tumors in the breast, prostate and brain [1-7]. Certain liver diseases are also distinguished by an imbalance of iron (hemochromatosis) or copper (Wilson's Disease) [2, 8].

Elemental studies in animals have shown: decreased Cu and Fe in the brain of rats prone to seizures [9]; an increase in trace elements in organs and tumors of mice with skin tumors [10, 11]; and a change in trace element concentrations in the kidneys of mice with malignant ascites [12].

Current techniques for determining elemental composition of tissue samples require specific preparation of the sample that is incompatible with *in-vivo* studies.

*Send correspondence to Amy C Sharma, Dept . of Biomedical Engineering, DAI Labs, 2424 Erwin Rd, Suite 302, Durham, NC 27705; anc4@duke.edu

Neutron Stimulated Emission Computed Tomography (NSECT) is a spectroscopic imaging technique whereby the body is illuminated via a beam of neutrons causing elemental nuclei to become excited and emit characteristic gamma radiation. The gamma energy spectra are acquired in a tomographic geometry allowing reconstruction of elemental concentration images. Previously we have demonstrated the feasibility of NSECT using first generation CT approaches by scanning phantoms via a thin neutron beam at many different angles. While successful, the approach does not scale well and limits resolution to the size of the neutron beam.

Current gamma cameras operate in an energy range too low for NSECT imaging. Their performance is limited by both crystal size and collimation. Crystals of less then 2 cm provide adequate capture for most low-energy gammas generated in typical nuclear medicine applications, but are unable to adequately capture higher energy photons. Typical collimators are ineffectual when used with high-energy photons, thereby limiting spatial location information.

The orbiting Reuven Ramaty High Energy Solar Spectroscopic Imager (RHESSI) captures and images gamma rays over the high-energy range equivalent to NSECT's (3 keV to 17 MeV) by utilizing Collimator-based Fourier transform imaging. Nine High Purity Germanium (HPGe) detectors count the number of energy events per unit of time, providing spectroscopic data. Placed in front of each detector is a pair of rotating collimators that modulate the number of gamma events, providing spatial information. As the satellite rotates about its z-axis, the collimator pair allows between 0% and 50% of the events to reach the detector (Figure 1). Varying the size and spacing of the attenuating slates allows for measurement of different Fourier components of the source. Knowledge of the number of energy events at each discrete collimator angle allows for 2D image reconstruction. This method has proven successful at a focus of infinity in the RHESSI application [13-16].

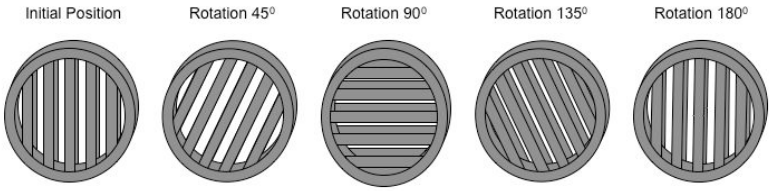


Figure 1. Change in event transmission as collimators rotate about the z-axis as drawn from the prospective of a source down and to the left. Note how after one half a rotation, the collimators are aligned in their initial position.

We aim to achieve high-energy spectroscopic imaging at a near-field focus via Collimator-based Fourier transform imaging. Current technology allows for high-energy spectroscopy at infinite focus, and relies on the subsequent simplifications. Near-field imaging is subject to fewer assumptions and provides a significant challenge. Near-field imaging is necessary in order to provide a practical size and geometry in order to apply NSECT to small animal imaging and/or human tissue imaging in the laboratory or clinic.

The purpose of this study is to focus on initial attempts to solve the near-field geometric problem within a Matlab simulated environment and to determine feasible geometries.

### 1.1 Rotating Modulation Collimator (RMC) Design

A RMC / HPGe detector unit is depicted in Figure 2 which defines the geometric frame of reference and the various parameters (including: slat width, slot width, slat height, height and distance) that can be varied in order to change the modulation of the incoming gamma rays. It should be noted that the collimators do not need to attenuate the gamma rays completely to achieve 2D reconstruction of an image, but rather they need only to modulate the signal over the rotational range of the collimator.

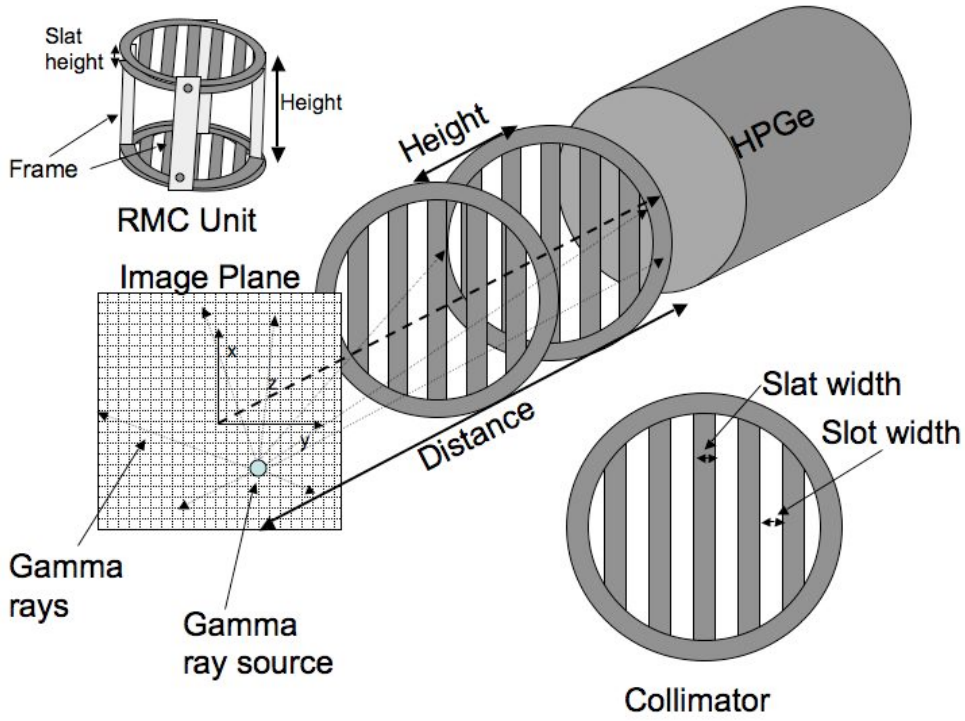


Figure 2. Layout and dimensions of detector, RMC unit, and imaging plane containing a point source.

**1.2 Geometric Parameter Estimation**

As the RMC rotates about the z-axis a certain number of counts are seen by the detector at each collimator angle, $\theta_i$. The resulting observation matrix contains the number of counts at each angle. This information is used to reconstruct a 2D image consisting of *m* pixels by using a probability matrix, P, which contains the probability that the counts at each collimator angle, $\theta_i$, originated at each pixel, *m*, located at a location (x,y) in a plane perpendicular to the axis of rotation in space. Schnopper, et al [17] and Hurford, et al. [13] proposed a method of determining this probability matrix based on the geometry of the RMC / detector unit.

$$P_{im} = \frac{1}{4}\left[1 + \frac{8}{\pi^2}\cos(\Phi)\right]$$

where:

$$\Phi = \frac{2\pi r_i \cos(\theta_i - \theta_m)}{\Delta}$$

$$r_i = \tan^{-1}\frac{r_m}{D}$$

$$\Delta = \tan^{-1}\frac{p}{height}$$

$$\theta_m = \tan^{-1}(y/x)$$

Where $r_m$ is radial distance of pixel *m* (located at position x,y) from the center of the 2D plane of reconstruction (the axis of rotation of the collimator assembly passes through the origin of the x,y coordinate system). *D* is the *z* distance of the detector from the imaging plane containing the source; *p* is the slot width plus slat width; height is the distance between the two collimators; and $q_i$ is the angle of the collimator (see Figure 2 and Figure 3).

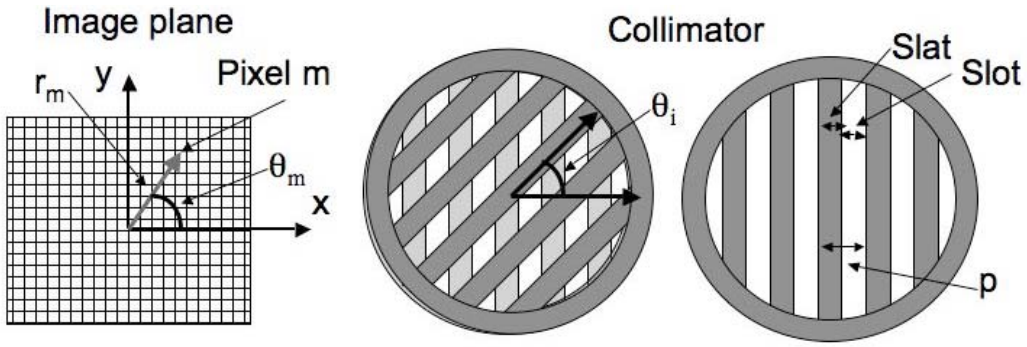


Figure 3. Dimensions associated with reconstruction using probably estimation.

## 2. METHODS

### 2.1 Matlab simulation environment / data generation

A Matlab script was written to generate the probability matrix described above. The user entered the size of the 2D imaging plane (FOV and pixel size), slat and slot width, slat height, height, distance to the 2D imaging plane and number of collimator rotation angles. Using this information the probability matrix, P, was generated.

Simulated observation data was obtained by creating a 2D image where gamma sources were given the value of '1000' or '1' and background '0'. This 2D image was then multiplied by the probability matrix, resulting in a 1D observation matrix (number of counts per collimator angle).

Reconstruction of images was performed using the maximum likelihood expectation maximization (MLEM) algorithm [18]. The MLEM algorithm was run for 20 iterations on each reconstruction and utilized the same probability matrix that was used in creating the observation data.

The following table lists the RMC parameters were chosen for testing because they are similar to those used by RHESSI, and also easily constructed.

| All RMCs had a slat width: 0.5mm, slot width: 1mm, slat height: 15mm, rotation angles: 600. | | | | | |
|---|---|---|---|---|---|
| | Setup 1 | Setup 2 | Setup 3 | Setup 4 | Setup 5 |
| Distance to imaging plane | 30 cm | 40 cm | 40 cm | 50 cm | 50 cm |
| Height between collimators | 20 cm | 20 cm | 30 cm | 20 cm | 30 cm |

**Table 1: Five RMC setups used for testing.**

Reconstruction pixel sizes of 2 mm, 4 mm and 8 mm were tested. The FOV was chosen to be a 10 cm square ranging from 5 cm to 15 cm in both the x and y direction. Point sources were tested at (6,6) (6,14) (10,10) (14,6) (14,14) to measure response throughout the FOV. Four extended sources were tested: a 3.2 cm square, a 1.6 cm square, two 1.6 cm squares and a step pattern (see Figure 4)

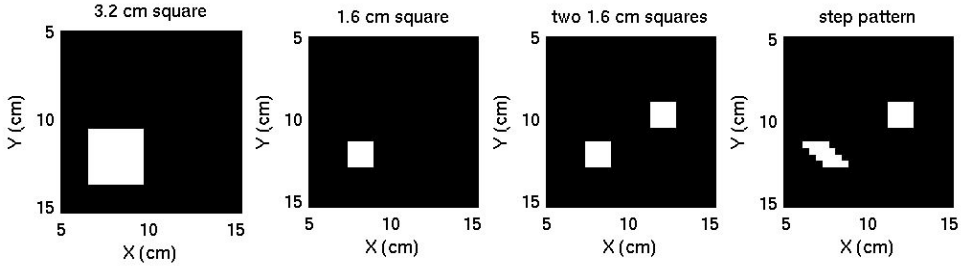


Figure 4. Four extended sources used to test the geometric model and subsequent reconstruction. From left to right: a 3.2 cm square, a 1.6 cm square, two 1.6 cm squares and a step pattern.

## 3. RESULTS / DISCUSSION

### 3.1 Point Sources

Adequate reconstruction was achieved of all point sources within the field of view. The same images were achieved by using sources with a value of '1' or '1000' except the higher numbers yielded maximum values that were increased by a factor of 1000; for the sake of clarity only those images are shown. **Figure 5** depicts the source located at (10,10) for all setups and pixel sizes, note how the strength of the reconstruction (as signified by the 'max' number) improves as the pixel size increases. For the 2 mm pixels a distinct ringing can been seen in the Setups 2 and 4 reconstructions, while the other three setups yield more of a cross shaped pattern. This periodic behavior is expected because of the trigonomic dependence of the prediction matrix.

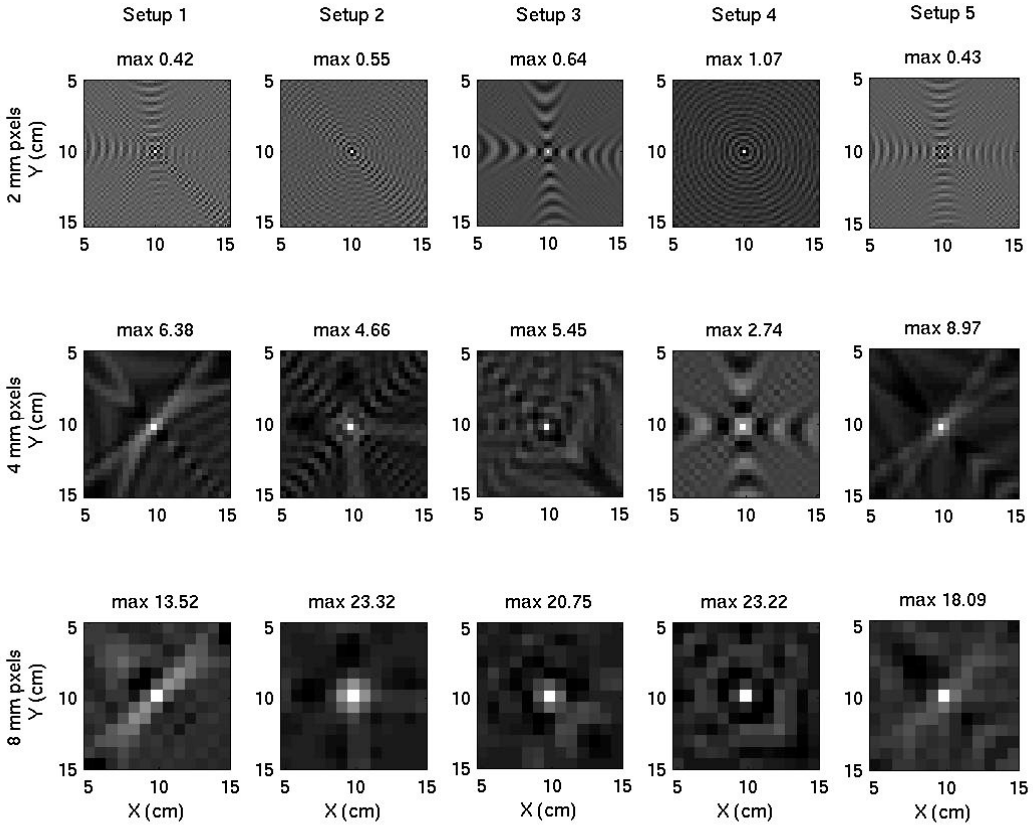


Figure 5. Point sources located at position (10,10). Pixel sizes range from 2 mm, 4 mm, and 8 mm (top to bottom rows). While the collimator parameters change from setup 1 to setup 5 (left to right).

### 3.2 Extended Sources

The results for the extended sources are shown in **Figure 6** and **Figure 7**. Reconstruction of the 3.2 cm square source breaks down completely for: all setups at 2 mm pixels, Setup 1 at all pixel sizes and Setup 3 at 2 mm and 4 mm pixel sizes. But it performs adequately for the other setups, especially at 8 mm. The 1.6 cm square is better reconstructed at all levels, except for Setup 1. The two 1.6 cm squares are resolvable in the same setups as performed well for the 3.2 cm square. Note how phantom sources appear in some of the 2 mm images. The step pattern is only shown for the best performing setups. Note how the step pattern is discernable in all the images, especially at the 8 mm pixel resolution with Setup 4.

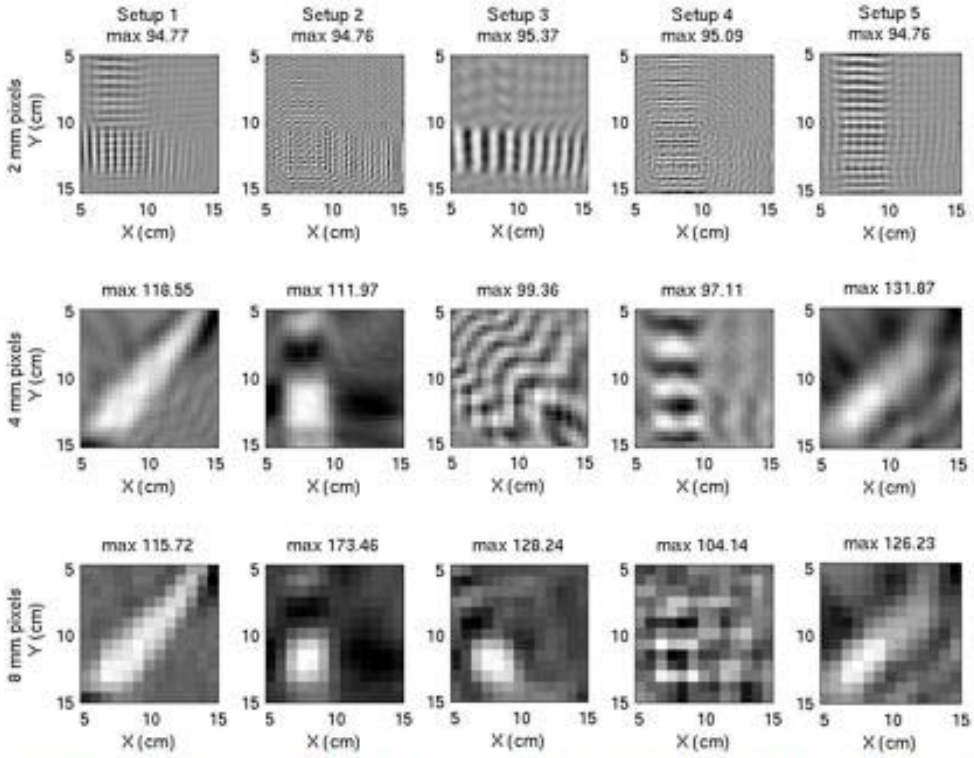


A) 3.2 cm square extended source. Top to bottom: 2 mm, 4 mm, and 8 mm pixels. Left to right: Setup 1 through 5.

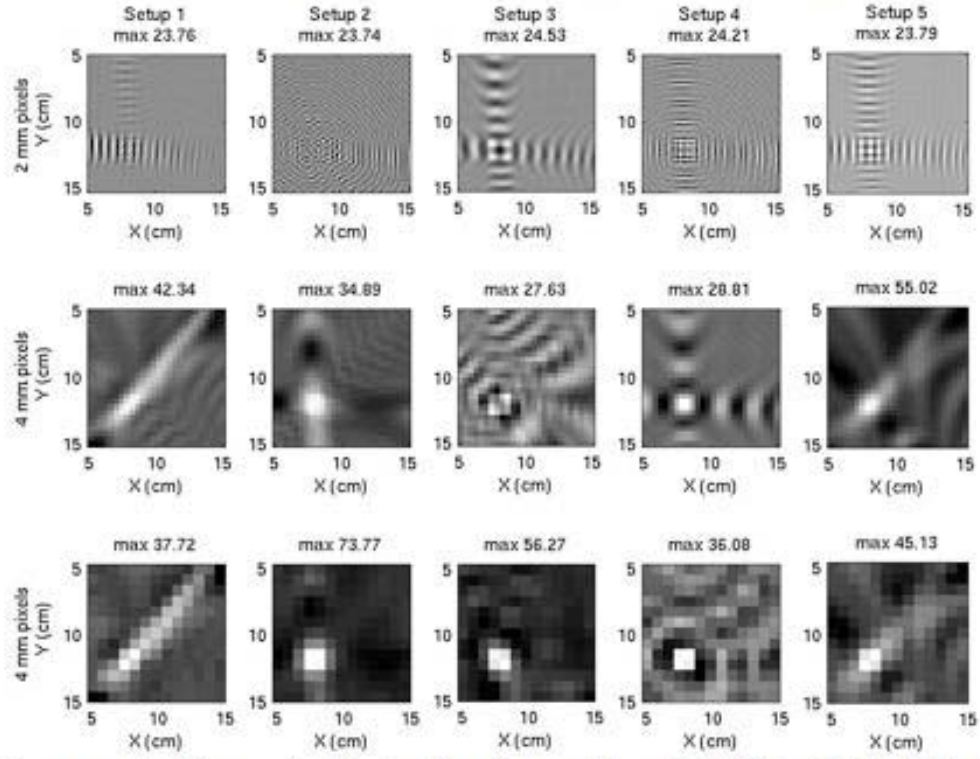


B) 1.6 cm square extended source. Top to bottom: 2 mm, 4 mm, and 8 mm pixels. Left to right: Setup 1 through 5.

Figure 6. Reconstruction of 3.2 cm square (top) and 1.6 cm square (bottom) for all setups. Note the 1.6 cm square is more easily reconstructed then the 3.2 cm square.

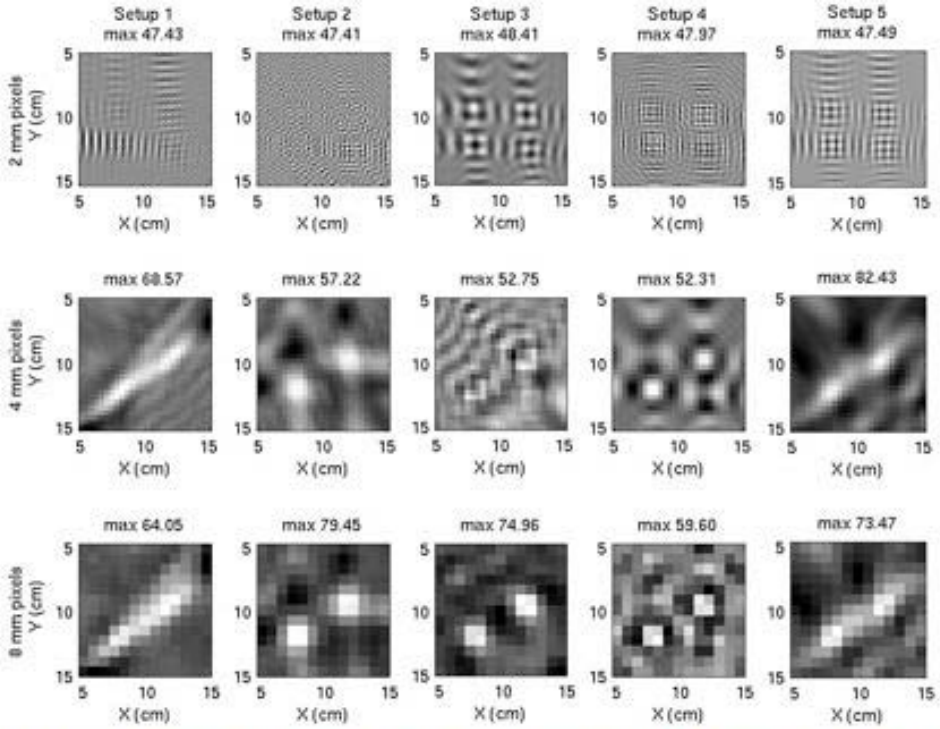


A) Two 1.6 cm square extended sources. Top to bottom: 2 mm, 4 mm, and 8 mm pixels. Left to right: Setup 1 through 5.

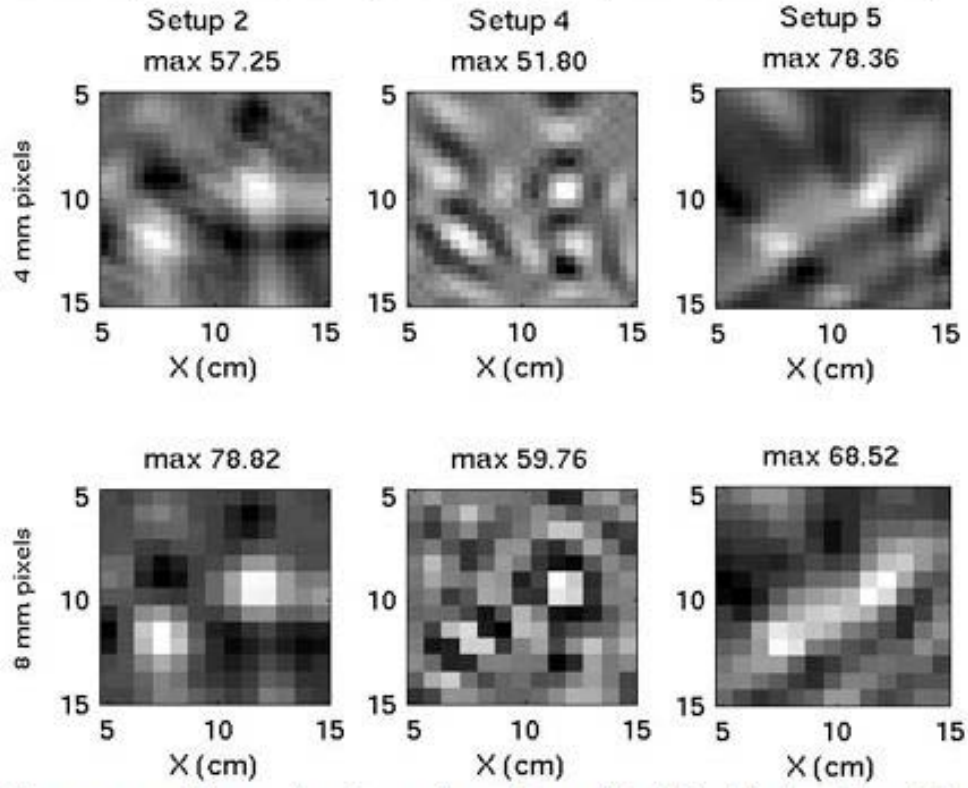


B) Step pattern extended sources. Top to bottom: 4 mm and 8 mm pixels. Left to right: Setup 2, Setup 4, Setup 5

Figure 7. Two 1.6 cm squares (top) and step pattern (bottom) reconstruction. Only the best Setups (2, 4 and 5) are shown in the bottom image.

According to our data it is clear that 2 mm resolution as well as Setups 1 and 3 are not feasible designs. While reconstruction with 8 mm pixels performs the best, images reconstructed with 4 mm pixels provide adequate results.

## 4. CONCLUSION

We achieved successful reconstruction using the MLEM algorithm demonstrating that the inverse reconstruction problem has a stable, predictable solution. The simulations have identified several possible RMC / detector configurations that are feasible to construct. Future work on this problem would include: simulation and reconstuction of images from Monte Carlo observation data as well as actual construction and testing.

## ACKNOWLEDGEMENTS

This work is supported in part by NIH Grant EB001040-01.

## REFERENCES

1. Andrasi, E., Suhajda, M., Saray, I., Bezur, L., Ernyei, L., Reffy, A. , *Concentration of elements in human brain: glioblastoma multiforme*. Sci. Total Env., 1993. **139/140**: p. 399-402.
2. Danielsen, A., Steinnes, E., *A study of some selected trace elements in normal and cancerous tissue by neutron activation analysis.* J. Nuclear Med., 1970. **11**(6): p. 260-264.
3. Garg, A.N., Weginwar, R.G., Chutke, N.L. , *Radiochemical neutron activation analysis of Fe, Co, Zn, Sb, and Se in biomedical and environmental samples*. Sci. Total Env. , 1993. **139/140**: p. 421-430.
4. Geraki, K., Farquharson, M.J., Bradley, D.A. , *X-ray fluorescence and energy dispersive x-ray diffraction for the quantification of elemental concentrations in breast tissue.* Phys. Med. Biol., 2004. **49**: p. 99-110.
5. Ng, K.H., Bradley, D.A., Looi, L.M., Seman Mahmood, C., Khalik Wood, A., *Differentiation of elemental composition of normal and malignant breast tissue by instrumental neutron activation analysis*. Appl. Radiat. Isot., 1993. **44**(3): p. 511-516.
6. Ng, K.H., Bradley, D.A., Looi, L.M. , *Elevated trace element concentrations in malignant breast tissues.* British J. Rad., 1997. **70**: p. 375-382.
7. Yaman, M., Atici, D., Bakirdere, S., Akdeniz, I. , *Comparison of Trace Metal Concentration in malign and Benign Human Prostate.* J. Med. Chem., 2005. **48**: p. 630-634.
8. Milman, N., Laursen, J., Podenphant, J., Staun-Olsen, P. , *Iron, copper, zinc, and selenium in lumen liver tissue measured by X-ray fluorescence spectrometry.* Scand. J. Clin. Lab. Invest., 1983. **43**: p. 691-697.
9. Carl, G.F., Critchfield, J.W., Thompson, J.L., McGinnis, L.S., Wheeler, G.A., Gallagher, B.B., Holmes, G.L. Hurley, L.S., Keen, C.L., *Effect of kainate-induced seizures on tissue trace element concentrations in the rat.* Neuroscience, 1989. **33**(1): p. 223-227.
10. Gulati, N., Mangal, P.C., *Trace element profiles in skin-tumor and tissues of tumour-bearing mice.* Indian J. Cancer, 1985. **22**: p. 308-314.
11. Mangal, P.C., Verma, K.B., *Effect of induced skin cancer on the concentrations of some trace elements in the mouse.* Indian J. Med. Res., 1979. **69**: p. 290-295.
12. Wei, Y.Y., Chung, C., *Analysis of experimental absorption and excretion in mice bearing malignant ascites* Biol. Trace Elem. Res., 1994. **43-45**: p. 397-403.
13. Hurford, G.J., Schmahl, E.J., Schwartz, R.A., Conway, A.J., Aschwanden, M.J., Csillaghy, A., Dennis, B.R., Johns-Krull, C., Krucker, S., Lin, R.P., McTiernen, J., Metcalf, T.R., Sato, J., Smith, D.M., *The RHESSI Imaging Concept.* Solar Physics, 2002. **210**(1-2): p. 61-86.
14. Lin, R.P., Dennis, B.R., Hurford, G.J., et. al., *The Reuven Ramety High-Energy Solar Spectroscopic Imager (RHESSI).* Solar Physics, 2002. **210**(1-2): p. 3-32.
15. Lin, R.P., Krucker, S., Hurford, G.J., Smith, D.M., Hudson, H.S., Holman, G.D., Schwartz, R.A., Dennis, B.R., Share, G.H., Murphy, R.J., Emslie, A.G., Johns-Krull, C., Vilmer, N., *REHSSI observations of particle acceleration and energy release in an intense solar gamma-ray line flare*. Astrophysical J, 2003. **595**: p. L69-L76.
16. Lin, R.P.P.I. *HESSI-SMEX Proposal*. 1997 [cited 2005; Available from: http://hesperia.gsfc.nasa.gov/~kim/toc.html.

17. Schnopper, H., Bradt, HV, Rappaport, S, Boughan, E, Burnett, B, Doxsey, R, Mayer, W, Watt, S., *Percise Location of Sagittarius X-ray sources with a Rocket-Borne Rotating Modulation Collimator*. Astrophysical J., 1970. **161**: p. L161-L167.
18. Lange, K., Carson, R., *EM reconstruction algorithms for emission and transmission tomography.* J. Comp. Assist. Tomo., 1984. **8**(2): p. 306-316.

Available online at www.sciencedirect.com
ScienceDirect
Nuclear Instruments and Methods in Physics Research B 254 (2007) 329–336
NIM B
Beam Interactions with Materials & Atoms
www.elsevier.com/locate/nimb

# Neutron stimulated emission computed tomography: Background corrections

Carey E. Floyd Jr. [a,b,c], Amy C. Sharma [a,b,*], Janelle E. Bender [a,b], Anuj J. Kapadia [a,b], Jessie Q. Xia [a,b], Brian P. Harrawood [b], Georgia D. Tourassi [b], Joseph Y. Lo [a,b,c], Matthew R. Kiser [d], Alexander S. Crowell [d], Ronald S. Pedroni [e], Robert A. Macri [g], Shigeyuki Tajima [f], Calvin R. Howell [c,d]

[a] *Department of Biomedical Engineering, Duke University, Durham, NC 27708, United States*
[b] *Duke Advanced Imaging Laboratories, Department of Radiology, Duke University, Durham, NC 27708, United States*
[c] *Medical Physics Graduate Program, Duke University, Durham, NC 27708, United States*
[d] *Department of Physics and Triangle Universities Nuclear Laboratory, Duke University, Durham, NC 27708, United States*
[e] *North Carolina A&T State University, Greensboro, NC, United States*
[f] *Department of Physics, University of Virginia, Charlottesville, VA, United States*
[g] *Lawrence Livermore National Laboratory, Livermore, CA, United States*

Received 25 August 2006; received in revised form 8 November 2006
Available online 12 January 2007

**Abstract**

Neutron stimulated emission computed tomography (NSECT) is an imaging technique that provides an in-vivo tomographic spectroscopic image of the distribution of elements in a body. To achieve this, a neutron beam illuminates the body. Nuclei in the body along the path of the beam are stimulated by inelastic scattering of the neutrons in the beam and emit characteristic gamma photons whose unique energy identifies the element. The emitted gammas are collected in a spectrometer and form a projection intensity for each spectral line at the projection orientation of the neutron beam. Rotating and translating either the body or the beam will allow a tomographic projection set to be acquired. Images are reconstructed to represent the spatial distribution of elements in the body. Critical to this process is the appropriate removal of background gamma events from the spectrum. Here we demonstrate the equivalence of two background correction techniques and discuss the appropriate application of each.


*PACS:* 82.80; 87.57; 87.64.−t; 25.40.−Fg

*Keywords:* Neutrons; Gamma-ray spectroscopy; Background corrections; Image quality; Biomedical imaging

## 1. Introduction

This Section will describe the physical concepts behind NSECT, followed by a description of the problem posed by the unwanted detection of background gamma events. Section 2 will describe two techniques for estimating and reducing this background. Section 3 will show spectra to illustrate the effect of implementing these techniques. Section 4 will present a comparison of the two background correction techniques along with suggestions for where each would be appropriate to use.

### 1.1. Physical concepts of NSECT

In previous papers, we have introduced neutron stimulated emission computed tomography (NSECT) as a new

* Corresponding author. Address: DAILabs, 2424 Erwin Rd, Suite 302, Durham, NC 27705, United States. Tel.: +1 919 684 1440; fax: +1 919 684 1491.
*E-mail address:* anc4@duke.edu (A.C. Sharma).

0168-583X/$ - see front matter © 2006 Elsevier B.V. All rights reserved.
doi:10.1016/j.nimb.2006.11.098

approach for biological spectroscopy and imaging [1,2]. NSECT provides spectroscopy by stimulating nuclei in the sample by inelastic scattering of fast neutrons. The stimulated nuclei emit characteristic gamma rays that are collected in a gamma spectrometer. Each neutron beam position defines a line of integration of the emitted gammas that are associated with known elements. By translating and rotating the beam with respect to the body, a set of tomographic projections is obtained. These projections are reconstructed for each element that is acquired in the spectrum to provide a spatial map of the elements in the body.

While similar in concept to gamma emission computed tomography (ECT), NSECT does not image radioactive pharmaceuticals but instead stimulates the emission of gammas from stable isotopes. NSECT requires different performance from the imaging technology than ECT. For all elements of interest, the emitted gammas have energies ranging from less then 300 keV to greater than 6000 keV. These energies are higher than those typically used in nuclear medicine and thus standard gamma cameras with lead collimation cannot provide sufficient energy or spatial resolution. In addition, the detection efficiency of these gamma cameras is too low for efficient imaging. For these reasons, we chose to use high purity germanium (HPGe) detectors that have excellent energy resolution within the NSECT range. HPGe detectors with sufficient detection efficiency do not report spatial information and so the spatial position of a single projection path is defined by the neutron beam position.

### 1.2. Unwanted background

Background events in the detected spectra introduce errors in the quantitative accuracy of the detected number of gamma photons acquired from the scattering sample. This results in an error in the estimation of the concentration of the elements in the reconstructed volumes. The background radiation is non-uniform over the energy spectrum and thus cannot be corrected by a simple offset. There are several potential sources of background in these experiments: beam uncorrelated photons, beam correlated events and detector dependent background.

Beam uncorrelated photons will be from the decay of radioactive materials in the detector area. These materials may be naturally radioactive (such as $^{40}$K) or may have become radioactive with a long half-life from extensive exposure to a particle beam (such as metal in the beam transport system and the deuterium gas cell). Photon events from these sources will be random in time and somewhat continuous.

Beam correlated events consists of short half-life radioactive materials, scattered photons and photons emitted from slow neutron capture. Photons emitted by materials that have become radioactive from exposure to the beam but which have short half-lives will be correlated with the beam flux itself. Many times, gamma photons created through inelastic scattering of neutrons in the sample are emitted along a path that initially does not intersect with the detector. These gammas can scatter off of some object in the experimental target area and arrive in the detector. These events will be offset in arrival time from those events where the gamma travels directly to the detector. While the neutrons used in these experiments are fast with energies of several MeV, many of these fast neutrons will scatter from light materials such as protons in plastics and water and thus become moderated down to thermal energies after many collisions. The gammas emitted from slow neutron capture reactions can have energies of many MeV and thus can contribute to background over the entire energy spectrum. One example is the capture of thermal neutrons by $^{23}$Na such as is found in NaI detectors. The $^{23}$Na nucleus captures a neutron to become $^{24}$Na which is unstable and decays by emitting 1.4 and 2.8 MeV gamma photons. This will contribute a large background in NaI detectors if they are used in the presence of thermal neutrons. The thermal neutron flux is correlated with the beam.

Detector dependant background comes in two forms. The first appears as discrete lines in the spectrum. These are caused when a photon with greater than 1022 keV of energy creates an electron–positron pair in the detector and one or both of these products escapes from the detector. Since each carries 511 keV of energy, these events appear as spectral lines that are displaced by 511 keV for a single escape and 1022 keV for a double escape. The second appears as a continuous background that increases at the lower energy region of the spectrum. This is due to photons that Compton scatter in the detector and then either the photon or the scattered electron escape. Since the energy transferred in a Compton collision is a continuous distribution, the offset due to these events is continuous also. Every source of photons will contribute some of this background to the energy channels below it and so the effect compounds at lower energy channels.

In summary, backgrounds can be considered to be of three classes: beam-uncorrelated photons (long half-life radioactive decay), beam-correlated events (short half-life radioactive decay, scattered, slow capture) and detector dependant events (electron escape, Compton scatter). In this work, we consider two techniques for estimating and compensating for these backgrounds. Each technique is sensitive to all classes of backgrounds.

## 2. Methods

The methods for NSECT data acquisition have been described previously [1,2] and only a brief overview will be presented here. For these experiments, a square pulsed beam, 7 mm on each side, of 7.5 MeV neutrons were produced from a pulsed beam of deuterons through the 2H(d,n)3He reaction. The deuterium target was a 5 cm long gas cell containing 100 psig of deuterium gas. The neutrons passed through the end of the gas cell and through a copper channel collimator that passed through

a 2 m thick shield wall. The wall shielded the detectors from the large flux of gammas produced in the 2H(d,n)3He reaction. The pulsed, collimated neutron beam emerged from the collimator to illuminate the scattering sample. Those nuclei along the neutron beam path in the scattering sample which interacted inelastically with the incident neutrons emitted characteristic gamma photons which were detected in HPGe detectors positioned at 135 deg on either side of the neutron beam and at a distance of 20 cm from the center of the scattering sample. These detectors were equipped with anti-Compton shields composed of BGO and NaI scintillators coupled to photomultiplier tubes. If a gamma were to Compton scatter in the primary detector and be captured in the shield, the coincidence of the two events would cause the event in the HPGe detector to be rejected. The HPGe detectors respond to gammas by producing a current pulse that is proportional to the energy of the detected photon. These signals were digitized and stored in the acquisition computer event by event along with the time of flight (TOF) for the event. This list-mode storage allowed the timing windows to be adjusted off line to optimize the acquisition after the experiment. To measure the TOF, the pulses in the deuteron beam were detected just before the gas cell and were used to start a clock to time the flight of the neutrons from the gas cell to the scattering sample along with the time of flight of the emitted gammas to the spectrometer. The energy gain of the detectors was calibrated using radioactive sources with known energy levels: $^{137}$Cs and $^{22}$Na. Gain and analog-to-digital-converter (ADC) ranges were set to give about 1 keV per channel and the exact calibration was calculated from the spectral channels of the calibration peaks. While NSECT has the capability to identify elements that produce gamma radiation between 300 and 6000 keV, the gamma emissions investigated in this study had energies below 2000 keV. Thus, the calibration of the detectors with $^{22}$Na and $^{137}$Cs was adequate for this experiment.

The iron samples used in these experiments were in the form of a rectangular solid 6 mm thick, 30 mm wide, and 60 mm tall. All were of natural density.

Two background correction techniques are evaluated herein. In the first, a Sample-In spectrum was acquired with the scattering sample in the neutron beam. The sample was then removed from the beam and an additional Sample-Out spectrum was acquired. To correct for background the two spectra are normalized to the same incident neutron flux and the Sample-Out spectrum is subtracted from the Sample-In spectrum to produce a background-corrected spectrum. In the second technique, TOF is used to restrict the spectrum of useable photon incident events to a window of time (True acceptance window) for which the arrival of the photon is consistent with the required time of flight for the neutron to reach the sample and for the emitted photon to reach the detector. This leaves some background in the form of photons from random sources whose time of arrival accidentally corresponds to the True acceptance window. This background is estimated by measuring incident events in a window of the same time length but outside the True acceptance window time. The events in such a window correspond to the amount of background that would have occurred in the True acceptance window. These are subtracted to achieve a background corrected spectrum. In Section 3, spectra are shown that correspond to these different background estimates and to the different correction techniques.

## 3. Results

The first background radiation to consider is due to naturally radioactive materials in the detector region. Fig. 1 shows a spectrum acquired with sample removed and with the beam off. This spectrum was acquired overnight (about 8 h) and demonstrates the structure and magnitude of the beam uncorrelated naturally radioactive background in the region of the detector.

An example of a Sample-In, Sample-Out energy spectrum is shown in Fig. 2. The Sample-In spectra (solid line) was obtained by illuminating a phantom constructed of natural iron (94% $^{56}$Fe, 6% $^{54}$Fe) with a beam of 7.5 MeV neutrons. The sample was removed from the beam and the Sample-Out spectra (dashed line) was obtained by counting for an equivalent number of incident neutrons. Note the large magnitude of the background at gamma energies below 600 keV. The background measured using this technique includes beam uncorrelated photons that are emitted from naturally occurring radioactivity in the experimental area (Fig. 1) as well as beam correlated photons that are generated by the neutron beam interacting with objects other than the target and slow neutron capture. All of these sources of background would be present in a clinical imaging environment. Fig. 3 depicts the Sample-In spectra minus the Sample-Out spectra (as shown in Fig. 2).

The second form of background correction was implemented by computing the likely TOF between the production of the neutron pulse and the detection of an associated scattered photon. This is done for a known neutron velocity, distance from neutron source to sample, speed of light for the gamma and the distance from the sample to the gamma detector. The number of incident events at each time (TOF spectrum) is shown in Fig. 4. Examining the TOF spectrum, it is evident that there is a large peak between ~170 and 200 ns, the True acceptance window. There were also a number of gamma detections at times that were well outside this True time window. The gate for the True acceptance window that had believable flight times is shown as a thickened line over the peak. A gate for a False window was set for accidental photons. This gate occurs in a time region corresponding to non-physical neutron and gamma velocities and was set to an equivalent time width as that of the True acceptance window (also shown as a thickened line in Fig. 4).

The energy spectrum for events falling within the Accidental gate is shown in Fig. 5. As can be seen, there is some

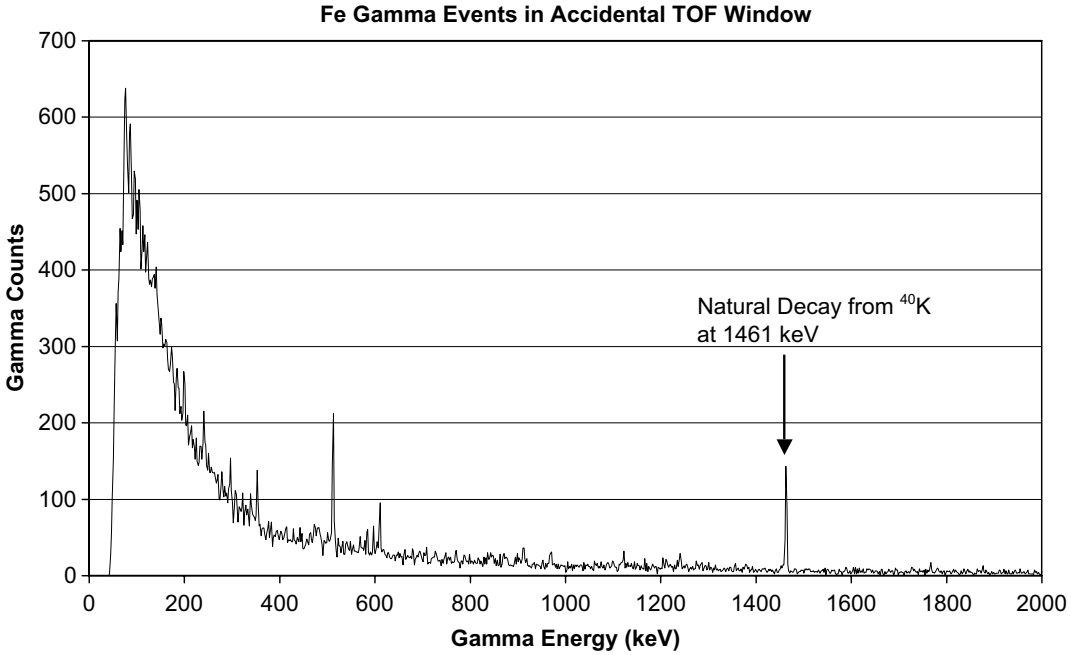


Fig. 1. Spectrum acquired with no beam and no sample to estimate the background photon incidents in the room from radioactive sources not associated with the sample. This spectrum was acquired over a time of several hours to demonstrate the shape and relative size of this background.

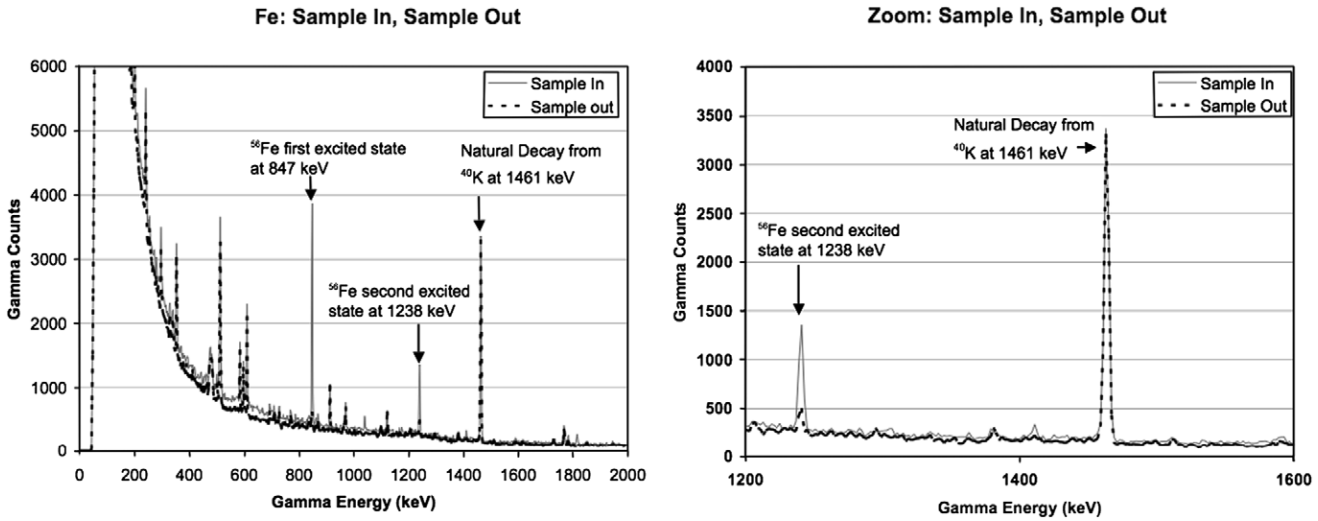


Fig. 2. Energy spectrum from iron sample. Two spectra are shown: the solid grey curve is the sample in the beam and the dashed curve is the sample removed from the beam to estimate the beam-correlated background. The left figure is a complete spectrum from 0 to 2000 keV, while the right figure zooms in on 1400–1600 keV. In the figure at right it is clear that the second excited state in $^{56}$Fe is present only in the Sample-In spectrum while the natural decay line from $^{40}$K is present in both spectra.

structure to the spectra. The peaks correspond to naturally radioactive gamma emissions from objects near the detector.

After the energy events corresponding to the accidental TOF window are subtracted from the energy events corresponding to the true TOF window, the corrected energy spectrum is computed as shown in Fig. 6.

To illustrate that the TOF and sample subtraction methods are equivalent for estimating the background-free spectrum, Fig. 7 shows a comparison the two background estimates.

The equivalence of these techniques for estimating the background is evident from Fig. 7. The difference in the two background spectra is because the Sample-Out spectrum was acquired for a longer time and the two spectra were normalized for plotting. Subtraction of the estimated background results in the excellent energy spectrum shown in Fig. 6 where the signal to background ratio for the first

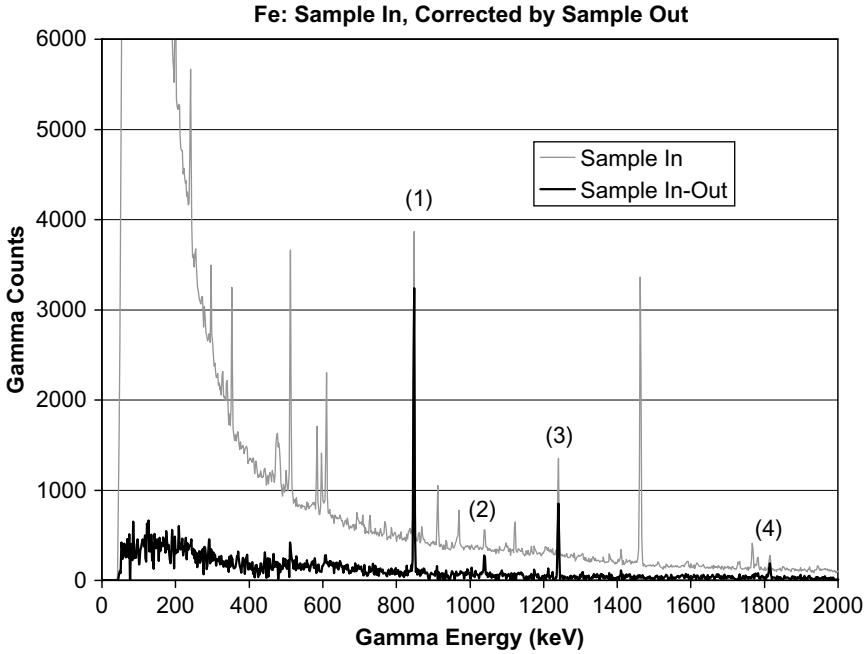


Fig. 3. Experimental spectrum from a thin iron sample. The grey line is the initial spectrum collected and the black line is the same spectrum background corrected by subtracting a Sample-Out spectrum. Four gamma peaks from $^{56}$Fe are clearly identified: (1) at 847 keV is the gamma from the transition from the first excited state to the ground state; (2) at 1038 keV is the gamma from the transition from the 7th excited state at 3123 keV down to the 2nd excited state at 2085 keV; (3) at 1238 keV is the gamma from the transition from the 2nd excited state at 2085 keV down to the 1st excited state at 847 keV and (4) at 1811 keV is the gamma for the transition from the 3rd excited state at 2658 keV down to the 1st excited state at 847 keV. Note the complete removal of the background gammas from the decay of $^{40}$K at 1461 keV.

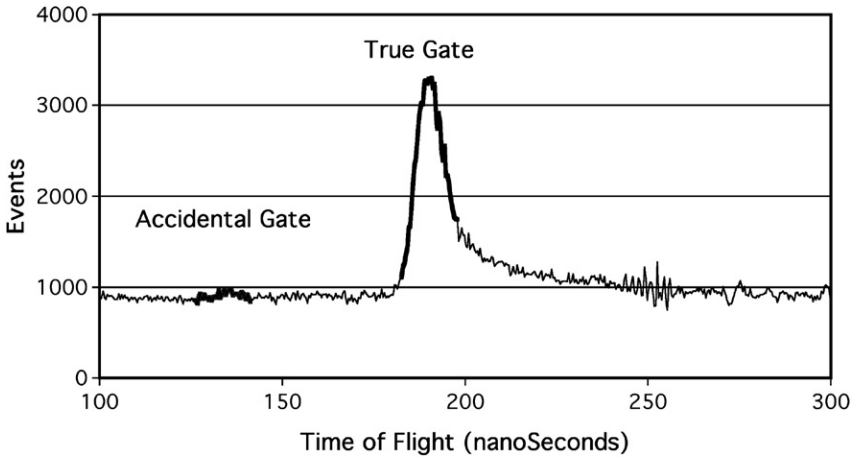


Fig. 4. Time of flight (TOF) spectrum showing a peak for gamma events with a time window correlated with the neutron beam pulse (True Gate) and time window set for non-physical flight times (Accidental Gate). Events falling within the Accidental Gate are not correlated with the neutron pulse.

excited state in $^{56}$Fe at 847 keV is about 33:1 compared to a ratio of only 8:1 in the uncorrected spectrum of Fig. 2.

## 4. Discussion

Two techniques for background correction of spectra acquired using the NSECT technique have been described and have been shown to be equivalent. The TOF technique is more convenient for laboratory experiments where acquisition geometries and parameters are changed frequently and the acquisition of separate backgrounds using the Sample-Out technique would cost valuable acquisition time. The Sample-Out technique is more appropriate to the clinical environment where the acquisition geometry and parameters do not often change and could be performed at the beginning of the day in a manner similar to the way gamma camera uniformity measurements are currently performed in clinical nuclear medicine imaging divisions. Also, the additional hardware required for the TOF implementation would add considerable complexity and cost.

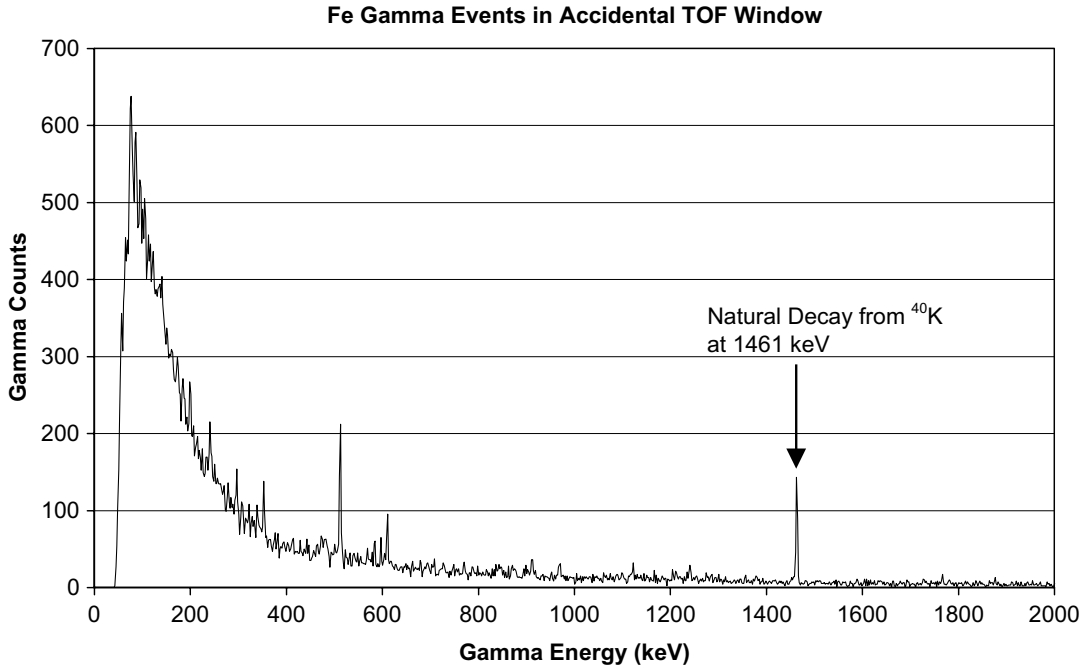


Fig. 5. The energy spectrum for those time uncorrelated events detected within the accidental TOF gate window. The structure is due to radioactive decay of isotopes near the detector.

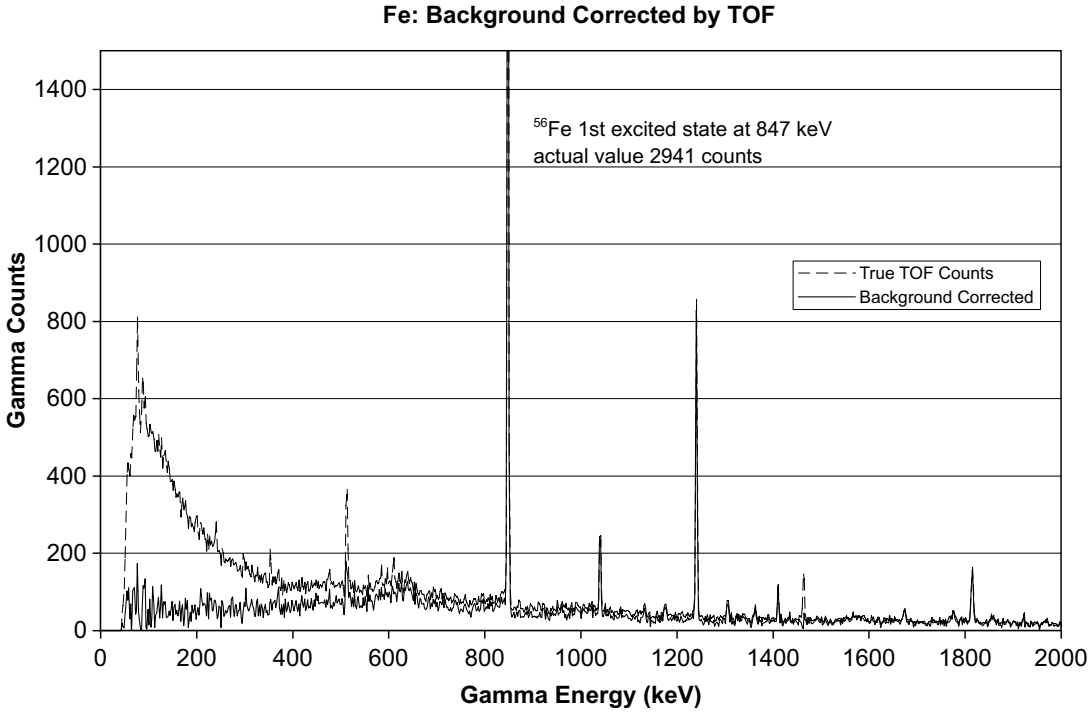


Fig. 6. The energy spectra for the events arriving in the true TOF window (dashed line), and the same spectrum after background correction (solid line) resulting from subtracting the events arriving in the accidental window.

In theory, both the Sample-Out technique and the TOF technique would adequately measure beam uncorrelated background; however, measurement of beam correlated background would be different between the two techniques. The Sample-Out technique measures all events that occur while the neutron beam is firing regardless of the TOF. With the TOF windowing, events are only counted during a certain time window. Beam correlated events may change in number depending on the TOF. But, it appears that the background radiation measured by both techniques is

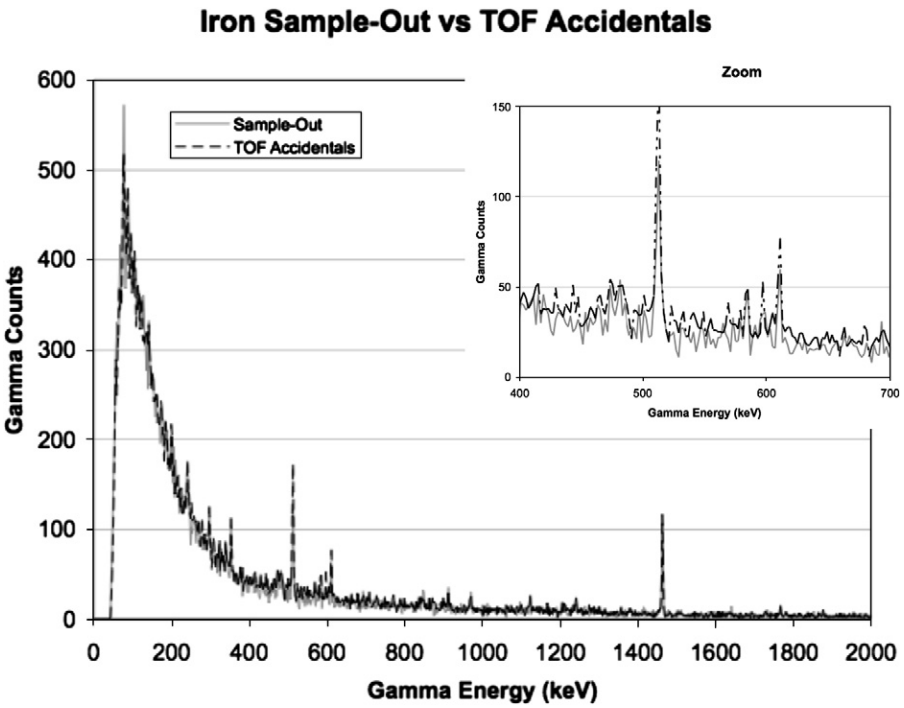


Fig. 7. A comparison of the background acquired with the sample removed (Sample-Out: Solid Line) and the background acquired as events with time of flight (TOF) in the accidental window (TOF Accidentals: dashed line). It is clear that both techniques provide equivalent estimates of the background and that either a Sample-Out measurement or a TOF technique will provide excellent background correction. The inset zooms in on counts collected in the energy range of 400–700 keV.

similar, rendering the differences insignificant. Neither technique can adequately correct for detector dependant background as both electron escape and Compton scatter increase with increased gamma photons. These increase when a sample is present during the proper TOF interval; therefore, this increase cannot be recreated without a sample. A small number of events occurring during the proper TOF with a sample present are background that cannot be filtered out regardless of technique. This is indeed a small amount of background events as both techniques greatly improve SNR.

In spectral analysis, true peaks are typically identified with a certain statistical certainty. Care must be taken to propagate the counting errors during each step in the background correction process; thereby, ensuring the accuracy of both the counting statistics and peak identification. This is achieved in software by maintaining a data set that includes both the spectral information (counts at each energy level) and its corresponding statistical uncertainty. Each time the spectral data is modified in the background correction process, its corresponding uncertainty must be updated as well. This update propagates the counting error through the entire background correction process. Enough initial data must be obtained so that the increase in counting caused by the data manipulation error does not overwhelm the benefits gained by background reduction.

NSECT has potential for a broad range of application in both medical and biological research by providing a three-dimensional map of the spatial distribution of all elements (with the exception of H and He) in a subject from one scan. There are no fundamental physical limitations to the detection sensitivity or spatial resolution of NSECT although there may be considerable technological challenges as we strive for high sensitivity at high spatial resolution.

Several potential applications for NSECT were identified in a previous work [2] including: cancer detection (based on previous work where a change in elemental concentration was associated with malignancy [3–27]), measurements of iron overload in the liver (important for thalassemia patients; sickle cell patients at risk for stroke; individuals with hemochromatosis mutations, and for other patients who receive chronic blood transfusions [28]), and small animal imaging. The demonstration of successful background reduction provided by the current work is an important fist step toward realizing each of these applications.

## 5. Conclusion

In conclusion, we have demonstrated excellent potential for NSECT as a spectroscopic imaging technique. Several sources of gamma backgrounds have been identified and corrections have been implemented. Corrected spectra for NSECT projection acquisition from single-element phantoms have been presented. The equivalence of the two background correction techniques demonstrates that adequate background correction can be efficiently conducted in the laboratory using the TOF technique and can be

performed effectively in the clinical setting using the Sample-Out technique.

## Acknowledgments

The authors wish to acknowledge the team effort and contributions of the members of Duke Advanced Imaging Laboratories (DAILabs) and Triangle Universities Nuclear Laboratory (TUNL).

This work was supported in part by: NIH/NCI Grant 1-R21-CA106873-01 and NIH Training Grant 1-T32-EB001040.

## References

[1] C.E. Floyd Jr., C.R. Howell, B.P. Harrawood, A.S. Crowell, A.J. Kapadia, R. Macri, J.Q. Xia, R. Pedroni, J.E. Bowsher, M.R. Kiser, G.D. Tourassi, W. Tornow, R. Walter, Neutron stimulated emission computed tomography of stable isotopes, Proc. SPIE 5568 (2004) 248.

[2] C.E. Floyd Jr., J.E. Bender, A.C. Sharma, A.J. Kapadia, J.Q. Xia, B.P. Harrawood, G.D. Tourassi, J.Y. Lo, A.S. Crowell, C.R. Howell, Introduction to neutron stimulated emission computed tomography, Phys. Med. Biol. 51 (2006) 3375.

[3] A. Danielsen, E. Steinnes, A study of some selected trace elements in normal and cancerous tissue by neutron activation analysis, J. Nucl. Med. 11 (6) (1970) 260.

[4] I.L. Mulay, R. Roy, B.E. Knox, N.H. Suhr, W.E. Delaney, Trace-metal analysis of cancerous and noncancerous human tissues, J. Natl. Cancer Inst. 47 (1) (1971) 1.

[5] K. Geraki, M.J. Farquharson, D.A. Bradley, Concentrations of Fe, Cu and Zn in breast tissue: a synchrotron XRF study, Phys. Med. Biol. 47 (2002) 2327.

[6] H. Mussalo-Rauhamaa, S. Piepponen, J. Lehto, R. Kauppila, O. Auvinen, Cu, Zn, Se and Mg concentrations in breast fat of Finnish breast cancer patients and healthy controls, Trace Elem. Med. 10 (1993) 13.

[7] K.-H. Ng, D. Bradley, L.-M. Looi, Elevated trace element concentrations in malignant breast tissues, Brit. J. Radiol. (1997) 375.

[8] S. Rizk, H. Sky-Peck, Comparison between concentrations of trace elements in normal and neoplastic human breast tissue, Cancer Res. 44 (1984) 5390.

[9] P. Santoliquido, H. Southwick, J. Olwin, Trace metal levels in cancer of the breast, Surg. Gynecol. Obstet. 142 (1976) 65.

[10] E.J. Margalioth, J.G. Schenker, M. Chevion, Copper and zinc levels in normal and malignant tissues, Cancer 52 (5) (1983) 868.

[11] H. Kubo, S. Hashimoto, A. Ishibashi, Simultaneous determinations of Fe, Cu, Zn, and Br concentrations in human tissue sections, Med. Phys. 3 (4) (1976) 204.

[12] P. Ghadirian, P. Maisonneuve, C. Perret, G. Kennedy, P. Boyle, D. Krewski, A. Lacroix, A case-control study of toenail selenium and cancer of the breast, colon, and prostate, Cancer Detect. Prev. 24 (4) (2000) 305.

[13] I. Kato, A.M. Dnistrian, M. Schwartz, P. Toniolo, K. Koenig, R.E. Shore, A. Zeleniuch-Jacquotte, A. Akhmedkhanov, E. Riboli, Iron intake, body iron stores and colorectal cancer risk in women: A nested case-control study, Int. J. Cancer 80 (5) (1999) 693.

[14] R.L. Nelson, F.G. Davis, E. Sutter, L.H. Sobin, J.W. Kikendall, P. Bowen, Body iron stores and risk of colonic neoplasia, J. Natl. Cancer Inst. 86 (6) (1994) 455.

[15] K.Q. Xiao, W.J. Henderson, Electron microscopy microanalysis and quantitative detection of trace elements in carcinoma of the colon [Article in Chinese: from translated abstract], Zhonghua Bing Li Xue Za Zhi 21 (3) (1992) 142.

[16] W.P. Banner, J.J. DeCosse, Q.H. Tan, M.S. Zedeck, Selective distribution of selenium in colon parallels its antitumor activity, Carcinogenesis 5 (12) (1984) 1543.

[17] G.C. Gregoriadis, N.S. Apostolidis, A.N. Romanos, T.P. Paradellis, A comparative study of trace elements in normal and cancerous colorectal tissues, Cancer 52 (3) (1983) 508.

[18] J.O. Ogunlewe, D.N. Osegbe, Zinc and cadmium concentrations in indigenous blacks with normal, hypertrophic, and malignant prostate, Cancer 63 (7) (1989) 1388.

[19] Z. Chirulescu, C. Chiriloiu, A. Suciu, R. Pirvulescu, N. Gh, Variations of zinc, calcium and magnesium in normal subjects and in patients with neoplasias, Med. Int. 25 (4) (1987) 257.

[20] Z.M. Bataineh, I.H. Bani Hani, J.R. Al-Alami, Zinc in normal and pathological human prostate gland, Saudi Med. J. 23 (2) (2002) 218.

[21] M. Brys, A.D. Nawrocka, E. Miekos, C. Zydek, M. Foksinski, A. Barecki, Krajewska, Zinc and cadmium analysis in human prostate neoplasms, Biol. Trace Elem. Res. 59 (1–3) (1997) 145.

[22] V.Y. Zaichick, T.V. Sviridova, S.V. Zaichick, Zinc in the human prostate gland: Normal, 3hyperplastic and cancerous, Int. Urol. Nephrol. 29 (5) (1997) 565.

[23] R. Wennrich, H. Dittrich, Investigations of trace elements in metastases and primary carcinoma of the prostate, Feustel Urol. Res. 17 (2) (1989) 107.

[24] I. Romics, L. Katchalova, Spectrographic determination of zinc in the tissues of adenoma and carcinoma of the prostate, Int. Urol. Nephrol. 15 (2) (1983) 171.

[25] A. Feustel, R. Wennrich, D. Steiniger, P. Klauss, Zinc and cadmium concentration in prostatic carcinoma of different histological grading in comparison to normal prostate tissue and adenofibromyomatosis (BPH), Urol. Res. 10 (6) (1982) 301.

[26] F.K. Habib, G.L. Hammond, I.R. Lee, J.B. Dawson, M.K. Mason, P.H. Smith, Y.K. Stitch Sr., A.G. Meade, E.P. Rack, A.J. Blotcky, Metal–androgen interrelationships in carcinoma and hyperplasia of the human prostate, J. Endocrinol. 71 (1) (1976) 133.

[27] E.A. Platz, K.J. Helzlsouer, S.C. Hoffman, J.S. Morris, C.K. Baskett, G.W. Comstock, Prediagnostic toenail cadmium and zinc and subsequent prostate cancer risk, Prostate 52 (4) (2002) 288.

[28] G.M. Brittenham, D.G. Badman, Noninvasive measurement of iron: Report of an NIDDK workshop, Blood 101 (1) (2003) 15.

# Design and Development of a High-Energy Gamma Camera for Use With NSECT Imaging: Feasibility for Breast Imaging

Amy C. Sharma, *Student Member, IEEE*, Georgia D. Tourassi, *Member, IEEE*, Anuj J. Kapadia, *Student Member, IEEE*, Brian P. Harrawood, Janelle E. Bender, Alexander S. Crowell, Matthew R. Kiser, Calvin R. Howell, and Carey E. Floyd Jr., *Member, IEEE*

***Abstract*—A new spectroscopic imaging technique, Neutron Stimulated Emission Computed Tomography (NSECT), is currently being developed to non-invasively and non-destructively measure and image elemental concentrations within the body. NSECT has potential for use in breast imaging as several studies have shown a link between elemental concentration and tumor status. In NSECT, a region of interest is illuminated with a high-energy (3–5 MeV) beam of neutrons that scatter inelastically with elemental nuclei within the body. The characteristic gamma rays that are emitted as the excited nuclei relax allow the identification of elements and the formation of elemental composition images. This imaging technique requires high-resolution and high-energy gamma spectroscopy; thereby eliminating current scintillation crystal based position sensitive gamma cameras. Instead, we propose to adapt high-energy gamma imaging techniques used in space-based imaging. A High Purity Germanium (HPGe) detector provides high-resolution energy spectra while a rotating modulation collimator (RMC) placed in front of the detector modulates the incoming signal to provide spatial information. Counting the number of gamma events at each collimator rotation angle allows for reconstruction of images. Herein we report on the design and testing of a prototype RMC, a Monte Carlo simulation of this camera, and the use of this simulation tool to access the feasibility of imaging a breast with such a camera. The prototype RMC was tested with a $^{22}$Na point source and verified that the RMC modulates the gamma rays in a predictable manner. The Monte Carlo simulation accurately modeled this behavior. Other simulations were used to accurately reconstruct images of a point source located within a 10 cm cube, suggesting NSECT's potential as a breast imaging method.**

***Index Terms*—Biomedical imaging, gamma camera, gamma-ray spectroscopy, neutrons, nuclear imaging, tomography.**

Manuscript received December 29, 2006; revised June 1, 2007. This work was supported in part by NIH/NCI under Grants 1-R21-CA106873-01 and NIH Training Grant No. 1-T32-EB001040 and in part by the Department of Defense BCRP under Grant W81XWH-06-1-0484.

A. C. Sharma is with the Department of Biomedical Engineering and the Duke Advanced Imaging Labs (DAILabs) of the Department of Radiology, Duke University, Durham, NC 27705 USA (e-mail: anc4@duke.edu).

G. D. Tourassi, B. P. Harrawood and C. E. Floyd, Jr. are with the DAILabs of the Department of Radiology, Duke University, Durham, NC 27710 USA (e-mail: gt@deckard.duhs.duke.edu; brian.harrawood@duke.edu).

A. J. Kapadia is with the Department of Biomedical Engineering and the DAILabs of the Department of Radiology, Duke University, Durham, NC 27710 USA (e-mail: anuj.kapadia@duke.edu).

J. E. Bender is with the Department of Biomedical Engineering, Duke University, Durham, NC 27708 USA (e-mail: jeb9@duke.edu).

A. S. Crowell, M. R. Kiser, and C. R. Howel are with the Department of Physics Duke University and the Triangle Universities Nuclear Laboratory, Durham, NC 27708 USA (e-mail: crowell@tunl.duke.edu; kiser@tunl.duke.edu; howell@tunl.duke.edu).

Color versions of one or more of the figures in this paper are available online at http://ieeexplore.ieee.org.

Digital Object Identifier 10.1109/TNS.2007.906058

## I. Introduction

SEVERAL studies have found a correlation between trace element concentration and certain disease states. We are developing a new elemental composition imaging technique, Neutron Stimulated Emission Computed Tomography (NSECT), that has potential to both identify and classify suspicious lesions within the breast [1].

NSECT generates elemental composition images by illuminating the region-of-interest with a high-energy (3–5 MeV) beam of neutrons. These neutrons scatter inelastically off the body's elemental nuclei, exciting them and causing them to emit characteristic gamma radiation. By detecting these gammas with a high-spectral-resolution detector, it is possible to identify the elements present within the sample. Furthermore, gathering these gammas in a tomographic geometry allows for the formation of elemental concentration images [2], [3].

Several studies have shown trace element concentration may be able to distinguish between malignant and benign tumors in the breast [4]–[8], possibly due to the elements' roles in DNA and nucleotide excision repair (e.g., As, Cd, Co, Mg and Zn) or toxicity at high levels (e.g., Cu, Se, Sb) [5], [9]. Unfortunately, current methods for measuring elemental concentrations are not compatible with *in vivo* methods [4], [6], [10]–[18]. NSECT has the potential to non-invasively measure and image elemental concentrations; thereby, it has the potential to identify and map regions of the breast containing elemental abnormalities. One non-invasive scan could be developed to detect and classify suspicious areas of tissue as malignant, benign or normal. There are several possible advantages to NSECT imaging of the breast. One, the high penetration of neutrons may be more effective in imaging of dense breasts. Two, imaging could be performed in the more comfortable "pendant breast" position. Three, both identifying and classifying suspicious lesions in one step could eliminate a large majority of follow-up exams or biopsies, thereby simplifying and speeding diagnosis and treatment.

NSECT requires high-resolution, high-energy (up to several MeV) gamma spectroscopy that cannot be achieved via conventional nuclear medicine scintillation cameras. The cameras operate in too low of an energy range and are limited by collimator and crystal size [19]. Instead, we currently obtain spectral information with High Purity Germanium (HPGe) semi-conductor

detectors that provide approximately 1% full width half-maximum (FWHM) energy resolution over the energy range of interest (0.3–1.5 MeVs). HPGe detectors are the preferred choice for high-energy spectroscopy [20]. These detectors are 7 cm diameter single crystal elements and therefore provide no spatial information. In order to obtain spatial information while still using the single crystal HPGe detectors, we are currently investigating adapting space-based imaging technology [21]–[23]. A rotating modulation collimator (RMC), consisting of two parallel slat collimators, is placed in front of the HPGe detector. As the RMC rotates it modulates the incident gamma flux in a manner predicted by its geometry. The modulation profile (number of incident gammas at each RMC angle) of a single point source is unique to that source's location in space. Using this property it is possible to reconstruct images by measuring the intensity of incident gammas at each collimator rotation angle. To reconstruct images the RMCs need only to provide adequate modulation, not absolute collimation of gamma rays. This collimator design has already proven functional in the far field within the NSECT energy range of interest [24]–[28].

We recently studied the theoretical geometry of such a system in the near field and determined a simple geometric model to predict modulation profiles based on a point source's location in space [23]. This model showed that the modulation profile from a point source in the near field is a simple peak over one 180° RMC rotation and that this modulation profile is unique to the point source's location in 180° of three-dimensional (3-D) space. Three properties define the modulation profile's shape: 1) peak location, 2) FWHM, and 3) peak height. The peak location in the modulation profile corresponds to the angular location of the point source in polar coordinates. The FWHM is determined by the distance of the point source from the axis of rotation. When a point source is located on the axis of rotation no modulation will occur. As the point source moves farther from the axis of rotation the peak becomes more distinct and the FHWM decreases. The peak height depends on the source to image distance (SID), and peak height decreases according to the inverse square law [23].

The uniqueness of a point source's modulation profile allows reconstruction of images. When a gamma producing object (point source or extended) is viewed by the system, an observation matrix (gamma counts at each collimator angle) is obtained. The observation matrix for an extended object can be thought of as the sum of all the modulation profiles for each pixel comprising that object. To reconstruct images a probability matrix must be generated by determining the modulation profile for each pixel in the imaging plane. Using both the probability matrix and the observation matrix, images are reconstructed with the Maximum Likelihood Expectation Maximization (MLEM) algorithm [29]. While one camera view is sufficient to reconstruct a point source image, multiple camera views are necessary to provide enough complementary information to reconstruct images of extended images. For a more detailed description of the imaging and reconstruction method, please see [23].

The objective of this study is to design and test a prototype camera, create a Monte Carlo simulation tool for this camera, and use this simulation tool to assess the feasibility of imaging the breast. The manuscript is organized as follows. The methods section provides an overview of the camera and its coordinate system and then describes the design, construction and testing of a prototype RMC to verify the near-field geometry. The section also describes the development of a Monte Carlo simulation to mimic the experimental setup. To assess the feasibility of imaging a breast-like object, the simulation of a 10 cm × 10 cm × 10 cm field-of-view (FOV) as viewed by multiple cameras is also described. The results section presents the comparison between the experimental data and the simulated data to confirm the validity of the Monte Carlo simulations. The reconstruction of simulated point sources in a volume is also presented. Finally, the discussion section summarizes the findings of this study, lessons learned from the experiment and the feasibility of breast imaging via NSECT.

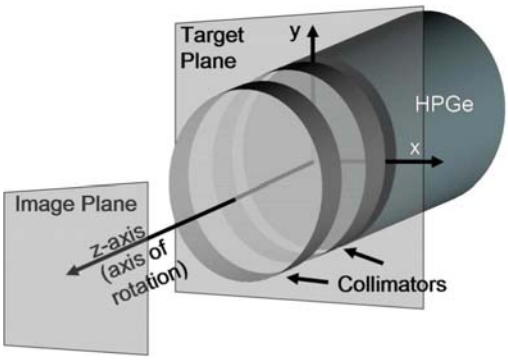


Fig. 1. Schematic of RMC camera system.

## II. Methods

### A. RMC Layout and Coordinate System

A schematic representation of the RMC camera is shown in Fig. 1. The object space x,y,z coordinate system is fixed at the detector face with the x,y plane (target plane) flush to the detector face and the z-axis extending out of the detector as the axis of rotation. The Monte Carlo simulation uses the target plane when directing the path of gammas. The image plane is a plane parallel to the face of the detector and positions of gamma sources on this plane are defined by their x,y,z object space location. The z-distance (SID) is measured from the face of the detector to the image plane. The z-distance between the two collimators is referred to as "height." With the collimator slats aligned horizontally (parallel to the x-axis), the slats are a certain "slat width" in the y-direction and have a 'slat height' in the z-direction. The distance between the slats is referred to as the "slot width."

### B. Prototype RMC Construction

A prototype RMC was constructed (Fig. 2). Extruded aluminum was used to build a rectangular frame. This frame held two collimators comprised of lead slats separated by plastic 'slots.' A piece of plastic PVC pipe was fitted around each end of the frame, and the entire unit then rested on rollers. To rotate the RMC, a steel ring gear was fitted around the frame and coupled to a gear fixed to a computer controlled rotational stage.

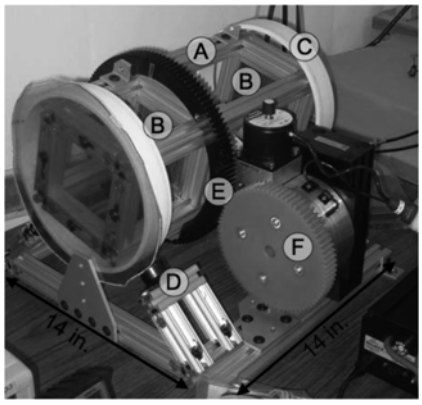


Fig. 2. Prototype RMC. A rectangular frame (A) holds the two collimators (B), which are made of lead and plastic. These slats and slots can be switched out or slid along the frame to test different configurations. The frame (A) is fitted inside PVC pipe (C), which allows the RMC to roll on rollers (D). A metal ring gear (E) attached to the frame is coupled to a plastic gear (F) mounted to a rotational stage to provide controlled rotation.

TABLE I
RMC TEST PARAMETERS

Constant parameters were: slat width: 0.5mm, slot width: 1.0mm, slat height: 15mm and point source energy: 0.511 MeV and 1.274 MeV. The point source was always located along the y-axis, so the y-axis location was also a measure of the source's radius from the axis of rotation.

| RMC Orientation | Distance to Detector (cm) | Distance Between Collimators (cm) | Point Source Location (radius, cm) |
|---|---|---|---|
| 1 | 40 | 10 | 0, 4, 5 and 6 |
| 2 | 40 | 20 | 0, 3, 4 and 5 |
| 3 | 50 | 10 | 0, 5, 6 and 7 |
| 4 | 50 | 20 | 0, 4, 5 and 6 |

The prototype RMC was designed for flexibility, as the distance between the collimators can be varied, and the collimator slats and slots can be exchanged for ones with different widths and heights. Fig. 2 depicts the prototype RMC coupled to the rotational stage.

### C. Experimental Testing With Prototype RMC

To test the RMC's ability to modulate gamma rays, a 17.9 $\mu$Ci point source of $^{22}$Na (which emits both 0.511 MeV and 1.274 MeV gamma rays) was positioned at various locations within the x,y image plane. Measurements were taken with an HPGe detector located directly behind the rear collimator of the RMC. The RMC orientation and point source locations are listed in Table I. For each RMC orientation, modulation profiles were obtained for four different point source locations by recording the number of gammas detected in a two-minute timeframe at 10° intervals between 0° and 180°, resulting in 19 measurements per location. Fig. 3 is a picture of the experimental setup.

### D. Monte Carlo Simulation

A model world consisting of a gamma-ray point source, two collimators and a HPGe detector was developed in the GEANT4 Monte Carlo simulation package [30] (see Fig. 4). The simulation setup includes collimators modeled as slats floating in space with no structural support or separators. In reality a support structure would be necessary, and should be constructed from

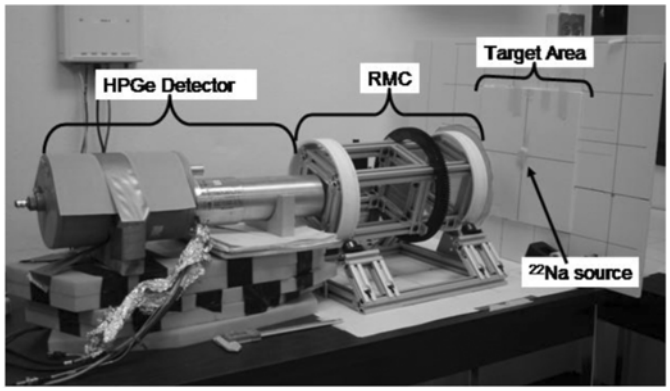


Fig. 3. Experimental setup including: HPGe detector, RMC and point source on the image plane (the poster board).

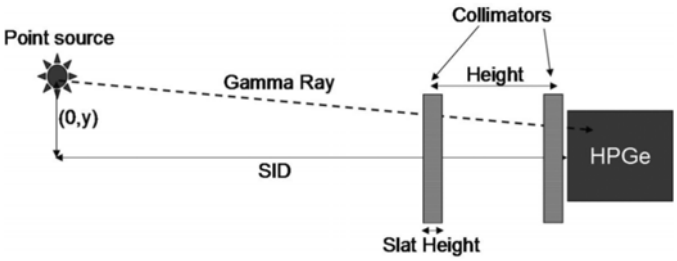


Fig. 4. Schematic of the GEANT4 simulation with the point source, two collimators, and HPGe.

material with a low-attenuation coefficient. Simulating only the point source, slats and detector results in a less-complex and faster-running simulation. This simulation allows for changes to the following collimator dimensions (slat width, slot width, slat height, distance between collimators (height), distance to source (SID), slat material and collimator offset), as well as, point source location and strength.

The simulation proceeds as follows:

A true gamma point source emits gammas in all directions with only a small fraction reaching the detector. To save simulation time, the gammas emitted from the point source are aimed only in the direction of the detector. However, if they were aimed solely at the detector face, the solid angle of the emitted gammas would decrease as the SID increased. This solid angle inconsistency would prevent comparison of modulation profiles obtained for gamma sources at different locations. To ensure that a detector located 5 cm away sees four times the number of gammas as one located 10 cm away, the solid angle is held constant by aiming the gammas at a "target plane" located at the face of the detector (see Fig. 1). This target plane is increased in size as the point source moves away from the detector and gammas follow a path from the source to a randomly selected location on the target plane.

To compare the GEANT4 simulations to the experimental data, simulations were conducted with both 0.511 MeV and 1.274 MeV point sources generating 100 000 counts at each collimator angle from 0° to 180° in 10° increments. The simulations were conducted in the same configurations as used to test the prototype (see Table I).

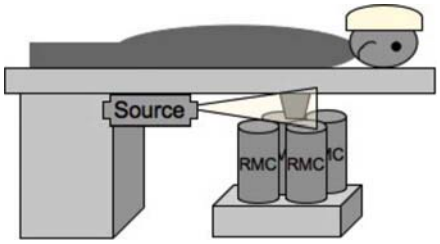


Fig. 5. Hypothetical NSECT breast imaging system with four RMC cameras located beneath the pendant breast and a portable neutron source illumining the breast.

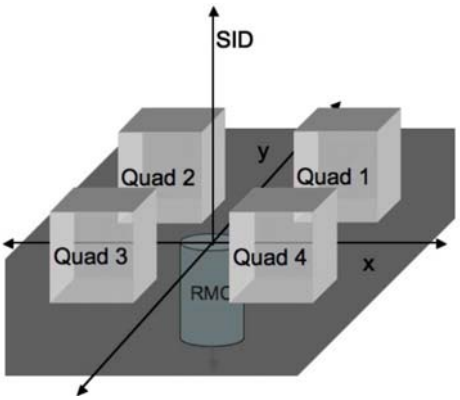


Fig. 6. Four identical fields-of-view as seen by one RMC camera located at the origin. This is equivalent to imaging one FOV with the four different RMCs.

TABLE II
PROBABILITY MATRIX SIMULATION PARAMETERS

The following parameters were constant: slat width 2 mm, slot width 2 mm, slat height 20 mm, height 5 cm. The collimator was rotated in 5° steps and 10,000 0.511 MeV gammas generated at each angular increment. The point source was located in 2 cm increments in the FOVs outlined below.

| Quadrant | Dimension in x Direction (cm) | Dimension in y Direction (cm) | Dimension in SID (z) Direction (cm) |
|---|---|---|---|
| 1 | 3 to 13 | 3 to 13 | 10 to20 |
| 2 | -3 to -13 | 3 to 13 | 10 to 20 |
| 3 | -3 to -13 | -3 to -13 | 10 to 20 |
| 4 | 3 to 13 | -3 to -13 | 10 to 20 |

### *E. Simulation and Reconstruction of 3-D Images*

A possible "pendant breast" imaging system could be setup as in Fig. 5 with four RMC cameras located below the breast. To demonstrate reconstruction of a 3-D FOV GEANT4 simulations were conducted for a 10 cm × 10 cm × 10 cm volume (2 $cm^3$ pixels). For each pixel a GEANT4 simulation was run, generating a modulation profile for that pixel. The modulation profiles were then combined into a single probability matrix. Our previous research has shown multiple camera views enhance reconstruction [23]; thus, a simulation was run for quadrant 1 and quadrant 2 as depicted in Fig. 6. Two other camera views (quadrant 3 and 4) were obtained by using mirror images of calculated quadrants. Simulation parameters are outlined in Table II.

Initially it seems counterintuitive that observation profiles generated with mirror images of quadrant 1 and 2 would provide different information to the system. However, it can be shown that camera views corresponding to quadrants 3 and 4 provide new information to aid in image reconstruction. This

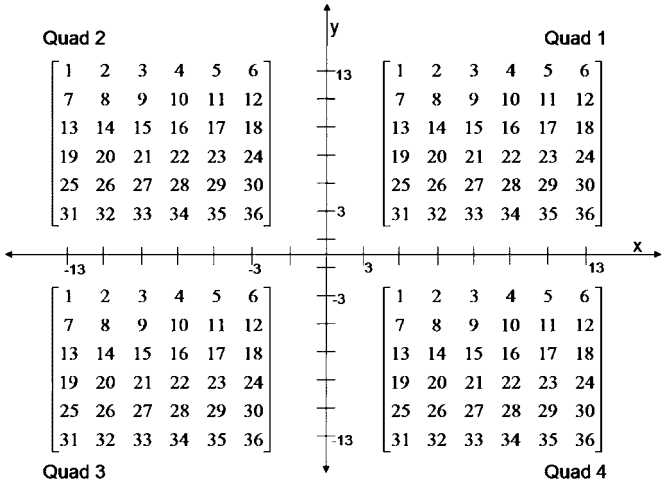


Fig. 7. Pixel numbers for four imaging quadrants.

is best illustrated by example. Fig. 7 depicts the pixels in the four different FOVs used in the simulation. If a point source is located at pixel 17, its location in space is different according to each camera's point of view. Thus, each camera view will obtain a different observation profile. The four different observations contain complimentary information allowing for clearer reconstructions.

To generate images the following procedure was followed. First, a 3-D $6 \times 6 \times 6$ matrix "true image" was generated by giving point sources a value of 100 and background pixels a value of 0. Second, for each quadrant, the true image was multiplied by the probability matrix to generate an observation matrix. Finally, each observation matrix and corresponding probability matrix were fed into the MLEM algorithm for reconstruction. All four camera views were reconstructed at once. For further detail on MLEM reconstruction with multiple camera views please see [23].

## III. RESULTS

### *A. Experimental Tests of the Prototype RMC*

The prototype camera modulated the incoming gamma rays in the manner predicted by the geometric model of the RMC's behavior [23]. No modulation was observed when the point source was located at the axis of rotation; when the radius increased, the modulation profiles thinned. The modulation profiles for the 1.274 MeV gammas were less distinct than those for the 0.511 MeV gammas. This is due to both an increased gamma ray penetration of the lead slats and a decreased number of gammas as $^{22}$Na produces half as many 1.274 MeV gammas as 0.511 MeV gammas. Fig. 8 depicts modulation profiles from RMC orientation 4 (SID 50 cm, height 20 cm) for the four different point source locations and is representative of the results obtained from the four different RMC orientations.

### *B. Monte Carlo Simulation*

The Monte Carlo simulation produced similar modulation profiles to those obtained experimentally. Accurate modeling

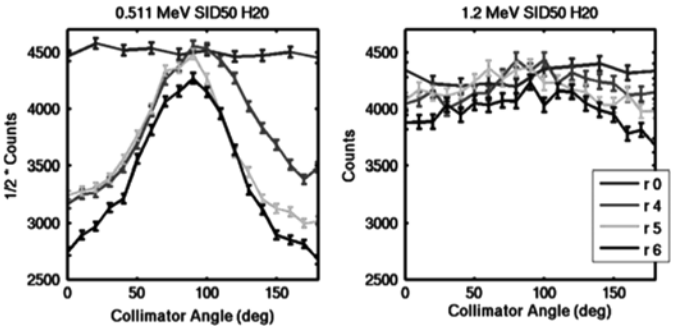


Fig. 8. Modulation profiles obtained for 0.511 MeV gammas (left) and 1.274 MeV gammas (right) at four different point source locations for RMC orientation 4. For easier comparison, the number of 0.511 MeV gammas has been halved as twice as many are produced during $^{22}$Na decay.

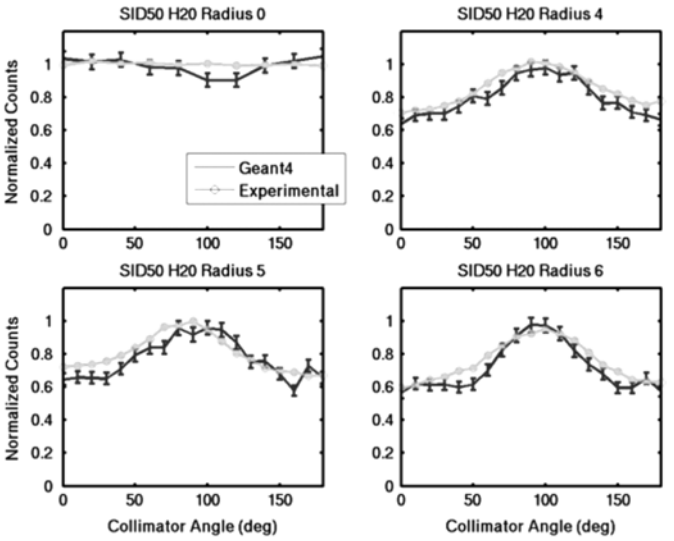


Fig. 9. Experimental versus Monte Carlo results for RMC orientation 4 (SID 50 cm, height 20 cm, gamma energy 0.511 MeV) at four different radii. There were more experimental counts than simulated data counts, resulting in error bars located inside the markers for the experimental data.

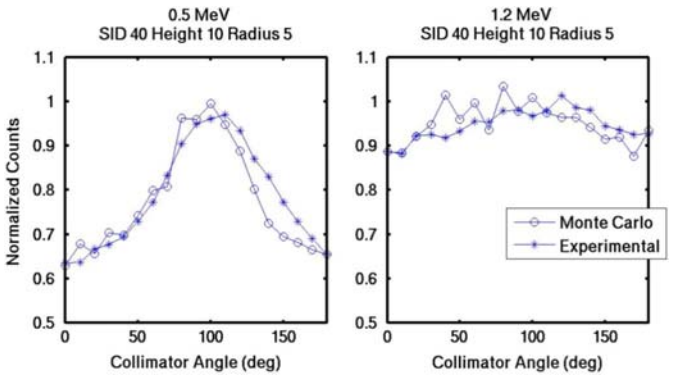


Fig. 10. Side by side comparison of modulation profiles obtained by experiment $(*)$ and Monte Carlo simulation $(o)$ for both 0.511 MeV (left) and 1.274 MeV gamma energies (right). The data is from RMC orientation 1 and the point source located at a radius of 5 cm.

of both 0.511 MeV and 1.274 MeV gammas was achieved (see Figs. 9 and 10).

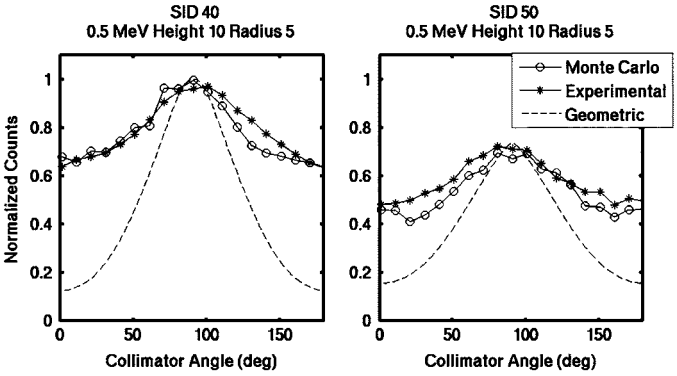


Fig. 11. Modulation profiles obtained by experiment $(*)$, Monte Carlo simulation $(o)$ and geometric model $(--)$ of a point source located at a 5 cm radius and SID 40 cm (left) and SID 50 cm (right). The data from each SID 50 cm data set was normalized by the maximum counts from the 40 cm data. The RMC had the following geometry: height 10 cm, slat height 1.5 cm, slat width 0.05 cm, and slot width 0.1 cm.

### C. Comparison of Experimental and Simulated Results

In Figs. 9 and 10, visual comparisons of the experimental and Monte Carlo results show similar profiles are obtained. Septal penetration in both the experiment and simulation results in less distinct modulation profiles for the 1.274 MeV gammas. In Fig. 10 the distinct peak seen in the 0.511 MeV data is hardly visible for the 1.274 MeV data.

The modulation profiles from the experimental, Monte Carlo and geometric model [23] are shown in Fig. 11. The figure shows modulation profiles for SID 40 cm and SID 50 cm, normalized to the SID 40 counts. Note how the peaks of all three profiles are aligned, but that only the experimental and Monte Carlo data are similar because the geometric model is unable to account for penetration of the lead slats. The figure also reflects the decrease in counts that occurs when the source is moved farther from the detector. From 40 cm to 50 cm, $1/r^2$ decreases 36%; correspondingly, the peak counts decrease about 30%.

The geometric model predicts that no modulation will occur when a point source is located on the axis of rotation. This is also the maximum number of counts that can be obtained from a point source located anywhere on a plane parallel to the front face of the detector located a certain SID away. For each RMC orientation in Table I, the counts were recorded for a point source located on the axis of rotation and the average of these counts used to normalize the modulation profiles obtained from other point source locations at that RMC orientation. This allowed numerical comparison between the simulation and experimental data. The counting error was propagated through normalization resulting in normalized experimental counts: $\mathrm{E}\pm\sigma_{\mathrm{E}}$ and normalized simulated counts: $\mathrm{S}\pm\sigma_{\mathrm{S}}$. Count rates are considered to have an error of $\pm\sigma$ where $\sigma$ is defined as the square root of the counts.

The number of overlapping data points (defined as a point plus or minus its error) was counted for each data set and the percentage of overlapping points calculated. For point source locations not on the axis of rotation there were 19 data points (1 every 10°) while for sources on the axis of rotation there were only 10 data points (1 every 20°). Better agreement was seen for the 1.274 MeV data than the 0.511 MeV data with only 2 data

TABLE III
SUMMARY OF COMPARISON BETWEEN MONTE CARLO SIMULATION AND EXPERIMENTAL DATA

Percent overlap over 68% (i.e. greater than one standard deviation) is highlighted in gray.

| SID (cm) | Height (cm) | Radius (cm) | % Overlap 0.5 Mev | % Overlap 1.2 MeV |
|---|---|---|---|---|
| 40 | 10 | 0 | 80 | 80 |
| | | 4 | 73.7 | 84.2 |
| | | 5 | 63.2 | 89.4 |
| | | 6 | 21.1 | 15.8 |
| 40 | 20 | 0 | 70 | 70 |
| | | 3 | 36.8 | 94.7 |
| | | 4 | 52.6 | 68.4 |
| | | 5 | 57.9 | 78.9 |
| 50 | 10 | 0 | 80 | 90 |
| | | 5 | 63.2 | 84.2 |
| | | 6 | 78.9 | 84.2 |
| | | 7 | 52.6 | 47.3 |
| 50 | 20 | 0 | 100 | 70 |
| | | 4 | 52.6 | 89.4 |
| | | 5 | 68.4 | 78.9 |
| | | 6 | 52.6 | 89.4 |

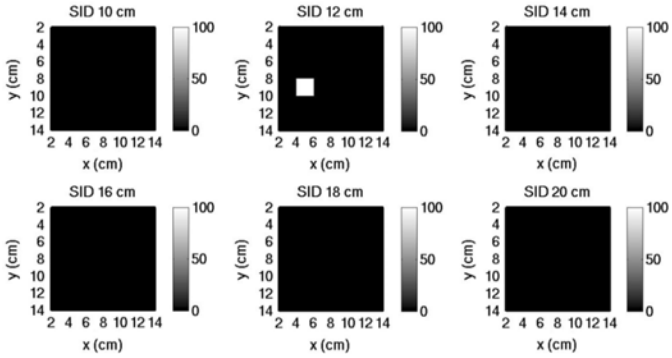


Fig. 12. 2-D slices of the true image. Each slice is of the x,y plane.

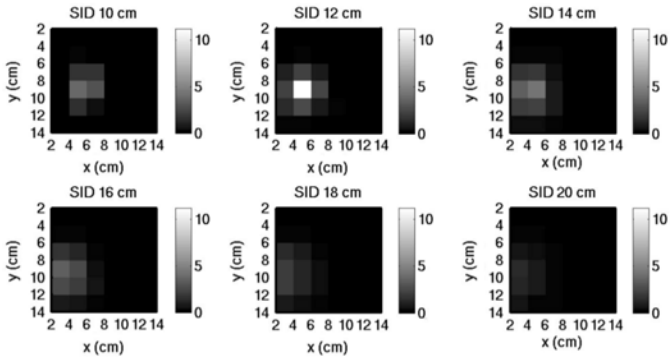


Fig. 13. 2-D slices of the 3-D reconstructed volume.

sets matching below 68% (one standard deviation). Results are shown in Table III.

### *D. 3-D Reconstruction*

Utilizing all four camera views at once, it was possible to reconstruct point sources located within the three-dimensional (3-D) volume. Fig. 12 depicts two-dimensional (2-D) slices of a point source true image and Fig. 13 shows the subsequent reconstruction.

## IV. DISCUSSION

To adequately visualize NSECT data it is necessary to develop a position sensitive, high energy, gamma camera. A Monte Carlo simulation that adequately models real-world performance is essential for developing and designing a RMC that provides adequate modulation for image reconstruction. Herein we described the design and construction of a prototype camera, the development of a Monte Carlo simulation and provided reconstructions of a point source in a 3-D volume.

A prototype RMC allowed for experimental validation of the near-field geometric behavior [23]. The RMC modulated the gamma rays in a predictable manner, and those modulation profiles were unique to the point source's location in space, providing proof of concept for the use of RMCs in generating images from near-field high-energy gamma rays.

While the modulation profiles were wide, and barely visible for the 1.274 MeV gamma rays, it is encouraging that modulation profiles were at all visible when using 0.5 mm in width by 15 mm in height slats. This is not a large quantity of lead, but absolute collimation of gamma rays is not necessary to reconstruct images, just adequate modulation. If some modulation was achieved using those slats, it should be possible to identify reasonable collimator parameters that provide adequate modulation for reconstruction and maintain reasonable camera efficiency within the expected energy range of NSECT (0.3 and 1.5 MeV).

The Monte Carlo simulation produces similar modulation profiles to those obtained experimentally. In both the experimental and simulated data the modulation profiles were less distinct for the 1.274 MeV gamma rays than for the 0.511 MeV. This is expected because higher energy gamma rays have greater penetrating power. Additionally, a decrease in overall counts was observed as the source was moved farther from the detector, as expected.

While there was a visual similarity between the Monte Carlo and experimental data, the numerical data analysis found that the data sets for a wide range of implementation parameters matched below one standard deviation. This indicates a less than ideal match. There are many factors that would prevent a closer match between the experimental and simulated data. In the prototype the slats and slots were not perfectly aligned, the slots were comprised of plastic and not air, the aluminum frame and ring gear attenuated some of the gamma rays and the 0.511 MeV gammas from $^{22}$Na were not from a specific point, but rather they were generated by the annihilation reaction and therefore have an inherent blur. Separately, all these discrepancies are expected to have minimal effects on the measured modulation profiles. We are currently studying the system tolerance for slat alignment and initial results show a high tolerance for offset. Plastic has a low attenuating effect on high-energy gammas. The frame and gear were not in the flight path of a majority of the incident gammas. The inherent annihilation blur is on the order of millimeters. However, when all of these discrepancies are combined, the net result will be experimental modulation profiles that are slightly different from those generated in an ideally configured simulation. A large majority of the mismatched camera orientations and point source locations were with the 0.511 MeV

gamma rays. These gammas are more likely to be modulated than the higher energy 1.274 MeV gammas. Thus, camera orientation inconsistencies are more likely to be highlighted by the 0.511 MeV gammas than the 1.274 MeV gammas.

Despite these disparities the Monte Carlo simulation environment is an adequate tool for use in identifying RMC parameters that can be used to image gamma rays in the near field. The RMC has eight parameters (SID, height, slat height, slat width, slot width, field-of-view, slat alignment and slat material) that all affect modulation profiles and consequently image reconstruction quality. It is far more practical to iterate through these parameters in a simulation environment and establish a RMC design that functions in the energy range of interest to provide images feasible for clinical applications.

Once an adequate RMC orientation is identified, future generations of cameras can be constructed taking into account the lessons learned from the prototype camera. Specifically 1) the aluminum frame and steel ring gear were too bulky and attenuated some the gamma rays and 2) the small area of the first collimator limited the field-of-view. The distance of the source from the axis of rotation is limited by the ratio of SID to height multiplied by the difference between the radius of the collimator and radius of the detector face. Gamma rays from sources located greater than this distance away from the axis of rotation would come over the top of the first collimator and only be attenuated by the second. Many modifications can be incorporated into the next generation RMC design such as a less bulky, less attenuating frame and drive mechanism and a larger first collimator that permits an adequate FOV.

The RMC modulates the incident gamma rays in a manner unique to their location in space. Although the information recorded is only one dimensional (counts at each collimator angle), the information contains a signal unique to a location in three-dimensional space. Adequate reconstruction was achieved of point sources within a 3-D volume. This reconstruction was performed by reconstructing the entire volume at once and not by stacking two-dimensional slices (as in traditional CT) because the information is inherently three-dimensional.

The small volume reconstruction presented in this study, while primitive and limited in scope, is a critical step towards the application of NSECT to breast cancer imaging. Several additional issues need to be addressed so that NSECT can become a viable breast imaging tool. These issues include, but are not limited to: dose, quantity of trace elements necessary to distinguish between malignant and benign tissue and development of a position sensitive gamma camera. We are currently investigating these issues [1], [31], [32].

## V. Conclusion

To summarize, we have built and successfully tested a prototype RMC. To our knowledge, this is the first successful experimental demonstration of an RMC modulating gammas in the near-field. Modulation was consistent with the predicted near-field behavior.

We have also demonstrated development of a Monte Carlo simulation that accurately models the near-field RMC behavior. There are eight RMC variables to optimize and iteration on each variable in a simulation environment will help to determine how each effects gamma modulation and subsequent reconstructed images. Use of this environment will allow us to identify an RMC design that will produce images feasible for clinical applications. In terms of breast imaging, we must identify an imaging configuration with an adequate FOV to image the entire breast and resolution comparable with other nuclear-medicine applications.

Additionally, data from the Monte Carlo environment demonstrates that 3-D image reconstruction is possible with the RMC concept. Imaging the elemental composition will possibly allow identification and classification of breast tumors in one non-invasive scan.

In conclusion, the design of a near field, high energy, gamma camera is a necessary step for NSECT development and its application as a breast imaging tool. This high-energy resolution gamma camera also has other possible nuclear medicine uses including dual-isotope imaging.

## Acknowledgment

The authors would like to thank Triangle Universities Nuclear Laboratory for the use of their expertise, spectroscopy equipment, and laboratory space. They also wish to thank J. Owen for his help in machining several collimator parts.

## References

[1] C. E. Floyd *et al.*, "Breast cancer diagnosis using neutron stimulated emission computed tomography: Dose and count requirements," in *Proc. SPIE Symp. Medical Imaging*, San Diego, 2006, pp. 597–603.

[2] C. E. Floyd *et al.*, "Neutron stimulated emission computed tomography of a multi-element phantom," *IEEE TMI*, Sept. 2006, submitted.

[3] C. E. Floyd *et al.*, "Introduction to neutron stimulated emission computed tomography," *Phys. Med. Biol.*, vol. 51, pp. 3375–3390, Jul. 2006.

[4] A. Danielsen and E. Steinnes, "A study of some selected trace elements in normal and cancerous tissue by neutron activation analysis," *J. Nucl. Med.*, vol. 11, pp. 260–264, 1970.

[5] A. N. Garg, R. G. Weginwar, and N. L. Chutke, "Radiochemical neutron activation analysis of Fe, Co, Zn, Sb, and Se in biomedical and environmental samples," *Sci. Total Env.*, vol. 139/140, pp. 421–430, 1993.

[6] K. Geraki, M. J. Farquharson, and D. A. Bradley, "X-ray fluorescence and energy dispersive x-ray diffraction for the quantification of elemental concentrations in breast tissue," *Phys. Med. Biol.*, vol. 49, pp. 99–110, 2004.

[7] K. H. Ng, D. A. Bradley, L. M. Looi, C. Seman Mahmood, and A. Khalik Wood, "Differentiation of elemental composition of normal and malignant breast tissue by instrumental neutron activation analysis," *Appl. Radiat. Isot.*, vol. 44, pp. 511–516, 1993.

[8] K. H. Ng, D. A. Bradley, and L. M. Looi, "Elevated trace element concentrations in malignant breast tissues," *British J. Rad.*, vol. 70, pp. 375–382, 1997.

[9] M. Yaman, D. Atici, S. Bakirdere, and I. Akdeniz, "Comparison of trace metal concentration in malign and benign human prostate," *J. Med. Chem.*, vol. 48, pp. 630–634, 2005.

[10] R. Cesareo and G. Viezzoli, "Trace element analysis in biological samples by using XRF spectrometry with secondary radiation," *Phys. Med. Biol.*, vol. 28, pp. 1209–1218, 1983.

[11] N. Milman, J. Laursen, J. Podenphant, and P. Staun-Olsen, "Iron, copper, zinc, and selenium in lumen liver tissue measured by X-ray fluorescence spectrometry," *Scand. J. Clin. Lab. Invest.*, vol. 43, pp. 691–697, 1983.

[12] J. D. Stedman and N. M. Spyrou, "Major and trace element concentration differences between right and left hemispheres of the 'normal' human brain," *Nutrition*, vol. 11, pp. 542–545, 1995.

[13] S. Takahashi, I. Takahashi, H. Sato, Y. Kubota, S. Yoshida, and Y. Muramatsu, "Determination of major and trace elements in the liver of Wistar rats by inductively coupled plasma-atomic emission spectrometry and mass spectrometry," *Lab. Anim.*, vol. 34, pp. 97–105, 2000.

[14] N. I. Ward, F. R. Abou-Shakra, and S. F. Durrant, "Trace elemental content of biological materials: A comparison of NAA and ICP-MS analysis," *Biol. Trace Elem. Res.*, vol. 26–27, pp. 177–187, Jul./Dec. 1990.

[15] R. Zeisler, P. Ostapczuk, S. F. Stone, and M. Stoeppler, "Effective tools for trace element characterization of tissue: Neutron activation analysis and voltammetry," *Sci. Total Env.*, vol. 139/140, pp. 403–410, 1993.

[16] G. Brewer, , D. Kasper, A. S. Fawci, D. L. Longo, E. Braunwald, S. L. Hauser, and J. L. Jameson, Eds., "Wilson disease," in *Harrison's Principles of Internal Medicine*, 16th ed. New York: McGraw-Hill, 2005, vol. 2, pp. 2313–2315.

[17] L. Powell, , D. Kasper, A. S. Fawci, D. L. Longo, E. Braunwald, S. L. Hauser, and J. L. Jameson, Eds., "Hemochromatosis," in *Harrison's Principles of Internal Medicine*, 16th ed. New York: McGraw-Hill, 2005, vol. 2, pp. 2298–2303.

[18] L. Tierney, S. J. McPhee, and M. A. Papadkis, *Current Medical Diagnosis and Treatment*, 45th ed. New York: McGraw-Hill, 2006.

[19] J. Bushberg, J. A. Seibert, E. M. Leidholdt Jr, and J. M. Boone, *The Essential Physics of Medical Imaging*, 2nd ed. Philadelphia, PA: Lippincott Williams Wilkins, 2002.

[20] G. F. Knoll, *Radiation Detection and Measurement*, 3rd ed. Hoboken, NJ: Wiley, 2000.

[21] A. C. Sharma *et al.*, "Rotating slat collimator design for high-energy near-field imaging," in *Proc. SPIE Symp. Medical Imaging*, Feb. 2006, vol. 6142, pp. 405–413.

[22] A. C. Sharma *et al.*, "Design and construction of a prototype rotation modulation collimator for near-field high-energy spectroscopic gamma imaging," presented at the NSS and MIC, San Diego, CA, 2006.

[23] A. C. Sharma, T. G. Turkington, G. D. Tourassi, and C. E. Floyd, "Near-field high-energy spectroscopic gamma imaging using a rotation modulation collimator," *IEEE Trans. Nucl. Sci.*, Mar. 2007, accepted with revisions.

[24] G. J. Hurford *et al.*, "The RHESSI imaging concept," *Solar Phys.*, vol. 210, pp. 61–86, Nov. 2002.

[25] R. P. Lin *et al.*, "The Reuven Ramety high-energy solar spectroscopic imager (RHESSI)," *Solar Phys.*, vol. 210, pp. 3–32, Nov. 2002.

[26] R. P. Lin *et al.*, "REHSSI observations of particle acceleration and energy release in an intense solar gamma-ray line flare," *Astrophys. J.*, vol. 595, pp. L69–L76, Oct. 1, 2003.

[27] R. P. Lin, HESSI-SMEX Proposal vol. 2005. Berkeley, CA, 1997.

[28] H. Schnopper *et al.*, "Percise location of sagittarius X-ray sources with a rocket-borne rotating modulation collimator," *Astrophys. J.*, vol. 161, pp. L161–L167, Sept. 1970.

[29] K. Lange and R. Carson, "EM reconstruction algorithms for emission and transmission tomography," *J. Comp. Assist. Tomo.*, vol. 8, pp. 306–316, 1984.

[30] CERN, "GEANT4" 4th ed. [Online]. Available: http://geant4.web.cern.ch/geant4/.

[31] J. Bender, C. E. Floyd, B. P. Harrawood, A. J. Kapadia, A. C. Sharma, and J. L. Jesnek, "The effect of detector resolution for quantitive analysis of neutron stimulated emission computed tomography," in *Proc. SPIE Symp. Medical Imaging*, Feb. 2006, vol. 6142, pp. 1597–1605.

[32] J. E. Bender, A. J. Kapadia, A. C. Sharma, G. D. Tourassi, B. P. Harrawood, and C. E. Floyd, Jr., "2007 Breast cancer detection using Neutron Stimulated Emission Computed Tomography: Prominent elements and dose requirements," *Med. Phys.*, vol. 34.

IOP PUBLISHING PHYSICS IN MEDICINE AND BIOLOGY

Phys. Med. Biol. **52** (2007) 6117–6131 doi:10.1088/0031-9155/52/20/003

# Neutron stimulated emission computed tomography: a Monte Carlo simulation approach

**A C Sharma[1,2], B P Harrawood[2], J E Bender[1], G D Tourassi[2] and A J Kapadia[1,2]**

[1] Department of Biomedical Engineering, Duke University, 136 Hudson Hall, Durham, NC 27708, USA
[2] Duke Advance Imaging Labs, Department of Radiology, 2424 Erwin Rd, Suite 302, Durham, NC 27705, USA

E-mail: anc4@duke.edu (A C Sharma)

Received 23 April 2007, in final form 29 August 2007
Published 1 October 2007
Online at stacks.iop.org/PMB/52/6117

**Abstract**

A Monte Carlo simulation has been developed for neutron stimulated emission computed tomography (NSECT) using the GEANT4 toolkit. NSECT is a new approach to biomedical imaging that allows spectral analysis of the elements present within the sample. In NSECT, a beam of high-energy neutrons interrogates a sample and the nuclei in the sample are stimulated to an excited state by inelastic scattering of the neutrons. The characteristic gammas emitted by the excited nuclei are captured in a spectrometer to form multi-energy spectra. Currently, a tomographic image is formed using a collimated neutron beam to define the line integral paths for the tomographic projections. These projection data are reconstructed to form a representation of the distribution of individual elements in the sample. To facilitate the development of this technique, a Monte Carlo simulation model has been constructed from the GEANT4 toolkit. This simulation includes modeling of the neutron beam source and collimation, the samples, the neutron interactions within the samples, the emission of characteristic gammas, and the detection of these gammas in a Germanium crystal. In addition, the model allows the absorbed radiation dose to be calculated for internal components of the sample. NSECT presents challenges not typically addressed in Monte Carlo modeling of high-energy physics applications. In order to address issues critical to the clinical development of NSECT, this paper will describe the GEANT4 simulation environment and three separate simulations performed to accomplish three specific aims. First, comparison of a simulation to a tomographic experiment will verify the accuracy of both the gamma energy spectra produced and the positioning of the beam relative to the sample. Second, parametric analysis of simulations performed with different user-defined variables will determine the best way to effectively model low energy neutrons in tissue, which is a concern with the high hydrogen content in biological tissue. Third, determination of

  

the energy absorbed in tissue during neutron interrogation in order to estimate the dose. Results from these three simulation experiments demonstrate that GEANT4 is an effective simulation platform that can be used to facilitate the future development and optimization of NSECT.

## 1. Introduction

This paper describes the use of the GEANT4 (Agostinelli *et al* 2003) toolkit to develop Monte Carlo simulations of a new, non-destructive, spectroscopic imaging technique, neutron stimulated emission computed tomography (NSECT) (Floyd *et al* 2004, 2006, 2007, Kapadia 2007). NSECT uses a beam of high-energy neutrons (2–10 MeV) to stimulate the nuclei of the elements within a sample. Through inelastic scatter, these nuclei are excited and then decay rapidly, each emitting their own characteristic gamma ray. Analysis of the emitted gamma spectrum allows identification of the elements within the sample. Elemental concentration images can be reconstructed by collecting separate gamma spectra from multiple neutron interrogation lines within the sample. This tomographic method is similar to first-generation CT techniques (Kapadia 2007).

The logistics of securing a neutron beam source and the time-consuming nature of performing experiments make the development of a simulation environment a desirable design methodology for NSECT. Monte Carlo computer simulations permit the modeling of nuclear interactions and offer a valuable tool for the rapid design, development and testing of NSECT materials, techniques and configurations. The GEANT4 toolkit's main design purpose is the simulation of high-energy particles interacting with matter in high energy physics applications. It was selected for NSECT Monte Carlo simulations primarily because its design encompasses NSECT's domain of interest: high-energy neutron interactions in matter. GEANT4 offers many features such as geometry visualization, adjustments to the model at runtime, and user control over tracking particles and reporting interactions. The GEANT4 toolkit is a collection of C++ class libraries and the GEANT4 Neutron Data Libraries (G4NDL) (Agostinelli *et al* 2003).

This paper will first describe the GEANT4 simulation environment created to model the NSECT spectral interrogation and imaging process. It will then describe three models developed in this environment: an 'N' phantom comprised of independent sections of iron and copper, and two biological tissue models, one of the breast and one of the liver. Finally, three simulations involving these models will be described: (i) a simulation to mimic an NSECT experiment and verify the simulation environment, (ii) a simulation to determine appropriate handling of neutron interaction with hydrogen-rich tissue and (iii) a simulation to determine energy deposited in tissue to estimate the radiation dose. These simulations will be used to address the following modeling issues: the relative motion between the beam line and the sample, the effective modeling of very low energy neutrons in tissue (where hydrogen scatter is a concern) and the measuring of energy deposited in the tissue during neutron interrogation.

## 2. Methods

### *2.1. GEANT4 environment*

A GEANT4 simulation environment is established by writing C++ applications and objects that are linked with GEANT4 libraries (CERN). We have established a common GEANT4

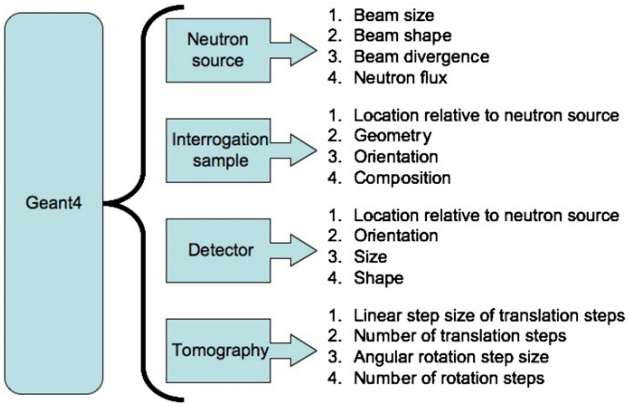


**Figure 1.** User-defined variables necessary to describe the experimental simulation.

C++ code base that all NSECT simulation applications utilize and build upon. This base model includes the fundamental framework of the C++ code that may be reused from one simulation to another. Additionally, the physical processes which are modeled, such as elastic and inelastic neutron scattering, are the same for each application.

A flexible framework has been built atop this base code that allows the user to simulate an NSECT experimental design. This framework includes a neutron source, a sample to be interrogated and a high purity germanium (HPGe) detector. The sample can be rotated and translated in order to simulate tomographic acquisitions. The parameters typically specified by the user are outlined in figure 1.

The first experiment described herein is a tomographic simulation. These simulations are accomplished in the following manner. All logical volumes, modeling constructs designed to hold an object or material for a model, are assigned an angle about the vertical axis and a displacement along the horizontal axis. Along with these values, step sizes are assigned so that the tomographic experiment can be implemented by specifying the integer angular step and the integer lateral step. These are specified through the Messenger class, which is a class that allows the modification of model parameters during a simulation run. To achieve tomographic reconstruction each sample can be translated through $X$ steps at $Y$ number of angles. These commands are input into the simulation at runtime and rebuilding is not necessary for each configuration.

Simulations involving models of biological tissue present a problem as tissue contains an abundance of hydrogen. Hydrogen nuclei have a high probability of elastically scattering with an energetic neutron. The elastic scattering depletes the neutron's energy without emitting energy in the form of photons. As initially configured, GEANT4 has no default lower energy limit on the tracking of a neutron. In hydrogen rich environments (such as a simulation of neutron interactions with biological tissue) some neutrons continue to scatter elastically with hydrogen nuclei many thousands of times until their energy becomes less than an electron volt and they are eventually captured by a nucleus or escape from the simulation world. While this is an accurate representation of the neutron's behavior, a large fraction of the simulation time is devoted to these low energy neutron events that are of little interest to NSECT research. For example, in one simulation that tracked 1 million incident neutrons, the tracking of a single neutron as it slowly lost energy scattering from hydrogen more than doubled the simulation time.

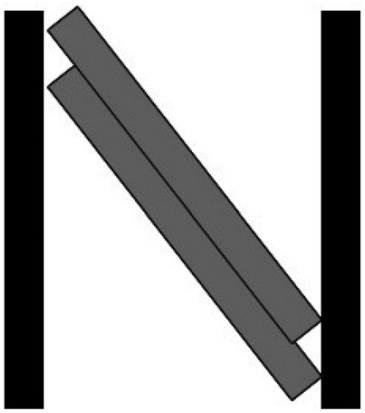

**Figure 2.** The '*N*' phantom made from bars of copper (black) and iron (gray).

GEANT4 includes user-defined input variables that provide a mechanism to limit the tracking of particles in any of the model's logical volumes with the logical volume's SetUserLimit method. This method allows limits to be imposed on particles tracked within the specified volume based on one of the following four parameters: track length, time, kinetic energy, or remaining range. The latter two limits are applicable only to charged particles. To limit the tracking of neutrons the GEANT4 documentation recommends the selection of a time constraint and the second experiment described herein was conducted to determine an acceptable setting for this variable (CERN).

Of note, the GEANT4 framework needs only to be compiled once. Models are built with the GEANT4 release 4.6.1 using the Gnu C++ compiler built by Apple for OSX. Environment settings are then specified as input variables at the beginning of a simulation run. All calculations present herein are performed on a Macintosh G5 class computer running the OSX operating system. Additionally, a correction was made to the G4NDL cross sectional tables for Chlorine. What should have been a numerical value in the table was incorrectly published as 'not a number' (NaN). This is a known problem with the table and we followed the GEANT4 online user forum's suggestions (CERN 2007) and replaced the 'NaN' with a value of 0.0 that is consistent with neighboring values.

### *2.2. Experimental model environments*

Three experimental models were developed for use in simulating various NSECT experiments: an 'N' phantom made of copper and iron, a biological model of the breast and a biological model of the liver. For all experiments described below the HPGe detector is modeled as a solid cylinder of germanium, 8 cm in diameter and 10 cm long.

*2.2.1. The 'N' phantom environment.* The 'N' phantom application is designed to simulate the experimental conditions used to tomographically image a multi-element phantom with NSECT (Kapadia 2007). The simulated 'N' phantom is modeled as four rectangular solids corresponding to the four bars used in the physical phantom. Each rectangle is 0.3 cm thick, 6.0 cm long and 2.5 cm wide. The four bars are arranged into the shape of the letter 'N' as shown in figure 2. The two upright legs are constructed of copper, and the diagonal legs are constructed of iron. Both elements are modeled in their naturally occurring isotopic ratio.

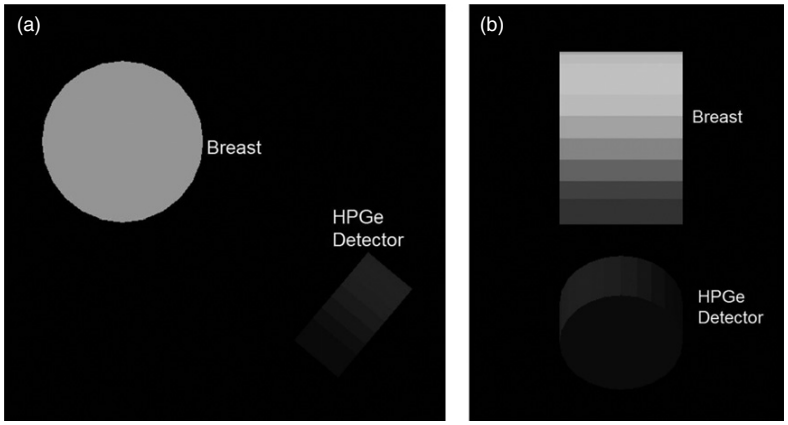


**Figure 3.** View 1 (a) and view 2 (b) of the breast phantom.

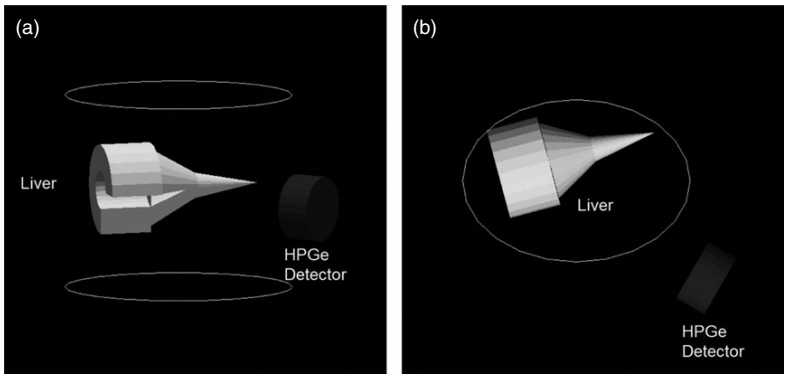


**Figure 4.** Coronal view (a) and transverse view (b) of the liver phantom.

This phantom was then placed in a GEANT4 model world consisting of a neutron source that emits 7.5 MeV neutrons and an HPGe detector. The beam is modeled as a square profile with no beam divergence. The HPGe detector is located 14 cm from the 'N' phantom off axis from the beam line at 45° within the plane defining a trans-axial slice of the phantom (see figures 5 and 6). All dimensions were set to mimic the actual experimental setup.

*2.2.2. The biological model environments.* Two different applications were created to simulate NSECT imaging on biological tissue, a breast model and a liver model. The primary use of the breast model was to determine the absorbed energy in order to estimate the absorbed dose. To simplify these dose calculations that depend on exposure volume, the breast is modeled simply as a cylinder 14.0 cm in diameter and 10.0 cm long. It is placed in a GEANT4 world with a neutron source where the neutron energy could be specified at runtime, and an HPGe detector. Figures 3(a) and 3(b) depict two views of the breast model environment geometry.

The geometric design for the liver model is more complex and is formed from one cylinder and two truncated cones (see figures 4(a) and (b)). One quarter of the volume of this assembly

**Table 1.** Component table for the breast and liver. Tissue density: 1.200 g cm$^{-3}$.

| Element | Breast fractional mass (%) | Liver fractional mass (%) |
|---|---|---|
| O | 61.43 | 61.43 |
| C | 22.86 | 22.86 |
| H | 9.88 | 9.62 |
| N | 2.57 | 2.57 |
| Ca | 1.43 | 0.01 |
| P | 1.11 | 1.11 |
| K | 0.20 | 0.99 |
| S | 0.20 | 0.79 |
| Na | 0.14 | 0.24 |
| Cl | 0.14 | 0.28 |
| Mg | 0.025 | 0.06 |
| Fe | 0.007 | 0.02 |
| F | 0.004 | |
| Zn | 0.003 | 0.01 |
| Si | 0.003 | |
| Cu | | 0.02 |

is then removed to more accurately model the shape of the human liver in the region of the spleen. This cut-out can be seen in figure 4(a). In all figures the white ellipses show the outline of the trunk of the body.

The elemental composition by weight for the breast and liver tissue used in the above models is shown in table 1 (Floyd *et al* 2006, NIST 2007, Bender *et al* 2007).

In GEANT4, the model developer specifies the atomic weight and number for each element, and then the percentage of each element within the sample. For this model, naturally occurring isotopic abundances were used for each element. The densities of the organs were artificially enhanced from the actual density of 1.02 g cm$^{-3}$ to 1.2 g cm$^{-3}$ to increase the gamma yield. The implications of this density increase are addressed in the discussion section.

### *2.3. Simulation experiments*

*2.3.1. The 'N' phantom experiment.* Using the 'N' phantom environment the following experiment was conducted to mimic the tomographic acquisition of the physical phantom in a nuclear laboratory described in Kapadia (2007). In this experiment, a 7.5 MeV neutron beam was created from an accelerated deuteron beam through the 2H(d,n)3He reaction and was collimated to be 7 mm square. The sample rested on a stage which was translated and rotated across the beam line to acquire tomographic projections. There were 11 translation stage stops at intervals of 8 mm, at each of which there were eight rotations at intervals of 22.5°. This resulted in a total of 88 projection sets. All 88 experimental projections were also simulated in the GEANT4 environment.

Gamma production in the sample was measured in the germanium crystal detector. Out of all the gamma rays produced in the sample due to inelastic scattering of a neutron with a target nucleus, only a small fraction will enter the HPGe detector. Of these gammas entering the crystal, only a fraction will deposit their energy into the detector through one or more interactions in the germanium crystal. The total energy deposited per gamma is the sum of the deposited energy from each of these interactions. This information was used to generate a gamma emission energy spectrum of the sample at each projection.

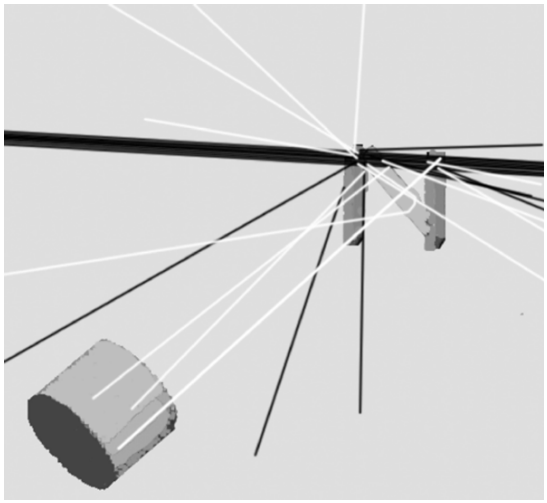

**Figure 5.** Graphic output of GEANT4 depicting one projection of the simulated tomography experiment using the 'N' phantom.

*2.3.2. User-defined limits experiment.* To determine an appropriate time limit (in ns) for tracking the lifetime of the neutrons, we examined five output variables (runtime, number of neutrons affected by the cap, number of detector events, energy deposited in the detector and energy deposited in the target) for simulations of 1 million neutron histories for six different neutron lifetime cutoffs (20, 100, 200, 500, 1000 and 2000 ns). This simulation was performed in all three environments outlined above as each phantom had different concentrations of hydrogen, a primary contributor to neutron inelastic scattering.

*2.3.3. Estimate of the radiation dose.* Simulations were conducted on the two biological models to determine the amount of energy absorbed in the target. This value was then used to obtain a dose estimate. Each simulation consisted of 1 million incident neutrons at 7.5 MeV contained in a 1 cm square beam with a square profile. Energy deposited in the sample due to both neutron and other secondary interactions (such as gamma absorption) was reported for each incident neutron and appropriate dose calculations were then performed.

## 3. Results

### *3.1. 'N' Phantom*

Our first simulation successfully simulated the tomography experiment. Figures 5 and 6 show the phantom at three different projection orientations from the tomography simulation.

In figures 5 and 6, neutrons are represented by black tracks, gammas by white tracks, and the detector by a shaded cylinder. The neutron beam (solid dark lines) enters from the left. The 'N' phantom in the upper right corner is shown with the outer copper pieces shaded dark gray and the inner iron pieces shaded lighter gray. As can be seen, most incident neutrons do not interact with the sample and simply pass through the phantom (solid dark lines exiting to the right of the figure). Some neutrons scatter elastically and emerge at new angles. Neutrons

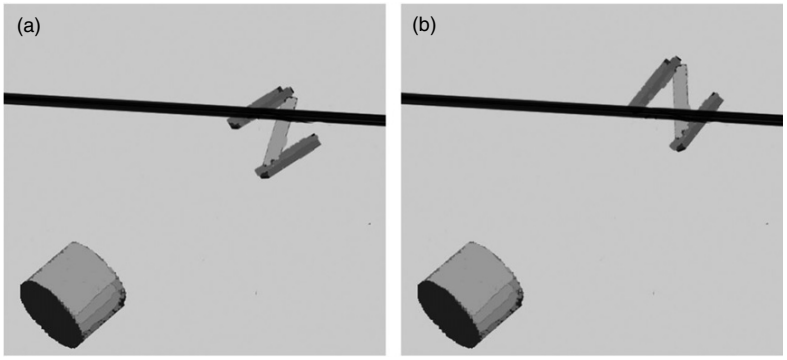


**Figure 6.** The phantom at the second (a) and third (b) of three different projection orientations. As seen here, most neutrons pass through the phantom without any interactions.

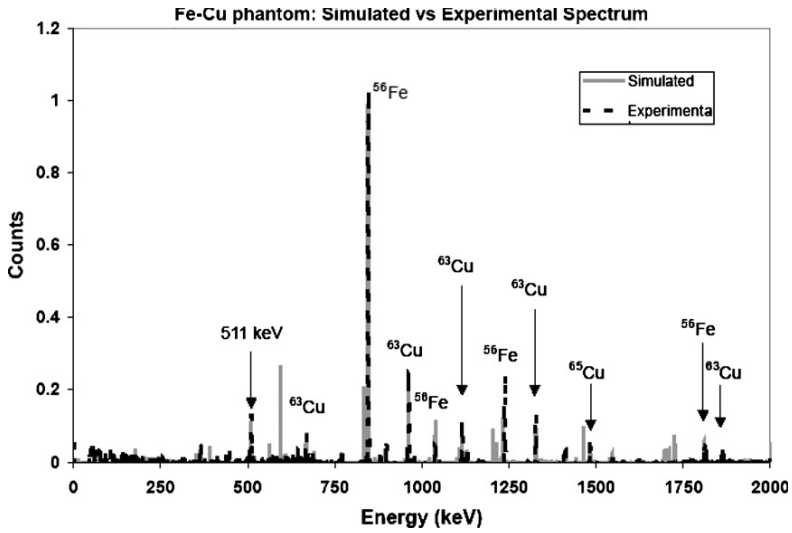


**Figure 7.** Comparison of experimental and simulated spectra for the 'N' phantom.

of interest to NSECT scatter inelastically and produce gammas (white tracks). A fraction of these gammas are then stopped in the detector.

Figure 7 shows a comparison between the experimental spectra from the tomographic acquisition of the iron and copper phantom (dashed black line) and the GEANT4 simulation of the same experiment (solid gray line). There is very good agreement between the two spectra for gamma energies above 500 keV and was achieved on the first run of the simulation. This agreement provides convincing evidence that the GEANT4 simulations are accurately representing the experimental conditions including the majority of the sources of gamma backgrounds for energies above 511 keV (Kapadia 2007).

Additionally, a plot of the number of iron and copper counts at each projection was compiled to determine if the simulation environment was translating and rotating the sample as expected. Figure 8 is a comparison between the simulation and experiment for the iron

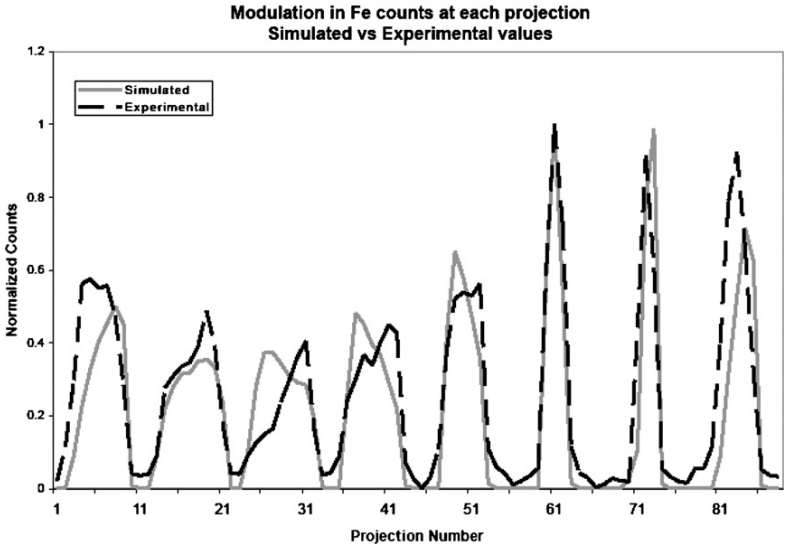


**Figure 8.** Comparison of Fe counts achieved at all projections for the experimental and simulated data.

**Figure 9.** Reconstructed simulated data. Left: copper, center: iron, right: combined copper and iron reconstructions.

counts obtained at each projection. While the peaks are not completely overlapping, the shape of the data is consistent. Some variation between the simulated and experimental setup is expected because the experimental setup is prone to minor positioning errors originating from the finite precision of the translation stage. In reality translation is only as good as the translation and rotation stages that are being used, while in simulation, translation is perfect. What is important is that the modulation trend in the number of gamma events is consistent between the experimental and simulated data.

The simulated data were then reconstructed using the maximum likelihood expectation maximization (MLEM) algorithm (Lange and Carson 1984) which was used to reconstruct the original experimental data described in Kapadia (2007). Figure 9 shows the resulting image after attenuation correction (Kapadia and Floyd 2005). The 'N' shape is clear and consistent with the shape of the phantom. Both the modulation profile and match in reconstructed

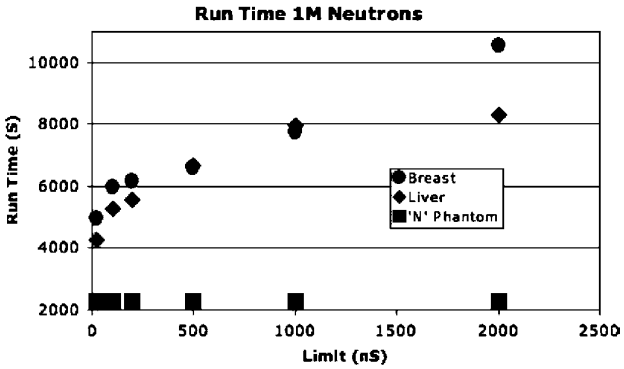


**Figure 10.** Monte Carlo runtime as a function of neutron lifetime cutoff limit for the three different phantoms. ●– breast phantom. ♦– liver phantom. ■– 'N' phantom.

images confirm that a different part of the phantom is being interrogated at each projection, and therefore the phantom is being translated through the beam.

### *3.2. User-defined limits*

The second simulation determined the effect of user-defined limits on five different aspects of an NSECT simulation. The first aspect examined was runtime as a function of user-selected cutoff on the neutron lifetime. The results are shown in figure 10, where a sharply decreasing runtime for the breast and liver models is observed as the cutoff is lowered below 100 ns.

As expected, little effect from cutoff time was seen for the hydrogen-lacking 'N' phantom model, and as the cutoff was raised to 2000 ns, the runtimes increase in the hydrogen-rich biological models. While the minimum runtime would occur at a cutoff time that is less than the time needed for neutrons to interact with the target, this would eliminate all reactions of interest. Therefore, the following four parameters must be considered when choosing an optimal cutoff time.

The second aspect examined was the fraction of incident neutrons whose lifetimes were truncated by the user limit. The results are presented in figure 11. As expected, the fraction was high for short cutoff lifetimes and then becomes asymptotically constant for longer times.

Again, no effect is seen for the hydrogen-lacking 'N' phantom. This fraction would have a maximum value of 1.0 when the cutoff time was less than that necessary for the neutrons to interact with the target.

The third aspect examined was the effect of user-defined limits on the number of detected events (shown in figure 12). As gamma detection follows Poisson counting statistics, the counting error in these measurements is the standard counting error for Poisson distributions, which is the square root of the number of events detected. For each of the data points, these errors are within the size of the figure markers.

As expected, there is a sharp decrease in detected events as the cutoff time becomes shorter and the number of events becomes asymptotic as the cutoff time grows.

The fourth aspect analyzed was the impact of the cutoff time on the energy deposited in the detector (shown in figure 13). It is difficult to discern any pattern as the results are variable depending on the type of tissue, especially below 1000 ns. The error in measuring the energy deposited depends on the energy resolution of the detector, which is less than 1% FWHM at 7.5 MeV. This error is within the confines of the figure marker.

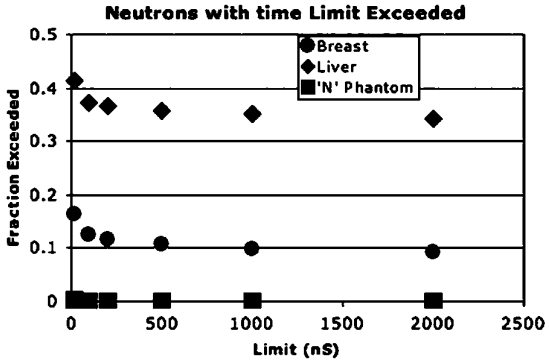


**Figure 11.** Number of neutrons that were terminated as a result of their exceeding the user-defined cutoff on the neutron lifetime plotted as a function of the cutoff limit.

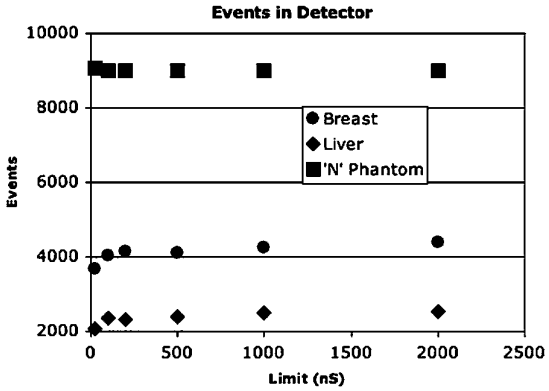


**Figure 12.** Number of detected events in the HPGe detector as a function of the cutoff on the neutron lifetime.

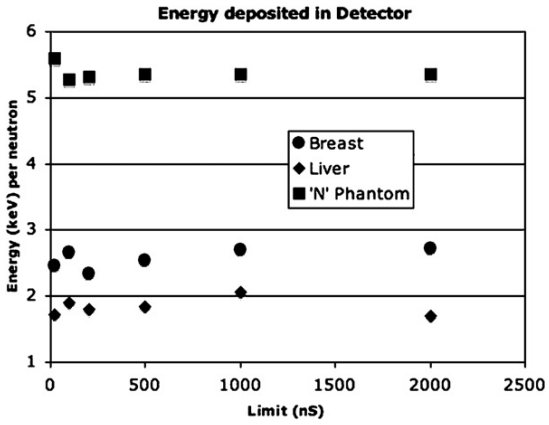


**Figure 13.** Energy deposited in the detector as a function of the cutoff on the neutron lifetime.

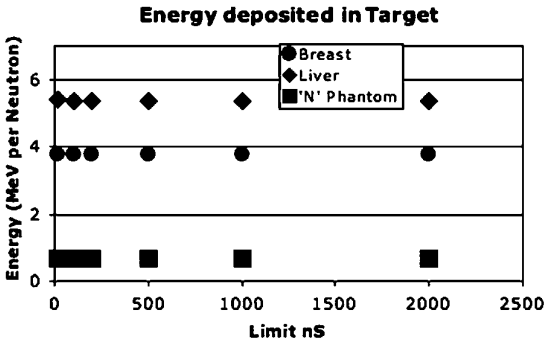


**Figure 14.** Energy deposited in the target volume as a function of the cutoff on the neutron lifetime.

For both figures 12 and 13 there would be no events or energy deposited in the detector if the cutoff limit was shorter than the time necessary for neutrons to interact in the target and stimulate a gamma event.

The final aspect examined was the dependence of the energy deposited in the target as a function of the cutoff time (shown in figure 14).

This figure shows no impact over the range of cutoff values considered and there was no change in the energy deposited in the sample as the time was varied from 20 to 2000 ns. Therefore, the smallest lifetime cutoff of 20 ns is enough time for the neutrons to reach, interact and deposit their energy in the sample. Because all energy is deposited in the sample within a small timeframe, limiting the neutron tracking lifetime should not affect the measurement of energy deposited in the sample. Only the non-instantaneous measurement of detected events and energy in the detector will be affected by the neutron lifetime cutoff (figures 12 and 13).

Based on the above data we have chosen to run our simulations with a cutoff time limit of 1000 ns. This choice will be further explained in the discussion section.

### *3.3. Estimate of the radiation dose*

The third simulation was to measure the total energy deposited in the sample and use this value to calculate the absorbed dose to the breast and liver. Based on the results from the second experiment, the energy deposited in the target per 7.5 MeV incident neutron is 3.74 MeV for the breast and 5.38 MeV for the liver (see figure 14). 82% of the incident neutrons were seen to interact in the breast while 93% were seen to interact in the liver. From this data the total energy absorbed in the breast and the liver was calculated for 1 million incident neutrons. Using the total energy absorbed and the exposed volume of tissue we calculate the absorbed dose to the breast and liver. To calculate the equivalent dose, the absorbed dose is multiplied by the particle weighting factor for neutrons (10 at 7.5 MeV) (Turner 2004). For the breast, the equivalent dose was calculated to be 0.498 mSv. The same computation for liver found an equivalent dose of 0.239 mSv. Table 2 shows the complete calculations. Note that these dose calculations are limited to the target organs only, not the entire body.

## 4. Discussion

In order to design a functional NSECT system, a valid simulation environment must be developed. Due to the logistics surrounding the neutron beam source and the long experimental

**Table 2.** Equivalent dose to the breast and liver.

| | Breast | Liver |
|---|---|---|
| **Energy absorbed** = number of neutrons × energy deposited | $1 \times 10^6$ neutrons × 3.74 MeV/ neutron × $1.6 \times 10^{-13}$ J $MeV^{-1}$ = **$5.98 \times 10^{-7}$ J** | $1 \times 10^6$ neutrons × 5.38 MeV/ neutron ∗ $1.6 \times 10^{-13}$ J $MeV^{-1}$ = **$8.61 \times 10^{-7}$ J** |
| Exposure volume | 10 $cm^3$ | 30 $cm^3$ |
| Density | 1.2 g $cm^{-3}$ | 1.2 g $cm^{-3}$ |
| Mass | 0.012 kg | 0.036 kg |
| **Absorbed dose** = energy absorbed per kg of exposed tissue | $5.98 \times 10^{-7}$J/0.012 kg = **$4.98 \times 10^{-5}$** Gray (J $kg^{-1}$) | $8.61 \times 10^{-7}$J/0.036 kg = **$2.39 \times 10^{-5}$** Gray (J $kg^{-1}$) |
| **Equivalent dose** = Absorbed Dose × particle weighting factor | $4.98 \times 10^{-5}$ Gray × 10 = **0.498 mSv** | $2.39 \times 10^{-5}$ Gray × 10 = **0.239 mSv** |

times, it is not practical to develop a system by experimentation alone. A simulation environment allows more rapid development and iteration on new ideas and setups.

This paper demonstrates that the GEANT4 simulation environment successfully addresses three major concerns of modeling NSECT: positioning of the beam line relative to the sample, effective modeling of low energy neutrons in hydrogen rich tissue and measuring the absorbed energy to quantify the dose.

The first simulation demonstrated successful modeling of the tomographic experimental NSECT interrogation of the 'N' phantom. Due to the complexity of the Monte Carlo method, the GEANT4 toolkit and the model, it is prudent to validate the simulations with experimental data. The simulated spectra were in close agreement with experimentally acquired spectra. This result indicates that GEANT4 can successfully model the gamma radiation due to neutron inelastic scattering and the subsequent detection of the gammas in the HPGe detector crystal. Additionally, the simulated tomographic runs achieved similar modulation in the energy spectrum as that of the experiment, indicating that the model was able to produce a neutron beam of expected width and successfully translate the phantom through this beam. This simulation allowed comparison of both the spectral results and the tomographic results. It also demonstrated the toolkit's ability to generate legitimate gamma energy spectra and to simulate the relative position between the beam line and the sample.

The second simulation was performed to develop a solution for a challenge presented by simulation of biological tissue. Neutrons in a hydrogen rich environment are sometimes slowed through elastic scatter and continue to 'drift' within the tissue sample for very long computation times making the simulation far too slow to be feasible. A GEANT4 modeling feature allows the limiting of tracking time for a neutron and the imposition of tracking limitations in order to increase the speed of the simulation. In order to determine the effect of these cutoff times, a parametric analysis was performed on all three models and an appropriate time limit was determined.

The results of the user-defined time limit experiments have led us to choose a limit of 1000 ns. Implementation of this limit decreased the runtime of the code in general by a factor of over 2 and in one extreme case runtime was decreased from over a week down to 2 h. Initially it may seem reasonable to consider cutoff values less then 1000 ns as the cutoff appears to have little impact on energy deposited in the target (figure 14). For example, dropping the cutoff from 1000 ns to 100 ns would decrease the runtime by up to 30% (from 8000 s to 5500 s). However, the energy deposited in the detector appears somewhat unstable for cutoff values less than 500 ns (figure 13). Additionally, a primary limitation for interpreting the spectra from these simulations is the small number of detected events, and as the cutoff

time is shortened there is a slight decrease in the number of events in the detector (figure 12). For the above reasons, the cutoff should be kept as high as practical (1000 ns).

It is important to note that the measure of energy deposited in the target did not change based on the cutoff time (figure 14). This finding bolsters confidence that, regardless of the chosen cutoff time, the dose calculations will remain constant. This is important because a major benefit of simulations is the ability to determine the dose in the interrogated tissue.

In the third and final simulation both the breast and liver models were interrogated to determine energy deposited in tissue samples during an NSECT imaging exposure. This quantity was then used to determine the radiation dose to a specific organ that results from a typical NSECT interrogation of biological tissue. Both dose levels were below 1 mSv, which is the dose delivered by a standard two-view mammogram. To decrease simulation time, experiments in this study are performed with an artificially enhanced tissue density. An artificially enhanced tissue density results in a larger number of neutron scattering events per incident neutrons, and therefore fewer incident neutrons are needed to generate a significant number of gamma rays in the energy spectrum. In reality, with normal tissue density, a larger number of incident neutrons would be necessary to generate a significant number of counts at spectral energy peaks. However, while increasing the number of incident neutrons from 1 to 10 million would increase the dose by a factor of 10, the dose would increase to approximately 5 mSv, which is more than a mammogram but less than a chest CT (approximately 20 mSv).

## 5. Conclusion

This paper has demonstrated that the GEANT4 simulation environment produces accurate gamma spectra and effectively models tomographic translations by mimicking an NSECT experiment. A limit on neutron tracking has been determined that does not affect integral simulation results and this limit has been used in a simulation environment to determine the neutron dose. The data presented herein not only demonstrate the successful modeling of the NSECT experimental acquisition environment, but also indicate that GEANT4 is an adequate Monte Carlo toolkit for NSECT simulation. Given this powerful tool for simulating the NSECT environment, rapid development of NSECT as a biomedical investigational tool is envisioned.

## Acknowledgments

The authors wish to thank Carey E Floyd Jr for his vision and effort in the creation and development of NSECT. He began this work, which we finish is his memory and name. This research is funded in part by NIH/NCI grant no 1-R21-CA106873-01; NIH Training grant no. 1-T32-EB001040; DOD Breast Cancer Research Program award no. W81XWH-06-1-0484.

## References

Agostinelli S *et al* 2003 Geant4—a simulation toolkit *Nucl. Instrum. Methods* A **506** 250–303

Bender J, Kapadia A J, Sharma A C, Tourassi G D, Harrawood B P and Floyd C E 2007 Breast cancer detection using neutron stimulated emission computed tomography: prominent elements and dose requirements *Med. Phys.* **34** at press

CERN GEANT4 available from: http://geant4.web.cern.ch/geant4/

CERN 2007 GEANT4 HyperNews Forums. In: http://geant4-hn.slac.stanford.edu:5090/Geant4-HyperNews/index

Floyd C, Bender J E, Sharma A C, Kapadia A J, Xia J Q, Harrawood B P, Tourassi G D, Lo J Y, Crowell A S and Howell C R 2006 Introduction to neutron stimulated emission computed tomography *Phys. Med. Biol.* **51** 3375–90

Floyd C E *et al* 2004 Neutron stimulated emission computed tomography of stable isotopes *Proc. SPIE* **5368** 248–54

Floyd C *et al* 2007 Neutron stimulated emission computed tomography: background corrections *Nucl. Instrum. Methods* B **254** 329–36

Kapadia A J 2007 Accuracy and patient dose in neutron stimulated emission computed tomography for diagnosis of liver iron overload: simulations in GEANT4 *Doctoral Dissertation* Duke University

Kapadia A and Floyd C E 2005 An attenuation correction technique to correct for neutron and gamma attenuation in the reconstructed image of a neutron stimulated emission computed tomography (NSECT) system *Proc. SPIE* **5745** 737–43

Lange K and Carson R 1984 EM reconstruction algorithms for emission and transmission tomography *J. Comput. Assist. Tomogr.* **8** 306–16

NIST 2007 *Database of Natural Matrix Reference Materials: Bovine Liver* (National Institute of Standards and Technology)

Turner J 2004 *Atoms, Radiation, and Radiation Protection* (Strauss: Wiley)

# Breast cancer detection using neutron stimulated emission computed tomography: Prominent elements and dose requirements

Janelle E. Bender,[a] Anuj J. Kapadia, and Amy C. Sharma
*Department of Biomedical Engineering and Duke Advanced Imaging Laboratories, Department of Radiology, Duke University, Durham, North Carolina 27708*

Georgia D. Tourassi and Brian P. Harrawood
*Duke Advanced Imaging Laboratories, Department of Radiology, Duke University, Durham, North Carolina 27708*

Carey E. Floyd, Jr.
*Department of Biomedical Engineering and Duke Advanced Imaging Laboratories, Department of Radiology, Duke University, Durham, North Carolina 27708*

(Received 14 March 2007; revised 25 July 2007; accepted for publication 26 July 2007; published 18 September 2007)

Neutron stimulated emission computed tomography (NSECT) is being developed to noninvasively determine concentrations of trace elements in biological tissue. Studies have shown prominent differences in the trace element concentration of normal and malignant breast tissue. NSECT has the potential to detect these differences and diagnose malignancy with high accuracy with dose comparable to that of a single mammogram. In this study, NSECT imaging was simulated for normal and malignant human breast tissue samples to determine the significance of individual elements in determining malignancy. The normal and malignant models were designed with different elemental compositions, and each was scanned spectroscopically using a simulated 2.5 MeV neutron beam. The number of incident neutrons was varied from 0.5 million to 10 million neutrons. The resulting gamma spectra were evaluated through receiver operating characteristic (ROC) analysis to determine which trace elements were prominent enough to be considered markers for breast cancer detection. Four elemental isotopes ($^{133}$Cs, $^{81}$Br, $^{79}$Br, and $^{87}$Rb) at five energy levels were shown to be promising features for breast cancer detection with an area under the ROC curve ($A_Z$) above 0.85. One of these elements—$^{87}$Rb at 1338 keV—achieved perfect classification at 10 million incident neutrons and could be detected with as low as 3 million incident neutrons. Patient dose was calculated for each gamma spectrum obtained and was found to range from between 0.05 and 0.112 mSv depending on the number of neutrons. This simulation demonstrates that NSECT has the potential to noninvasively detect breast cancer through five prominent trace element energy levels, at dose levels comparable to other breast cancer screening techniques. © *2007 American Association of Physicists in Medicine*. [DOI: 10.1118/1.2775669]

Key words: Monte Carlo, neutrons, tomography, gamma-ray spectroscopy, breast cancer

## I. INTRODUCTION

Neutron stimulated emission computed tomography (NSECT) is a new technique being developed to noninvasively image the elemental composition of tissues within the human body.[1–3] When a high-energy fast neutron (2.5–5 MeV) inelastically scatters off an atomic nucleus, the nucleus is excited, and a gamma ray is emitted. The energy of the gamma is characteristic of the atomic nucleus with which it interacted. By analyzing the energy levels of the emitted gammas when a sample is bombarded with many neutrons, the elemental composition can be determined.

Many studies have shown there to be a difference in the elemental composition of normal, benign, and malignant tissue in humans for a large variety of cancers, including breast cancer,[4–8] prostate cancer,[9] and glioblastoma multiforme.[10] To determine compositional differences, these studies have required invasive methods such as biopsy. The NSECT technique has the potential to measure these differences noninvasively, *in vivo*, with a reduced dose compared to four-view screening mammography.[2]

NSECT has the potential to evolve into a powerful, low-dose screening or diagnostic technology for breast cancer. Numerous studies using x-ray fluorescence (XRF)[6,11] and neutron activation analysis (NAA)[8,12] have shown increased concentrations of trace elements in malignant breast tissue compared to adjacent normal tissue. One XRF study showed that there were elevated levels of Fe, Cu, Zn, and K in human breast tumor tissue when compared to healthy breast tissue.[11] This study utilized fluorescence emitted from the elements in *ex vivo* breast tissue samples with a synchrotron-based system. In XRF, tissue samples remain intact and there is direct quantification of the elements, but the system necessitates the use of biopsied tissue. Another study found that malignant breast tissue has significantly higher concentrations of 12 trace elements (Al, Br, Ca, Cl, Co, Cs, Fe, K, Mn, Na, Rb, and Zn) when compared to adjacent normal breast tissue.[12] This study employed NAA, an invasive and destruc-

tive technique, which typically involves freeze-drying of excised breast tissue.[13] Because measurements were made on dried tissue, a wet-to-dry ratio had to be implemented in order to convert values to ones relevant in intact breast tissue. Additionally, NAA renders the interrogated sample radioactive. While NAA is high in sensitivity, it lacks the ability to be translated to a low-dose *in vivo* method.

We present NSECT as an imaging modality that has the potential to be translated to the clinic, due to its noninvasive nature. NSECT is intended to provide tomographic projections by scanning a sample with a high-energy fast neutron beam, formed via the $d(d,n)^3He$ fusion reaction. We have already demonstrated spectroscopic acquisition over a broad energy range that encompasses many elements of interest for biological imaging.[1] The present study uses Monte Carlo simulations and receiver operating characteristic (ROC) analysis to investigate the performance of different elements in differentiating malignant and normal breast tissue at appreciably low-dose levels, in accordance with the As Low As Reasonably Achievable (ALARA) concept and at levels used in currently approved screening techniques. Before evaluations can be performed on anatomic models of the breast containing lesions and nodules with trace element concentration differences, it must be tested whether it is possible to detect any trace element concentration changes in the presence of all the scatter noise generated by the tissue. Hence this study is restricted to single projection spectra of models of bulk breast tissue to investigate the feasibility of NSECT in trace element quantification to detect breast cancer.

## II. METHODS

### II.A. Monte Carlo simulations

Monte Carlo simulations were designed using GEANT4.[14] Bulk breast tissue was modeled as an ellipsoid 10 cm $\times$6 cm$\times$5 cm. Two high-purity germanium (HPGe) detectors[15] were modeled as cylinders of 5.32 g/cm$^3$ density germanium with 12 cm diameter and 5 cm height. The two HPGe detectors flanked the breast tissue and were separated by 11.6 cm. The neutron source was modeled in GEANT4 as a fast neutron (2.5 MeV) beam of 1 cm$^2$ area with a square profile, which was directed incident upon bulk breast tissue. See Fig. 1 for a schematic of the GEANT4 setup.

In the case of neutron inelastic scattering, the nucleus is excited and emits a characteristic gamma ray. GEANT4 determines the direction of the emitted gamma, which may then be deposited in one of the two gamma detectors. The gamma ray energy deposited in each detector was tabulated to form a gamma spectrum showing energy levels and corresponding gamma counts, or intensity. The energy was then matched to the element with which the neutron had an interaction, which was deduced using a lookup table from the Evaluated Nuclear Data Files (ENDF) database.[16]

Breast tissue was modeled as either being normal or malignant, with elemental compositions[12] as seen in Table I. Despite a broad distribution of concentrations in the malignant specimens from the study in which these values were derived, the authors were able to see significantly higher concentrations of all elements in the freeze-dried malignant specimens in comparison with the normal ones. The normal breast tissue was modeled with a density of 0.93 g/cm$^3$, and the malignant breast tissue was modeled with a density of 1.058 g/cm$^3$, which correspond to adipose tissue and masses, respectively.[17] Over 99% of the breast tissue is comprised of O, C, H, and N so we used a neutron energy (2.5 MeV) low enough to avoid excitation of O, C, and N. The 2.5 MeV was also high enough to excite the trace elements of interest. We did see neutron capture on H, which was easily distinguishable. The remainder of the peaks can be attributed to excitations from the trace elements, which are of interest because they can be linked to malignancy.

One hundred simulations of 10 million incident neutrons were run on both the normal and malignant models. For each simulation, a new random seed was generated, which was different between the malignant and normal runs, so that the runs were uncorrelated. Additionally, 100 runs each of 0.5

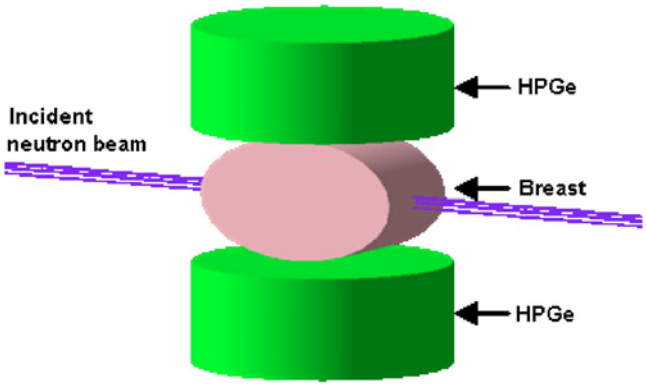


FIG. 1. GEANT4 setup. Two HPGe detectors flank the breast tissue. Incoming neutrons strike at the face of the breast.

TABLE I. Breast tissue composition for normal and malignant models. The percentages were calculated by first converting dry weights to wet weights.

| | Normal (%) | Malignant (%) |
|---|---|---|
| Oxygen | 61.429 | 61.429 |
| Carbon | 22.857 | 22.857 |
| Hydrogen | 12.649 | 12.510 |
| Nitrogen | 2.571 | 2.571 |
| Chlorine | 1.98E−1 | 2.15E−1 |
| Sodium | 1.85E−1 | 2E−1 |
| Potassium | 8.94E−2 | 1.96E−1 |
| Iron | 9.8E−3 | 7.85E−3 |
| Calcium | 8.29E−3 | 1.13E−2 |
| Zinc | 1.17E−3 | 1.14E−3 |
| Bromine | 7.07E−4 | 6.55E−4 |
| Aluminum | 6.67E−4 | 5.7E−4 |
| Rubidium | 5.98E−4 | 5.84E−4 |
| Manganese | 3.88E−5 | 3.16E−5 |
| Cobalt | 2.06E−5 | 1.98E−5 |
| Cesium | 3.27E−7 | 3.6E−7 |

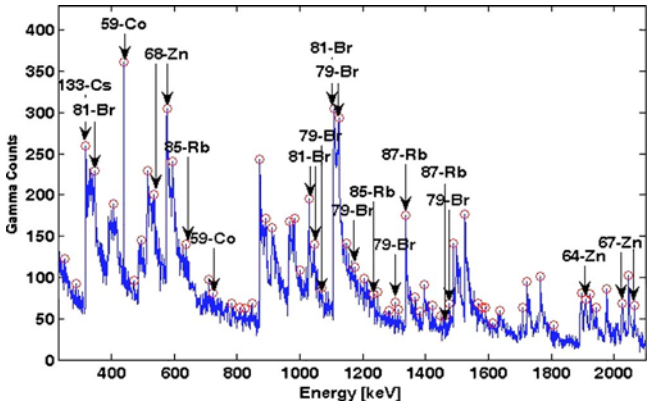


FIG. 2. Spectrum of 10 million incident neutrons from the normal breast model. The circles represent energy levels at which the counts exceeded 40 and at which the counts exceeded all counts in a ±10 keV window. Labels are provided for those peaks that matched elements found in the modeled breast tissue.

million, 1 million, 2 million, 3 million, and 5 million incident neutrons were produced. This yielded a total of 600 spectral scans per tissue type.

### II.B. Peak-identification algorithm

For each output file, the energies in keV were tabulated to yield spectra of gamma energy and corresponding gamma intensity. The first task was to determine whether or not the intensity at a specific energy could be considered a peak in the spectrum. To be called a peak, three criteria had to be met: (1) the peak had to exceed a set minimum count level, (2) the peak had to be larger than all other peaks in a specified window, and (3) the peak energy had to match to one of the elements in the breast tissue model. The minimum peak height was set to be 40 counts, which exceeded the underlying noise throughout the energy range (0–2500 keV). An iterative technique was used to optimize the window width. Window widths were varied form ±2 to ±20 keV, and the number of detected peaks was correlated with the number of expected peaks in the simulated spectra. The best results were seen for a window width of ±10 keV. The element that the characteristic energy represented was determined using the ENDF tables. Figure 2 shows an example of the peak-identification technique for one of the runs of 10 million incident neutrons. The circles mark the energies that fit the first two criteria, and the labels note the corresponding element if the peak fit the third criterion.

The process of peak identification was performed on output files from the 100 normal and 100 malignant simulations for the 10 million incident neutrons level. Peak identification was performed only for the highest incident neutron level as a best-case scenario to identify peaks that could be detected in the breast tissue.

### II.C. ROC analysis

The detectability index was the area under the binormal ROC curves, or $A_z$. The significance of a peak at lower levels of incident neutrons was determined by monitoring the degradation in the area under the ROC curve for that peak as the number of incident neutrons was reduced. In order for a specific energy peak to be used in the ROC analysis, more than 50 of the 100 files for each case (normal or malignant) had to register the given peak. The purpose of this criterion was to focus only on the peaks found in the majority of each tissue model. Note that as long as more than half of the files registered the peak, the counts for all files were entered for ROC analysis. The ROC analysis was conducted for each of the matched energies using the counts for that energy level from all 100 runs for normal and 100 runs for malignant as the input data to the software, ROCKIT.[18] ROCKIT uses maximum likelihood estimation to fit a binormal ROC curve to continuously distributed data and/or categorical data.[19] There were two categories for the ROC analysis: "actually negative" and "actually positive," which respectively correspond to normal and malignant status.

Because ROC analysis was performed on a moderately small sample size ($n=200$), it was expected that $A_z$ estimates would have a relatively large variance. To ensure that the peaks selected had good discriminatory ability, we applied a minimum threshold of $A_z=0.85$.

### II.D. Dose calculations

One of the primary concerns with any potential clinical imaging technique is the absorbed patient dose. The dose was calculated for each run as follows. Using a separate Monte Carlo simulation with the same parameters and setup as described in Sec. II A, the average energy due to both neutron and other secondary interactions deposited in the breast tissue per 2.5 MeV incident neutron was determined to be 1.4 MeV.[9] As the neutrons irradiated a 10 $cm^3$ volume of tissue, corresponding to a neutron beam surface of 1 $cm^2$ over a 10 cm depth, the total irradiated mass could be calculated using the density of the breast tissue. This was then converted into the absorbed dose, $D_{T,R}$, in a tissue or organ T due to radiation R, measured in J/kg or Sv. The equivalent dose, $H_{T,R}$, was then calculated as in Eq. (1), where $\omega_R$ is the radiation weighting factor. For neutrons with energy between 2 and 20 MeV, $\omega_R=10$ (Ref. 20). The effective dose, E, to the breast tissue was calculated using Eq. (2), where $\omega_T$ is the tissue weighting factor, which for breast is equal to 0.05 (Ref. 21).

$$H_{T,R}=\omega_R \cdot D_{T,R}, \tag{1}$$

$$E=\omega_T \cdot H_{T,R}. \tag{2}$$

Using the method described above, the effective dose was estimated to be 1.12E-8 mSv/neutron.

## III. RESULTS

For the 100 normal tissue runs of 10 million incident neutrons, 28 energy levels were found to be peaks in over half of the runs. For the 100 corresponding malignant runs, 30 energy levels were designated as peaks in over half of the runs. These energy levels were queried in the ENDF tables; eight levels in the normal model and ten levels in the malignant

TABLE II. Number of energy levels and corresponding elemental matches for both the normal and malignant models. A checkmark indicates the matches were found in over half of the output files. The number in parentheses is the number of output files that had a match out of the total 100 files.

| | | Normal | Malignant |
|---|---|---|---|
| 319 keV | $^{133}$Cs | √ (98) | √ (90) |
| 439 keV | $^{59}$Co | √ (100) | √ (100) |
| 1029 keV | $^{81}$Br | √ (100) | √ (99) |
| 1109 keV | $^{81}$Br | √ (85) | √ (56) |
| 1124 keV | $^{79}$Br | (43) | √ (51) |
| 1191 keV | $^{79}$Br | √ (51) | √ (60) |
| 1338 keV | $^{87}$Rb | √ (95) | √ (97) |
| 1476 keV | $^{79}$Br | √ (79) | √ (61) |
| 1697 keV | $^{41}$K | (49) | √ (54) |
| 2065 keV | $^{67}$Zn | √ (60) | √ (70) |

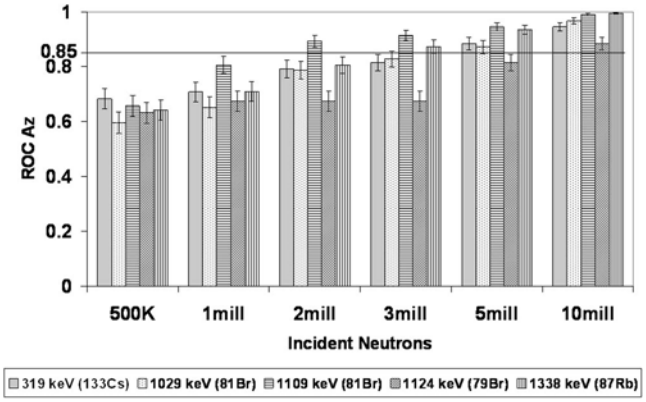


FIG. 3. ROC $A_z$ for the prominent energy levels over all incident neutron count levels. The horizontal line at 0.85 marks the cutoff for prominence.

model corresponded to elements from the breast tissue model. All eight energy peaks from the normal model were also found in the malignant model, suggesting that they robustly appear in the majority of tissue samples from each population. Table II summarizes the energy levels and the corresponding number of matches for normal and malignant models.

A total of ten energy levels was found to be peaks in over half the runs in either tissue model using 10 million incident neutrons. Only these peaks were further analyzed with ROC at the six different incident neutron levels considered in this simulation. ROC analysis on the 60 total energy level/incident neutron combinations yielded 12 total combinations with ROC $A_z > 0.85$. As seen in Table III, each of these combinations corresponded to one of five separate energy levels—319, 1029, 1109, 1124, and 1338 keV, representing elements $^{133}$Cs, $^{81}$Br, $^{81}$Br, $^{79}$Br, and $^{87}$Rb, respectively. Aside from 1124 keV, all these prominent energy levels satisfied the condition of element matching in over 50 of 100 normal and malignant output files. For 1124 keV, this condition was satisfied only for the malignant tissue model. One combination—1338 keV with 10 million incident neutrons—yielded a perfect $A_z$ value of 1.00. Figure 3 summarizes the mean and standard deviation of the ROC $A_z$ values as a function of number of neutrons for all energy levels.

No discriminatory elements were found at the lowest two incident neutron levels (0.5 million and 1 million), but $^{81}$Br at 1109 keV was found to be significant at the 2 million incident neutron level. Figure 4 shows the summation of all

TABLE III. Elements and corresponding average and standard error for ROC Az values obtained from ROCKIT software. The values in bold are above the significance threshold of Az=0.85 and are considered significant. The significant error ranged from 0.01 to 0.05.

| | Millions of Incident Neutrons | | | | | |
|---|---|---|---|---|---|---|
| keV | 0.5 | 1 | 2 | 3 | 5 | 10 |
| 319 $^{133}$Cs | 0.68±0.04 | 0.71±0.04 | 0.79±0.03 | 0.81±0.03 | **0.88±0.02** | **0.95±0.01** |
| 439 $^{59}$Co | 0.54±0.04 | 0.58±0.04 | 0.58±0.04 | 0.64±0.04 | 0.61±0.04 | 0.67±0.04 |
| 1029 $^{81}$Br | 0.60±0.04 | 0.65±0.04 | 0.79±0.03 | 0.83±0.03 | **0.87±0.02** | **0.97±0.01** |
| 1109 $^{81}$Br | 0.66±0.04 | 0.81±0.03 | **0.89±0.02** | **0.91±0.02** | **0.95±0.02** | **0.99±0.01** |
| 1124 $^{79}$Br | 0.63±0.04 | 0.67±0.04 | 0.67±0.04 | 0.67±0.04 | 0.81±0.03 | **0.89±0.02** |
| 1191 $^{79}$Br | 0.57±0.04 | 0.57±0.04 | 0.58±0.04 | 0.64±0.04 | 0.64±0.04 | 0.74±0.03 |
| 1338 $^{87}$Rb | 0.64±0.04 | 0.71±0.04 | 0.81±0.03 | **0.87±0.02** | **0.93±0.02** | **1.00** |
| 1476 $^{79}$Br | 0.60±0.04 | 0.67±0.04 | 0.72±0.04 | 0.75±0.03 | 0.76±0.03 | 0.85±0.03 |
| 1697 $^{41}$K | 0.52±0.04 | 0.49±0.04 | 0.50±0.04 | 0.56±0.04 | 0.58±0.04 | 0.66±0.04 |
| 2065 $^{67}$Zn | 0.47±0.04 | 0.54±0.04 | 0.54±0.04 | 0.58±0.04 | 0.60±0.04 | 0.66±0.04 |

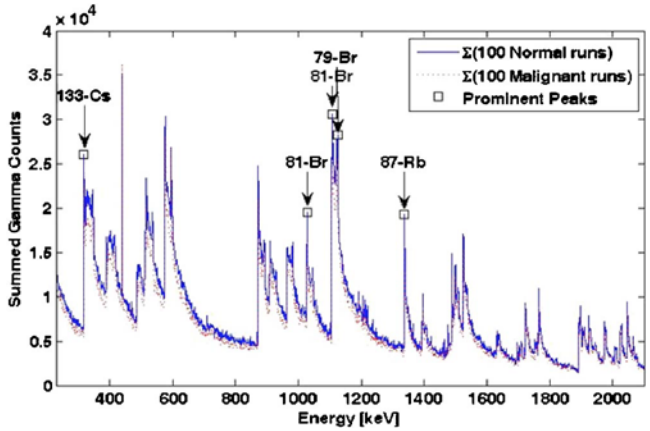


FIG. 4. The 100 normal and ten malignant spectra of 10 million incident neutrons were summed. The squares mark the energy levels found to be highly discriminatory in the ROC analysis.

normal and malignant runs for 10 million incident neutrons and indicates the peaks that were found to be prominent in the ROC analysis.

The dose values calculated for the neutron count levels that yielded prominent elements ranged from 0.0224 to 0.112 mSv, depending on the number of incident neutrons. For 2 million neutrons, the total dose to the volume of breast tissue that was irradiated was only 0.0224 mSv, which is only a fraction of the dose reported for other breast cancer screening methods,[22] and even when the number of incident neutrons is maximized to 10 million, the dose to the breast tissue is still low enough to indicate NSECT's potential as a breast cancer screening technique.

## IV. DISCUSSION

This simulation study demonstrates NSECT's feasibility to detect differences in the concentration of several discriminatory trace elements that indicate cancer in breast tissue. We have demonstrated the ability to see peaks corresponding to elements in both the normal and malignant bulk breast tissue model. The results indicate that four elemental isotopes, $^{133}$Cs, $^{81}$Br, $^{79}$Br, and $^{87}$Rb, are prominent in differentiating normal from malignant tissue at neutron flux values corresponding to clinically relevant dose levels. One of these elements achieved perfect classification at 10 million neutrons and was able to differentiate normal and malignant tissue at a neutron flux as low as 3 million neutrons. As low neutron flux directly implies low dose, these elements are vital for a low-dose clinical implementation of NSECT for breast cancer detection. Further, the ability of these elements in differentiating normal and malignant tissue suggests that NSECT has the potential to be translated into a clinical breast cancer screening modality.

The breast in this study was modeled as a bulk section of malignant or normal breast tissue. This was done to test the feasibility of NSECT to detect breast cancer markers in malignant tissue and determine which marker elements are most indicative of cancer. As this feasibility has now been demonstrated, a logical extension to this study will be to model the anatomy of the normal and malignant breast more accurately to investigate the feasibility of detecting element changes within tumors. The issue of patient-specific variability in elemental composition has been studied using several different techniques, including neutron activation analysis, x-ray fluorescence, and atomic absorption spectrophotometry. Although these studies do indicate patient-specific variability, they still show significant increases in elemental concentrations in cancerous tissue. Therefore, patient variability does not does not outweigh the elemental concentration differences in malignant and normal tissue. We plan to investigate this further in the future using the NSECT technique to analyze the composition of *ex vivo* benign, normal, and malignant tissue specimens.

Dose calculated in this study indicates that the dose from an NSECT scan for cancer detection is only a fraction of the dose delivered from a screening mammogram. The ROC analysis from this simulation study suggests that cancer detection can be achieved with a dose of 0.0224 mSv (2 million incident neutrons). Although the present work calculates the dose from a single projection image, which is not directly comparable to the dose calculated for current high-resolution screening technologies, NSECT shows promise as a low-dose cancer screening technique. We could increase the number of neutrons and still be within dose guidelines, but we used 10 million as the maximum number of incident neutrons for two main reasons. First, it was determined in an earlier study that 10 000 gamma counts are required in the detectors to obtain 5% accuracy.[23] Second, 10 million incident neutrons is a computationally feasible number that provides sufficient statistical accuracy while keeping dose at a minimum. Keeping these two factors in mind, 10 million neutrons were considered optimal for this scan.

The dose value obtained in this study is calculated for a model of the breast that does not account for sources of background, which would otherwise be present in the clinical scanning environment. Before translating this technique to the clinic, an expansion of this study is required to determine the performance when noise is added into the signal. Simulation experiments to model the sources of noise in a clinical environment are currently underway. This study assumes a relatively clean, low-noise signal in detecting an element peak, which results in a low-dose estimate. The presence of noise in the system will raise the detection threshold, requiring a larger total concentration of the element for successful detection. Experiments to determine the detection threshold of NSECT in both simulation and clinical environments are being conducted.

From a detection point of view, a logical extension of this study is to develop a fusion classifier to test whether combining elements could be used to detect differences in normal and malignant breast tissue with greater accuracy at lower neutron fluxes. Another extension would be to perform the same set of simulations using a benign breast tissue model to test NSECT's ability to distinguish malignant from benign breast, which is of clinical interest diagnostically. We are encouraged because our current dose estimate is only a fraction of a standard mammography dose. Thus, there is plenty

of room to increase the dosage to overcome noise and still conduct an NSECT scan that is within clinically acceptable dose limits.

## ACKNOWLEDGMENTS

This work was supported by NIH/NCI Grant 1-R21-CA106873-01 and in part by the Department of Defense (Breast Cancer Research Program) under award number W81XWH-06-1-0484 and by NIH Training Grant No. 1-T32-EB001040.

[a]Author to whom correspondence should be addressed. Electronic mail: jeb9@duke.edu

[1]C. E. Floyd *et al.*, "Introduction to neutron stimulated emission computed tomography," Phys. Med. Biol. **51**, 3375–3390 (2006).
[2]C. E. Floyd *et al.*, "Breast cancer diagnosis using neutron stimulated emission computed tomography: Dose and count requirements," in *Proceedings of SPIE Medical Imaging 2006: Physics of Medical Imaging* (SPIE, 2006), Vol. 6142, pp. 597–603.
[3]C. E. Floyd *et al.*, "Neutron stimulated emission computed tomography: Background corrections," Nucl. Instrum. Methods Phys. Res. B **254**, 329–336 (2007).
[4]A. E. Schwartz *et al.*, "Trace elements in normal and malignant human breast tissue," Surgery **76**, 325–329 (1974).
[5]K. H. Ng, D. A. Bradley, L. M. Looi, Mahmood Seman, C. Khalik, and A. Wood, "Differentiation of elemental composition of normal and malignant breast tissue by instrumental neutron activation analysis," Appl. Radiat. Isot. **44**, 511–516 (1993).
[6]S. Rizk and H. Sky-Peck, "Comparison between concentrations of trace elements in normal and neoplastic human breast tissue," Cancer Res. **44**, 5390–5394 (1984).
[7]N. Mussalo-Rauhamaa *et al.*, "Cu, Zn, Se, and Mg concentrations in breast fat of Finnish breast cancer patients and healthy controls," Trace Elements in Medicine **10**, 13–15 (1993).
[8]A. Garg *et al.*, "An elemental correlation study in cancerous and normal breast tissue with successive clinical stages by neutron activation analysis," Biol. Trace Elem. Res. **46**, 185–202 (1994).
[9]M. Yaman *et al.*, "Comparison of trace metal concentrations in malign and benign human prostate," J. Med. Chem. **48**, 630–634 (2005).
[10]E. Andrasi *et al.*, "Concentration of elements in human brain: glioblastoma multiforme," Sci. Total Environ. **139–140**, 399–402 (1993).
[11]K. Geraki, M. J. Farquharson, and D. A. Bradley, "X-ray fluorescence and energy dispersive x-ray diffraction for the quantification of elemental concentrations in breast tissue," Phys. Med. Biol. **49**, 99–110 (2004).
[12]K. H. Ng, D. A. Bradley, and L. M. Looi, "Elevated trace element concentrations in malignant breast tissues," Br. J. Radiol. **70**, 375–382 (1997).
[13]B. Sansoni and V. Iyengar, "Sampling and Sample Preparation Methods for the Analysis of Trace Elements in Biological Materials," Jül-Spez-13, Report KFA Jülich, ISSN 0343-7639 (1978).
[14]CERN. *Geant4*. [cited, Available from: wwwinfo.cern.ch/asd/geant4/geant4.html.
[15]J. E. Bender *et al.*, "The effect of detector resolution for quantitative analysis of neutron stimulated emission computed tomography," in *Proceedings of SPIE Medical Imaging 2006: Physics of Medical Imaging* (SPIE, 2006), Vol. 6142, pp. 1597–1605.
[16]Cross Section Evaluation Working Group, ENDEIB-VI Summary Documentation, Report BNL-NCS-17541 (ENDF-201), edited by P. F. Rose, National Nuclear Data Center, Brookhaven National Laboratory, Upton, New York (1991).
[17]G. Ullman *et al.*, "Implementation of pathologies in the Monte Carlo model in chest and breast imaging," Report 94 (ISSN 11-2-1799, 2003).
[18]C. E. Metz, *ROC analysis software*—ROCKIT. [cited, available from: http://www.radiology.uchicago.edu/krl/KRL_ROC/software_index.htm.
[19]C. E. Metz, B. A. Herman, and J. H. Shen, "Maximum likelihood estimation of receiver operating characteristic (ROC) curves from continuously distributed data," Stat. Med. **17**, 1033–1053 (1998).
[20]J. E. Turner, *Atoms, Radiation, and Radiation Protection*, 2nd ed. (John Wiley & Sons, Inc., New York, 1995).
[21]International Commission on Radiological Protection, *1990 Recommendations of the International Commission on Radiological Protection*, ICRP Publication 60 (Pergamon Press, Oxford, 1991).
[22]J. Law, "The development of mammography," Phys. Med. Biol. **51**, R155–R167 (2006).
[23]A. Kapadia, C. Floyd, C. Howell, and B. Harrawood, "Sampling Requirements for Neutron stimulated emission computed tomography," presented at RSNA, Physics (Digital Imaging, PACS) session, Chicago, Illinois, 2004 (unpublished).

# Elemental Spectrum of a Mouse Obtained via Neutron Stimulation

Amy C. Sharma[1,2], Georgia D. Tourassi[2], Anuj J. Kapadia[1,2], Alexander S. Crowell[3], Matthew R. Kiser[3], Anthony Hutcheson[3], Brian P. Harrawood[2], Calvin R. Howell[3], Carey E. Floyd, Jr.[1,2]
[1]Department of Biomedical Engineering, Duke University, Durham, NC 27708
[2]Duke Advanced Imaging Laboratories, Department of Radiology, Duke University Medical Center, Durham, NC 27705
[3]Triangle Universities Nuclear Laboratory, Department of Physics, Duke University, Durham, NC 27706

## ABSTRACT

Several studies have shown that the concentration of certain elements may be a disease indicator. We are developing a spectroscopic imaging technique, Neutron Stimulated Emission Computed Tomography (NSECT), to non-invasively measure and image elemental concentrations within the body. The region of interest is interrogated via a beam of high-energy neutrons that excite elemental nuclei through inelastic scatter. These excited nuclei then relax by emitting characteristic gamma radiation. Acquiring the gamma energy spectrum in a tomographic geometry allows reconstruction of elemental concentration images. Our previous studies have demonstrated NSECT's ability to obtain spectra and images of known elements and phantoms, as well as, initial interrogations of biological tissue. Here, we describe the results obtained from NSECT interrogation of a fixed mouse specimen. The specimen was interrogated via a 5MeV neutron beam for 9.3 hours in order to ensure reasonable counting statistics. The gamma energy spectrum was obtained using two High-Purity Germanium (HPGe) clover detectors. A background spectrum was obtained by interrogating a specimen container containing 50mL of 0.9% NaCl solution. Several elements of biological interest including $^{12}C$, $^{40}Ca$, $^{31}P$, and $^{39}K$ were identified with greater then 90% confidence. This interrogation demonstrates the feasibility of NSECT interrogation of small animals. Interrogation with a commercial neutron source that provides higher neutron flux and lower energy (~2.5MeV) neutrons would reduce scanning time and eliminate background from certain elements.

Keywords: imaging, neutrons, tomography, spectroscopy, small animal imaging, emerging technology

## 1. INTRODUCTION

Previous studies on mice and rats have found that several disease states correspond to a change in elemental concentration. In the rat brain ischemia leads to a decrease in potassium and phosphorus [1, 2] and radiation exposure leads to a decrease in levels of chlorine, iron and zinc [2]. Mice with skin tumors had increased trace element concentrations in both internal organs and the tumors [3, 4]. Additionally, a change in trace element concentration was found in the kidneys of mice with malignant ascites [5].

This link between trace element concentration and diseases has also been noted in humans. Specifically in distinguishing between malignant and benign tumors in the breast, prostate and brain [6-12].

While MRI is being explored to measure elemental concentration *in vivo*, it has limitations on the amount and type of elements it can detect [13-16]. Other methods of measuring elemental concentration are invasive and not compatible with *in vivo* methods [1, 9, 17-20].

We are developing a new method, Neutron Stimulated Emission Computed Tomography (NSECT), to measure and image trace element concentrations *in vivo*. With this method, the body is interrogated with a beam of high energy (3-5 MeV) neutrons. When these neutrons scatter inelastically off of elemental nuclei within the body, the nuclei become excited and relax through characteristic gamma emission. Acquiring the gamma spectrum in a tomographic manner allows for reconstruction of elemental composition images [21].

Our previous studies have focused on NSECT's ability to obtain spectra and images from known elements and phantoms [21-23]. The purpose of this study was to acquire a spectrum from a fixed mouse specimen. The specimen was interrogated for a long period (over nine hours) of time in order to obtain enough counts to identify elements with a certain level of confidence.

## 2. METHODS

A mouse specimen was obtained from the Duke Center for In-Vivo Microscopy (CIVM) that had been fixed in a gadolinium / formalin mixture and then placed in a 50mL specimen tube. To allow for a background measurement, we obtained a similar tube filled with 50mL of 0.9% NaCl solution.

A pulsed 5MeV neutron beam was generated at Triangle Universities Nuclear Laboratory and the specimen tubes place lengthwise in the beam (see Figure 1). In order normalize the data by the incident neutron flux, a neutron monitor was placed in the beam in front of the sample. To measure the resultant gamma radiation, two high-purity germanium (HPGe) clover detectors were placed at 135° and 105° relative to the beam line. For a more detailed description of the typical NSECT interrogation setup please see [21].

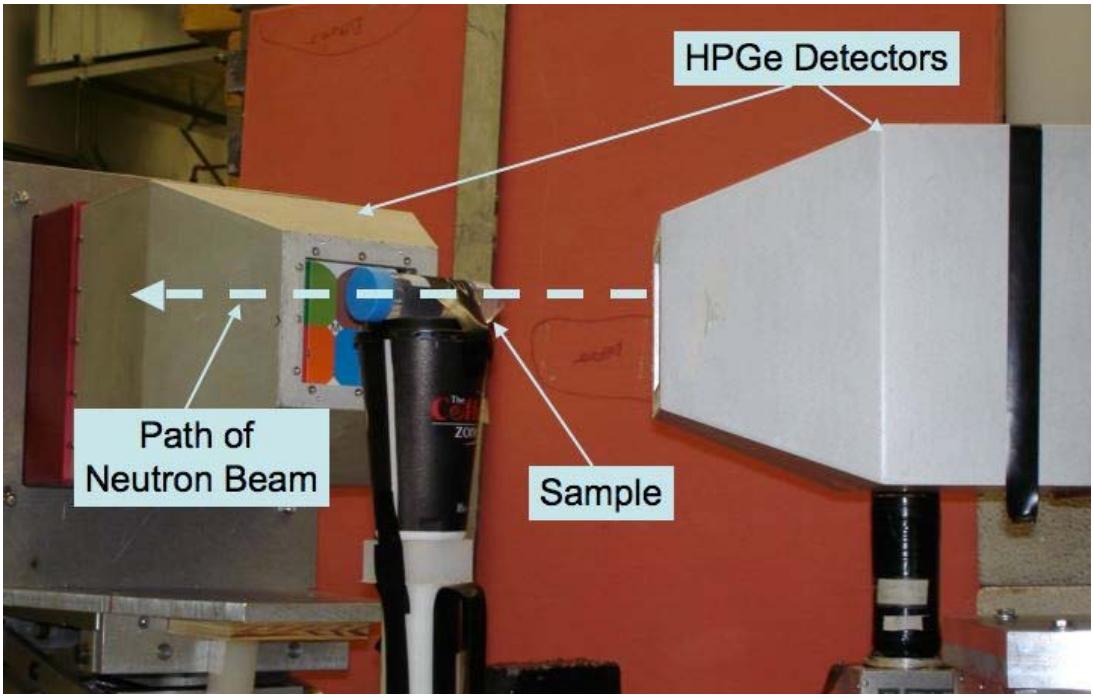


Figure 1: Photo of mouse interrogation setup. Pictured: the sample container (the background saline sample), both HPGe detectors. The sample container is oriented to maximize the amount of sample in the neutron beam.

The mouse specimen was interrogated for a total of 9 hours and 19 minutes (2,228,758 total neutrons in monitor). The saline tube was interrogated for a total of 4 hours and 58 min (966, 939 neutrons) and an empty room measurement was taken for 43 min (132,844 neutrons). The gamma spectral data acquired included the number of counts obtained at each energy level (between 0-3500 keV) segmented into time bins over the length of the neutron pulse sequence; therefore, each spectrum contains foreground (beam on) data and background (beam off).

The spectral data was analyzed as follows. First, the time binned data was used to create a time-of-flight (TOF) corrected spectrum for each the mouse, saline and empty room data by subtracting the beam-on from the beam-off data. Second, the empty room and saline data set were then normalized by the number of incident neutrons and multiplied by the number of mouse incident neutrons to allow for comparison of the spectrums. Third, two mouse spectrums were

created. One by subtracting out the TOF corrected saline data and one by subtracting out the TOF corrected empty room data. For further information on our background correction techniques please see [22].

Finally, true peaks were identified by calculating the difference between the foreground (mouse TOF corrected spectrum) and background (empty room or saline TOF corrected spectrum) in terms of error (*D* below).

$$D = \frac{FG - BG}{\sqrt{FG + BG}}$$

If *D* was above 20 for the empty room corrected mouse spectra and above 1.6 for the saline correct mouse spectra, the peak at the gamma energy bin was considered a significant true peak. A *D* value of 1.6 gives a confidence interval (calculated using the ERF error function) of 90% that the peak is actually a peak and not just noise. A larger *D* value was chosen for the empty room corrected spectrum because the empty room data was collected from approximately $1/15^{th}$ of the neutron flux of the mouse spectra. Thus, a large error is introduced when the empty room spectrum is normalized and therefore, the difference between the foreground counts (TOF corrected mouse spectrum) and background counts (TOF corrected empty room spectrum) must be much larger in order for the peak to be considered significant. The gamma energy peaks were then matched to elements by searching the NuDat database from National Nuclear Data Center (NNDC) at Brookhaven National Labs [24].

## 3. RESULTS

Many peaks corresponding to biologically significant elements were identified within the mouse spectrum. Figures 2, 3, 4, and 5 depict both the saline and empty room corrected mouse spectrum at different energy levels (it has been broken out for simplification of viewing).

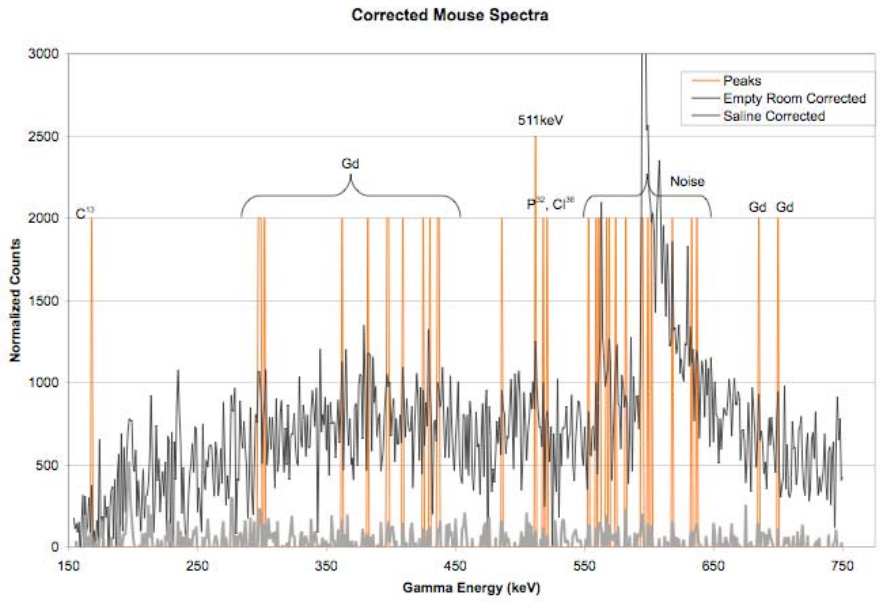


Figure 2. Spectra from the mouse specimen from 0-750 keV. The thin black line is the empty room corrected spectrum while the thick gray line is the saline corrected spectrum. Significant peaks are highlighted. "Noise" corresponds to known spectral noise associated with the neutron interrogation setup.

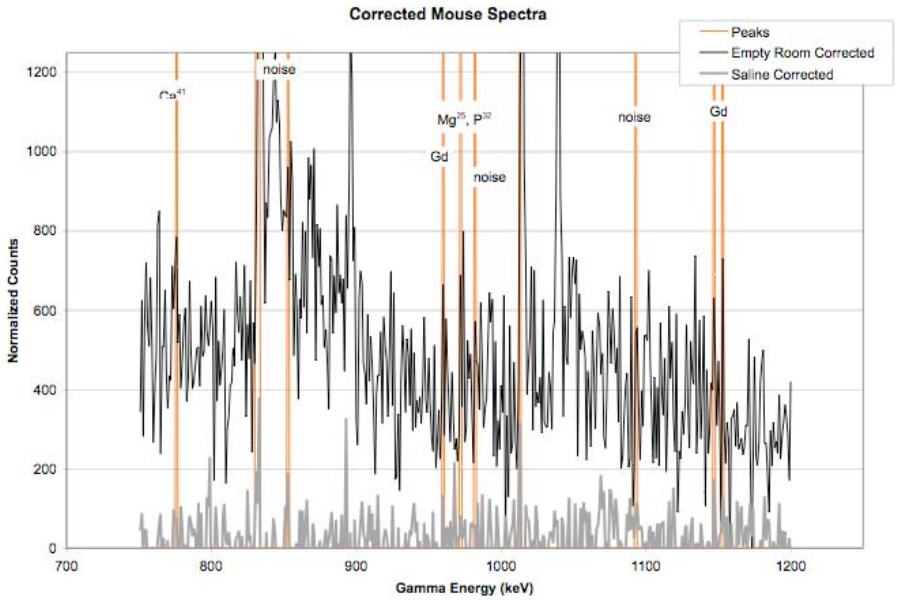


Figure 3. Spectra from the mouse specimen from 750-1200 keV. Significant peaks are highlighted.

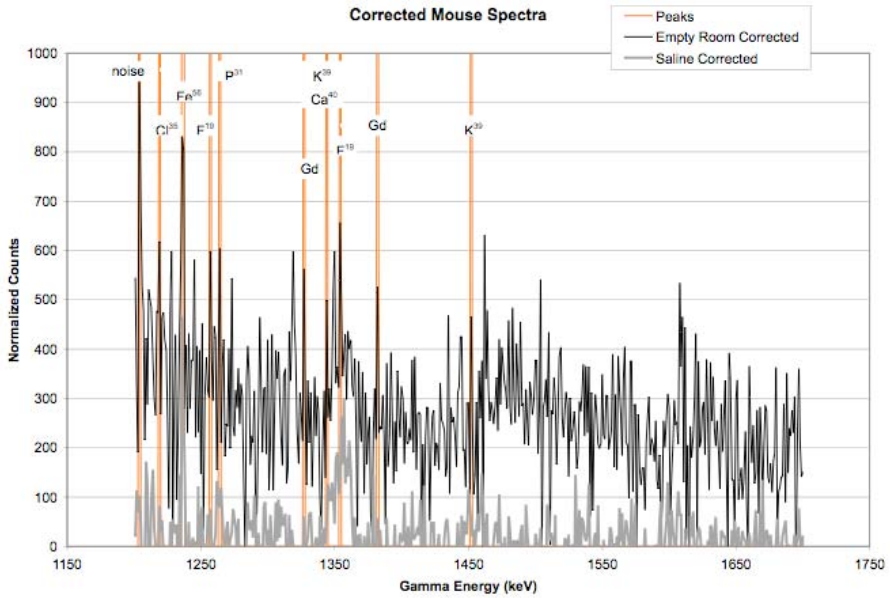


Figure 4. Spectra from the mouse specimen from 1200-1700 keV. Significant peaks are highlighted.

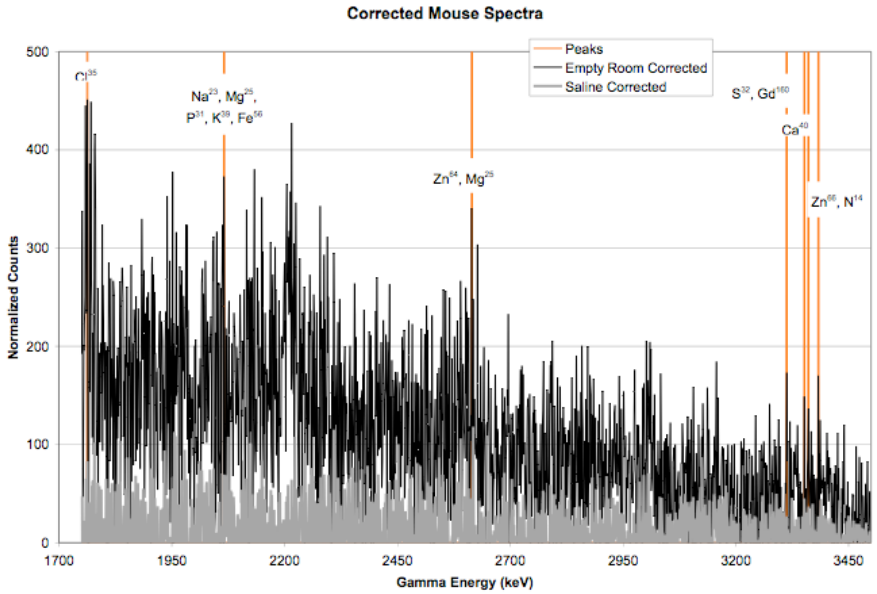


Figure 5. Spectra from the mouse specimen from 0-750 keV. Significant peaks are highlighted. Note how the number of counts has decreased significantly from Figure 2. As the gamma energy increases, the detectibility decreases.

Table 1 below lists the elemental composition of a human by percent. One can infer that the elemental breakdown of a mouse would be similar. Beside each is listed the energy peaks identified within the spectra that correspond to each element. Several peaks could correspond to more then one element, and those energy peaks are labeled with a letter. Also, sometimes the elemental nuclei react with the incident neutron in ways other then inelastic scatter. These reactions temporarily create unstable isotopes and their gamma de-excitation can also be detected; these peaks are also identified.

Table 1: Energy peaks corresponding to elements of biological interest.

| Element | % comp | Gamma Energy Levels Detected (keV) |
|---|---|---|
| Oxygen$^{16}$ | 61.4% | Oxygen's first excitation level is above the limit for a 5MeV incident neutron |
| Carbon$^{12}$ | 22.8% | $C^{13}$ – 169 and 2066$^{C}$ (double escape from 3089) |
| Hydrogen$^{1}$ | 10.0% | Does not excite |
| Nitrogen$^{14}$ | 2.57% | 3383$^{A}$ (both a peak and a single escape from 3890) |
| Calcium$^{40}$ | 1.42% | 1344$^{B}$, 3361 $Ca^{41}$ – 776 |
| Phosphorus$^{31}$ | 1.11% | 1264, 2066$^{C}$ $P^{32}$ – 520$^{D}$, 972$^{E}$ |
| Potassium$^{39}$ | 0.20% | 1344$^{B}$, 1452, 2066$^{C}$ $Cl^{36}$ – 520$^{D}$ |
| Sulfer$^{32}$ | 0.20% | 3313 |
| Sodium$^{23}$ | 0.14% | 2066$^{C}$ |
| Chlorine$^{35}$ | 0.13% | 1219, 1763 $P^{32}$ – 520$^{D}$, 972$^{E}$ |
| Magnesium$^{25}$ | 0.027% | 972$^{E}$, 2066$^{C}$, 2615 |
| Iron$^{56}$ | 0.006% | 1238, 2066$^{C}$ |
| Flourine$^{19}$ | 0.004% | 1257, 1354 |
| Zinc$^{64,66}$ | 0.003% | 2615, 3383$^{A}$ |

Along with the biologically relevant elements, gadolinium was seen in many places within the spectra. This was expected because of the specimen had been perfused with gadolinium.

## 4. DISCUSSION

Many elements of biological interest were detected via the NSECT interrogation process. These are encouraging results because in order for NSECT to provide biologically and clinically relevant information, it is necessary for it to be able to detect trace amounts of these elements.

A typical mouse weighs approximately 25g. That would mean that much less then 1g of most trace elements would be present in the mouse. It is very encouraging that several peaks corresponding to trace elements were detected. To confirm these results, the mouse has been sent away for NAA analysis, which is the gold standard spectral analysis method.

The experiment pointed out several areas that must be improved in NSECT. The first is the lack of a simple way to unwrap the gamma energy spectrum. There are many possible elements that emit a certain gamma radiation. This list of possible matches can be easily narrowed down, as most of the elements that correspond to a certain gamma energy are rare or uncommon. But, this can introduce errors into the element identification process. By interrogating the sample for a long period of time, it is now possible to say our level of confidence in each energy peak detected, but it is still difficult to attach a level of confidence to the certainly a peak corresponds to a specific element.

The second problem is the overlap of some gamma energy states. This is overcome because most elements produce several characteristic gammas, and the appearance of several energy peaks that correspond to one element increases the probability of determining that element is actually present within the sample.

Third, relevant peaks are sometimes removed when the background is subtracted out. For example, sodium will be hard to detect when a saline solution is used as a background sample. Also, several peaks from iron correspond closely to germanium peaks, and thus must be ignored because the gamma detectors are comprised of germanium.

To correct these uncertainties, it would be desirable to interrogate a small pure sample of each element of interest and determine which gamma energy peaks rise above the background noise. Unfortunately, this experiment would require an enormous amount of neutron beam time, and cannot be achieved in a simulation environment.

Using a neutron source that provides higher neutron flux and lower energy neutrons (~2.5MeV is available in most commercial sources) would provide the means to complete the experiment proposed above, as well as, reduce scanning time and eliminate background in two ways. First, an element will not excite unless the incident neutron is of greater energy then its first excitation level. Carbon has a high first energy level, and only serves to clutter the spectrum as finding that a biological sample contains carbon will provide little clinical information. Eliminating these peaks would reduce noise from the spectra and help to focus on trace elements. Second, background counts increase in a linear fashion, so the longer the scan time, the more background counts that are acquired. But, with a high neutron flux, true gamma energy peaks would accrue counts at a much faster rate then background peaks; thereby, both reducing the scanning time and the background counts.

## 5. CONCLUSION

The spectrum obtained from the mouse specimen is quite noisy and it is a complicated process to parse information out of it. Still, this experiment is a positive first step in determining the biological relevance of NSECT imaging. Many elements of biological interest were detected with a high level of certainly. While this experiment highlighted challenges for NSECT to overcome, it also provided positive proof of concept that NSECT has the potential to be a viable technique for nondestructive, *in vivo*, spectral imaging and analysis of biological tissue.

## ACKNOWLEDGEMENTS

The authors would like to thank the Center for In Vivo Microscopy (CIVM), Duke University (esp. Dr. G. Allan Johnson, Dr. Laurence Hedlund and Boma Fubara) for their generous donation of a fixed mouse and sample containers. We also wish to thank everyone at Triangle Universities Nuclear Laboratory for their time and help.

This work was supported in part by NIH/NCI grant no. 1-R21-CA106873-01 and NIH Training grant no. 1-T32-EB001040.

## REFERENCES


1. Takahashi, S., Hatashita, S., Taba, Y., Sun, X.Z., Kubota, Y., Yoshida, S., *Determination of the spatial distribution of major elements in the rat brain with X-ray fluorescence analysis.* J. Neurosci. Meth., 2000. **100**: p. 53-63.
2. Takahashi, S., Sun, X.Z., Kubota, Y., Takai, N., Nojima, K., *Histological and elemental changes in rat brain after local irradiation with carbon ion beams.* J. Radiat. Res., 2002. **43**: p. 143-152.
3. Gulati, N., Mangal, P.C., *Trace element profiles in skin-tumor and tissues of tumour-bearing mice.* Indian J. Cancer, 1985. **22**: p. 308-314.
4. Mangal, P.C., Verma, K.B., *Effect of induced skin cancer on the concentrations of some trace elements in the mouse.* Indian J. Med. Res., 1979. **69**: p. 290-295.
5. Wei, Y.Y., Chung, C., *Analysis of experimental absorption and excretion in mice bearing malignant ascites* Biol. Trace Elem. Res., 1994. **43-45**: p. 397-403.
6. Andrasi, E., Suhajda, M., Saray, I., Bezur, L., Ernyei, L., Reffy, A. , *Concentration of elements in human brain: glioblastoma multiforme.* Sci. Total Env., 1993. **139/140**: p. 399-402.
7. Danielsen, A., Steinnes, E., *A study of some selected trace elements in normal and cancerous tissue by neutron activation analysis.* J. Nuclear Med., 1970. **11**(6): p. 260-264.
8. Garg, A.N., Weginwar, R.G., Chutke, N.L. , *Radiochemical neutron activation analysis of Fe, Co, Zn, Sb, and Se in biomedical and environmental samples.* Sci. Total Env. , 1993. **139/140**: p. 421-430.
9. Geraki, K., Farquharson, M.J., Bradley, D.A. , *X-ray fluorescence and energy dispersive x-ray diffraction for the quantification of elemental concentrations in breast tissue.* Phys. Med. Biol., 2004. **49**: p. 99-110.
10. Ng, K.H., Bradley, D.A., Looi, L.M., Seman Mahmood, C., Khalik Wood, A., *Differentiation of elemental composition of normal and malignant breast tissue by instrumental neutron activation analysis.* Appl. Radiat. Isot., 1993. **44**(3): p. 511-516.
11. Ng, K.H., Bradley, D.A., Looi, L.M. , *Elevated trace element concentrations in malignant breast tissues.* British J. Rad., 1997. **70**: p. 375-382.
12. Yaman, M., Atici, D., Bakirdere, S., Akdeniz, I. , *Comparison of Trace Metal Concentration in malign and Benign Human Prostate.* J. Med. Chem., 2005. **48**: p. 630-634.
13. Alustiza, J., Artexe, J, Castiella, A, Agirre, C, Emparanza, JI, Otazua, P, Garcia-Bengoechea, M, Barrio, J, Mujica, F, Recondo, JA, *MR quantification of Hepatic Iron Concentration.* Radiology, 2004. **230**: p. 479-484.
14. Angelucci, E., Giovagnoi, A, Valeri, G, Paci, E, Ripalti, M, Miretto, P, McLaren, C, Brittenham, GM, Lucarelli, G, *Limitations of Magnetic Resonance Imaging in Measurement of Hepatic Iron.* Blood, 1997. **90**(12): p. 4736-4742.
15. Bonkovsky, H., Rubin, RB, Cable, EE, Davidoff, A, Pels Rijcken, TH, Stark, DD, *Hepatic Iron Concentration: Noninvasive Estimatin by Means of MR Imaging Techniques.* Radiology, 1999. **212**: p. 227-234.
16. Wood, J., Wnriquez, C, Ghuge, N, Tyzka, JM, Carson, S, Nelson, MD, Coates, TD, *MRI R2 and R2* mapping accurately estimates hepatic iron concentration in transfusion-dependent thalassemia and sickle cell disease patients.* Blood, 2005. **106**(4): p. 1460-1465.
17. Cesareo, R., Viezzoli, G., *Trace element analysis in biological samples by using XRF spectrometry with secondary radiation.* Phys. Med. Biol., 1983. **28**(11): p. 1209-1218.
18. Stedman, J.D., Spyrou, N.M., *Major and trace element concentration differences between right and left hemispheres of the 'normal' human brain.* Nutrition, 1995. **11**(5): p. 542-545.
19. Ward, N.I., Abou-Shakra, F.R., Durrant, S.F., *Trace elemental content of biological materials: a comparison of NAA and ICP-MS analysis.* Biol. Trace Elem. Res., 1989. **26-27**: p. 177-187.
20. Zeisler, R., Ostapczuk, P., Stone, S.F., Stoeppler, M., *Effective tools for trace element characterization of tissue: neutron activation analysis and voltammetry.* Sci. Total Env., 1993. **139/140**: p. 403-410.
21. Floyd, C., Bender, JE, Sharma, AC, Kapadia, AJ, Xia, JQ, Harrawood, BP, Tourassi, GD, Lo, JY, Crowell, AS, Howell, CR. , *Introduction to Neutron Stimulated Emission Computed Tomography.* Phys Med Biol, 2006. **51**: p. 3375-3390.

22. Floyd, C., Bender, JE, Sharma, AC, Kapadia, AJ, Xia, JQ, Harrawood, BP, Tourassi, GD, Lo, JY, Crowell, AS, Howell, CR. , *Neutron Stimulated Emission Computed Tomography: Background Corrections*. Nuc. Inst. and Meth. B, 2005. **(accepted Nov 2006)**.
23. Floyd, C., Bender, JE, Sharma, AC, Kapadia, AJ, Xia, J, Harrawood, BP, Tourassi, GD, Lo, JY, Crowell, A, Howell, CR. , *Neutron Stimulated Emission Computed Tomography of a Multi-Element Phantom.* IEEE TMI, 2006. **(submitted Sept 2006)**.
24. National Nuclear Data Center, B.N.L. *NuDat Database*. 2006 [cited 2006; Available from: http://www.nndc.bnl.gov/nudat2/.

# GEANT4 Simulation of an NSECT System for Iron Overload Detection

Anuj J. Kapadia, Amy C. Sharma, Brian P. Harrawood, Georgia D. Tourassi

*Abstract*– **Hemochromatosis (iron overload in liver) is a condition that causes serious consequences for the patient through an increase in the body's iron stores. Diagnosis of the excess iron, which is often stored in the liver, requires an invasive biopsy. We are developing neutron stimulated emission computed tomography (NSECT) as a non-invasive alternative to measure liver iron concentration to diagnose hemochromatosis. This measurement is performed using an incident neutron beam that scatters inelastically with iron nuclei in the liver, causing them to emit characteristic gamma-rays. An energy-sensitive gamma-ray detector is used to detect these gamma-rays and quantify the iron in the liver. Preliminary experiments have demonstrated an implementation of NSECT to quantify concentrations of iron and potassium in bovine liver tissue. Due to the prohibitive nature of these experiments, it is not feasible to perform system evaluation and optimization at each step using a nuclear accelerator. Here we describe a GEANT4 simulation of NSECT as a feasible alternative to perform system evaluation for iron overload diagnosis using computing resources only. The simulation model uses a 5 MeV neutron beam to scan a human liver phantom with induced iron overload. The liver is modeled as a composite shape combining a half-cylinder and a polyhedron, and is housed in a human torso filled with water. Gamma-ray spectra are generated to show element concentration within the liver. To determine the lower limit of iron overload detection, the concentration of iron in the liver is reduced from an initial high value, and the p-value of detecting peaks corresponding to iron is calculated at each step. The lower limit of detection is defined as the concentration at which the p-value of peak detection exceeds 0.05. The limit of iron overload detection from this simulation was found to be 4 mg/g, which represents a clinically relevant value for iron overload.**

## I. Introduction

HEMOCHROMATOSIS (liver iron overload) is a condition that causes serious consequences for the patient through an increase in the body's iron stores. The excess iron, which is often stored in the liver, can cause extensive tissue damage, liver cirrhosis, cardiac failure, hepatic failure and hepatocellular carcinoma [1]. Diagnosis of iron overload requires an invasive biopsy [2], which is an unpleasant procedure with several associated complications including death. Neutron stimulated emission computed tomography (NSECT) is being developed as a non-invasive alternative to measure element concentration in the liver to diagnose liver iron overload [3-5]. Preliminary experiments have demonstrated NSECT's potential in quantifying concentrations of iron and potassium in bovine liver tissue [4, 5]. The basic principle of NSECT is as follows: An incident neutron that scatters inelastically with a target atomic nucleus excites the nucleus to a higher energy state. The unstable nucleus then rapidly decays to its ground state, emitting the excess energy as a characteristic gamma-ray. The energy of the emitted photon can be measured by an energy-sensitive gamma-ray detector to identify the atom. This project aims at developing a Monte-Carlo simulation of the NSECT system to investigate NSECT's ability to detect hemochromatosis.

## II. Motivation

Experimental investigation of NSECT's detection sensitivity is difficult due to the prohibitive nature of the experiments. Each laboratory experiment requires 7 days of beam time per sample from an accelerator source that is in high demand by a large number of research groups. A simulation environment will allow development and evaluation to continue without access to the nuclear accelerator source. This project aims at determining the limit of detection sensitivity in determining iron overload in the human liver.

## III. Method

NSECT experiments are performed in the Triangle Universities Nuclear Laboratory at Duke University. A 5 MeV collimated neutron beam is used to scan a target liver sample (usually bovine liver for quantification experiments). The gamma-ray photons emitted by the liver sample are counted by two high purity germanium (HPGe) clover detectors hooked up to a data acquisition system. Data is acquired by illuminating the sample with the beam and counting until sufficient gamma events have been acquired to quantify the element with a p-value $\leq 0.05$. The system has been described in detail elsewhere [3, 6]. A simulation of this setup was implemented in GEANT4 as described below.

GEANT4 is an object-oriented Monte-Carlo programming package that allows modeling of particle interactions with matter over a wide range of energies (meV to GeV) [7]. The simulated model consists of 3 parts – (a) Neutron Source, (b)

Manuscript received November 16, 2007. This work was supported by the Department of Defense (Breast Cancer Research Program) under award number W81XWH-06-1-0484

A. J. Kapadia is with the Department of Biomedical Engineering and the Duke Advanced Imaging Laboratories (DAILabs) of the Department of Radiology, Duke University, Durham, NC 27710, USA (phone: 919-684-1442; fax: 919-684-1491; email: anuj.kapadia@duke.edu).

A.C. Sharma is with the Department of Biomedical Engineering and the DAILabs of the Department of Radiology, Duke University, Durham, NC 27710, USA (phone: 919-684-1471; fax: 919-684-1491; email: anc4@duke.edu).

B.P. Harrawood is with the DAILabs of the Department of Radiology, Duke University, Durham, NC 27710, USA (phone: 919-684-7782; fax: 919-684-1491; email: brian.harrawood@ duke.edu).

G.D. Tourassi is with the DAILabs of the Department of Radiology, Duke University, Durham, NC 27710, USA (phone: 919-684-1447; fax: 919-684-1491; email: gt@deckard.duhs.duke.edu).

Gamma-ray Detectors, and (c) Liver phantom. Each part has been designed as a separate GEANT4 object to facilitate modifying individual parameters on one object independently of the others. Fig 1 shows a complete simulation built by combining each of these components.

### A. Neutron Source

The neutron source was created by defining a 'GEANT4 Particle Gun', set to emit 5 MeV neutrons. The gun was placed at the left edge of the world so that every particle exiting the gun entered directly into the world, forming a neutron beam that illuminated the target phantom. The neutron beam was given a 1.6 cm width, similar to that used in the physical experiment.

### B. Gamma-ray Detectors

Two gamma-ray detectors were created as solid cylinders with user-defined diameter and height, filled with high-purity germanium (Ge density= 5.32 g/cm3). Detector dimensions for each detector crystal were set to 10 cm diameter and 9 cm height, modeled after each crystal of the clover detectors used in the physical experiment. Four such detector crystals were combined to form one complete clover detector. The detector was sensitized to track particle interactions and record the energy deposited at each interaction, and placed at a backward angle of 135 degrees in the beam plane, mimicking the position of the detector in the physical experiment where a backward angle is used to minimize damage to the detector from forward scattered neutrons. Detector efficiency was modeled by collecting information from all events occurring in the detector and then retaining only a required fraction of these events. For example, for a 60% efficient HPGe detector, 100% of events were recorded, but only 60% of these were used to generate spectral results.

### C. Liver Phantom

The liver phantom was made up of two parts - a human torso and a liver phantom housed in the torso. The torso was modeled as an elliptical tube with axes 30 cm x 25 cm, and 11 cm height. The torso phantom was filled with water, to simulate the presence of noise-generating tissue in the human torso. The liver was modeled as a combination of an elliptical tube and a hemisphere to form a complex shape, partially shown in Fig 1. This liver was then placed inside the torso. The composition of the liver was obtained from ICRU report 46 [8] as reported for a healthy human adult, and is shown in Table 1. To simulate iron overload in the liver, the concentration of iron was changed in steps from the initial value of 0 to 25.0 mg/g (approximately 5 times the concentration of clinical hemochromatosis) as shown in table 2. Gamma spectra were generated for each overloaded liver sample, and counts for energies corresponding to iron were identified and summed. A background noise sample was generated by substituting the liver with water and repeating the scan with the same number of neutron counts as used for the liver. The p-value of detecting peaks for iron was calculated using the t-test to compare counts at energies corresponding to iron with the counts from the water background. The lower limit of detection was defined as the concentration at which the p-value exceeded 0.05.

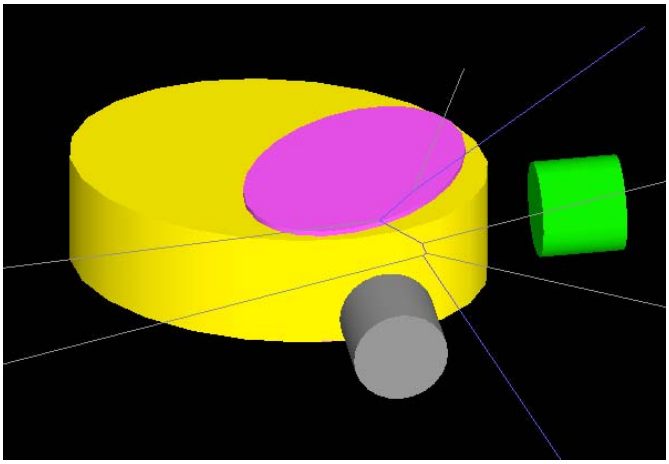

Fig.1. GEANT4 simulation of the NSECT experiment showing the liver (pink) inside an elliptical torso (yellow). Gamma detectors are shown in green and gray. Incident neutrons are shown in blue and scattered particles in gray.

TABLE I
ELEMENTAL COMPOSITION OF THE LIVER PHANTOM (OBTAINED FROM ICRU REPORT 46 [8]).

| Element | Normal (%) |
|---|---|
| O | 71.6 |
| C | 13.9 |
| H | 10.2 |
| N | 0.3 |
| P | 0.3 |
| S | 0.3 |
| K | 0.3 |
| Cl | 0.2 |
| Na | 0.2 |
| Fe | 0.0 |
| Density | 1.06 g/cm3 |

## IV. RESULTS

Figs. 2, 3 and 4 show the simulated spectrum from the iron overload liver phantom with 25 mg/g, 10 mg/g and 3 mg/g Fe concentration. Energy peaks for $^{56}$Fe are observed at 847 keV. Peaks are also seen at energies corresponding to several states in Ge (from the HPGe gamma detectors) and $^{1}$H from neutron capture on hydrogen in water (2.22 MeV).

In figs. 2 and 3, the $^{56}$Fe peak at 847 keV can be seen clearly above the underlying background as the iron concentration in these phantoms is high ( > 10 mg/g). However in fig. 4, the peak corresponding to lower iron concentration (3 mg/g) is not clearly observed above the underlying background.

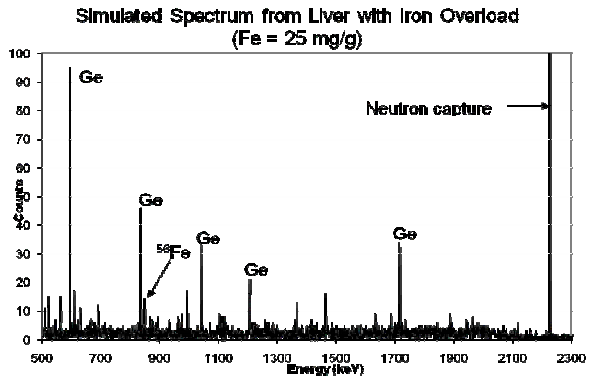


Fig.2. Spectrum corresponding to an iron overloaded liver phantom with 25 mg/g Fe. Peaks are identified for $^{56}$Fe, Ge from the detector, and $^{1}$H from water in the torso.

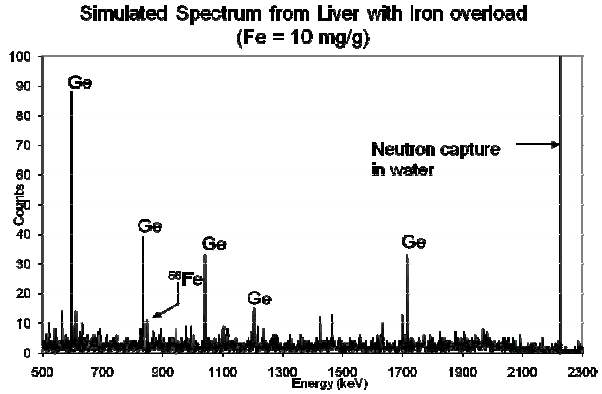


Fig.3. Spectrum corresponding to an iron overloaded liver phantom with 10 mg/g Fe. The peak from $^{56}$Fe can be detected above background with $p \leq 0.05$.

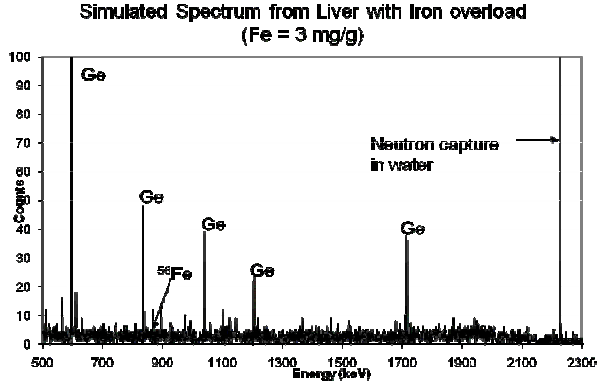


Fig.4. Spectrum corresponding to an iron overloaded liver phantom with 3 mg/g Fe. The peak from $^{56}$Fe cannot be detected above background with $p \leq 0.05$.

Table 2 shows the simulated measurement results of the different iron overloaded livers scanned. The p-value of detecting peaks corresponding to iron was seen to decrease with decreasing iron concentration. The lowest concentration of iron corresponding to $p \leq 0.05$ was found to be 4 mg/g Fe. This concentration was described as the lower limit of detection for the system using the currently available configuration.

TABLE II
SIGNIFICANCE TESTING FOR FE PEAK COUNTS MEASURED IN THE SIMULATED GEANT4 SPECTRA FOR DIFFERENT IRON CONCENTRATIONS.

| Fe Conc | t | p-value |
|---|---|---|
| 25 mg/g | 4.12 | 0.001 |
| 10 mg/g | 2.40 | 0.05 |
| 5 mg/g | 2.24 | 0.05 |
| 4 mg/g | 2.06 | 0.05 |
| 3 mg/g | 1.89 | 0.1 |

## V. CONCLUSION AND FUTURE WORK

The simulation developed here presents a feasible and valid alternative to continue evaluation and optimization of NSECT without the use of a nuclear accelerator. Significance testing results demonstrate that NSECT has the potential to detect hemochromatosis in patients with iron concentration as low as 4 mg/g. As clinical iron overload is reported for iron concentrations between 1mg/g to 6 mg/g [1, 2], this value of sensitivity represents a clinically significant concentration. System sensitivity for $^{56}$Fe through experimental techniques has been determined as 6 mg/g [6], which demonstrates the validity of this preliminary simulation. While the simulation presented here accounts for the neutron scatter noise generated by the torso, there are several other sources of noise in the experimental system, such as electronic noise in detectors and scatter noise from objects in the experimental area that decrease the overall sensitivity of the system. These sources must be taken into consideration to determine the experimental detection limit for NSECT. Work is underway to model these sources of noise in the simulation.

## REFERENCES

[1] L. Powell, "Hemochromatosis," in *Harrison's Principles of Internal Medicine*, 16 ed. vol. 2, D. Kasper, Fawci, AS, Longo, DL, Braunwald, E, Hauser, SL, Jameson, JL, Ed. NY: McGraw Hill, 2005, pp. 2298-2303.

[2] L. W. Powell, "Diagnosis of hemochromatosis," *Semin Gastrointest Dis,* vol. 13, pp. 80-8, Apr 2002.

[3] C. E. Floyd, Jr., J. E. Bender, A. C. Sharma, A. Kapadia, J. Xia, B. Harrawood, G. D. Tourassi, J. Y. Lo, A. Crowell, and C. Howell, "Introduction to neutron stimulated emission computed tomography," *Phys Med Biol,* vol. 51, pp. 3375-90, Jul 21 2006.

[4] A. J. Kapadia, C. E. Floyd, J. E. Bender, C. R. Howell, A. S. Crowell, and M. R. Kiser, "Non-invasive quantification of iron 56-Fe in beef liver using neutron stimulated emission computed tomography," in *IEEE Nuclear Science Symposium, Medical Imaging Conference*, Puerto Rico, 2005, pp. 2232-2234.

[5] A. J. Kapadia, A. C. Sharma, G. D. Tourassi, J. E. Bender, A. S. Crowell, M. R. Kiser, C. R. Howell, and C. E. Floyd, "Non-Invasive Estimation of Potassium (39K) in Bovine Liver Using Neutron Stimulated Emission Computed Tomography (NSECT)," in *IEEE Nuclear Science Symposium, Medical Imaging Conference*, San Diego, CA, 2006, pp. 2076-2078.

[6] A. J. Kapadia, A. C. Sharma, J. E. Bender, G. D. Tourassi, C. R. Howell, A. S. Crowell, M. R. Kiser, B. P. Harrawood, and C. E. Floyd, "Neutron Stimulated Emission Computed Tomography for Diagnosis of Breast Cancer," *IEEE Trans Nuc Sci (in press),* 2007.

[7] V. N. Ivanchenko, "Geant4 toolkit for simulation of HEP experiments," *Nuclear Instruments and Methods in Physics Research Section A,* vol. 502, pp. 666-668, 2003.

[8] ICRU, "Photon, electron, proton and neutron interaction data for body tissues.," International Commission on Radiation Units and Measurements, Bethesda, MD, 46, 1992.

# Optimization of a Rotating Modulation Collimator for Neutron Stimulated Emission Computed Tomography (NSECT) Imaging

Amy C. Sharma, *Student Member, IEEE*, Anuj J. Kapadia, *Member, IEEE*, Brian P. Harrawood, Georgia D. Tourassi, *Member, IEEE*

***Abstract*– A high-energy gamma camera design is being developed for use with Neutron Simulated Emission Computed Tomography (NSECT). NSECT is a spectroscopic imaging technique that measures elemental concentrations in vivo through neutron interrogation and collection of the subsequent prompt characteristic gamma emission. NSECT operates in an energy range above that of typical nuclear medicine gamma cameras (0.3 – 2 MeV), and requires high-resolution gamma spectroscopy. We are developing a camera using a rotating modulation collimator (RMC) placed in front of a High Purity Germanium (HPGe) detector. The RMC consists of a pair of parallel slat collimators rotating in unison and as it rotates it modulates the number of incident gammas. Counting the number of incident gammas at each angle provides spatial information and allows reconstruction of images. There are six parameters in the camera system that can be optimized to improve image quality. A preliminary experiment was performed to determine the six parameters' relationship to each other and to image quality. Four subsequent experiments were performed based on the preliminary data to optimize the camera configuration. Results of these experiments found a tradeoff between system efficiency and spatial resolution, much like that for high-energy gamma collimation for standard gamma cameras. Point source reconstructions are provided to illustrate this tradeoff.**

## I. Introduction

Neutron Stimulated Emission Computed Tomography (NSECT) is a non-invasive, *in vivo* spectroscopic imaging method. The body is interrogated with neutrons that scatter inelastically off of elemental nuclei, exciting the nuclei and causing prompt characteristic gamma emission. Collecting the emitted gamma spectrum allows identification of elemental concentration within the body of interest. The link between elemental concentration and certain disease states has been established previously by interrogation methods that are not compatible with *in vivo* study [1-4].

We are currently developing a high energy gamma camera for use with NSECT imaging. NSECT requires high energy resolution in the range of 0.3 – 2 MeV. Spectral information is provided by High Purity Germanium (HPGe) detectors. These detectors provide superior energy resolution [5] but no spatial information due to their large crystal size (3.5 cm radius). To facilitate imaging, we are modifying space-based gamma imaging technology. This camera consists of a pair of parallel slat collimators rotating in unison (referred to as a rotating modulation collimator or RMC), placed in front of an HPGe [6-8]. As the RMC rotates it modulates the incident gammas. Counting the number of incident gammas at each rotation angle results in an observation profile. For a point source in space, the observation profile is unique to that source's location and referred to as a modulation profile. A set of estimated modulation profiles from each pixel in the imaging plane forms a probability matrix. Our previous studies have found that using the probability matrix and observation profile, images can be reconstructed successfully. Additionally, the modulation profile is a single curve with the maximum value occurring at the collimator angle corresponding to the polar angle of the gamma point source. The full width at half maximum (FWHM) of the curve profile thins as the source is moved further from the axis of rotation [8].

Fig. 1 below shows a side view of the RMC system. It consists of a gamma source, the two parallel slat collimators and the HPGe detector. Our previous studies have shown that the configuration of these elements affects the shape of the individual modulation profiles [7-11]. Herein, we discuss the optimization of six parameters to produce modulation profiles that facilitate near-field imaging. A Monte Carlo simulation has been developed in GEANT4 and was used to test various camera setups [10, 12]. The following parameters were optimized (i) height (ii) collimator alignment (iii) slat material and (iv) slat height, slot width and slat width. Using these parameters sample data was simulated and images reconstructed.

Manuscript received November 16, 2007. This work was supported in part by NIH/NCI grant no 1-R21-CA106873-01; NIH Training grant no. 1-T32-EB001040; DOD Breast Cancer Research Program award no. W81XWH-06-1-0484.

A. C. Sharma is with the Department of Biomedical Engineering, and Duke Advanced Imaging Labs (DAILabs), Department of Radiology, Duke University, Durham, NC 27705 USA (telephone: 919-684-1440, e-mail: anc4@duke.edu).

A. J. Kapadia is with Duke Advanced Imaging Labs (DAILabs), Department of Radiology, Duke University, Durham, NC 27705 USA (e-mail: ajk17@duke.edu).

B. P. Harrawood is with Duke Advanced Imaging Labs (DAILabs), Department of Radiology, Duke University, Durham, NC 27705 USA (e-mail: brian.harrawood@duke.edu).

G. D. Tourassi is with Duke Advanced Imaging Labs (DAILabs), Department of Radiology, Duke University, Durham, NC 27705 USA (e-mail: gt@deckard.duhs.duke.edu).

1-4244-0923-3/07/$25.00 ©2007 IEEE.

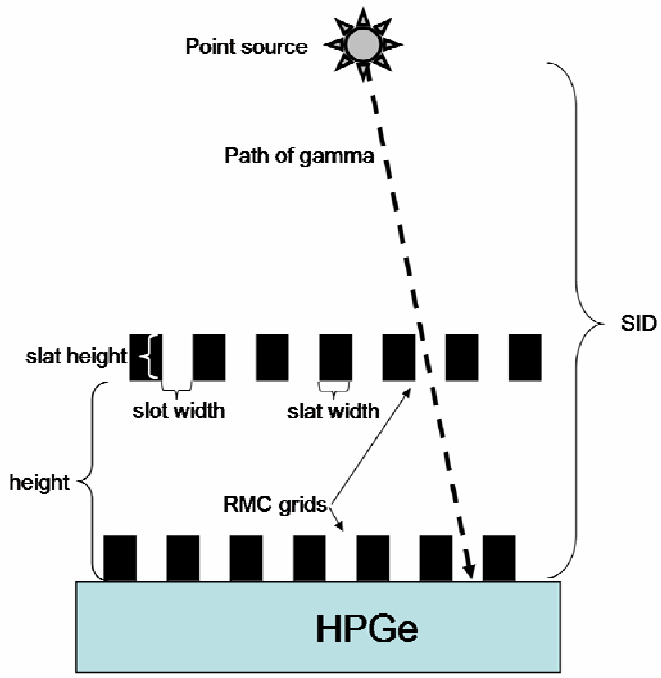


Figure 1. Side view of RMC system.

TABLE I. PROPERTIES OF POSSIBLE COLLIMATOR MATERIALS.

| *Name* | *Composition* | *Equivalent Z* | *Density ($g/cm^3$)* |
|---|---|---|---|
| Low 158 | Bismuth – 58%<br>Lead – 26.7%<br>Tin – 13.3%<br>Cadmium – 10% | 81.5 | 9.57 |
| Low 203 | Bismuth – 52.5%<br>Lead – 32%<br>Tin – 15.5% | 77.6 | 9.69 |
| Low 217-440 | Bismuth – 48%<br>Lead – 28.5%<br>Cadmium – 14.5%<br>Antimony – 9% | 74.76 | 10.13 |
| Low 255 | Bismuth – 55.5%<br>Lead – 44.5% | 82.5 | 10.43 |
| Lead | Lead – 100% | 82 | 11.34 |

## II. METHODS

### A. Height

To determine the effect of collimator separation on modulation profile behavior a GEANT4 simulation was conducted. Matched modulation profiles were obtained from 108 different RMC configurations that varied only in collimator separation (5, 10 and 20 cm). Nineteen points were obtained for each modulation profile and a set was considered matched if more then 12 points matched (one standard deviation) within the standard error (square root of the counts).

### B. Slat Alignment

A similar experiment was run to determine the effect of slat alignment on modulation profile behavior. Two hundred and ninety seven matched modulation profiles were simulated where the RMC configuration only differed in the slat alignment (with the slats aligned or offset from one another). The profiles were then matched as in the 'height' experiment.

### C. Slat Material

In order to determine an acceptable slat material four commercially available low melting point lead alloys were tested against lead. Modulation profiles were obtained from 27 matched RMC configurations that varied only in slat material. The modulation profiles were analyzed in terms of full-width at half-maximum (FWHM) and peak-to-valley (PV). A well formed modulation profile will have a low FWHM and a high PV. Table 1 lists the four alloys tested.

### D. Slat Height, Slat Width and Slot Width

Initial experiments found that there was no simple way to distinguish between the individual effects of slat height, slat width and slot width. The three parameters were assumed to be correlated and therefore had to be optimized together. Optimization was achieved by determining the effect of modulation profile shape on image quality.

The first step was to reconstruct point source images. Using the GEANT4 simulation, probability matrices were generated for a 10 pixel by 10 pixel (1 $cm^2$ pixels) field-of-view (FOV) for fifteen different RMC parameter setups. Three point source images were reconstructed for each setup. The images were given a quality score based one three things: (i) the difference between the maximum and minimum reconstructed pixel value (ii) the average point spread function in both the x and y direction and (iii) the location of the reconstructed point relative to the true image.

Second, to link the modulation profile shape to image quality, the FWHM, and maximum and minimum values of modulation profiles from three points within the imaging plane were measured for each of the 15 data sets. A series of regressions were performed in Matlab and a regression function was determined that linked profile shape to image quality.

Third, modulation profiles were simulations for three point source locations for 160 difference slat height, slat width and slot height combinations. For each the FWHM, maximum and minimum value was measured. Using the regression function an image quality score was predicted for each RMC configuration.

### E. Image Reconstruction

Once the RMC configuration had been optimized, a complete probability matrix for a 10 pixel by 10 pixel FOV

consisting of one cm square voxels was generated in GEANT4. Using this matrix, several point source images were reconstructed using the MLEM algorithm for both 500 keV and 1 MeV gamma ray energies. For more information on our current reconstruction technique please see [8].

## III. Results / Discussion

### A. Height

The number of overlapping modulation profiles between the three different collimator separations is listed in Table 2 below.

TABLE II. RESULTS OF MODULATION PROFILE COMPARISONS BETWEEN RMC CONFIGURATIONS OF DIFFERENT HEIGHTS.

| *Height Comparison* | *Number of Matching Sets* | *% total* |
|---|---|---|
| 5 to 10 | 108 | 100 |
| 5 to 20 | 97 | 89.8 |
| 10 to 20 | 97 | 89.8 |
| All 3 match | 71 | 65.7 |

While a larger number of data points overlap between two modulation profiles then all three, a majority of the grouped sets had overlapping modulation profiles. Fig. 2 is an example of two sets of grouped modulation profiles. Due to both the visual and numerical comparisons, we conclude the distance between the collimators has a minimal effect on modulation profile shape. Therefore, a collimator separation of 5 cm is chosen to allow the gamma point sources to be as close to the detector as possible.

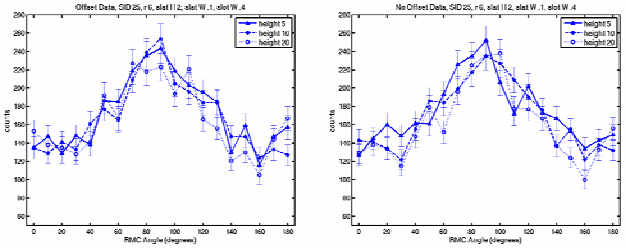

Figure 2. Modulation profiles from matching sets of RMCs that only vary in height. Pictured at left is data from RMCs with offset slats and at right is data from RMCs with aligned slats.

### B. Slat Alignment

Fig. 2 depicts modulation profiles from matching sets of RMCs. It appears that modulation profile shape is not affected by either collimator separation or slat alignment. The number of overlapping points between 297 matched RMC configurations that differed only by slat alignment was measured. Of the 297 sets, 284 (95.6%) sets matched. The alignment of the slats also does not affect modulation profile shape. Unaligned slats were chosen to mimic imperfections in RMC construction.

### C. Slat Material

Modulation profiles were generated that differed only in the slat material used. For each modulation profile the FWHM and PV were measured. Fig. 3 below shows the results.

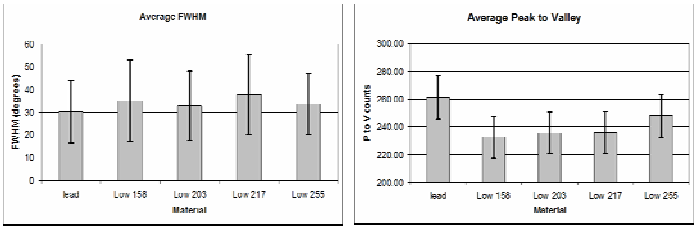


Figure 3. Average FWHM (left) and PV (right) of modulation profiles obtained from five different collimator materials.

Lead has the lowest FWHM but all the materials had large variances and lead is not outside the range of error for the other materials. However, lead appears to have the highest PV value. This indicates that the other materials are not as effective at stopping the gammas, and "noise floor" (signal due only to septal penetration) of the modulation profile is high. This result was expected due to the high Z and density of lead, which contributes to a greater stopping power. Lead will be the collimator material of choice due to its effective stopping power.

### D. Slat Height, Slat Width and Slot Height

The regression linking modulation profile properties to image quality was performed for both 500 keV and 1 MeV gamma energies. Fig. 4 below shows the predicted image quality vs. the PV (a measure of camera efficiency). There is a clear inverse relationship between image quality and camera efficiency, which is the typical trade-off in gamma cameras [13]. A slat height, slat width and slot width combination was chosen that was a good compromise between image quality and camera efficiency for both 500 keV and 1 MeV gammas. In the future, if the energy range of interest can be narrowed to a smaller range, the camera should be optimized for that energy range.

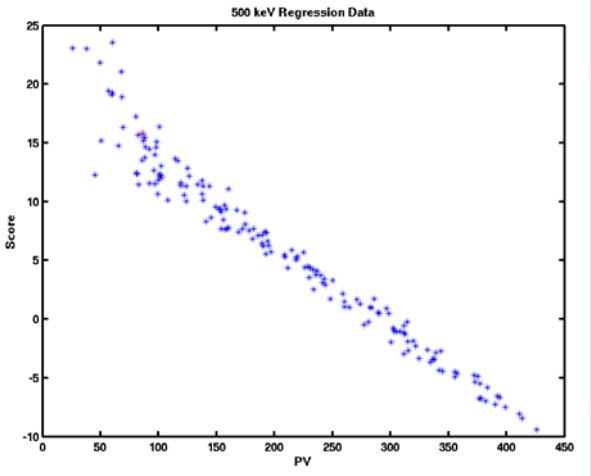


Figure 4. Predicted image quality score vs. the PV.

### E. Image Reconstruction

Using the following camera configuration: (offset, lead slats; 5 cm separation; 3 cm slat height; 3 mm slat width and 3.5 mm slot width) a GEANT4 simulation was conducted.

Four probability matrices were generated for a 10 by 10 pixel FOV located 20 cm from the camera face centered at (8,8) (-8,8) (-8,-8) and (8,-8) in the x,y plane. Earlier research determined that four camera views are necessary to reconstruct images [7, 8, 10, 11]. Images were reconstructed for both 500 keV and 1 MeV gamma energies.

Fig. 5 below shows reconstructed images of a line and a series of points at both 500 keV and 1 MeV. Note how the resolution degrades from the 500 keV to the 1 MeV. This degradation is due to increased septal penetration. However, the images clearly depict line and point source images.

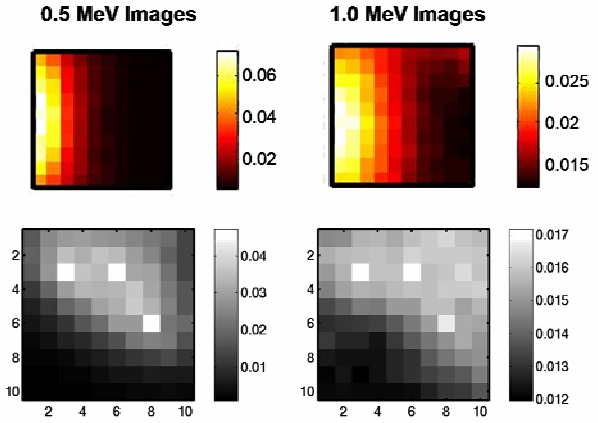


Figure 5. Reconstructed images at both 500 keV (left column) and 1 MeV (right column).

## IV. Conclusions

The RMC system has many component parameters that must be optimized in order to provide a signal that can be reconstructed. Herein, we described the optimization of six of these parameters for a large energy window. The current energy range of interest for NSECT is 0.3 – 2 MeV. In the future, if this energy range can be narrowed, the optimization process should be repeated to create a more specific RMC application.

Future work should focus on further refinements in the camera system and reconstruction methods to achieve full 3D imaging as opposed to the current 2D planar imaging.

## Acknowledgment

The authors wish to thank Carey E. Floyd, Jr. for his vision and effort in the creation and development of NSECT.

## References

[1] A. Danielsen, and E. Steinnes, "A study of some selected trace elements in normal and cancerous tissue by neutron activation analysis," *J. Nuclear Med.,* vol. 11, pp. 260-264, 1970.

[2] C. Floyd, J.E. Bender, A.C. Sharma, et. al., "Introduction to Neutron Stimulated Emission Computed Tomography," *Phys Med Biol,* vol. 51, pp. 3375-3390, Jul 2006.

[3] K. H. Ng, D. A. Bradley, L. M. Looi, C. Seman Mahmood, and A. Khalik Wood, "Differentiation of elemental composition of normal and malignant breast tissue by instrumental neutron activation analysis," *Appl. Radiat. Isot.,* vol. 44, pp. 511-516, 1993.

[4] M. Yaman, D. Atici, S. Bakirdere, and I. Akdeniz, "Comparison of Trace Metal Concentration in malign and Benign Human Prostate," *J. Med. Chem.,* vol. 48, pp. 630-634, 2005.

[5] G. F. Knoll, *Radiation Detection and Measurement*, 3 ed. Hoboken, NJ: Wiley, 2000.

[6] G. J. Hurford, E. J. Schmahl, R. A. Schwartz, et. al., "The RHESSI Imaging Concept," *Solar Physics,* vol. 210, pp. 61-86, Nov 2002.

[7] A. C. Sharma, G. D. Tourassi, A. J. Kapadia, et. al., "Design and Construction of a Prototype Rotation Modulation Collimator for Near-Field High-Energy Spectroscopic Gamma Imaging," in *IEEE NSS & MIC*, San Diego, CA, 2006.

[8] A. C. Sharma, T. G. Turkington, G. D. Tourassi, and C. E. Floyd, "Near-Field High-Energy Spectroscopic Gamma Imaging Using a Rotation Modulation Collimator," *IEEE TNS,* vol. Accepted with revisions Feb 2007.

[9] A. C. Sharma, C. E. Floyd, B. P. Harrawood, et. al., "Rotating slat collimator design for high-energy near-field imaging," *Proceedings of the 2006 SPIE Symposium on Medical Imaging,* vol. 6142, pp. 405-413, Feb. 2006.

[10] A. C. Sharma, G. D. Tourassi, A. J. Kapadia, et. al., "Design and Development of a High-Energy Gamma Camera for use with NSECT Imaging: Feasibility for Breast Imaging," *IEEE TNS,* in press Sept 2007.

[11] A. C. Sharma, G. D. Tourassi, A. J. Kapadia, et. al., "Development of a High-Energy Gamma Camera for use with NSECT Imaging of the Breast," in *IEEE NSS-MIC*, San Diego, CA, 2006.

[12] A. C. Sharma, B. P. Harrawood, J. E. Bender, G. D. Tourassi, A. J. Kapadia, "Neutron Stimulated Emission Computed Tomography: a Monte Carlo simulation approach," *Phys. Med. Biol.,* vol. 52, pp. 6117-6131, Oct 2007.

[13] J. Bushberg, J. A. Seibert, E. M. Leidholdt Jr, and J. M. Boone, *The Essential Physics of Medical Imaging*, 2 ed. Philadelphia, PA: Lippincott Williams & Wilkins, 2002.

# Neutron Stimulated Emission Computed Tomography for Diagnosis of Breast Cancer

Anuj J. Kapadia, Amy C. Sharma, Georgia D. Tourassi, Janelle E. Bender, Calvin R. Howell, Alexander S. Crowell, Matthew R. Kiser, Brian P. Harrawood, Ronald S. Pedroni, and Carey E. Floyd, Jr.

***Abstract*—Neutron stimulated emission computed tomography (NSECT) is being developed as a non-invasive spectroscopic imaging technique to determine element concentrations in the human body. NSECT uses a beam of fast neutrons that scatter inelastically from atomic nuclei in tissue, causing them to emit characteristic gamma photons that are detected and identified using an energy-sensitive gamma detector. By measuring the energy and number of emitted gamma photons, the system can determine the elemental composition of the target tissue. Such determination is useful in detecting several disorders in the human body that are characterized by changes in element concentration, such as breast cancer. In this paper we describe our experimental implementation of a prototype NSECT system for the diagnosis of breast cancer and present experimental results from sensitivity studies using this prototype. Results are shown from three sets of samples: (a) excised breast tissue samples with unknown element concentrations, (b) a multi-element calibration sample used for sensitivity studies, and (c) a small-animal specimen, to demonstrate detection ability from *in-vivo* tissue. Preliminary results show that NSECT has the potential to detect elements in breast tissue. Several elements were identified common to both benign and malignant samples, which were confirmed through neutron activation analysis (NAA). Statistically significant differences were seen for peaks at energies corresponding to $^{37}$Cl, $^{56}$Fe, $^{58}$Ni, $^{59}$Co, $^{66}$Zn, $^{79}$Br and $^{87}$Rb. The spectrum from the small animal specimen showed the presence of $^{12}$C from tissue, $^{40}$Ca from bone, and elements $^{39}$K, $^{27}$Al, $^{37}$Cl, $^{56}$Fe, $^{68}$Zn and $^{25}$Mg. Threshold sensitivity for the four elements analyzed was found to range from 0.3 grams to 1 gram, which is higher than the microgram sensitivity required for cancer detection. Patient dose levels from NSECT were found to be comparable to those of screening mammography.**

***Index Terms*—Breast cancer detection, gamma-ray spectroscopy, neutron, NSECT, tomography.**

## I. Introduction

NEUTRON techniques are rapidly evolving as methods of measuring trace element concentrations in the human body [1]–[6] and in animal tissue [7], [8]. We have successfully implemented a tomographic non-invasive *in-vivo* imaging technique called Neutron Stimulated Emission Computed Tomography (NSECT) to obtain two-dimensional tomographic information about element concentration within a target tissue sample [9]–[17]. NSECT uses spectral information obtained from inelastic scattering interactions between neutrons and atomic nuclei in the target sample to identify the target atoms and determine their concentration *in-vivo*.

Such a technique has several potential applications in both humans and small animals. Several studies have indicated that changes in trace element concentrations in human tissue may be a precursor to malignancy in several organs, for example, brain, prostate and breast [1], [5], [6], [18]–[20]. Measuring these concentration changes would provide the ability to differentiate between malignant and benign tissue, and their quantification could enable *in-vivo* cancer diagnosis at very early stages. Element concentration changes have also been observed in iron for diseases such as sickle cell anemia, thalassemia major, hemosiderosis and hemochromatosis [21]–[27], and in copper for Wilson's disease [28]. NSECT has the potential to image element concentrations in tomographic regions of interest within affected organs, which can help in diagnosis and management of these disorders.

The underlying NSECT principle is the following. NSECT relies on inelastic scattering interactions that occur when atomic nuclei are bombarded with fast neutrons. When an incident neutron scatters inelastically with a target atomic nucleus, the nucleus gets excited to one of its quantized higher-energy states which is often unstable. This excited nucleus then rapidly decays to a lower state, emitting a gamma ray photon whose energy is equal to the difference between the energies of the two states. These non-overlapping energy states are well established and somewhat unique to each element and isotope. Thus, detection and analysis of the emitted gamma energy spectrum can be used to identify the emitting target atom.

Manuscript received January 5, 2007; revised July 2, 2007. This work was supported in part by the NIH/NCI under Grant 1-R21-CA106873-01, in part by the Department of Defense (Breast Cancer Research Program) under award number W81XWH-06-1-0484, and in part by the U.S. Department of Energy, Office of High Energy and Nuclear Physics under Grant DE-FG02-97ER41033.

A. J. Kapadia and A. C. Sharma are with the Department of Biomedical Engineering and the Duke Advanced Imaging Laboratories (DAILabs), Department of Radiology, Duke University, Durham, NC 27710 USA (e-mail: anuj.kapadia@duke.edu; anc4@duke.edu).

G. D. Tourassi and B. P. Harrawood are with the Duke Advanced Imaging Laboratories (DAILabs), Department of Radiology, Duke University, Durham, NC 27710 USA (e-mail: gt@deckard.duhs.duke.edu; brian.harrawood@duke.edu).

J. E. Bender is with the Department of Biomedical Engineering, Duke University, Durham, NC 27710 USA (e-mail: janelle.bender@duke.edu).

C. R. Howell, A. S. Crowell, and M. R. Kiser are with the Department of Physics, Duke University, Durham, NC 27710 USA and also with Triangle Universities Nuclear Laboratory, Durham, NC 27708 USA (e-mail: howell@tunl.duke.edu; crowell@tunl.duke.edu; kiser@tunl.duke.edu).

R. S. Pedroni is with the Department of Physics, North Carolina A&T State University, Greensboro, NC 27411 USA.

C. E. Floyd Jr. is with Duke Advanced Imaging Laboratories (DAILabs), Department of Radiology, Duke University Medical Center and also with the Department of Biomedical Engineering Duke University, Durham, NC 27710 USA.

Color versions of one or more of the figures in this paper are available online at http://ieeexplore.ieee.org.

Digital Object Identifier 10.1109/TNS.2007.909847

While the NSECT technique may seem somewhat similar to prompt gamma neutron activation analysis (PGNAA) as gamma rays emitted due to interactions with incident neutrons are measured simultaneously while irradiating the sample, the two techniques differ greatly in the method of gamma ray production. PGNAA relies on neutron capture with prompt gamma emission, while NSECT uses inelastic scatter spectroscopy to identify the scattering isotope without inducing radioactivity. The NSECT technique is a computed tomography extension of neutron inelastic scatter spectroscopy.

Emitted gamma photons are captured using an energy-sensitive gamma-ray detector. Tomography is performed by acquiring a complete set of projections of line integrals using the translate-rotate configuration as in first generation CT scanners, i.e. the beam is translated horizontally through the entire sample length, then the sample is rotated through some fixed angle and the process is repeated. This tomographic scanning technique yields a two-dimensional map of element concentration and distribution within the sample. This translate-rotate geometry is appropriate for initial proof of concept studies using phantoms, specimens or small animals. Once feasibility is demonstrated, other geometries can be used in future clinical systems. Images are reconstructed using the Maximum Likelihood Expectation Maximization algorithm, an iterative technique to optimize an image reconstructed from a finite set of its projections [29]–[31].

This manuscript presents NSECT as a potential application for diagnosis of breast cancer. Early detection has proven to be the most effective technique to increase survival rates of patients with breast cancer. While screening mammography has been proven to be effective in screening for breast cancer, it suffers from the following limitations: (a) it requires that the mammograms have good contrast, which is often difficult to achieve in dense breasts; (b) its anatomic approach in trying to identify abnormalities in mammograms makes it essential that the abnormality be in an advanced stage of development; and (c) it has limitations in classifying detected abnormalities as benign or malignant. NSECT's sensitivity to metabolic changes seen in malignant tumors in very early developmental stages has the potential to overcome the disadvantages of screening mammography.

Several studies have demonstrated that breast cancer is associated with changes in trace element concentration in the malignant tissue at very early stages. These changes have been observed in concentration of elements such as Al, Br, Ca, Cl, Co, Cs, Cu, Fe, K, Mn, Na, Rb, Sb, Se and Zn, and often occur much earlier than morphologic changes such as tumors and calcifications begin to appear [1], [6], [18]–[20], [32]. Quantifying these element concentrations could potentially enable diagnosis of breast cancer much before the tumor grows large enough to be detected by existing imaging techniques. Generally, NSECT's role in diagnosing breast cancer is to (i) spectroscopically quantify the concentration of elements of interest in the tissue to diagnose the disorder, and (ii) generate three dimensional tomographic image of the element concentration in the organ to isolate the region affected by the disorder. As most of these trace elements occur in the body in microgram quantities, a primary objective of this study is to determine whether NSECT has the required sensitivity to detect micro-gram concentration changes *in-vivo*.

In this paper we describe our experimental implementation of a prototype NSECT system for the diagnosis of breast cancer and present experimental results from sensitivity studies using this prototype. This manuscript presents the first results from a spectroscopic examination of the breast as a preliminary step in determining whether it is realistic to develop NSECT for diagnosis of breast cancer in a clinical scenario.

## II. Materials and Methods

### A. Description of NSECT Prototype System

NSECT experiments have been performed at the Triangle Universities Nuclear Laboratory (TUNL) accelerator lab located at Duke University. TUNL is a low energy nuclear physics research laboratory with a variety of ion beam sources and a 10 megavolt tandem Van de Graaff accelerator capable of producing 20 MeV proton or deuteron beams and a host of other light ion beams. The shielded neutron source provides researchers with an intense pulsed collimated mono-energetic neutron beam. The shape and cross sectional dimension of the beam can be selected with collimator inserts in the 1.5 meter thick shielding wall. For instance, beams with rectangular cross sections are available with sides ranging from 1 mm to 60 mm. The reduction in the background by the 1.5 meter thick wall is sufficient to permit gamma-ray detectors to be used without extensive shielding. The key NSECT components are described below.

*1) Neutron Source:* Neutrons are produced through the $^{2}\mathrm{H}(\mathrm{d},\mathrm{n})^{3}\mathrm{He}$ reaction by directing an accelerated and pulsed beam of deuterons onto a deuterium gas target. Deuterons are accelerated to energies between 3 and 20 MeV by the tandem Van de Graaff accelerator. The charged deuteron beam is directed onto a pressurized deuterium gas cell located behind a 1 meter thick shielding wall composed of concrete, steel, lead, and paraffin loaded with boron and lithium. Beam positioning and focusing on target are performed using magnetic steering coils and magnetic quadrupole lenses, respectively. A collimated channel made of copper with swappable inserts is used to select the beam profile. Copper is chosen because it adequately attenuates neutrons at energies available at TUNL, is fairly simple to machine and is reasonably low cost. For this experiment, the beam profile was selected to be cylindrical with 6 cm diameter.

The neutron beam created is highly peaked in the forward direction and has a narrow energy width of approximately 1 MeV. Neutron beam energies between 5 and 23.2 MeV are available at TUNL.

The beam is pulsed to provide 2 ns wide bunches at the target to allow measurement of neutron and gamma time of flight (TOF), enabling TOF background correction. The repetition rate of the beam pulses is adjustable from 2.5 MHz down to 39 kHz. This pulsed neutron beam allows researchers to measure the background simultaneously with the foreground.

*2) Neutron Flux Monitors:* After exiting the collimator channel, the beam is incident on a thin neutron flux monitor made of a 1.6 mm thick plastic scintillator attached to a

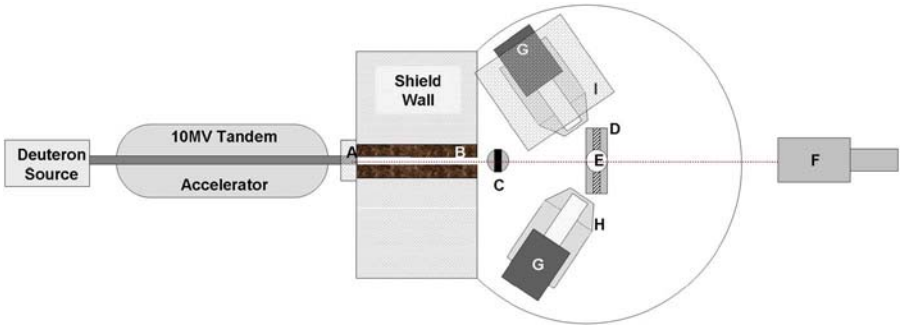


Fig. 1. Schematic drawing of the experimental setup used in NSECT measurements. Components are labeled as follows: A—Deuterium Gas Cell; B—Copper Collimator; C—Neutron Flux Monitor; D—Sample Manipulator; E—Sample; F—Zero-degree Liquid Scintillator Detector; G—HPGe detector; H—Anti-coincidence Compton Shield; I—Detector Shielding Enclosure.

photomultiplier tube. The attenuation of neutrons by the flux monitor in the energy range of our studies is less than 0.1%. The threshold setting on the discriminator of the flux monitor is set sufficiently high to reject more than 90% of the pulses due to recoil electrons from Compton scattering of gamma rays. The efficiency of the thin flux monitor is calibrated relative to a liquid scintillator detector positioned at 0 degrees with respect to the beam. This detector has an active volume 5 inches diameter $\times$ 0.74 inches thick and is filled with Bicron Corporation's BC519 scintillator fluid that enables gamma-ray rejection by pulse shape analysis. The absolute efficiency of this detector has been determined in a separate measurement to an accuracy of $\pm$5% [33]. The zero degree liquid scintillator detector is also used to obtain the neutron transmission image of the sample which is required to make attenuation corrections.

*3) Sample Manipulator:* A computer-controlled sample holder allows precise horizontal, vertical and rotational positioning of small samples remotely. This holder allows tomographic acquisition by translating and rotating the sample with respect to the neutron beam. In the current implementation, tomography is performed by using the translate-rotate geometry to obtain a complete set of projections of line integrals through a slice of the sample. For NSECT, these projections are defined by the angular and spatial sampling intervals between successive positions of the sample as positioned by the sample manipulator.

*4) Gamma Detectors:* Two high-purity germanium (HPGe) detectors are used to detect gamma rays emitted from the sample. These detectors are the 2-Fold Segmented Clover Detectors (CLOVER $4 \times 50 \times 80$ SEG2) manufactured by Canberra Eurysis S.A. Each detector consists of four co-axial n-type germanium crystals mounted together in the shape of a 4-leaf clover. Each germanium crystal is 50 mm in diameter and 80 mm in length, with minimum relative efficiency of 22% and full width at half maximum less than or equal to 2.25 keV for 1.332 MeV gamma rays of $^{60}$Co. Both detectors were calibrated against known energy peaks from a $^{22}$Na source and positioned at $\pm$135 degrees from the incident neutron beam at a distance of 20 cm from the sample. A majority of the states of interest decay by an electric quadrupole transition whose distribution has a maximum intensity at about 45 and 135 degrees. Using the 135 degree orientation helps prevent the gamma detector from being illuminated by either the direct neutron beam or by neutrons that elastically scatter from the target. Active Compton shielding is used to reduce the effects of Compton scattering in the detectors. These shields have a minimum peak-to-Compton ratio of 41 for $^{60}$Co gamma rays at 1.332 MeV.

A schematic drawing of the source, detector and shielding configuration is shown in Fig. 1.

*5) Passive Shielding:* The gamma detector is shielded from the neutron source by a 1.5 m thick wall composed of concrete, steel, lead, borated plastic and lithium-loaded paraffin. In addition to this wall, an enclosure of lead bricks and lithium-loaded paraffin built around each detector provides additional shielding to further reduce particles incident on the active area of the detector.

*6) Computers and Acquisition Software:* Data is acquired using SpecTcl, a nuclear event data acquisition and analysis software package developed at the National Superconducting Cyclotron Laboratory at Michigan State University. SpecTcl allows acquisition and storage of raw data using an object oriented C++ framework, and allows online and offline data visualization through the Xamine display program. Complete as well as partial sets of raw data can be retrieved at any time, including during acquisition, and analyzed using any combination of data parameters. The Xamine display program allows simultaneous display of multiple spectra including spectrum overlay.

*7) Amplifiers:* Canberra 2026 spectroscopy amplifiers are used to integrate and shape the signals from the gamma detectors before they are digitized by peak-sensing ADC's at the data acquisition interface. Adjustable gain settings on these amplifiers allow 'zooming' in or out on a specific range of nuclear energy levels. For example, acquiring data for a gamma energy range of 0–2 MeV would require double the gain as that for 0–4 MeV. However, as the number of channels in the ADC is finite, focusing the entire range of the ADC into a smaller energy range gives better energy resolution in the measured gamma ray energy spectrum. This feature is important when looking for specific energy peaks from certain elements, which lie close to energy peaks from other elements, as in the case of iron (56Fe at 846.7 keV) and germanium (74Ge at 841.1 keV).

### *B. Spectral Acquisition Methodology*

Spectral acquisition for samples was performed by using SpecTcl to digitize two measurable quantities for each gamma count observed: gamma TOF and gamma photon energy. For each data acquisition run, several quantities were counted

using scalars and recorded. These scalars include neutron flux, accelerator beam current and the zero-degree monitor counts. For tomography, the sample position was recorded by reading the sample manipulator's x,y,z positions at each projection as the sample was translated and rotated. Each projection was then analyzed separately and results were fed to the reconstruction algorithm. Data were recorded for each projection until a statistical accuracy of 95% was obtained.

Recorded data sets could be retrieved and analyzed in both real-time while acquiring data as well as at a later time for off-line analysis. Analysis parameters such as TOF windows and detector calibration bias were applied and adjusted in software to allow replaying the experiment with different windows for off-line optimization of these parameters. Spectra were generated using the Xamine display program with different combinations of timing and energy windows applied to the acquired data.

*1) Background Reduction:* Background reduction was performed to account for three contributing sources of background: time uncorrelated events via a TOF background suppression technique [34], [35], sample uncorrelated backgrounds that are time correlated by a sample-out scan subtraction [35], and polynomial curve-fitting of the residual background, i.e. the background that remains after the measured contributions are subtracted. [13]–[15]. The TOF suppression technique is used to correct for the time-uncorrelated backgrounds that are due mostly to gamma rays created and noise generated from the neutron interactions in the shielding material and target apparatus. This technique uses a pulsed neutron beam to allow selection of gamma rays which appear within the prompt peak that corresponds to the time of flight for a neutron from the source to the sample plus the time of flight for the subsequently emitted gamma from the sample to the detector. The remaining gamma rays are suppressed as 'background noise'. The time zero for the TOF measurement is set by using pulsing information from the deuteron beam to control a clock that measures the time of flight of the neutrons from the gas cell to the sample plus the time of flight of the emitted gamma rays from the sample to the detector. Our implementation of this technique has been described in detail elsewhere [35].

Background events that are due to processes that don't involve the sample are measured by acquiring data with the sample removed. Examples of such processes are interactions of neutrons with the collimator or sample holder. This data is subtracted from the sample-in data to produce an estimate of the spectrum due to neutron interactions in the sample. This technique has been described in detail elsewhere [35]. In this study, the samples of interest were only the elements present in the tissue. Hence, the sample-out scan was acquired by substituting the tissue sample with an equivalent mass of water, i.e. removing only the elements of interest while retaining the neutron scatter properties of hydrogen and oxygen nuclei in tissue.

Polynomial curve fitting is used to remove residual background due to Compton scattering of detected gammas. When high energy gamma photons are incident on a detector, some of the gammas will deposit their full energy in the detector while others will scatter out of the detector active volume. As a result, there is a trend of increasing counts in the lower energy channels of the detector. A polynomial curve-fit is used to model this trend and subtract this residual background.

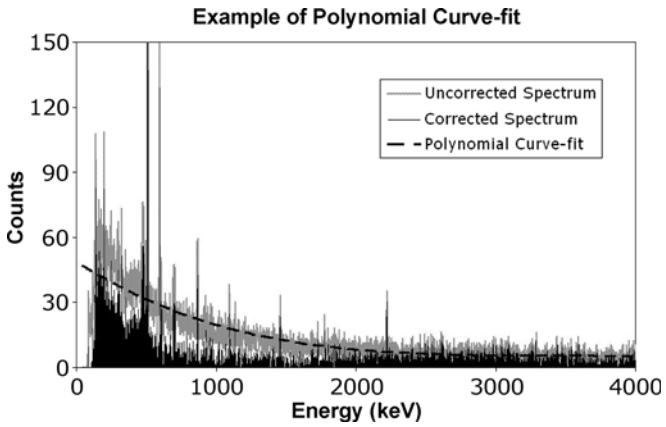


Fig. 2. Example of polynomial curve-fitting for residual background correction. The uncorrected spectrum is shown in grey with the polynomial curve overlaid in dotted black. The resulting corrected spectrum is shown in the foreground as a solid black line in the lower part of the image.

An example of this is shown in Fig. 2, which shows an original uncorrected spectrum (light gray), the polynomial curve fit to underlying background (dotted black line), and the spectrum after residual background correction (solid black line in the lower part of the image).

*2) Samples:* A total of 5 samples were scanned for this study investigating our ability to use NSECT to detect element concentration changes in human tissue. Samples I and II comprised breast biopsy tissue samples with matched tumors excised from the same patient. Sample I had a benign tumor and Sample II was malignant. Each sample weighed approximately 40 g and was scanned with a 6.0 MeV neutron beam while placed in a plastic container, delivering an integrated dose of approximately 1 mSv. Sample III comprised 40 g of distilled water in an identical plastic container, and was used to get an estimate of sample related background originating mainly from hydrogen and oxygen nuclei in tissue cells. Sample IV was made of varying concentrations of $^{56}$Fe, $^{23}$Na, $^{39}$K, $^{35}$Cl and $^{37}$Cl in distilled water and was used as a calibration sample to determine the lower detection threshold of NSECT. Finally, as none of the above samples were of *in-vivo* tissue, Sample V comprising a fixed mouse specimen was scanned to demonstrate NSECT's ability in detecting elements from an intact biological specimen. The mouse specimen was prepared as follows. A freshly sacrificed mouse was flushed with saline and then fixed for one week using a 1:10 gadolinium/formalin solution. After flushing the fixed mouse with saline once again, it was enclosed and sealed in a glass tube along with diluted formalin solution. This enclosed specimen was scanned for 95 minutes with a 5.0 MeV monochromatic neutron beam.

Gamma spectra obtained from each sample were normalized against neutron flux monitor counts for the duration of the scan and corrected for sample uncorrelated backgrounds.

### C. Spectral Analysis Methodology

After correcting for sample uncorrelated backgrounds, each spectrum was analyzed to identify the location of a peak using an automated peak-finding algorithm. The algorithm identifies a peak as a region of high intensity within a pre-specified energy window and peak height above a certain pre-specified threshold [36]. For the breast spectra in this experiment, the energy window width was defined as $\pm 10$ keV and peak height threshold was set to 7. Each detected peak was compared to its underlying background using a z-score test for difference of means. Collection of gamma rays in the detectors is assumed to follow Poisson counting statistics, where, for each energy peak, the mean and variance are equal to the number of counts in the peak. With this assumption, the statistical significance for any two energy peaks can be calculated using the z-score test for a difference of means. Peaks with a two-tailed p-value $\leq 0.05$ are considered significant. For each energy peak in the spectrum, an underlying background was calculated using a polynomial curve-fit as described earlier. The significance of the energy peak was determined by calculating the value of z as shown in (1), comparing the counts in the energy peak against counts in the underlying background

$$z = \frac{\mu_{peak} - \mu_{background}}{\sqrt{\mu_{peak} + \mu_{background}}}. \quad (1)$$

Only peaks detected with a 95% confidence level (i.e., two-tailed p-value $\leq 0.05$) were reported for element matching. This analysis was performed separately for the benign and malignant breast spectra.

Each reported peak was then matched with potential elements using the National Nuclear Data Center's Nuclear structure and decay data online tool (NuDat 2.3) [37]. This identification was made in three steps: (a) a list of all elements with gamma lines at the energy peak of interest were listed; (b) isotopes of elements not expected to be present in the breast, including radioactive isotopes and stable isotopes with low abundance, were discarded from the list; (c) prior information about the remaining isotopes' line contributions to prominent gamma lines was used to identify a possible element match. Several elements such as $^{12}$C, $^{40}$Ca, $^{35}$Cl $^{63}$Cu, $^{56}$Fe and, $^{16}$O, which are present in the breast, have been scanned and studied in earlier NSECT experiments where several of these elements were scanned individually [9]–[11]. These individual element scans were used to experimentally establish the relative contribution of prominent gamma lines for each of these elements. This prior information was used in identifying the corresponding element in the breast spectra. However, there are many other elements in the breast spectrum that have not yet been scanned individually, and their contributions to different gamma lines have not been experimentally established. As a result, certain gamma energy peaks in the breast spectra were found to have multiple element matches, and these are labeled accordingly.

After identifying energy peaks in the individual spectrum, a z-score test for the difference of means was used to analyze the comparative differences in peak heights between the benign and malignant spectra. Counts in an energy peak identified as a potential element peak in a benign spectrum were compared to counts from the same energy peak in the malignant spectrum using the formula in (1). Each peak was considered individually for this analysis. Energy peaks that differed from each other at the 95% confidence level (i.e. two-tailed p-value $\leq 0.05$) were reported as possible markers for malignancy.

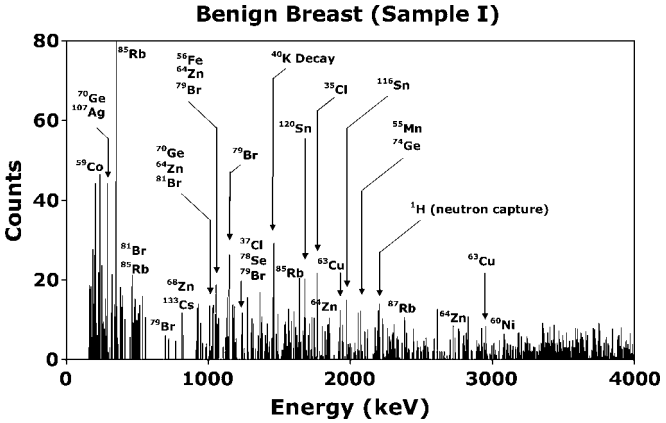


Fig. 3. Gamma energy spectrum from benign breast sample showing energy peaks for several potential elements identified. Gamma peaks are seen for $^{72}$Ge and $^{74}$Ge from the germanium detector. Peaks with multiple potential element matches are labeled accordingly.

For the multi-element calibration sample, prominent peaks corresponding to $^{56}$Fe, $^{39}$K, $^{23}$Na and $^{35}$Cl were identified in the spectrum, taking into consideration prior information about their line contributions to the peaks, and the intensity of their peaks was associated with the known concentration of the element in the sample. Assuming the statistical noise in the system to remain constant, threshold sensitivity for each element was calculated as the concentration at which the resulting peak could be detected with two-tailed p-value $\leq 0.05$ above its underlying background using the z-score test for difference of means.

## III. Results

The results below show sample-uncorrelated background corrected spectra from each of the samples scanned except for Sample III, which was used to estimate background.

Fig. 3 and Fig. 4 show background corrected spectra from the benign and malignant tumor samples respectively. Several elements were identified common to both samples. Energy peaks were seen for Ag, Br, Cl, Co, Cr, Cs, Cu, Fe, Mg, Mn, Ni, Rb, Se, Sn, and Zn. Energy peaks were also seen for Ge from the gamma detectors. While several gamma energy peaks were seen to vary in intensity between the two samples, statistically significant differences were observed for the peaks listed in Table I. These peaks were found to correspond to Al, Br, Cl, Co, Fe, K, Rb and Zn.

Both breast samples were sent for spectral examination through neutron activation analysis (NAA). Results from the NAA indicated significant increases in the concentration of Cl, Fe, K, Na, and Zn and is shown in Table II.

Fig. 5 shows the gamma spectrum from the mixed Fe-Na-K-Cl sample containing 5 g Fe, 0.98 g Na, 1.31 g K, and 2.71 g Cl. Peaks were seen for each of the elements present in the sample. Assuming the statistical noise in the system to remain constant, the detection threshold for NSECT was calculated for each element and is shown in Table III.

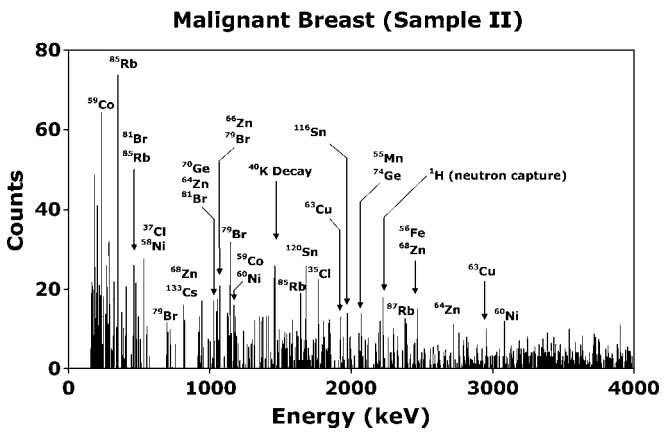


Fig. 4. Gamma energy spectrum from malignant breast sample showing energy peaks for several potential elements identified. Gamma peaks are seen for $^{72}\mathrm{Ge}$ and $^{74}\mathrm{Ge}$ from the germanium detector. Peaks with multiple potential element matches are labeled accordingly.

TABLE I
LIST OF ENERGY LEVELS SHOWING STATISTICALLY SIGNIFICANT DIFFERENCES IN INTENSITIES BETWEEN BENIGN AND MALIGNANT SPECTRA ALONG WITH A LIST OF POTENTIAL MATCHING ELEMENTS. ELEMENTS WITH NEGATIVE DIFFERENCES SHOWED A DECREASE IN CONCENTRATION IN THE MALIGNANT SAMPLE. THE STATISTICAL SIGNIFICANCE WAS CALCULATED USING A Z-SCORE TEST FOR DIFFERENCE OF MEANS

| Energy keV | Element Match | Counts Benign | Counts Malignant | Diff | p-val |
|---|---|---|---|---|---|
| 219 | $^{79}$Br | 6 | 19 | 13 | 0.01 |
| 397 | $^{59}$Co, $^{79}$Br | 16 | 2 | -14 | 0.01 |
| 1028 | $^{81}$Br | 13 | 29 | 16 | 0.05 |
| 1128 | $^{39}$K, $^{68}$Zn | 0 | 13 | 13 | 0.001 |
| 1306 | $^{56}$Fe | 10 | 0 | -10 | 0.01 |
| 2299 | $^{27}$Al | 0 | 13 | 13 | 0.001 |
| 2469 | $^{37}$Cl, $^{56}$Fe, $^{66}$Zn | 5 | 15 | 10 | 0.05 |
| 3635 | $^{35}$Cl | 3 | 14 | 11 | 0.01 |

TABLE II
LIST OF ELEMENTS SHOWING STATISTICALLY SIGNIFICANT DIFFERENCES IN CONCENTRATION BETWEEN BENIGN AND MALIGNANT TISSUE DETERMINED THROUGH NAA

| Element | Cl | Fe | K | Na | Zn |
|---|---|---|---|---|---|
| Benign (µg/g) | 2170 | <172 | <507 | 1440 | 3.96 |
| Malignant (µg/g) | 4000 | 902 | 834 | 3110 | 13.1 |

Fig. 6 shows the gamma energy spectrum accumulated for the fixed mouse specimen. Gamma peaks were observed for several elements expected from the mouse specimen as well as some from materials present in the scanning setup. Energy peaks were identified for $^{12}\mathrm{C}$ from tissue, $^{40}\mathrm{Ca}$ from bone, and elements $^{39}\mathrm{K}$, $^{27}\mathrm{Al}$, $^{37}\mathrm{Cl}$, $^{56}\mathrm{Fe}$, $^{68}\mathrm{Zn}$ and $^{25}\mathrm{Mg}$ which could be present in the specimen. Elements $^{27}\mathrm{Al}$ and $^{56}\mathrm{Fe}$ could also be system dependent as many components used to mount the detectors and other hardware were made of aluminum and iron. Peaks were seen for $^{158}\mathrm{Gd}$ and $^{160}\mathrm{Gd}$ from the 1:10 gadolinium/formalin fixing solution in the sample, along with peaks from several naturally occurring states in germanium in the HPGe detectors.

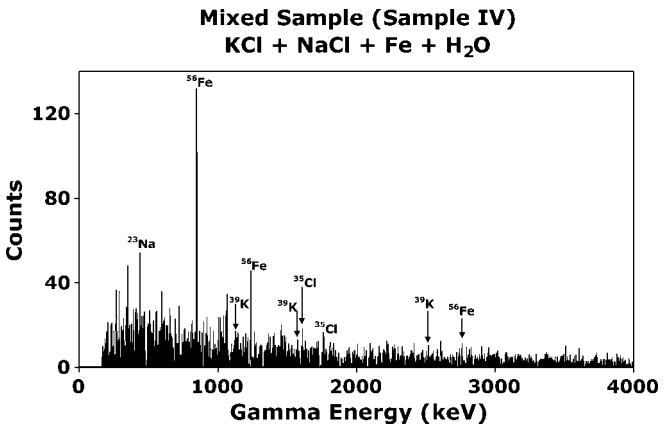


Fig. 5. Gamma energy spectrum from a mixed sample of 2.5 g KCl, 2.5 g NaCl and 5 g Fe in 40 g $\mathrm{H_2O}$. Peaks are seen for each of the elements in the sample.

TABLE III
RESULTS OF SENSITIVITY ANALYSIS FOR THE MULTI-ELEMENT CALIBRATION SAMPLE. ALSO LISTED FOR A COMPARATIVE ANALYSIS IS THE CORRESPONDING NAA SENSITIVITY FOR THE ELEMENT

| | Mass | Peak | Threshold | Sensitivity | |
|---|---|---|---|---|---|
| | (g) | counts | counts | NSECT (g) | NAA (µg) |
| $^{23}$Na | 0.98 | 140.21 | 40 | 0.28 | 5 |
| $^{56}$Fe | 5 | 519.79 | 72 | 0.69 | 90 |
| $^{39}$K | 1.31 | 71.47 | 32 | 0.59 | 1000 |
| $^{35}$Cl | 2.71 | 52.46 | 19 | 0.98 | 20 |

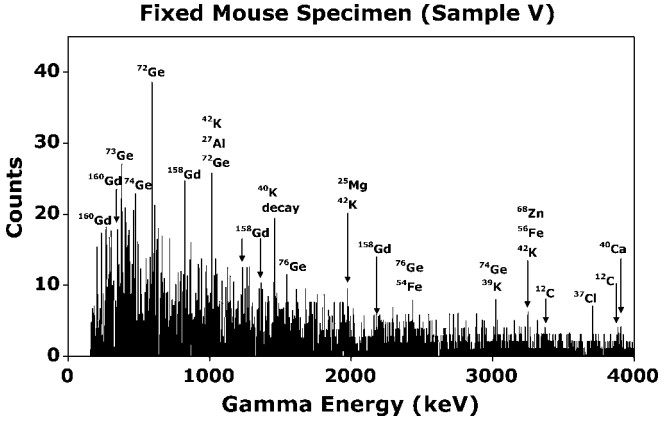


Fig. 6. Gamma energy spectrum from a formalin fixed mouse specimen showing peaks corresponding to excited states in various elements. Gamma peaks are seen for $^{12}\mathrm{C}$ (escape peaks), $^{40}\mathrm{Ca}$, $^{39}\mathrm{K}$, $^{27}\mathrm{Al}$, $^{37}\mathrm{Cl}$, $^{56}\mathrm{Fe}$, $^{68}\mathrm{Zn}$ and $^{25}\mathrm{Mg}$. Gamma peaks are also seen for $^{72}\mathrm{Ge}$ and $^{74}\mathrm{Ge}$ from the germanium detector, and $^{158}\mathrm{Gd}$ and $^{160}\mathrm{Gd}$ from the fixing solution. Peaks with multiple potential element matches are labeled accordingly.

## IV. DISCUSSION

This work demonstrates that NSECT shows significant potential in developing into a modality capable of detecting breast cancer in early stages. Results from preliminary scans of breast tissue samples demonstrate its ability to detect individual elements within breast tissue. Energy peaks seen to vary in intensity between the benign and malignant samples facilitate future hypothesizing of these peaks as potential markers of breast cancer. Although the spectra obtained in this study were from

excised tissue, results from the whole mouse specimen indicate that element detection is possible for *in-vivo* tissue without the need for biopsy. The lower detection threshold for accurate quantification of an element using this preliminary NSECT system was found to range from 0.28 grams to 0.98 grams for the four elements analyzed. This threshold value is much higher than the microgram sensitivity required to detect cancer-indicating trace elements in the breast. Accurate element quantification using the current NSECT system requires at least the threshold concentration of the target element to be present in the beam. However, simulation experiments conducted to test the feasibility of breast cancer detection for *in-vivo* tumors have demonstrated the ability to detect microgram concentrations of trace elements that are markers of breast cancer for tumors that are *in-vivo* [36]. In some cases, it may be possible to increase the total mass of the element in the beam by using a broad neutron beam to illuminate a larger volume of the sample. Generally, a significant sensitivity improvement will be required in order to facilitate breast cancer diagnosis. Efforts are under way to improve sensitivity while maintaining the lowest possible dose level delivered to the patient. Using high-flux neutron sources and multiple gamma detectors will increase the overall detection efficiency and reduce scan time, which will both in turn reduce the time-dependent background noise. Optimizing the detector shielding will reduce the sample-related and room-related background, which will increase signal to noise ratio and improve the sensitivity of the system. Increasing the gamma detection efficiency to reduce overall scan time will also reduce the associated patient dose. Neutron and gamma attenuation correction algorithms are being developed and implemented simultaneously to improve sensitivity and detection accuracy [38].

Three background correction techniques were used in this experiment, TOF correction, sample-related background subtraction, and polynomial curve-fitting. The TOF correction technique is used to reduce the time-uncorrelated backgrounds. This background can also be estimated by acquiring a spectrum from a sample-out scan. Both techniques have been tested and are seen to suppress time-uncorrelated background sufficiently. We prefer to implement the TOF subtraction technique here because not only does it require less time by not having to acquire a separate sample-out scan, but the electronics are also readily available at TUNL. In a clinical environment however, it may be easier to use the sample-out subtraction technique to avoid the added complexity in required hardware.

Slowing and attenuation of neutrons in the body depends largely on the concentration of hydrogen and oxygen nuclei in the sample, and is of significant concern when interrogating large samples such as the abdomen. However, for the size of tumor samples that have been used in this study, simulations have shown that neutron slowing is not of significant concern. As larger samples are interrogated, neutron slowing and attenuation will be corrected in one of two ways: (a) Neutron energy slowing: Incident neutrons lose a part of their energy through interactions with nuclei encountered in the sample while traveling towards target trace element nuclei. As a result, the energy of the neutron available to interact with the target nucleus is lower. As the criterion for successful interrogation of a target nucleus through inelastic scatter spectroscopy is that the energy of the incident neutron must be larger than the target nuclear energy level to be excited, the reduction in energy through slowing of neutrons is taken into consideration when selecting the original incident energy of the neutron beam. For example, to interrogate a sample containing $^{12}$C with its first excited state at 4.4 MeV, a 5 MeV neutron beam is used to ensure that there will be sufficient energy left to excite the 4.4 MeV energy state even after minor energy losses through slowing. (b) Neutron attenuation: Interactions such as elastic scatter between incident neutrons and nuclei encountered while traveling towards target trace elements often result in a change in direction of the incident neutron. As a result, fewer neutrons are able to reach the target trace element nucleus, leading to a reduction in the number of observed gamma counts for that nucleus. For spectroscopic examination of a homogeneous sample, this neutron attenuation is accounted for by using a calibration sample with the same geometric dimensions as the target tissue sample. For non-homogeneous samples which require tomographic examination, a neutron attenuation-correction algorithm has been developed for use with NSECT and has been described elsewhere [38].

Using neutrons as the incident radiation leads to significant concerns about patient dose. At our energies of interest (2 MeV to 8 MeV), neutrons are known to damage the body 10 times more than x-rays. However, as it takes fewer neutrons to create an NSECT image than x-rays required to create a mammogram, it is possible to maintain patient dose level at values comparable to other ionizing radiation modalities. In previous studies, it has been established that only 10,000 gamma events are required in the detectors to obtain quantitative accuracy of 95% in a tomographic image. Geant4 simulations to evaluate the efficiency of inelastic scatter interactions have shown that 10,000 gamma events can be obtained in the detectors using 10 million incident neutrons, which corresponds to an effective patient dose of less than 1 mSv. Our preliminary simulation experiments suggest that for breast cancer detection, it may be possible to achieve effective patient dose levels lower than 5 mSv [36], [39]. By increasing the number of detectors and using high-flux neutron sources to reduce scan time, dose levels can potentially be brought down even further. Dose assessments are currently performed through a Geant4 simulation which models the acquisition geometry, neutron beam characteristics and tissue sample data [39]. The simulation is used to count the energy deposited in the tissue sample from which an effective dose equivalent for the organ can be calculated by using the appropriate weighting factors for the organ of interest. For the breast, the weighting factor relative to whole body exposure is 0.05.

An important issue to address for breast cancer diagnosis using NSECT is the accurate quantification of a particular element in the spectrum despite line contributions to its gamma peaks from other elements. This involves an understanding of the nuclear transition structure of the element under evaluation, and subsequent correction for the 'noise' line-contributions from other elements. These line contributions have been evaluated experimentally for several samples. Before quantification experiments can be performed for micro-gram concentrations of breast trace elements, it is imperative to analyze the line contributions from each of the elements of interest and develop a model to identify an element based on its gamma line contributions throughout the spectrum. Efforts are under way to evaluate gamma spectra from several such elements using Geant4 simulation.

NSECT is a new alternate diagnosis method with the potential to detect breast cancer. Its advantage lies in its ability to detect and identify malignant tissue in the breast and generate a two-dimensional image through a single non-invasive *in-vivo* tomographic scan without the need for breast compression or biopsy. Through the use of portable neutron sources and portable gamma detectors, NSECT can potentially be translated to clinical use as a screening and diagnostic technique for breast cancer. Our final goal is to implement a portable, low-dose breast cancer screening system which can detect breast cancer without the need for breast compression or invasive biopsies.

## ACKNOWLEDGMENT

The authors thank all the members of the Triangle Universities Nuclear Laboratory for their help with data acquisition and the members of the Duke Advanced Imaging Laboratories for their help with data analysis. They also thank the Center for In-vivo Microscopy at Duke University for providing the fixed mouse specimen.

## REFERENCES

[1] A. Garg and V. Singh *et al.*, "An elemental correlation study in cancerous and normal breast tissue with successive clinical stages by neutron activation analysis," *Biol. Trace Element Res.*, vol. 46, pp. 185–202, 1994.

[2] Y. Katoh, T. Sato, and Y. Yamamoto, "Use of instrumental neutron activation analysis to determine concentrations of multiple trace elements in human organs," *Arch. Environ. Health*, Oct. 2003.

[3] G. S. Knight, A. H. Beddoe, S. J. Streat, and G. L. Hill, "Body composition of two human cadavers by neutron activation and chemical analysis," *Am. J Physiol. Endocrinol. Metab.*, vol. 250, pp. E179–E185, 1986.

[4] M. Yukawa, M. Suzuki-Yasumoto, K. Amano, and M. Terai, "Distribution of trace elements in the human body determined by neutron activation analysis," *Arch. Environ. Health*, vol. 35, pp. 36–44, 1980.

[5] A. Danielsen and E. Steinnes, "A study of some selected trace elements in normal and cancerous tissue by neutron activation analysis," *J. Nucl. Med.*, vol. 11, pp. 260–264, 1970.

[6] K. H. Ng, D. A. Bradley, L. M. Looi, C. Seman Mahmood, and A. Khalik Wood, "Differentiation of elemental composition of normal and malignant breast tissue by instrumental neutron activation analysis," *Appl. Radiat. Isot.*, vol. 44, pp. 511–516, 1993.

[7] G. V. Iyengar, K. Kasperek, and L. E. Feinendegen, "Determination of certain bulk and trace elements in the bovine liver matrix using neutron activation analysis," *Phys. Med. Biol.*, vol. 23, pp. 66–76, 1978.

[8] W. E. Kollmer, P. Schramel, and K. Samsal, "Simultaneous determination of nine elements in some tissues of the rat using neutron activation analysis," *Phys. Med. Biol.*, vol. 17, pp. 555–562, 1972.

[9] C. E. Floyd, J. E. Bender, A. C. Sharma, A. J. Kapadia, J. Q. Xia, B. P. Harrawood, G. D. Tourassi, J. Y. Lo, A. S. Crowell, and C. R. Howell, "Introduction to neutron stimulated emission computed tomography," *Phys. Med. Biol.*, vol. 51, pp. 3375–3390, 2006.

[10] C. E. Floyd, A. J. Kapadia, J. E. Bender, A. C. Sharma, J. Q. Xia, B. P. Harrawood, G. D. Tourassi, J. Y. Lo, A. S. Crowell, and C. R. Howell, "Neutron stimulated emission computed tomography of a multi-element phantom," *Phys. Med. Biol.*, submitted for publication.

[11] C. E. Floyd, C. R. Howell, B. P. Harrawood, A. S. Crowell, A. J. Kapadia, R. Macri, J. Q. Xia, R. Pedroni, J. Bowsher, M. R. Kiser, G. D. Tourassi, W. Tornow, and R. Walter, "Neutron stimulated emission computed tomography of stable isotopes," in *Proc. SPIE Medical Imaging 2004*, vol. 5368, pp. 248–254.

[12] A. J. Kapadia, C. E. Floyd, J. E. Bender, C. R. Howell, A. S. Crowell, and M. R. Kiser, "Non-invasive quantification of iron 56-Fe in beef liver using neutron stimulated emission computed tomography," in *Proc. IEEE Nuclear Science Symp., Medical Imaging Conf. 2005*, vol. 4, pp. 2232–2234.

[13] A. J. Kapadia, A. C. Sharma, G. D. Tourassi, J. E. Bender, A. S. Crowell, M. R. Kiser, C. R. Howell, and C. E. Floyd, "Neutron spectroscopy of mouse using Neutron Stimulated Emission Computed Tomography (NSECT)," in *Proc. IEEE Nuclear Science Symp., Medical Imaging Conf. 2006*, vol. 6, pp. 3546–3548.

[14] A. J. Kapadia, A. C. Sharma, G. D. Tourassi, J. E. Bender, A. S. Crowell, M. R. Kiser, C. R. Howell, and C. E. Floyd, "Neutron Stimulated Emission Computed Tomography (NSECT) for early detection of breast cancer," in *Proc. IEEE Nuclear Science Symp., Medical Imaging Conf. 2006*, vol. 6, pp. 3928–3931.

[15] A. J. Kapadia, A. C. Sharma, G. D. Tourassi, J. E. Bender, A. S. Crowell, M. R. Kiser, C. R. Howell, and C. E. Floyd, "Non-invasive estimation of potassium (39K) in bovine liver using Neutron Stimulated Emission Computed Tomography (NSECT)," in *Proc. IEEE Nuclear Science Symp., Medical Imaging Conf. 2006*, vol. 4, pp. 2076–2078.

[16] J. E. Bender, C. E. Floyd, B. P. Harrawood, A. J. Kapadia, A. C. Sharma, and J. L. Jesneck, "The effect of detector resolution for quantitative analysis of neutron stimulated emission computed tomography," in *Proc. SPIE Medical Imaging 2006*, vol. 6142, pp. 1597–1605.

[17] A. C. Sharma, G. D. Tourassi, A. J. Kapadia, J. E. Bender, J. Q. Xia, B. P. Harrawood, A. S. Crowell, M. R. Kiser, C. R. Howell, and C. E. Floyd, "Development of a high-energy gamma camera for use with NSECT imaging of the breast," in *Proc. IEEE Nuclear Science Symp., Medical Imaging Conf. 2006*, vol. 6, pp. 3925–3927.

[18] K. H. Ng, D. A. Bradley, and L. M. Looi, "Elevated trace element concentrations in malignant breast tissues," *Brit. J. Radiol.*, vol. 70, pp. 375–382, 1997.

[19] S. Rizk and H. Sky-Peck, "Comparison between concentrations of trace elements in normal and neoplastic human breast tissue," *Cancer Res.*, vol. 44, pp. 5390–5394, 1984.

[20] A. Schwartz and R. Fink, "Trace elements in normal and malignant human breast tissue," *Surgery*, vol. 76, pp. 325–329, 1974.

[21] R. Engelhardt, J. H. Langkowski, R. Fischer, P. Nielsen, H. Kooijman, H. C. Heinrich, and E. Bucheler, "Liver iron quantification: Studies in aqueous iron solutions, iron overloaded rats, and patients with hereditary hemochromatosis," *Magn. Reson. Imaging*, vol. 12, pp. 999–1007, 1994.

[22] J. P. Villeneuve, M. Bilodeau, R. Lepage, J. Cote, and M. Lefebvre, "Variability in hepatic iron concentration measurement from needle-biopsy specimens," *J. Hepatol.*, vol. 25, pp. 172–177, 1996.

[23] J. M. Alustiza, J. Artetxe, A. Castiella, C. Agirre, J. I. Emparanza, P. Otazua, M. Garcia-Bengoechea, J. Barrio, F. Mujica, and J. A. Recondo, "MR quantification of hepatic iron concentration," *Radiology*, vol. 230, pp. 479–484, 2004.

[24] L. W. Powell, "Diagnosis of hemochromatosis," *Semin. Gastrointest. Dis.*, vol. 13, pp. 80–88, 2002.

[25] S. R. Hollan, "Transfusion-associated iron overload," *Curr. Opin. Hematol.*, vol. 4, pp. 436–441, 1997.

[26] S. Joffe, "*Hemochromatosis*" [Online]. Available: http://www.emedicine.com/radio/topic323.htm 2005

[27] L. Powell, "Hemochromatosis," in *Harrison's Principles of Internal Medicine*, D. Kasper, A. S. Fawci, D. L. Longo, E. Braunwald, S. L. Hauser, and J. L. Jameson, Eds., 16th ed. New York: McGraw Hill, 2005, vol. 2, pp. 2298–2303.

[28] G. Brewer, "Wilson disease," in *Harrison's Principals of Internal Medicine*, D. Kasper, A. S. Fawci, D. L. Longo, E. Braunwald, S. L. Hauser, and J. L. Jameson, Eds., 16th ed. New York: McGraw Hill, 2005, vol. 2, pp. 2313–2315.

[29] A. P. Dempster, N. M. Laird, and D. B. Rubin, "Maximum likelihood from incomplete data via the EM algorithm," *J. Royal Stat. Soc. Series B*, vol. 39, pp. 1–38, 1977.

[30] R. Sundberg, "Maximum likelihood theory for incomplete data from an exponential family," *Scand. J. Stat.*, vol. 1, pp. 49–58, 1974.

[31] L. Shepp and Y. Vardi, "Maximum likelihood reconstruction for emission tomography," *IEEE Trans. Med. Imag.*, vol. MI-1, pp. 113–122, Oct. 1982.

[32] H. Mussalo-Rauhamaa, S. Piepponen, J. Lehto, R. Kauppila, and O. Auvinen, "Cu, Zn, Se and Mg concentrations in breast fat of Finnish breast cancer patients and healthy controls," *Trace Elements in Med.*, vol. 10, pp. 13–15, 1993.

[33] C. R. Howell and Q. Chen *et al.*, "Toward a resolution of the neutron-neutron scattering length issue," *Phys. Lett. B*, vol. 444, pp. 252–259, 1998.

[34] P. Håkansson, "An introduction to the time-of-flight technique," *Braz. J. Phys.*, vol. 29, pp. 422–427, 1999.

[35] C. E. Floyd, A. C. Sharma, J. E. Bender, A. J. Kapadia, J. Q. Xia, B. P. Harrawood, G. D. Tourassi, J. Y. Lo, M. R. Kiser, A. S. Crowell, R. S. Pedroni, R. A. Macri, S. Tajima, and C. R. Howell, "Neutron stimulated emission computed tomography: Background corrections," *Nucl. Instrum. Methods Phys. Res. Section B*, vol. 254, pp. 329–336, 2007.

[36] J. E. Bender, A. J. Kapadia, A. C. Sharma, G. D. Tourassi, B. P. Harrawood, and C. E. Floyd, "Breast cancer detection using neutron stimulated emission computed tomography: Prominent elements and dose requirements," *Med. Phys.*, vol. 34, pp. 3866–3871, 2007.

[37] National Nuclear Data Center BNL, NuDat 2.3 2007.

[38] A. J. Kapadia and C. E. Floyd, "An attenuation correction technique to correct for neutron and gamma attenuation in the reconstructed image of a neutron stimulated emission computed tomography (NSECT) system," in *Proc. SPIE Medical Imaging 2005*, vol. 5745, pp. 737–743.

[39] A. C. Sharma, B. P. Harrawood, A. J. Kapadia, J. E. Bender, and G. D. Tourassi, "Neutron stimulated emission computed tomography: A Monte Carlo simulation approach," *Phys. Med. Biol.*, vol. 52, pp. 6117–6131, 2007.

IOP PUBLISHING PHYSICS IN MEDICINE AND BIOLOGY

Phys. Med. Biol. **53** (2008) 2313–2326 doi:10.1088/0031-9155/53/9/008

# Neutron-stimulated emission computed tomography of a multi-element phantom

**Carey E Floyd Jr[1,2], Anuj J Kapadia[1,2], Janelle E Bender[2], Amy C Sharma[1,2], Jessie Q Xia[1,2], Brian P Harrawood[1], Georgia D Tourassi[1], Joseph Y Lo[1,2], Alexander S Crowell[3,4], Mathew R Kiser[3,4] and Calvin R Howell[3,4]**

[1] Department of Radiology, Duke Advanced Imaging Laboratories, Durham, NC 27705, USA
[2] Department of Biomedical Engineering, Duke University, Durham, NC 27708, USA
[3] Department of Physics, Duke University, Durham, NC 27706, USA
[4] Triangle Universities Nuclear Laboratory, Duke University, Durham, NC 27706, USA

E-mail: anuj.kapadia@duke.edu

Received 4 December 2007, in final form 17 March 2008
Published 17 April 2008
Online at stacks.iop.org/PMB/53/2313

**Abstract**

This paper describes the implementation of neutron-stimulated emission computed tomography (NSECT) for non-invasive imaging and reconstruction of a multi-element phantom. The experimental apparatus and process for acquisition of multi-spectral projection data are described along with the reconstruction algorithm and images of the two elements in the phantom. Independent tomographic reconstruction of each element of the multi-element phantom was performed successfully. This reconstruction result is the first of its kind and provides encouraging proof of concept for proposed subsequent spectroscopic tomography of biological samples using NSECT.

## 1. Introduction

Neutron-stimulated emission computed tomography (NSECT) is a technique for non-invasive *in vivo* imaging of stable isotopes in the body (Floyd *et al* 2004, 2006). It uses a thin beam of fast neutrons to stimulate stable nuclei in a sample, which emit characteristic gamma radiation. The energy of the emitted gamma is unique to the nucleus and is used to identify the emitting nucleus. NSECT is a technique of tomographic spectroscopy. In the current implementation, the tomographic path of integration is defined by the neutron beam while the emitting nuclear species is identified by gamma spectroscopy. The result is a tomographic and spectroscopic image of element distribution in the body acquired through a non-invasive *in vivo* scan. While other techniques have been developed for identifying the concentrations of elements in tissue samples (Geraki and Farquharson 2002, Ng *et al* 1993, 1997), NSECT is the first technique with properties that will allow non-invasive and *in vivo* spectroscopic imaging

  

in humans or small animals with a non-lethal radiation dose. Previously, we have presented an introduction to NSECT along with some preliminary results to demonstrate proof of concept for some of the required key components of the system (Floyd *et al* 2004, 2006, Kapadia *et al* 2005, 2006a, 2006b, 2006c, 2007, 2008). Here, we present a full description of the tomographic technique as successfully applied to acquire and reconstruct tomographic images from a multi-element phantom.

The motivation for this work is to develop a technique that can image the elemental composition of biomedical volumes *in vivo*. Potential applications include cancer diagnosis and staging by examining the concentration of certain elements in regions of suspicion based on an observed difference in the trace element concentration between benign and malignant tissues (Dobrowolski *et al* 2002, Ng *et al* 1993, 1997, Schwartz and Fink 1974, Gregoriadis *et al* 1983, Rizk and Sky-Peck 1984); quantitative assessment of the iron load in the liver (Brittenham and Badman 2003), following the transport of nutrients through the body; and the role of metals in dementia (Stedman and Spyrou 1995).

The physical principles behind NSECT are based on neutron inelastic scattering and nuclear spectroscopy, and include the physics of computed tomography. Each of these principles that are important for NSECT is described below.

### *1.1. Neutron inelastic scatter*

When a neutron collides with an atomic nucleus at incident neutron energies of interest (1–7.5 MeV), one of several processes may occur. The most probable interaction is elastic scattering, while inelastic scattering is the next most likely interaction (Evans 1955). Other interactions, such as neutron capture (n,$\gamma$), charge exchange (n,p), knockout (n,d), (n,t), (n, $^3$He), (n, $^4$He), or fission (n,x), are less likely. When the neutron scatters inelastically, some of the energy of the neutron is transferred to the nucleus leaving it in an excited state. After a short time (typically several picoseconds), the excited nucleus decays to a lower energy state, usually by emitting a gamma photon. The photon has energy equal to the difference in energy between the two states, and an angular distribution specified by the difference in angular momentum and parity of these states (Cottingham and Greenwood 1986). The energy of the emitted gamma ray is used to identify the emitting nucleus.

### *1.2. Gamma spectroscopy*

The gamma emissions that are stimulated by inelastic neutron scattering are characteristic of the isotope and energy states involved. While the energy of emitted gamma rays is not absolutely unique to each element, there is very little overlap over the range of elements and neutron energies of interest to NSECT. A high-resolution gamma detector acquires the energy spectrum emitted by the elements along the path of the neutron beam. NSECT uses the characteristic signature of these inelastic collisions to identify the isotope from which the neutron scatters. The incident neutron flux is shaped into a beam that defines a path of integration. The emitted gamma flux that is characteristic of a particular element is proportional to the concentration of that element in the body integrated over the path of the neutron beam weighted by the incident flux of the neutron beam. In this way, multiple energy integrals are acquired simultaneously for each spatial path integral defined by the orientation of the neutron beam. The spatial projections of each combination of energy channels associated with a given element can be reconstructed separately to provide tomographic image reconstructions that represent the spatial distribution of each respective element within the illuminated volume of the sample.

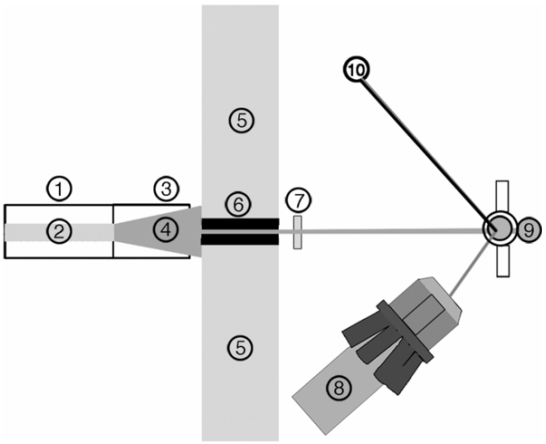


**Figure 1.** Geometry for NSECT tomography experiment. (1) Neutron accelerator tube, (2) deuteron beam, (3) deuterium gas cell, (4) neutron production region, (5) shield wall, (6) copper collimator, (7) thin plastic neutron monitor, (8) HPGe gamma detector with Compton shield, (9) sample target on translational and rotational stages, (10) inelastically scattered neutron.

### *1.3. Computed tomography*

The projection-slice theorem states that if line integrals (referred to as projections) of a property of a body are acquired such that these line integrals cover the area at all angles of a slice through the body, then the interior density of the slice can be reconstructed from these projections. The process of reconstruction is called tomography and the image of the interior spatial density is known as the tomographic image. The simplest technique for reconstructing the interior from a complete set of projections is Fourier inversion (FI) (Kak and Slaney 1999). Unfortunately, practical limitations of sampling seriously limit the number of applications for which FI yields acceptable image quality. The most popular reconstruction algorithm over the past 30 years has been filtered back projection in which each projection ray is filtered by a $1/r^2$ function, and the resulting value is distributed uniformly along the projection path through the interior space to be reconstructed (Kak and Slaney 1999). With a sufficient signal-to-noise ratio (SNR) and sufficient spatial and angular sampling in the acquisition of the projections, this technique can provide high-quality images. Unfortunately, in many applications (including NSECT), the SNR and the number of spatial and angular samples are related to the acquisition time and to the patient dose, both quantities that should ideally be minimized. For this reason, statistical-based algorithms are used. For the work presented here, we have chosen the maximum likelihood through expectation maximization (MLEM) algorithm as developed for emission computed tomography (ECT) (Lange and Carson 1984). The advantage of this algorithm for applications like NSECT is that it is more tolerant of a limited SNR and sampling than FBP or FI (Lange and Carson 1984). A feature of MLEM that is of advantage to NSECT is the ability to incorporate several physical features of the acquisition system and geometry directly into the reconstruction algorithm through a forward-modeling approach. For example, MLEM is able to model the Poisson nature of gamma counting, number and location of gamma detectors, and non-uniform acquisition geometries. MLEM still requires projection data that reflect the line integral of the elemental concentrations within the sample. These line integrals are provided by a neutron beam that defines the path and geometry of integration. The neutron

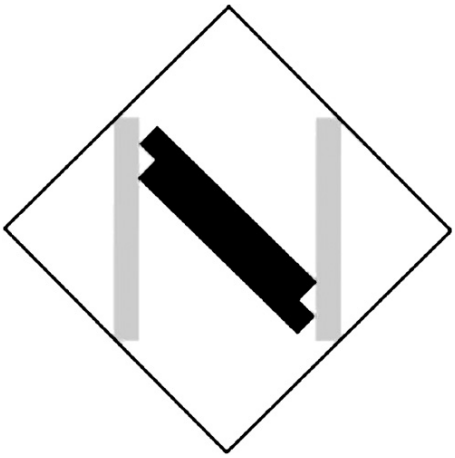

**Figure 2.** Geometry of the phantom imaged in the tomography experiment. The gray bars represent copper, while the black bars represent iron. Each bar measures 0.6 cm in width, 6 cm in height and 2.5 cm in depth (into the page).

beam stimulates the emission of characteristic gamma photons that are integrated in a gamma spectrometer.

## 2. Materials and methods

NSECT experiments are currently performed at the Triangle Universities Nuclear Laboratory (TUNL) at Duke University, Durham, NC. TUNL is a medium energy accelerator source with a tandem Van-de-Graaff accelerator capable of producing neutron beams up to 20 MeV.

### *2.1. Neutron illumination*

Neutrons for our experiments were produced at the shielded neutron source facility of TUNL. A 7.5 MeV neutron beam was produced through the d(d,n) reaction using the geometry shown in figure 1.

The 7.5 MeV neutron beam passed through a 1.5 m long copper collimator with swappable inserts that allowed manipulation of the size and shape of the beam profile. The profile of the neutron beam was measured using a 1 mm thick plastic scintillator that was moved across the beam at the location of the sample. The counts were recorded for each position in both the horizontal and the vertical planes to map the beam profile in two dimensions.

### *2.2. Sample phantom*

A phantom was constructed of solid bars of natural copper and natural iron to form the shape of the letter 'N'. A schematic drawing of the top view of this phantom is shown in figure 2. The gray bars represent copper, while the black bars represent iron. Each bar measured 0.6 cm in width, 6 cm in height and 2.5 cm in depth (into the page).

### *2.3. Sample transport*

The sample was held on a computer-controlled stage that permitted motion in the horizontal plane (across the beam path), the vertical plane and rotation about the vertical (tomographic) axis. With the beam fixed, the horizontal motion allowed selecting a projection path through

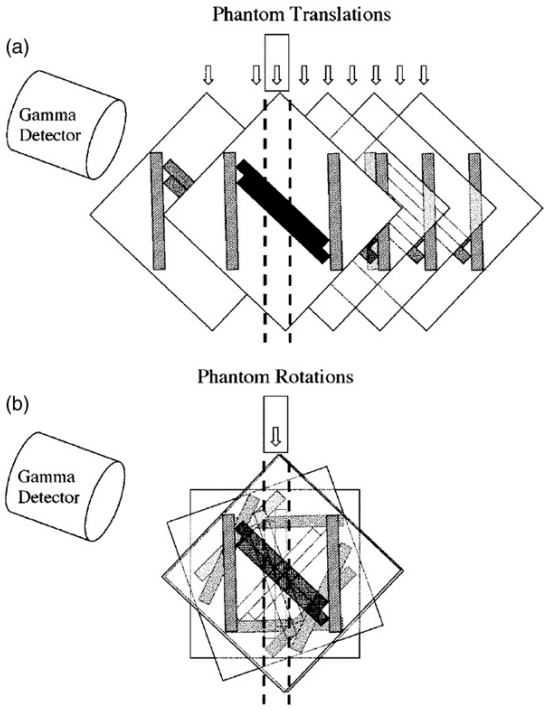


**Figure 3.** Top view of phantom showing (a) translations and (b) rotations used to achieve the tomographic acquisition geometry. The gray bars are copper and black bars are iron. All bars have height 6 cm, width 0.6 cm and depth 2.5 cm. The maximum dimension of the phantom is 9 cm (diagonal).

the sample, the vertical motion allowed selecting a trans-axial slice through the sample, and the rotation about the central axis of the sample allowed selecting a projection angle for the stimulating neutron beam. This arrangement is shown in figure 3.

### *2.4. Gamma spectroscopy*

The characteristic gamma photons emitted due to inelastic scattering of neutrons have energies between 100 and 6500 keV (National Nuclear Data Center 2007). Photons in this energy range are well transmitted through the body with transmission between 12% at low energies (300 keV), where the attenuation coefficient is 0.21 $cm^{-1}$, and 65% at higher energies (6500 keV), where the attenuation coefficient is 0.043 $cm^{-1}$ (NIST 1990). The emitted gamma photons were detected in a high purity germanium (HPGe) detector with an energy resolution of 0.1% full-width at half-maximum (FWHM) at 1 MeV detected energy, corresponding to $\pm 1$ keV (Knoll 2000). This resolution was sufficient to resolve most of the gamma photon energies that were characteristic of the isotopes of interest with incident neutron energy between 1 MeV and 7.5 MeV.

The HPGe detector was surrounded by an anti-Compton shield in the axial dimension of the germanium element. This shield was a cylindrical section of NaI and a conical section of BGO coupled to photomultiplier tubes with preamplifiers whose outputs were summed. If a photon produced a signal in the main detector by Compton scattering, there was a high

probability that the scattered photon would interact with the shield. These events would have a signature given by a coincidence between a signal in the main detector and a signal in the shield. The coincidence events were used to block the input to the spectroscopy amplifier that processed the main detector signal and thus reduced the processing of signals that were due to Compton-scattered events that escaped the main detector. The output of the spectroscopy amplifier was read into an analog-to-digital converter and was then read into the data acquisition computer.

### *2.5. Tomography*

The projection-slice theorem states that the interior density in plane passing through an object can be reconstructed from a complete set of projections that consist of line integrals of the density along all paths that lie within that plane. In transmission computed tomography (TCT), these line integrals consist of the total attenuation of a beam with known intensity passing from a point photon source through the object and ending in a photon detector. In ECT, the source of photons is distributed through the object, and the paths of the line integrals are defined by the acceptance beam of a lead collimator placed on the detector. For NSECT, the path is defined by the beam of the stimulating neutrons. Photons whose emission is stimulated by this beam are integrated in the gamma detector. In this experiment, the phantom was scanned at 8 angular positions at 22.5° intervals and 11 spatial positions at 8 mm intervals at each angle.

### *2.6. Reconstruction*

Images were reconstructed from the projection data sets using the MLEM algorithm as derived for positron emission tomography (PET) (Lange and Carson 1984). For our implementation of this technique, the probabilities were computed using Monte Carlo techniques as developed for single photon emission computed tomography (SPECT) (Floyd *et al* 1985). While these algorithms were developed for ECT, they are appropriate for extension to NSECT due to the shared principles of stimulated emission computed tomography. The algorithm is defined below following the notation in Lange and Carson (1984).

Let $\lambda_j$ represent the image intensity in the image voxel $j$ where $j = 1, \ldots, N_J$ with $N_J$ being the number of image voxels. Let $Y_i$ represent the projection ray $i$ where $i = 1, \ldots, N_I$ with $N_I$ being the number of projection measurements. Let $p_{ji}$ equal the probability that a photon emitted from the source voxel $j$ is detected when the stimulating neutron beam is at orientation $i$. $p_{ji}$ are pre-computed using a Monte Carlo calculation that accurately models the beam shape, the voxel shape, the angular spacing, and the detector size and location. For this experiment, the reconstruction voxels are square regions, 1 mm on a side. The MLEM algorithm for the $k + 1$th iteration is then given by

$$\lambda_j^{k+1} = \frac{\lambda_j^k}{\sum_{i''}^{N_I} p_{ji''}} \sum_{i'}^{N_I} \frac{p_{ji'} Y_{i'}}{\sum_{j'}^{N_J} p_{j'i'} \lambda_{j'}^k}. \tag{1}$$

The first factor on the right side of the equal sign is the estimate of the source voxel $j$ at the $k$th iteration and the rest is the correction to it. The second factor is a normalization factor. The sum over $i'$ is of the ratio of the measured projection data at projection $i'$ ($Y_{i'}$) to the estimated projection based on the $k$th estimate of $\lambda$, weighted by the probability that this projection originates from the voxel $j$ ($p_{ji'}$).

This algorithm converges absolutely to the maximum likelihood (ML) solution (Lange and Carson 1984). For image reconstruction, the ML solution often is not what we want to visualize as it can be very noisy looking. To overcome this, the MLEM algorithm should be

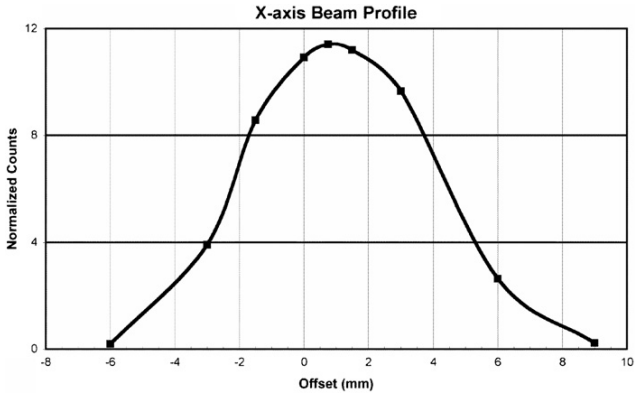


**Figure 4.** Neutron beam profile along the horizontal axis measured with a 1 mm thick plastic scintillator. The beam measured 0.70 cm at full-width at half-maximum.

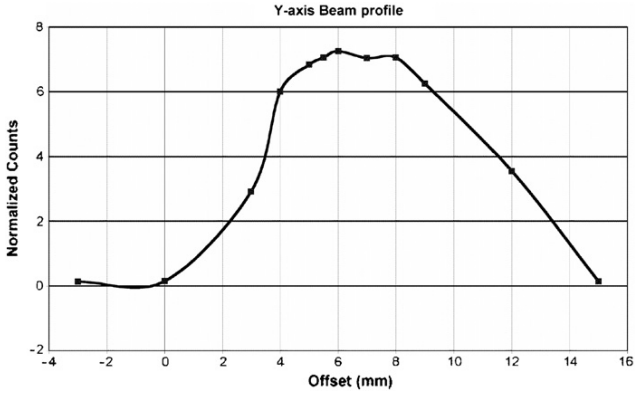


**Figure 5.** Neutron beam profile along the vertical axis measured with a 1 mm thick plastic scintillator. The beam measured 0.86 cm at full-width at half-maximum.

'regularized'. One of the easiest techniques for regularization is to terminate the iterations before the algorithm has completely converged. For our initial implementation, we performed this step visually by picking the iteration at which the structure of the phantom appeared to be well represented but where the noise was not objectionable. A uniform distribution was chosen for the initial guess of the source voxels $\lambda^{\circ}$. We examined reconstructed images at each iteration between 1 and 50 and chose 6 as the optimum. Reconstruction required about 1 s per iteration on a 1 GHz PC running Linux.

## 3. Results

### *3.1. Beam profiles*

The profiles along the horizontal and vertical axes are shown in figures 4 and 5, respectively. The beam profiles at FWHM measured as 0.70 cm in the horizontal dimension and 0.86 cm in the vertical dimension.

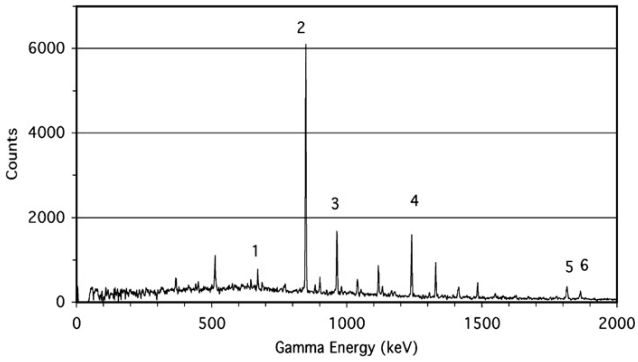


**Figure 6.** Gamma energy spectrum corrected for accidental background. Spectral lines corresponding to six states from $^{56}$Fe and $^{63}$Cu are indicated by numbers: (1) $^{63}$Cu from the first excited state to the ground state; energy 660 keV. (2) $^{56}$Fe from the first excited state to the ground state; energy 847 keV. (3) $^{63}$Cu from the second excited state to the ground state; energy 962 keV. (4) $^{56}$Fe from the third to the second excited state; energy 1239 keV. (5) $^{56}$Fe from the fourth to the second excited state; energy 1811 keV. (6) $^{63}$Cu from the sixth to the first excited state; energy 1864 keV.

### *3.2. Spectra*

Figure 6 shows the background-corrected spectrum from one spatial position at one projection angle. Six spectral lines were identified corresponding to energy transitions from iron and copper and are labeled 1–6 in the figure caption.

### *3.3. Sinograms*

The emissions from the first two states in each of $^{56}$Fe and $^{63}$Cu were summed to generate a projection profile for each element. The sums are shown plotted as sinograms for each element for angles 0° and 45° in figure 7.

From these projections, it can be seen that there is a change in the profile with a change of angle. At 0°, the iron bars are almost parallel to the beam and the iron projection shows its narrowest profile. The copper is spread fairly evenly except for some overlap near the center. As the angle increases from 0°, the copper bars become more parallel with the beam, reaching a maximum at 45° as can be seen by the narrowing of the copper peaks. The normalized yields in the sinograms represent the input projection values to the MLEM reconstruction algorithm.

### *3.4. Reconstructed images*

The reconstructed image for copper is shown in figure 8 and the image from iron is shown in figure 9. Each figure was reconstructed separately from projections for the individual element and attenuation corrected using the algorithm described in Kapadia *et al* (2005).

The combination of the two reconstructed images is shown in figure 10. Note that the combined figure was generated by adding the separately reconstructed images, and not by adding the projection data before reconstruction. Figure 11 shows the combined reconstructed image overlaid with the schematic of the phantom for comparison.

A horizontal profile of gamma intensity through the reconstructed image is shown in figure 12. From figures 11 and 12, it is evident that the reconstructed image shows a broader profile of the object than the object itself. This was entirely expected since the spatial sampling

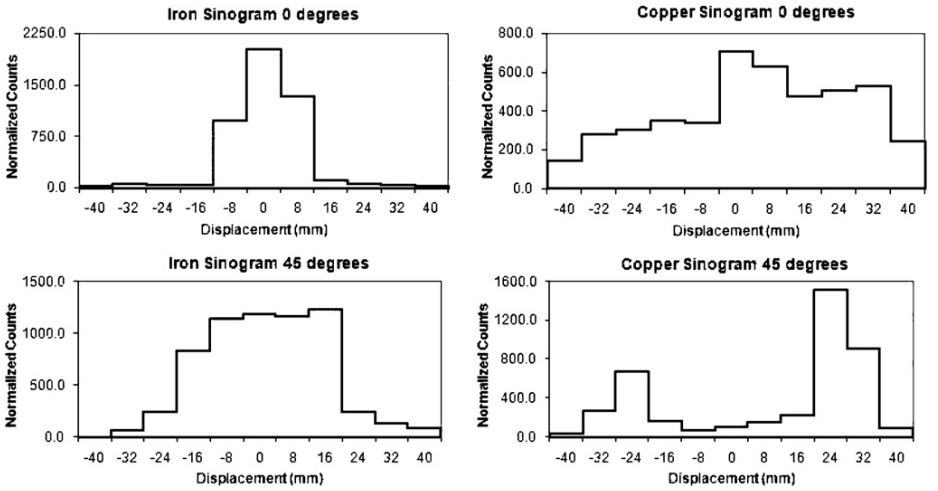


**Figure 7.** Projection profiles for iron (on the left) and copper (on the right) for projection angles 0° and 45°.

was performed in 8 mm intervals while the width of the individual bars was 6 mm. What is of note is that the result of reconstructing this under-sampled system was a smooth overestimation of size rather than an image with a significant artifact. The width of the line profiles for the two copper bars at FWHM was found to measure 1.05 cm.

## 4. Discussion

This paper presents the first tomographic image reconstruction from a multi-element phantom using NSECT. The reconstructed images demonstrate reasonable fidelity in imaging the spatial distribution of elements within an object through a non-invasive scan, especially given the sparse sampling of the data acquisition. Images were reconstructed on an $88 \times 88$ pixel matrix from an acquisition that sampled the object at only 88 projections. This reconstruction was possible due to the superior performance of the MLEM algorithm in severely under-sampled systems with non-uniform data sampling.

It can be noted that the original object space was acquired with 11 pixels on a side (11 spatial projections), but was reconstructed with 88 pixels on a side. This does not represent a true eight-fold increase in the resolution of the system. The apparent increase in resolution comes from the Monte Carlo code used to generate the probability matrix ($p_{ji}$) for the MLEM algorithm, where the image space is divided into a grid of $88 \times 88$ pixels. Probabilities are calculated for each pixel in this grid and are used to obtain pixel intensities based on the experimental projection data. As a result, the intensities in the reconstructed image are distributed into a higher resolution region than the original acquisition. The beam and acquisition parameters used in calculating MLEM probabilities were kept consistent with the experiment, i.e. 11 spatial projections at each of 8 angles. The true resolution of the system achieved in this experiment was found to be approximately 1 cm, which depends largely on the width of the neutron beam. The beam in this experiment measured 0.7 cm at FWHM in the horizontal direction, with tails extending up to 1.5 cm. The resolution obtained here is a reasonable value, given the limitations of this experimental system. It should be noted that

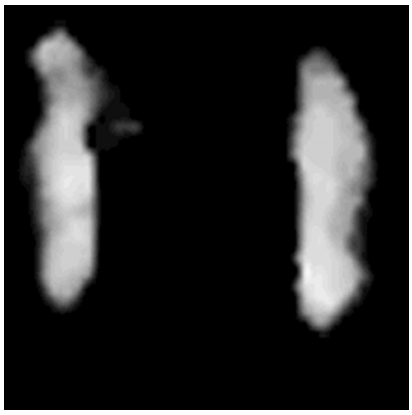

**Figure 8.** Reconstructed copper image.

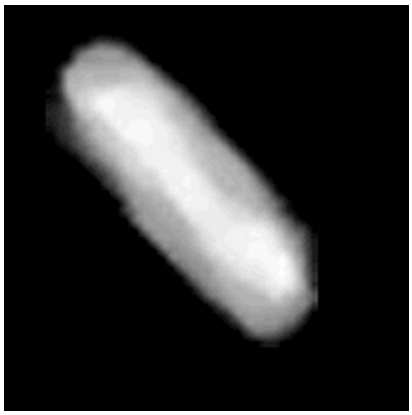

**Figure 9.** Reconstructed iron image.

**Figure 10.** Sum of the iron and copper images.

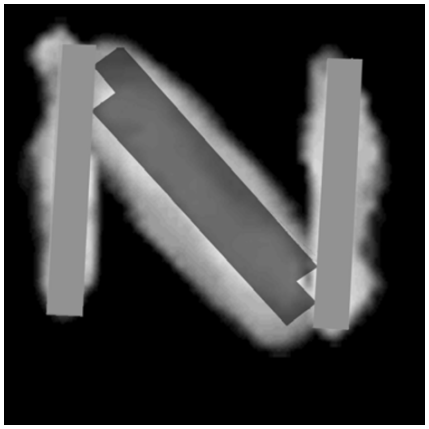

**Figure 11.** Sum of reconstructed iron and copper images overlaid with the schematic drawing of the phantom.

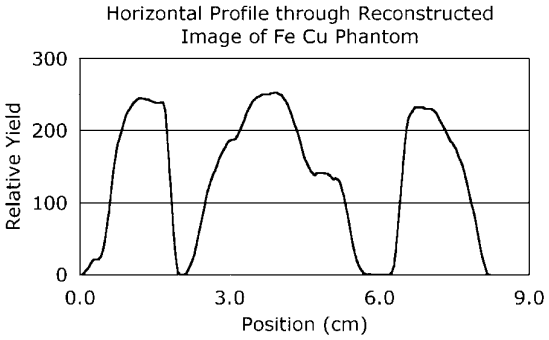


**Figure 12.** Profile through summed reconstructed image.

the sample used in this experiment describes an ideal experimental scenario with very a low scatter background due to the absence of hydrogen. In a biological sample, however, there will be considerable neutron scatter generated by hydrogen in tissue, which will affect the true resolution of the system. Neutrons that are meant to illuminate a certain voxel in the sample may scatter onto adjacent voxels containing an element of interest and induce inelastic gamma emission from that voxel. Detection of the adjacent-voxel gammas may lead to a spread in the tails of the resulting sinograms, which can lead to reduced resolution. While the resolution of the NSECT system depends primarily on the size of the incident neutron beam, the best resolution achievable in a hydrogen-rich biological sample will also be limited by the scatter noise component.

Images were corrected for attenuation using a technique developed specifically for NSECT applications (Kapadia *et al* 2005). This technique calculates the attenuation correction factors due to combined neutron and gamma attenuation effects and applies the correction to the individual projection data before it is reconstructed.

While no clinical applications have been described in this paper, the eventual goal is to develop NSECT into a clinical imaging modality. Therefore, it is necessary to address certain issues that will affect the clinical feasibility of the system. First, the neutron source used in this experiment is a Van-de-Graaff accelerator which is an immovable and expensive source that is difficult to use in a clinical system. A portable neutron source is more suited for this purpose. For dedicated applications, neutrons with energy of a few MeV are readily and economically produced using commercially available neutron generators. Neutrons of these energies can easily penetrate the body to allow good coverage of internal organs for a wide range of elements commonly observed in the human body. Second, using neutrons also leads to significant concerns about patient dose. We have performed several dose-analysis experiments using simulations in GEANT4, which have demonstrated that NSECT can detect biologically relevant concentrations of elements with doses lower than 10 mSv (Bender *et al* 2007, Kapadia 2007, Sharma *et al* 2007). Finally, NSECT must be able to achieve the sensitivity required to image clinically relevant concentrations of elements in finite localized lesions. Simulation studies performed to investigate NSECT sensitivity and resolution have demonstrated the ability to detect an iron concentration of 5 mg $g^{-1}$ in a 2 cm lesion in the liver using a 1 cm wide beam (Kapadia 2007, Kapadia *et al* 2007). Sensitivity analysis performed with the experimental system has shown the ability to detect as little as 0.3 g of sodium in a hydrogen-rich sample (Kapadia *et al* 2008). The detection of smaller lesions with lower element concentrations may be possible by optimizing the acquisition parameters to deliver maximum neutron flux to the illuminated volume of the lesion using a narrow beam while minimizing the volume of illuminated background tissue. Regardless, detection of smaller lesions with low element concentration will require improvement in the sensitivity of the current system.

The phantom used in this experiment consists of solid bars of iron and copper. While the concentration of elements and the physical size of this phantom do not represent a clinically realistic scenario, it provides an adequate starting point for proof-of-concept experimental acquisition. Future experiments will be performed with clinically relevant phantoms that model disease states in the human body.

## 5. Conclusion

This paper has described the first results from the tomographic reconstruction of a multi-element sample using NSECT. The results demonstrate proof of concept for imaging the spatial distribution of elements within a body through a non-invasive scan. The results and techniques described in this paper can be developed further to enable NSECT to evolve into a clinical diagnostic imaging modality. Work is currently underway to address the limitations of the system that will make it more suitable for clinical imaging, especially for diagnosis of breast and liver disorders.

## Acknowledgments

We, the co-authors, would like to dedicate this paper to Dr Carey E Floyd, Jr who pioneered the NSECT technique and developed it into a potential clinical diagnostic technique with several exciting applications. This paper remains Dr Floyd's last original work, which we are submitting posthumously in his name and memory. The authors would like to acknowledge the help of Robert Macri and the assistance of the faculty and staff of Triangle Universities Nuclear Laboratory who have helped with data acquisition and detector management. This

work was supported by the Department of Defense (Breast Cancer Research Program) under award number W81XWH-06-1-0484 and in part by the US Department of Energy, Office of High Energy and Nuclear Physics under grant no. DE-FG02-97ER41033.

## References

Bender J E, Kapadia A J, Sharma A C, Tourassi G D, Harrawood B P and Floyd C E 2007 Breast cancer detection using neutron stimulated emission computed tomography: prominent elements and dose requirements *Med. Phys.* **34** 3866–71

Brittenham G and Badman D 2003 Noninvasive measurement of iron: report of an NIDDK workshop *Blood* **101** 15–9

Cottingham W N and Greenwood D A 1986 *An Introduction to Nuclear Physics* (New York: Cambridge University Press)

Dobrowolski Z, Drewniak T, Kwiatek W and Jakubik P 2002 Trace elements distribution in renal cell carcinoma depending on stage of disease *Eur. Urol.* **42** 475–80

Evans R 1955 *The Atomic Nucleus* (New York: Addison-Wesley)

Floyd C E Jr, Bender J E, Sharma A C, Kapadia A, Xia J, Harrawood B, Tourassi G D, Lo J Y, Crowell A and Howell C 2006 Introduction to neutron stimulated emission computed tomography *Phys. Med. Biol.* **51** 3375–90

Floyd C E, Jaszczak R J and Coleman R E 1985 Inverse Monte Carlo: a unified reconstruction algorithm for SPECT *IEEE Trans. Nucl. Sci.* **32** 779–85

Floyd C E *et al* 2004 Neutron stimulated emission computed tomography of stable isotopes *SPIE Medical Imaging (San Diego, CA)* pp 248–54

Geraki K and Farquharson M 2002 Concentrations of Fe, Cu and Zn in breast tissue: a synchrotron XRF study *Phys. Med. Biol.* **47** 2327–39

Gregoriadis G C, Apostolidis N S, Romanos A N and Paradellis T P 1983 A comparative study of trace elements in normal and cancerous colorectal tissues *Cancer* **52** 508–19

Kak A C and Slaney M 1999 *Principles of Computerized Tomographic Imaging* (New York: IEEE)

Kapadia A J 2007 Accuracy and patient dose in neutron stimulated emission computed tomography for diagnosis of liver iron overload: simulations in GEANT4 *Biomedical Engineering* (Durham, NC: Duke University)

Kapadia A J, Floyd C E, Bender J E, Howell C R, Crowell A S and Kiser M R 2005 Non-invasive quantification of iron 56-Fe in beef liver using neutron stimulated emission computed tomography *IEEE Nuclear Science Symp. Conf. 2005* **4** 2232–4

Kapadia A J, Tourassi G D, Sharma A C, Crowell A S, Kiser M R and Howell C R 2007 Experimental detection of iron overload in liver through neutron stimulated emission spectroscopy *Phys. Med. Biol.* submitted

Kapadia A J, Sharma A C, Tourassi G D, Bender J E, Crowell A S, Kiser M R, Howell C R and Floyd C E 2006a Neutron spectroscopy of mouse using neutron stimulated emission computed tomography (NSECT) *IEEE Nuclear Science Symp. Conf. Rec. 2006* **6** 3546–8

Kapadia A J, Sharma A C, Tourassi G D, Bender J E, Crowell A S, Kiser M R, Howell C R and Floyd C E 2006b Neutron stimulated emission computed tomography (NSECT) for early detection of breast cancer *IEEE Nuclear Science Symp. Conf. Rec. 2006* **6** 3928–31

Kapadia A J, Sharma A C, Tourassi G D, Bender J E, Crowell A S, Kiser M R, Howell C R and Floyd C E 2006c Non-invasive estimation of potassium (39 K) in Bovine liver using neutron stimulated emission computed tomography (NSECT) *IEEE Nuclear Science Symp. Conf. Rec. 2006* **4** 2076–8

Kapadia A J, Sharma A C, Bender J E, Tourassi G D, Howell C R, Crowell A S, Kiser M R, Harrawood B P and Floyd C E 2008 Neutron stimulated emission computed tomography for diagnosis of breast cancer *IEEE Trans. Nucl. Sci.* **55** 501–9

Knoll G F 2000 *Radiation Detection and Measurement* (Hoboken, NJ: Wiley)

Lange K and Carson R 1984 EM reconstruction algorithms for emission and transmission tomography *J. Comput. Assist. Tomogr.* **8** 306–16

National Nuclear Data Center B N L 2007 *National Nuclear Database NuDat 2.3*, url: http://www.nndc.bnl.gov/nudat2, Accessed 10 November 2005

Ng K H, Bradley D A and Looi L M 1997 Elevated trace element concentrations in malignant breast tissues *Br. J. Radiol.* **70** 375–82

Ng K H, Bradley D A, Looi L M, Seman Mahmood C and Khalik Wood A 1993 Differentiation of elemental composition of normal and malignant breast tissue by instrumental neutron activation analysis *Appl. Radiat. Isot.* **44** 511–6

NIST 1990 *XCOM: Photon Cross Sections Database*, url: http://physics.nist.gov/PhysRefData/Xcom/Text/XCOM.html, Accessed 10 November 2005

Rizk S and Sky-Peck H 1984 Comparison between concentrations of trace elements in normal and neoplastic human breast tissue *Cancer Res.* **44** 5390–4

Schwartz A and Fink R 1974 Trace elements in normal and malignant human breast tissue *Surgery* **76** 325–9

Sharma A C, Harrawood B P, Bender J E, Tourassi G D and Kapadia A J 2007 Neutron stimulated emission computed tomography: a Monte Carlo simulation approach *Phys. Med. Biol.* **52** 6117–31

Stedman J D and Spyrou N M 1995 Major and trace element concentration differences between right and left hemispheres of the 'normal' human brain *Nutrition* **11** 542–5

IOP PUBLISHING PHYSICS IN MEDICINE AND BIOLOGY

Phys. Med. Biol. **53** (2008) 2633–2649 doi:10.1088/0031-9155/53/10/013

# Experimental detection of iron overload in liver through neutron stimulated emission spectroscopy

**A J Kapadia**[1,2,5] **, G D Tourassi**[1]**, A C Sharma**[1,2]**, A S Crowell**[3,4]**, M R Kiser**[3,4] **and C R Howell**[3,4]

[1] Department of Radiology, Duke Advanced Imaging Laboratories, Durham, NC 27705, USA
[2] Department of Biomedical Engineering, Duke University, Durham, NC 27708, USA
[3] Department of Physics, Duke University, Durham, NC 27706, USA
[4] Triangle Universities Nuclear Laboratory, Duke University, Durham, NC 27706, USA

E-mail: anuj.kapadia@duke.edu

Received 6 November 2007, in final form 4 April 2008
Published 28 April 2008
Online at stacks.iop.org/PMB/53/2633

**Abstract**

Iron overload disorders have been the focus of several quantification studies involving non-invasive imaging modalities. Neutron spectroscopic techniques have demonstrated great potential in detecting iron concentrations within biological tissue. We are developing a neutron spectroscopic technique called neutron stimulated emission computed tomography (NSECT), which has the potential to diagnose iron overload in the liver at clinically acceptable patient dose levels through a non-invasive scan. The technique uses inelastic scatter interactions between atomic nuclei in the sample and incoming fast neutrons to non-invasively determine the concentration of elements in the sample. This paper discusses a non-tomographic application of NSECT investigating the feasibility of detecting elevated iron concentrations in the liver. A model of iron overload in the human body was created using bovine liver tissue housed inside a human torso phantom and was scanned with a 5 MeV pulsed beam using single-position spectroscopy. Spectra were reconstructed and analyzed with algorithms designed specifically for NSECT. Results from spectroscopic quantification indicate that NSECT can currently detect liver iron concentrations of 6 mg $g^{-1}$ or higher and has the potential to detect lower concentrations by optimizing the acquisition geometry to scan a larger volume of tissue. The experiment described in this paper has two important outcomes: (i) it demonstrates that NSECT has the potential to detect clinically relevant concentrations of iron in the human body through a non-invasive scan and (ii) it provides a comparative standard to guide the design of iron overload phantoms for future NSECT liver iron quantification studies.

(Some figures in this article are in colour only in the electronic version)

[5] Address for correspondence: 2424 Erwin Road, Suite 302, Hock Plaza, Durham, NC 27705, USA.

  

## 1. Introduction

Iron overload disorders affect a significant part of the American population today. About 5 out of every 1000 Caucasians are susceptible to developing the disease (NIH 2007). These disorders may be due to genetic or acquired factors and cause an increase in the body's total iron content. In advanced stages of iron overload, the total body iron content is seen to increase by up to five times over normal, i.e. from 3 to 4 g to over 20 g total (Powell 2002, 2005, Powell *et al* 1998). The excess iron is stored in several vital organs in the body, especially in the liver, heart and spleen, and may cause extensive tissue damage, liver cirrhosis, cardiac failure, hepatic failure and hepatocellular carcinoma (Powell 2002, 2005, Powell *et al* 1998). Accurate measurement of the body's iron content is vital for effective diagnosis and management of the iron overload disorder. Since a significant part of the body's total iron is stored in the liver, an estimate of the liver's iron concentration is used as a measure of the body's total iron content. Currently, this measurement is obtained using an invasive liver biopsy, which is an unpleasant procedure associated with several potential complications. Repeated biopsy is required for monitoring the disease. The morbidity associated with performing repeated biopsy creates two obstacles: (1) in following the progress of patients obtaining therapeutic treatments and (2) in developing new forms of treatment for the disorder. Additionally, quantification results from biopsy suffer from as much as 20% margins of error in the presence of cirrhosis (Villeneuve *et al* 1996), primarily due to errors in tissue sampling (Bonkovsky *et al* 1999, Ratziu *et al* 2005, Regev *et al* 2002). There is an imminent need for an alternative technique to estimate liver iron concentration without a biopsy. A workshop conducted by the National Institute of Diabetes and Digestive and Kidney Diseases (NIDDK) to assess the needs for techniques to determine the iron concentration in the body concluded that 'physicians have a pressing clinical need for quantitative means of measuring body storage iron that are non-invasive, safe, accurate, and readily available to improve the diagnosis and management of patients with iron overload, including those with hereditary hemochromatosis, thalassemia major, sickle cell disease, aplastic anemia, myelodysplasia and other disorders' (Brittenham and Badman 2003).

Several different techniques have been attempted to detect and quantify the iron concentration in the liver *in vivo*, for example, x-ray computed tomography, MRI, MR spectroscopy, super-conducting quantum interference susceptometry (SQUID) and nuclear resonance scattering (NRS) (Alustiza *et al* 2004, Avrin and Kumar 2007, Bonkovsky *et al* 1999, Brittenham *et al* 2001, Cecchin *et al* 1990, Chapman *et al* 1980, Chezmar *et al* 1990, Dixon *et al* 1994, Gandon *et al* 2004, Guyader *et al* 1992, Howard *et al* 1983, Liu *et al* 1996, Nielsen *et al* 2000, 2002a, 2002b, Perrimond *et al* 1991, Sheth 2003, Vartsky *et al* 1979, 1982, Wielopolski *et al* 1985). While each has had varying degrees of success, few have found widespread acceptance in the clinical environment. Both x-ray CT and MRI lack the sensitivity required for detecting mild to moderate degrees of iron overload, and MRI also shows reduced sensitivity in cases of severe iron overload (Angelucci *et al* 1997, Chapman *et al* 1980, Chezmar *et al* 1990, Howard *et al* 1983). In MR spectroscopy (MRS), the low signal from bound Fe makes quantification studies difficult. MRS also has limited resolution (larger than 1 cm) (Wang *et al* 2002). While SQUID has found some success in detecting liver iron, there are only about four SQUID facilities in the world that offer iron overload testing, making it difficult to translate into a widely used clinical alternative. NRS has achieved some success in patients with iron overload but with high levels of dose (Wielopolski *et al* 1985).

Neutron spectroscopic techniques have demonstrated great potential in detecting element concentrations within biological tissue. Neutron activation analysis (NAA) and *in vivo* neutron activation analysis (IVNAA) have been used in several studies to map the elemental structure

of normal and diseased tissue in humans (McNeill *et al* 1990, Katoh *et al* 2003, Knight *et al* 1986, Ng *et al* 1993, Yukawa *et al* 1980, Zeisler *et al* 1993). Many of these studies have been successful in quantifying a large number of elements, and some have achieved sensitivity of a few micrograms (Arnold *et al* 2002). One NAA study has reported a detection limit of 58–60 mg Fe in a sample of mass 1.5 kg, corresponding to a concentration of 0.04 mg $g^{-1}$ (McNeill *et al* 1990). Patient dose values associated with neutron activation methods have been reported to be less than 10 mSv (Mattsson and Thomas 2006). However, despite their apparent success, neutron activation techniques have not been widely accepted in the clinic.

We are developing a neutron spectroscopic technique called neutron stimulated emission computed tomography (NSECT), which has the potential to diagnose iron overload in the liver at clinically acceptable levels of dose through a non-invasive *in vivo* scan (Floyd *et al* 2006, 2008, Kapadia *et al* 2005, 2008). The technique uses fast *N*eutrons to *S*timulate elements in the body to *E*mit characteristic gamma radiation, which is acquired and reconstructed using *C*omputed *T*omography. NSECT utilizes inelastic scatter interactions between atomic nuclei in the sample and incoming fast neutrons to non-invasively determine the concentration of elements in the sample. The working principle is described briefly as follows. Incoming fast neutrons interact with atomic nuclei in the sample through inelastic scatter interactions, exciting the nuclei to higher energy levels. The excited nuclei rapidly decay to their ground states emitting gamma rays with energy equal to the difference between the excited and ground energy states. These energy states are quantized, well known and unique to most elements and isotopes. The emitted gamma rays are detected by an energy-sensitive gamma-ray detector. Measuring the energy and intensity of the emitted gamma rays provides an accurate estimate of the concentration of the emitting atoms in the target tissue.

Although the NSECT technique incorporates tomographic ability, this experiment discusses a simple non-tomographic application as a first step toward clinical translation of the technique. The non-tomographic approach, henceforth referred to as single-position spectroscopy (or simply spectroscopy), involves scanning the sample at only a single position without translation or rotation. This approach can be used for iron quantification in cases of uniform iron overload, where the distribution of iron in the entire region of the liver being scanned is uniform. In cases where the iron is distributed in non-uniform regions of varying iron content, a tomographic scan is required to determine the concentration and location of iron in each such region in the liver. While the iron storage mechanism of the liver is generally well understood, it has not yet been clearly demonstrated whether the excess iron is stored uniformly or in localized regions of varying concentration within the liver. NSECT has the ability to investigate both scenarios by generating quantitative tomographic images of iron distribution in the liver. Each of the two acquisition methods, single-position spectroscopy and multi-position tomography, has the potential for clinical applicability in a different scenario. For the purpose of this paper, the readers should note that although the term NSECT appears when referring to the imaging technique, acquisition has been performed using single-position spectroscopy. Therefore, no tomographic results are presented here. Tomography experiments and resulting images have been described in other publications (Kapadia 2007, Sharma *et al* 2007, Floyd *et al* 2008).

In this paper, we present results from a study investigating the feasibility of detecting elevated iron concentrations in the liver through NSECT. As this technique is still in its initial stages, feasibility testing is essential in working toward the final goal of implementing a low-dose scanning solution for detecting and monitoring iron concentrations in the liver. In earlier work, we have demonstrated the technique's ability to perform spectroscopic quantitative evaluation in a variety of samples (Floyd *et al* 2004, 2006, Kapadia *et al* 2005, 2006c), most of which have been high-density elements with very low hydrogen content. Hydrogen, a

large constituent of biological tissue, is a primary generator of neutron scatter, which adds a significant level of noise to the NSECT system. Neutrons scattering by the sample interact with materials around the target (including instrumentation apparatus, shielding material and room constituents) leading to inelastic scatter gamma-ray emission from these materials, which is detected as noise along with signal from the sample. This study aims at achieving two objectives: (i) investigating the feasibility of detecting liver iron in the presence of scatter noise generated by the human torso and (ii) obtaining an estimate of the minimum concentration of iron that can be detected in the human torso with the current acquisition setup.

## 2. Materials and methods

### *2.1. Materials*

Bovine liver was used as liver tissue of choice in this experiment for several reasons. First, fresh bovine liver is easily available in large quantities. Second, there is considerable overlap in elements reported in the human and bovine liver (ICRU 1992, NIST). Third, it is easy to create artificial iron overload model phantoms by inserting iron into required regions of the bovine liver phantom. Thus, even though this study has been performed on a bovine liver model, the results are broadly transferable to a human liver.

### *2.2. Disease model phantom*

A model of iron overload in the human body was created using bovine liver tissue housed inside a human torso phantom, with uniform iron overload in the form of a solid plate of natural density iron. Due to the geometry of spectroscopic scanning, the concentration of excess iron was distributed uniformly across the entire volume of the liver tissue illuminated by the neutron beam. A uniform iron distribution forms one possible scenario of iron overload in the liver and can be detected through single-position spectroscopy without the need for a tomographic scan. As this scenario is the focus of the present study, a uniform iron distribution model was selected for this experiment to evaluate the feasibility of the spectroscopic technique. The construction of the phantom is described below.

The human torso phantom, shown in figure 1, is a dual-chamber plastic phantom of an adult human torso originally designed for nuclear medicine studies. It has two primary chambers—an outer chamber representing an adult torso and an inner chamber representing a typically sized adult human liver. The torso chamber measures 12 inches in height, 10 inches in diameter, 7.5 inches in depth, and has a volume of 11 200 ml. The inner liver chamber measures 5.5 inches in height and has a volume of 1520 ml. Volumes of both chambers were measured individually by measuring the amount of liquid required to fill each chamber separately. For the spectroscopic neutron scan, the outer torso chamber was filled with water and the inner liver chamber was filled with fresh bovine liver tissue.

Natural density iron was used to create a uniform distribution of iron overload in the liver chamber of the phantom. A square iron plate measuring 5 cm in height and 2.4 mm in thickness was inserted in a region of the liver illuminated by the neutron beam. The geometry of the scan was aligned to ensure that the beam was perpendicular to the face of the iron plate, and the entire beam illuminated the thickness of the plate. As the phantom was scanned with single-position spectroscopy, any iron in the path of the neutron beam would appear to be distributed along the entire volume of the liver illuminated by the neutron beam, thereby modeling a uniform distribution of iron overload in the liver. The acquisition geometry is shown in figure 2. In the iron overload phantom in this experiment, 4.18 g of iron were present in 33.2 g of

**Figure 1.** The dual-chamber human torso plastic phantom showing its two chambers. The outer chamber measuring 11 200 ml corresponds to an adult human torso, and the inner chamber measuring 1520 ml represents a typical-sized adult human liver. Both chambers can be filled separately with any desired material.

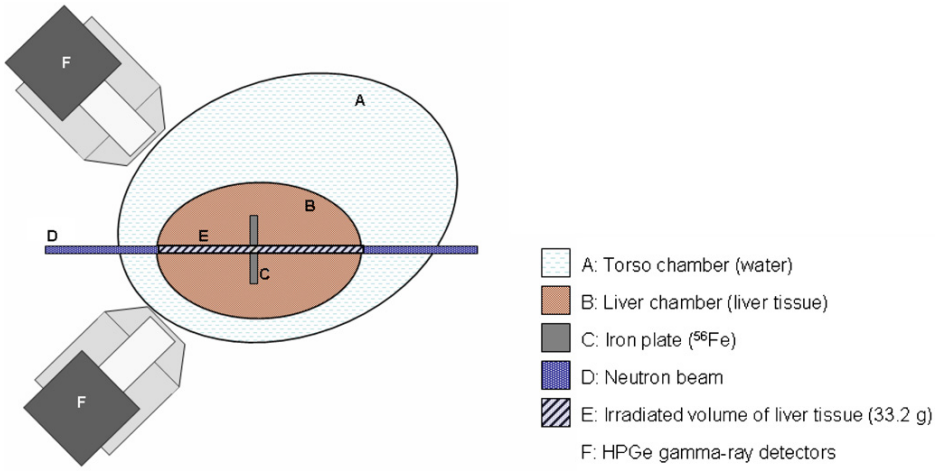


**Figure 2.** Schematic of the NSECT acquisition geometry for the liver scan. Iron overload was created in the liver tissue using a natural density iron plate. The mass of iron in the path of the neutron beam appeared to be distributed uniformly within the illuminated volume of the liver tissue (shown using gray stripes). The iron concentration obtained with this acquisition geometry was determined to be 126.1 mg $g^{-1}$.

tissue illuminated by a 1.3 cm $\times$ 1.7 cm rectangular neutron beam. From these measurements, the iron concentration in this phantom was calculated as 126.1 mg per gram (mg $g^{-1}$) of liver tissue. As this experiment is the first study of its nature with no previously known estimates of concentration for comparison, the value of iron concentration used here was set high enough to be detected with adequate statistical accuracy in the gamma-ray detectors.

The natural density iron plate is a mixture of the naturally occurring stable isotopes of iron, $^{54}$Fe (5.8%), $^{56}$Fe (91.8%), $^{57}$Fe (2.2%) and $^{58}$Fe (0.3%). While all four isotopes of iron are present in the sample, our early experiments and simulation studies demonstrate that at incident neutron energies of 5 MeV, gamma lines can be detected from four prominent transitions in $^{56}$Fe (at 847 keV, 1038 keV, 1238 keV and 1811 keV) and one in $^{54}$Fe (at 1408 keV) (Floyd *et al* 2008, Kapadia 2007). Energy transitions from the remaining isotopes are not detected clearly, likely due to a combination of low neutron cross-section and low concentrations of the remaining isotopes in the sample. Further, the five prominent transitions described above can be detected only when the sample contains a significantly high concentration of iron (as in the case of natural density solid iron) and is scanned in a noise-free environment, i.e. one that does not generate a large quantity of neutron scatter. In scans of biological tissue containing modest quantities of iron, only the first excited state in $^{56}$Fe (at 847 keV) is observed clearly (Kapadia *et al* 2005). Therefore, only the 847 keV gamma line from $^{56}$Fe has been reported and used in the quantification experiment. The 847 keV gamma line is relatively free from contaminating contributions from other elements in the sample. For example, radioactive manganese ($^{56}$Mn) emits gamma ray at 847 keV and can lead to errors in iron measurement through contamination of the 847 keV peak. However, a combination of very low $^{55}$Mn content in the sample and selection of a monochromatic fast-neutron beam makes the contribution of $^{55}$Mn negligible.

### *2.3. Experimental setup*

The NSECT experiments in this study were performed at the Triangle Universities Nuclear Laboratories at Duke University, Durham, NC. The experimental setup contains three major components, the neutron source, gamma detectors and a neutron-flux monitor. A schematic of the acquisition system is shown in figure 2 and a brief description of the individual components is provided below. Detailed description of the NSECT system hardware has been provided elsewhere (Floyd *et al* 2004, 2006, 2007, Kapadia *et al* 2008)

A Van-de-Graaff tunable accelerator was used to generate a 5 MeV pulsed neutron beam through the $^{2}$H(d, n)$^{3}$He reaction by directing an accelerated and pulsed beam of deuterons onto a deuterium gas target. While the tandem Van-de-Graaff accelerator allows the production of mono-energetic neutron beams with energies between 3.5 MeV and 23 MeV, an energy of 5 MeV was selected for this study in order to excite energy levels in $^{56}$Fe (at 847 keV) and $^{12}$C (at 4.4 MeV). The beam was pulsed to provide 2 ns wide bunches at the target, with a repetition rate adjustable from 2.5 MHz down to 39 kHz. Beam pulsing was used to facilitate time-of-flight (TOF) background correction through measurement of neutron and gamma TOF. Gamma emission originating from neutron interactions observed in beam pulses was acquired and retained as foreground data, while data acquired during the time gap between pulses were used to obtain a measure of background effects and subtracted from the foreground data. The TOF application for NSECT has been described in detail in an earlier study (Floyd *et al* 2007). The 5 MeV neutron beam was collimated to a rectangular profile measuring 1.7 cm in height and 1.3 cm in width at the target.

Two high-purity germanium (HPGe) gamma-ray detectors were used to acquire the emitted gamma spectrum showing gamma lines corresponding to energy transitions in various samples. The HPGe detectors used in this study were two-fold segmented clover detectors (CLOVER 4×50×80 SEG2) manufactured by Canberra Eurysis S.A. Each detector comprised four co-axial n-type germanium crystals mounted together in the shape of a four-leaf clover, with each germanium crystal measuring 50 mm in diameter and 80 mm in length. The detectors were rated for minimum relative efficiency of 22% and full width at half maximum less than or equal to 2.25 keV for 1.33 MeV gamma rays of $^{60}$Co. Both detectors used in

this study were calibrated against known energy peaks from a $^{22}$Na source and positioned at $\pm 135^{\circ}$ from the incident neutron beam. Backward angles of $135^{\circ}$ were selected to minimize detector activation and detector damage from forward scattering neutrons.

Neutron beam flux was monitored with a 1.6 mm thick plastic scintillator attached to a photomultiplier tube placed before the sample. Neutron attenuation from this scintillator was measured to be less than 0.5% at 5 MeV. Data from the scintillator were used to obtain an estimate of the total number of neutrons incident on the sample, which is required for dose calculation and to correct for minor temporal fluctuations in the flux of the neutron beam.

The iron overload phantom was scanned with the 5 MeV pulsed beam using single-position spectroscopy. Scanning was continued until 95% statistical accuracy was obtained in the gamma-ray detectors for gamma energy peaks corresponding to excited states from natural iron ($^{56}$Fe). After the torso phantom scan was completed, the iron plate was removed from the phantom and scanned again to obtain a spectrum corresponding to the iron plate without scatter from the torso. This iron spectrum was compared with the overload torso phantom spectrum to get an estimate of scatter generated by an adult human torso. Source and detector calibration was left unchanged between the two sample scans.

### *2.4. Data analysis*

Data obtained in this experiment were reconstructed and analyzed in three steps, spectral reconstruction, background correction and spectral analysis as follows.

*2.4.1. Spectral reconstruction.* Spectra were reconstructed from acquired data using SpecTcl to plot gamma counts detected as a function of energy for each detector. SpecTcl is a nuclear event data acquisition and analysis package developed at the National Superconducting Cyclotron Laboratory at Michigan State University (Fox *et al* 2004). The software package facilitates acquisition and storage of raw nuclear data using an object-oriented C$^{++}$ framework and allows online and offline retrieval of complete and partial data sets. Visualization is enabled through the Xamine display program. Data sets can be retrieved and analyzed using any combination of acquisition parameters and displayed with features such as spectrum overlay of multiple acquisitions. Spectra were reconstructed separately for each of the eight crystals of the HPGe detectors and summed to obtain the final energy spectrum.

*2.4.2. Background correction.* Background correction was performed using the time-of-flight (TOF) subtraction technique (Håkansson 1999) and sample-out background subtraction techniques as applied to NSECT (Floyd *et al* 2007). TOF gating information was acquired using the pulsed neutron beam simultaneously with the sample data and was used to reduce time-uncorrelated background from the resulting gamma spectra. The TOF technique is easily implemented in TUNL through readily available beam pulsing and TOF hardware, and provides the added advantage of being able to acquire background simultaneously with the foreground without the need for an additional sample-out scan. Figure 3 shows a TOF spectrum from the iron overload phantom, acquired during time gaps between neutron beam pulses. Three primary background effects can be observed in the spectrum: (a) a sharp peak at 2224 keV originating from neutron capture on hydrogen, (b) a sharp peak at 1461 keV originating from decay of $^{40}$K in the acquisition room and (c) a gradual rise in gamma counts observed at lower energies originating from Compton scattering of detected gamma rays. The first two effects directly cancel out after TOF subtraction while the Compton scatter effect is corrected using a polynomial curve-fit subtraction. The latter subtraction technique, described in Kapadia *et al* (2008), uses a polynomial curve fit to obtain an estimate of the Compton

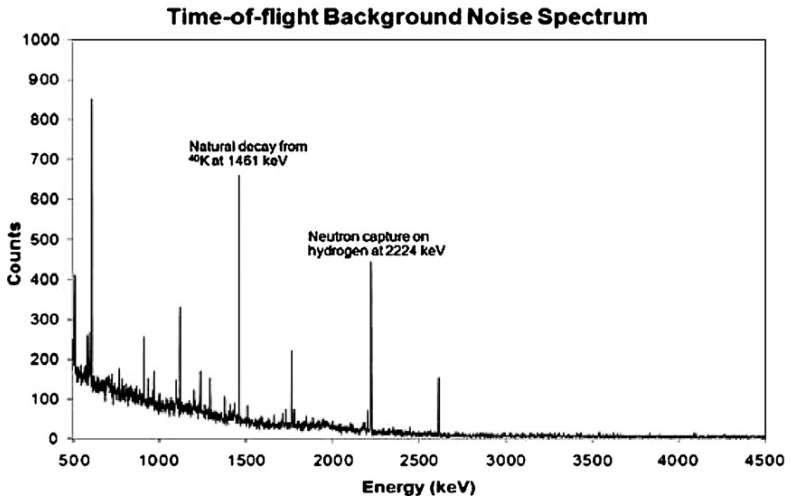


**Figure 3.** Time-of-flight background noise observed during experimental scanning of the iron-overloaded liver. The spectrum shows gamma counts that are observed during the time gaps between neutron pulses. Noise effects that dominate the spectrum include neutron capture on hydrogen (at 2.2 MeV) and natural decay of $^{40}$K from the experiment room (labeled peaks). The remaining peaks in the spectrum are primarily from germanium in the detectors. The spectrum is used to subtract these noise effects from the torso signal spectrum.

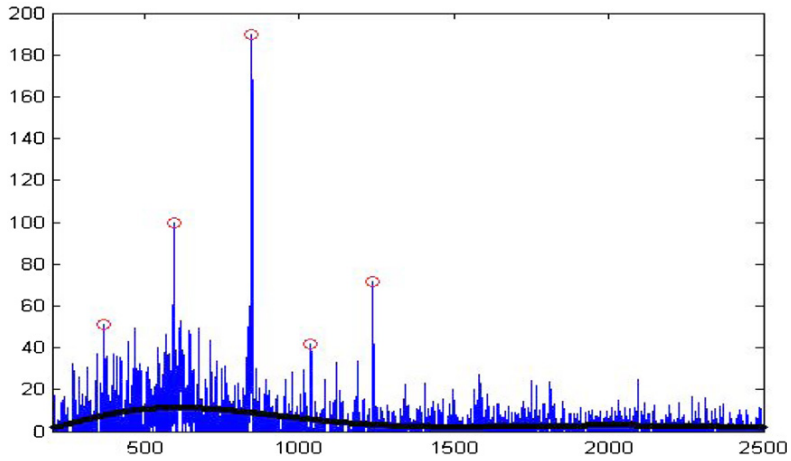


**Figure 4.** Example of automatic peak-detection algorithm applied to a sample iron spectrum. The spectrum is background-corrected. The superimposed black line shows the polynomial curve-fit pseudo-background used for calculating the peak-defining threshold. Energies identified as peaks are indicated by circles. For this iron spectrum, the identifier shows peaks at 369 and 595 keV corresponding to germanium, and at 847, 1037 and 1238 keV corresponding to iron.

scatter background (similar to the solid black line in figure 4) and subtracts the background from the signal.

TOF gating and subtraction was performed using SpecTcl. An estimate of the room-related sources of background was obtained by acquiring data from the empty room at the

beginning of the scan. While these data are able to account for room-related sources of background such as decay of $^{40}$K, they cannot take into account the sample-dependent noise generated by interactions between neutrons scattered in the phantom and elements in detection instruments around the experiment area. For example, this empty room acquisition is not able to account for energy peaks in the spectra resulting from germanium in the detectors, aluminum in the detector mounting assembly and hydrogen from neutron capture in water amongst other elements. These sources of noise may be corrected by acquiring a gamma spectrum from a water sample of the same mass as the torso and subtracting it from the liver spectrum. However, this correction has not been performed in this experiment in order to be able to evaluate the feasibility of detecting iron overload in the presence of this sample-dependent noise.

*2.4.3. Spectral analysis.* Background-corrected spectra from each scan were analyzed for the presence of gamma energy peaks using an automatic peak-detection algorithm designed for NSECT (Bender *et al* 2007). As originally designed, this algorithm looks for energy peaks with heights above a user-specified minimum threshold within a user-specified energy window and identifies energy peaks whose two-tailed $p$-value above the underlying background is $p \leqslant 0.05$ using a $z$-score test. Energy peaks with heights below the absolute threshold are not reported. While this technique works adequately for small energy ranges ($\sim$1 MeV), it presents a potential problem for the larger energy range ($\sim$4 MeV) used in this analysis. The HPGe gamma detectors used during data acquisition exhibit an energy-dependent decrease in efficiency of gamma-ray detection, where the detection efficiency of the crystal drops off as a function of the gamma energy. As a result, the detection efficiency at the upper end of the spectrum is lower, leading to gamma lines at the upper end of the spectrum being reported with lower peak values. Therefore, even though an energy peak may be real and significant, using an absolute detection threshold may lead to missed identification of a peak at higher energies. To prevent this missed identification event, the peak-detection algorithm was modified as follows. A pseudo-background was modeled using a 5th degree polynomial curve fit to the detector data. The peak height threshold was determined dynamically as a function of this pseudo-background for each channel of the detector. Thus, as the heights of the detected gammas at higher energies decreased, the value of the pseudo-background decreased simultaneously, thereby decreasing the threshold value for peak identification at higher gamma energies. An example of the algorithm's operation applied to the Fe plate spectrum is shown in figure 4. The solid (blue) line shows the original background-corrected spectrum. The black line shows the pseudo-background fit used to generate the peak threshold. Energy peaks identified with $p$-values $\leqslant$0.05 are shown by the circles. For this experiment, the peak threshold was set at a factor of 4 higher than the background, and the element detection window width was set at $\pm$6 keV. These values were optimized through a separate study (Bender *et al* 2007). Note that the pseudo-background employed here was used only to determine the peak-identification threshold only. No background correction or subtraction was performed using this fit.

Energy values reported as significant peaks were then compared against Brookhaven National Laboratory's National Nuclear Database (National Nuclear Data Center 2007) using the gamma level search tool web interface to obtain a list of probable element matches.

### *2.5. Sample validation through NAA analysis*

The liver sample was sent for neutron activation analysis (NAA) to determine the naturally occurring concentration of iron in the tissue in order to ensure that the iron detected in the torso scan was from the iron plate alone and not from a prior abnormally high liver

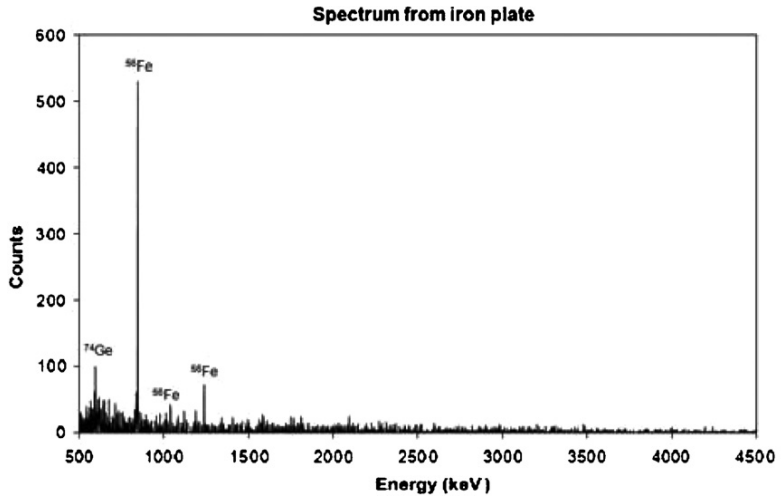


**Figure 5.** Gamma energy spectrum from the solid iron plate showing peaks corresponding to $^{56}$Fe from the sample. An energy peak is also seen for $^{74}$Ge from the detector.

**Table 1.** List of elements identified in the NSECT spectrum of the liver and confirmed through neutron activation analysis (NAA). The NSECT element identification was performed prior to NAA of the sample to eliminate identification bias.

| Element | Energy peaks (keV) | Concentration reported in NAA (mg g$^{-1}$) |
|---|---|---|
| Cl | 1944 | 0.90 |
| Cu | 422, 645 | 0.09 |
| Fe | 847 | 0.06 |
| K | 1377, 1960 | 3.18 |
| Na | 440, 629 | 0.68 |
| Zn | 629 | 0.05 |

iron concentration. NAA is considered the gold standard in tissue element quantification and demonstrates microgram sensitivity for several elements of biological interest including iron. NAA sensitivity for $^{56}$Fe has been reported as 90 mg with a short irradiation (Madison Nuclear Reactor Laboratory). A multi-element NAA analysis was performed to determine the quantity of iron and identify other elements in the liver sample as follows. A wet liver tissue sample was placed in a plastic vial and irradiated for 30 min with a flux of $1.8 \times 10^{12}$ n cm$^{-2}$ s$^{-1}$. Activity from the isotopes produced was counted at different times after irradiation, ranging from 1 min (for short-lived isotopes) to 3 weeks (for long-lived isotopes). The detected isotopes were used to establish a measure of the mass and concentration of the element present in the liver tissue sample. The NAA multi-element survey was able to confirm the presence of six elements detected in the NSECT scan (shown in table 1).

## 3. Results

### *3.1. Reconstructed spectra*

Figure 5 shows the gamma energy spectrum from the NSECT acquisition of the 2.4 mm thick Fe plate. Peaks for $^{56}$Fe are seen at 847 keV, 1039 keV and 1238 keV. The $^{56}$Fe peak at

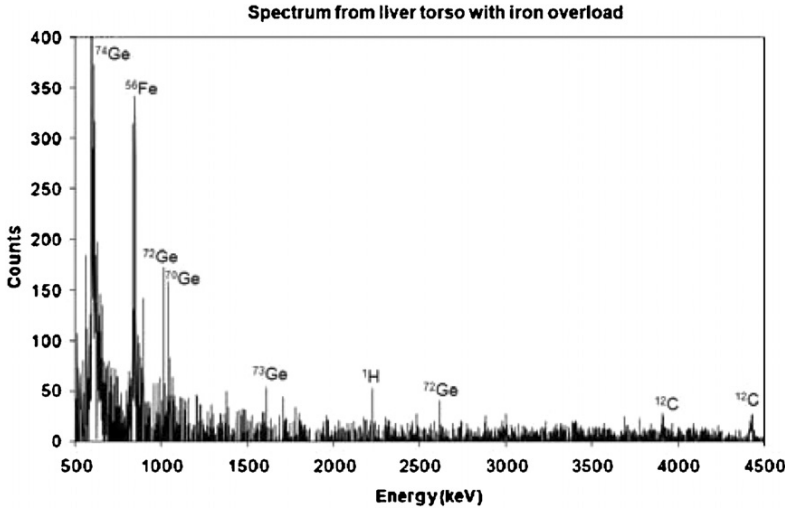


**Figure 6.** Gamma energy spectrum from the uniform iron overload torso phantom, showing peaks corresponding to several elements. The peak at 847 keV corresponds to $^{56}$Fe. Peaks are also seen for Ge from the detector, and $^{12}$C and $^{1}$H from the tissue.

1811 keV was not strong enough to be detected by the peak-detection algorithm. A total of 1276 gamma photons were counted in the peak at 847 keV, corresponding to a known concentration of 4.18 g of $^{56}$Fe. The spectrum also showed a peak at 595 keV, corresponding to $^{74}$Ge in the detector.

Figure 6 shows the gamma energy spectrum from the iron-overloaded torso phantom. A strong peak was detected at 847 keV corresponding to 4.18 g of $^{56}$Fe. A total of 1000 gamma photons were counted in this peak. Energy peaks were also identified for several other elements including $^{74}$Ge and $^{76}$Ge from the gamma-ray detectors, $^{42}$K, $^{1}$H (neutron capture) and $^{12}$C from the phantom. A list of the elements detected in the NSECT spectrum and verified through the NAA multi-element survey is given in table 1.

Six elements detected in the NSECT spectrum were confirmed through NAA. While each of these elements was present in the sample, their concentration was too low to be accurately quantified through NSECT. It can be noted from table 1 that the value of iron in the sample is extremely low. This value represents the naturally occurring concentration of iron in the liver tissue without the overload condition.

### *3.2. Spectral analysis of iron peaks*

As one of the designated criteria in the peak-detection algorithm was that the peak must be detected above background with $p$-value $\leqslant 0.05$, all the peaks reported in the spectral analysis have $p \leqslant 0.05$ calculated using a $z$-score test for difference of means. For the peak at 847 keV corresponding to $^{56}$Fe, 1000 peak counts were detected above an underlying background of 120 counts, corresponding to $p \leqslant 0.001$. The underlying background counts were measured using the pseudo-background polynomial curve fit used to model the dynamic threshold as shown in figure 4.

Table 2 presents an estimate of the neutron attenuation observed in the torso phantom calculated using the plate of natural iron. Gamma counts were obtained from the iron plate

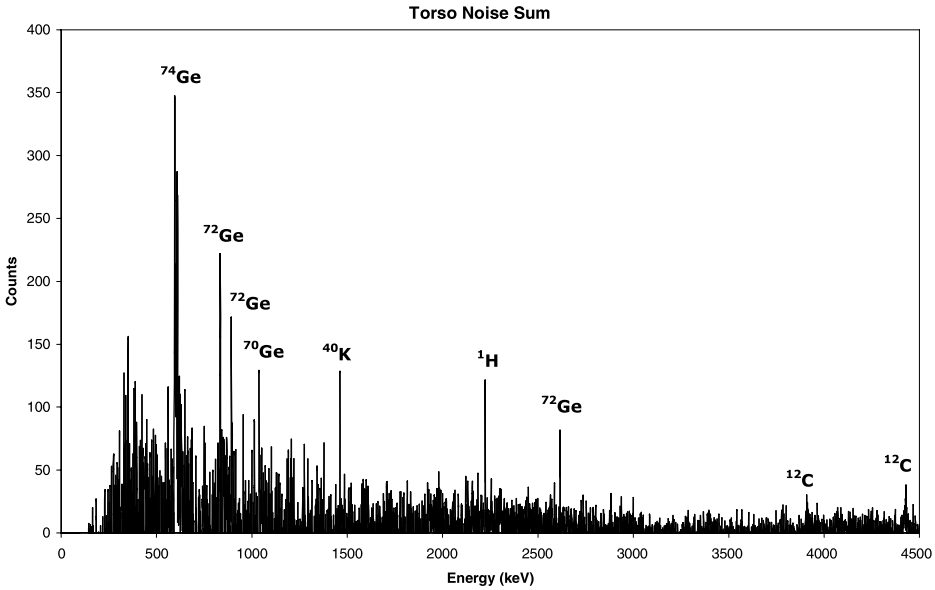


**Figure 7.** Subtraction spectrum of the torso phantom without iron.

**Table 2.** Calculation of neutron and gamma attenuation ratio in the human torso.

| | 847 keV counts | Neutron paddle counts | Normalized counts | Ratio of normalized counts |
|---|---|---|---|---|
| Fe plate in air | 1276 | 755 46 | $16.9 \times 10^{-3}$ | $\frac{\text{Plate\_in\_air}}{\text{Plate\_in\_torso}} = 3.15$ |
| Fe plate in torso phantom | 1000 | 186 443 | $5.36 \times 10^{-3}$ | |

placed in air and normalized to the incident neutron counts observed in the neutron paddle. A similar measurement was performed with the iron plate placed in the torso phantom surrounded by liver tissue. The ratio of the normalized gamma counts in air to normalized gamma counts in the torso phantom was used to obtain an estimate of the attenuation due to the torso. As shown in table 2, a normalized value of $16.9 \times 10^{-3}$ was observed for the plate in air, while a normalized value of $5.36 \times 10^{-3}$ was observed for the same plate placed in the torso. The ratio of the two values resulted in an attenuation factor of 3.15. Based on the known dimensions of the phantom, the corresponding theoretical value of attenuation was then calculated using an algorithm designed for attenuation correction in NSECT (Kapadia and Floyd 2005). The calculated value was found to be 2.44, representing a 30% difference from the measured value.

Figure 7 shows the difference spectrum of the overload torso phantom and the iron plate, generated by subtracting the normalized iron spectrum (figure 5) from the torso liver spectrum (figure 6). It can be seen in the subtracted spectrum that the peaks from $^{56}$Fe at 847 keV and 1238 keV are difficult to identify, while the peak from neutron capture on $^{1}$H at 2224 keV and peaks from $^{12}$C at 4439 keV and 3928 keV (escape peak) are identified clearly. Therefore, it is possible to conclude that the peaks at 847 keV and 1238 keV originate from the external source of iron, i.e. the 2.4 mm thick iron plate, while the remaining peaks originate from elements in the liver tissue.

**Table 3.** Effective dose delivered from NSECT spectroscopy scan of the torso.

| Parameter | Calculated value |
|---|---|
| Number of incident neutrons | $3.21 \times 10^{7}$ |
| Total energy deposited (MeV) | $1.56 \times 10^{8}$ |
| Total energy deposited (J) | $2.49 \times 10^{-5}$ |
| Mass of liver (kg) | $3.32 \times 10^{-2}$ |
| Absorbed dose (J kg$^{-1}$) Gy | $7.50 \times 10^{-4}$ |
| Neutron radiation weighting factor | 10 |
| Equivalent dose (Gy) | $7.50 \times 10^{-3}$ |
| Tissue weighting factor for liver | 0.05 |
| Effective dose equivalent (mSv) | $3.75 \times 10^{-1} = 0.375$ mSv |

### *3.3. Patient dose*

The patient dose for this study was calculated by using a GEANT4 model to determine the amount of energy deposited per neutron in a human liver torso and multiplying this information by the total neutron fluence incident on the torso phantom. The GEANT4 model for dose calculation has been developed and described elsewhere (Kapadia 2007, Sharma *et al* 2007), and results from the model were directly used to calculate dose values for this experiment. The number of neutrons incident on the sample was calculated from data acquired by the thin scintillation paddle detector and the zero-degree liquid scintillator neutron monitor. A neutron scan with no sample in the beam was used to establish a ratio of scintillation paddle counts to zero-degree liquid scintillator counts. The neutron detection efficiency of the zero-degree scintillator was known *a priori*. From this scan, the ratio of scintillator paddle counts to neutron flux was established as 172 neutrons per scintillator paddle count. Therefore, it was possible to estimate that the torso scan with 186 443 paddle counts was performed using $3.21 \times 10^{7}$ incident neutrons. The GEANT4 simulation was used to establish a ratio of the energy deposited in the torso per incident neutron as 4.85 MeV per neutron. The dose calculation for this scan is shown in table 3 and is explained as follows:

- The total number of neutrons required for spectroscopic quantification $= 3.21 \times 10^{7}$.
- The total energy deposited (MeV) = total number of neutrons $\times$ energy deposited per neutron.
- The total energy deposited (J) = total energy deposited (MeV) $\times$ $1.6 \times 10^{-13}$ J MeV$^{-1}$.
- Absorbed dose (Gy) = total energy deposited (J)/mass of irradiated tissue (kg).
- Radiation weighting factor for neutrons at 5 MeV = 10.
- Equivalent dose (Gy) = absorbed dose (Gy) $\times$ radiation weighting factor.
- Tissue weighting factor for liver = 0.05.
- Effective dose equivalent (Sv) = equivalent dose (Gy) $\times$ liver tissue weighting factor.

The detection limit observed in the study was 0.2 g with a dose of 0.375 mSv, corresponding to a liver iron concentration of 6 mg g$^{-1}$.

## 4. Discussion

This paper describes the first experiment to determine the feasibility of detecting iron overload in humans. Results from the experiment suggest that in its current form NSECT shows significant potential in being able to diagnose clinical iron overload in the human liver through

a scan that is both non-invasive and *in vivo*. Clinical iron overload in patients has been reported with concentrations between 1.8 mg $g^{-1}$ and 5.45 mg $g^{-1}$ for moderate to severe cases (Powell 2002, 2005, Powell *et al* 1998), and up to 9 mg $g^{-1}$ in very severe cases (Mazza *et al* 1995, Scharfetter *et al* 2003). As this experiment was the first study of its nature with no previous NSECT diagnostic values for comparison, the iron overload in this experiment was set at 126 mg $g^{-1}$, approximately 20 times the typical limit reported in patients, in order to ensure adequate signal and accuracy from the system. However, the results from this experiment can be used to obtain a projected sensitivity for iron overload diagnosis as follows. In the torso phantom scan, the noise background under the peak corresponding to $^{56}$Fe was determined to have a maximum height of 30 counts. With this noise background, for a peak to be determined with a $p$-value of $\leqslant 0.05$, the number of counts in the foreground peak would have to be 48, which, based on the iron concentration in this phantom, corresponds to an iron concentration of 0.2 g. This concentration of 0.2 g distributed over the 33.2 g of liver tissue scanned corresponds to an iron overload of 6 mg $g^{-1}$, which represents a clinically relevant value.

NSECT relies on the total quantity of iron that is present in the beam during a scan. Therefore, in order to increase signal strength in the case of low concentration livers, the acquisition geometry can be optimized to illuminate a larger volume of liver tissue (and consequently include more iron in the beam) while minimizing the illumination of surrounding tissue in the torso. Further, specialized components such as high-flux neutron sources and multiple gamma detectors can be used to increase the overall detection efficiency of the system and reduce scan time, which will both in turn reduce the time-dependent background noise. Implementing optimized detector shielding can reduce sample-related and room-related background, which will increase the signal-to-noise ratio and improve the overall sensitivity of the system. Increased gamma detection efficiency with reduced scan time will also reduce the levels of patient dose. Such system optimization has the potential to improve the sensitivity of the technique to facilitate the diagnosis of even lower concentrations of iron overload (less than 5 mg $g^{-1}$). System optimization has been explored using GEANT4 simulations (Kapadia 2007).

Although MRI is able to quantify moderate concentrations of iron overload, it suffers from a loss of accuracy for concentrations above 6 mg $g^{-1}$ wet weight (20 mg $g^{-1}$ dry weight) due to the signal intensity from the liver being reduced by high concentration of iron (Angelucci *et al* 1997). NSECT on the other hand shows an increase in the signal with increasing concentrations of iron in the beam, and therefore has the ability to detect severe degrees of iron overload in patients where MRI begins to lose accuracy. The experiment described in this paper demonstrates that NSECT in its current form can detect and quantify liver iron concentrations of 6 mg $g^{-1}$ or higher and has the potential to detect lower concentrations by scanning a larger volume of tissue with an optimized acquisition geometry.

The acquisition technique described in this study is that of single-position spectroscopy, where a thin neutron beam is used to illuminate a given volume of the tissue. Due to the nature of the spectroscopic acquisition, any iron present at any given location in the illuminated tissue appears to be distributed uniformly along the entire volume of the tissue. This mode of acquisition, therefore, is unable to identify high concentrations of iron located in small localized regions along the illuminated tissue volume. Localized iron concentrations will appear to be distributed uniformly along the entire tissue volume, with concentration that is lower than that in the original localized region. Detection of non-uniform distributions will require tomographic scanning of the patient. Although future clinical applicability of NSECT may appear to be more practical using the tomographic acquisition mode, it is important to understand the behavior of each individual projection in order to determine the optimal technique of generating a tomographic image. Further, through its tomographic mode of

acquisition, NSECT has the ability to investigate the effect of factors such as cirrhosis on the distribution of iron in liver iron overload.

Background correction was performed using TOF correction to reduce time-uncorrelated noise events and a beam-only scan to reduce effects from beam-correlated noise events from materials in the system. Noise generated from interactions between neutrons scattered in the human torso and materials in the experimental area other than the sample was not suppressed. In other experiments, this background has been suppressed using a spectrum obtained from an equivalent volume of water to model the neutron scatter background (Kapadia *et al* 2005, 2006a, 2006b, 2006c, 2008). In a clinical scenario, this scatter background can be corrected by subtracting a spectrum acquired from an equivalent volume water sample. Reducing scatter background will further improve the sensitivity of the system, thereby making it possible to detect lower concentrations of iron in the liver.

Patient dose for this experiment was found to be 0.375 mSv, which is significantly lower than an abdominal x-ray exam that typically delivers 2 mSv (RSNA 2007). Although neutrons have a higher radiation weighting factor than gamma rays, it takes fewer neutrons to create an NSECT image than x-rays required to create a radiograph. Therefore, it is possible to maintain patient dose levels at values comparable to other ionizing radiation modalities. Further, using high-flux neutron sources and increasing the number of detectors can bring down patient dose and reduce scan time further.

The results described in this paper have two important outcomes. First, they demonstrate that NSECT has the potential to detect clinically relevant concentrations of iron in the human body through a non-invasive scan. Second, they provide a comparative standard to guide the design of iron overload phantoms for future liver iron quantification studies using NSECT.

## Acknowledgments

We would like to express our deep gratitude to our late colleague Dr Carey E Floyd Jr, who pioneered the NSECT technique and nurtured it into what it is today. His vision has helped NSECT evolve from a simple idea into a clinically applicable diagnostic technique with several exciting applications. We would also like to thank the research personnel at Triangle Universities Nuclear Laboratory, especially Anthony Hutcheson and Anton Tonchev, who have been extremely helpful with gamma detector setup and calibration. This work was supported by the Department of Defense (Breast Cancer Research Program) under award number W81XWH-06-1-0484 and in part by the US Department of Energy, Office of High Energy and Nuclear Physics under grant no. DE-FG02-97ER41033.

## References

Alustiza J M, Artetxe J, Castiella A, Agirre C, Emparanza J I, Otazua P, Garcia-Bengoechea M, Barrio J, Mujica F and Recondo J A 2004 MR quantification of hepatic iron concentration *Radiology* **230** 479–84

Angelucci E, Giovagnoni A, Valeri G, Paci E, Ripalti M, Muretto P, McLaren C, Brittenham G M and Lucarelli G 1997 Limitations of magnetic resonance imaging in measurement of hepatic iron *Blood* **90** 4736–42

Arnold M L, McNeill F E, Stronach I M, Pejovic-Milic A, Chettle D R and Waker A 2002 An accelerator based system for *in vivo* neutron activation analysis measurements of manganese in human hand bones *Med. Phys.* **29** 2718–24

Avrin W F and Kumar S 2007 Noninvasive liver–iron measurements with a room-temperature susceptometer *Physiol. Meas.* **28** 349–61

Bender J E, Kapadia A J, Sharma A C, Tourassi G D, Harrawood B P and Floyd C E 2007 Breast cancer detection using neutron stimulated emission computed tomography: prominent elements and dose requirements *Med. Phys.* **34** 3866–71

Bonkovsky H L, Rubin R B, Cable E E, Davidoff A, Rijcken T H and Stark D D 1999 Hepatic iron concentration: noninvasive estimation by means of MR imaging techniques *Radiology* **212** 227–34

Brittenham G and Badman D 2003 Noninvasive measurement of iron: report of an NIDDK workshop *Blood* **101** 15–9

Brittenham G M, Sheth S, Allen C J and Farrell D E 2001 Noninvasive methods for quantitative assessment of transfusional iron overload in sickle cell disease *Semin. Hematol.* **38** 37–56

Cecchin E, De Marchi S, Querin F, Marin M G, Fiorentino R and Tesio F 1990 Efficacy of hepatic computed tomography to detect iron overload in chronic hemodialysis *Kidney Int.* **37** 943–50

Chapman R W, Williams G, Bydder G, Dick R, Sherlock S and Kreel L 1980 Computed tomography for determining liver iron content in primary haemochromatosis *Br. Med. J.* **280** 440–2

Chezmar J L, Nelson R C, Malko J A and Bernardino M E 1990 Hepatic iron overload: diagnosis and quantification by noninvasive imaging *Gastrointest. Radiol.* **15** 27–31

Dixon R M, Styles P, al-Refaie F N, Kemp G J, Donohue S M, Wonke B, Hoffbrand A V, Radda G K and Rajagopalan B 1994 Assessment of hepatic iron overload in thalassemic patients by magnetic resonance spectroscopy *Hepatology* **19** 904–10

Floyd C E, Bender J E, Sharma A C, Kapadia A J, Xia J Q, Harrawood B P, Tourassi G D, Lo J Y, Crowell A S and Howell C R 2006 Introduction to neutron stimulated emission computed tomography *Phys. Med. Biol.* **51** 3375–90

Floyd C E *et al* 2004 Neutron stimulated emission computed tomography of stable isotopes *SPIE Medical Imaging* (San Diego, CA: IEEE) pp 248–54

Floyd C E *et al* 2007 Neutron stimulated emission computed tomography: background corrections *Nucl. Instrum. Methods Phys. Res.* B **254** 329–36

Floyd C E *et al* 2008 Neutron stimulated emission computed tomography of a multi-element phantom *Phys. Med. Biol.* **53** 2313–26

Fox R, Bolen C, Orji K and Venema J 2004 NSCLSpecTcl meeting the needs of preliminary nuclear physics data analysis *11th Ann. Tcl/Tk Conference* (New Orleans, Louisiana)

Gandon Y, Olivie D, Guyader D, Aube C, Oberti F, Sebille V and Deugnier Y 2004 Non-invasive assessment of hepatic iron stores by MRI *Lancet* **363** 357–62

Guyader D, Gandon Y, Robert J Y, Heautot J F, Jouanolle H, Jacquelinet C, Messner M, Deugnier Y and Brissot P 1992 Magnetic resonance imaging and assessment of liver iron content in genetic hemochromatosis *J. Hepatol.* **15** 304–8

Håkansson P 1999 An introduction to the time-of-flight technique *Braz. J. Phys.* **29** 422–7

Howard J M, Ghent C N, Carey L S, Flanagan P R and Valberg L S 1983 Diagnostic efficacy of hepatic computed tomography in the detection of body iron overload *Gastroenterology* **84** 209–15

ICRU 1992 Photon, Electron, Proton and Neutron Interaction Data for Body Tissues *ICRU Report No 46* (Bethesda, MD: ICRU)

Kapadia A J 2007 Accuracy and patient dose in neutron stimulated emission computed tomography for diagnosis of liver iron overload: simulations in GEANT4 *Biomedical Engineering* (Durham, NC: Duke University)

Kapadia A J and Floyd C E 2005 An attenuation correction technique to correct for neutron and gamma attenuation in the reconstructed image of a neutron stimulated emission computed tomography (NSECT) system *SPIE Medical Imaging* (San Diego, CA: IEEE) pp 737–43

Kapadia A J, Floyd C E, Bender J E, Howell C R, Crowell A S and Kiser M R 2005 Non-invasive quantification of iron 56-Fe in beef liver using neutron stimulated emission computed tomography *IEEE Nucl. Sci. Symp., Med. Imag. Conf.* **4** 2232–4

Kapadia A J, Sharma A C, Bender J E, Tourassi G D, Howell C R, Crowell A S, Kiser M R, Harrawood B P and Floyd C E 2008 Neutron stimulated emission computed tomography for diagnosis of breast cancer *IEEE Trans. Nucl. Sci.* **55** 501–9

Kapadia A J, Sharma A C, Tourassi G D, Bender J E, Crowell A S, Kiser M R, Howell C R and Floyd C E 2006a Neutron spectroscopy of mouse using neutron stimulated emission computed tomography (NSECT) *IEEE Nucl. Sci. Symp., Med. Imag. Conf.* **6** 3546–8

Kapadia A J, Sharma A C, Tourassi G D, Bender J E, Crowell A S, Kiser M R, Howell C R and Floyd C E 2006b Neutron stimulated emission computed tomography (NSECT) for early detection of breast cancer *IEEE Nucl. Sci. Symp., Med. Imag. Conf.* **6** 3928–31

Kapadia A J, Sharma A C, Tourassi G D, Bender J E, Crowell A S, Kiser M R, Howell C R and Floyd C E 2006c Non-invasive estimation of potassium (39K) in bovine liver using neutron stimulated emission computed tomography (NSECT) *IEEE Nucl. Sci. Symp., Med. Imag. Conf.* **4** 2076–8

Katoh Y, Sato T and Yamamoto Y 2003 Use of instrumental neutron activation analysis to determine concentrations of multiple trace elements in human organs *Arch. Environ. Health* **58** 655–61

Knight G S, Beddoe A H, Streat S J and Hill G L 1986 Body composition of two human cadavers by neutron activation and chemical analysis *Am. J. Physiol. Endocrinol. Metab.* **250** E179–85

Liu P *et al* 1996 Quantification of cardiac and tissue iron by nuclear magnetic resonance relaxometry in a novel murine thalassemia-cardiac iron overload model *Can. J. Cardiol.* **12** 155–64

Madison Nuclear Reactor Laboratory *UW INAA: Estimated Interference-Free Sensitivity in Micrograms*

Mattsson S and Thomas B J 2006 Development of methods for body composition studies *Phys. Med. Biol.* **51** R203–28

Mazza P *et al* 1995 Iron overload in thalassemia: comparative analysis of magnetic resonance imaging, serum ferritin and iron content of the liver *Haematologica* **80** 398–404

McNeill F E, Franklin D M, Chettle D R, Ellis R E, Pittard S P, Scott M C and Vennart W 1990 Feasibility studies in the *in vivo* measurement of iron in synovial membrane *Basic Life Sci.* **55** 413–8

National Nuclear Data Center B N L 2007 *National Nuclear Database NuDat 2.3*

Ng K H, Bradley D A, Looi L M, Seman Mahmood C and Khalik Wood A 1993 Differentiation of elemental composition of normal and malignant breast tissue by instrumental neutron activation analysis *Appl. Radiat. Isot.* **44** 511–6

Nielsen P, Engelhardt R, Duerken M, Janka G E and Fischer R 2000 Using SQUID biomagnetic liver susceptometry in the treatment of thalassemia and other iron loading diseases *Transfus. Sci.* **23** 257–8

Nielsen P, Engelhardt R, Dullmann J and Fischer R 2002a Non-invasive liver iron quantification by SQUID-biosusceptometry and serum ferritin iron as new diagnostic parameters in hereditary hemochromatosis *Blood Cells Mol. Dis.* **29** 451–8

Nielsen P, Kordes U, Fischer R, Engelhardt R and Janka G E 2002b SQUID-biosusceptometry in iron overloaded patients with hematologic diseases *Klin. Padiatr.* **214** 218–22

NIH 2007 *NIH Publication No.* 07-4621

NIST *NIST-SRM 1577b Bovine Liver* http://www-naweb.iaea.org/nahu/nmrm/nmrm2003/material/ni1577b.htm accessed 4 April 2008

Perrimond H, Chagnon C, Moulanier I, Michel G, Guidicelli H and Bernard P J 1991 The value of nuclear magnetic resonance in the study of iron overload in thalassemia patients *Ann. Pediatr. (Paris)* **38** 175–84

Powell L W 2005 *Harrison's Principles of Internal Medicine*ed D Kasper, A S Fawci, D L Longo, E Braunwald, S L Hauser and J L Jameson (New York: McGraw-Hill) pp 2298–303

Powell L W 2002 Diagnosis of hemochromatosis *Semin. Gastrointest Dis.* **13** 80–8

Powell L W, George D K, McDonnell S M and Kowdley K V 1998 Diagnosis of hemochromatosis *Ann. Intern. Med.* **129** 925–31

Ratziu V, Charlotte F, Heurtier A, Gombert S, Giral P, Bruckert E, Grimaldi A, Capron F and Poynard T 2005 Sampling variability of liver biopsy in nonalcoholic fatty liver disease *Gastroenterology* **128** 1898–906

Regev A, Berho M, Jeffers L J, Milikowski C, Molina E G, Pyrsopoulos N T, Feng Z Z, Reddy K R and Schiff E R 2002 Sampling error and intraobserver variation in liver biopsy in patients with chronic HCV infection *Am. J. Gastroenterol.* **97** 2614–8

RSNA 2007 *Radiation Exposure in X-ray Examinations (USA: American College of Radiology (ACR) and the Radiological Society of North America (RSNA))*

Scharfetter H, Casanas R and Rosell J 2003 Biological tissue characterization by magnetic induction spectroscopy (MIS): requirements and limitations *IEEE Trans. Biomed. Eng.* **50** 870–80

Sharma A C, Harrawood B P, Bender J E, Tourassi G D and Kapadia A J 2007 Neutron stimulated emission computed tomography: a Monte Carlo simulation approach *Phys. Med. Biol.* **52** 6117–31

Sheth S 2003 SQUID biosusceptometry in the measurement of hepatic iron *Pediatr. Radiol.* **33** 373–7

Vartsky D, Ellis K J, Hull D M and Cohn S H 1979 Nuclear resonant scattering of gamma rays—a new technique for *in vivo* measurement of body iron stores *Phys. Med. Biol.* **24** 689–701

Vartsky D, Wielopolski L, Ellis K J and Cohn S H 1982 The use of nuclear resonant scattering of gamma-rays for *in vivo* measurement of iron *Nucl. Instrum. Methods Phys. Res.* **193** 359–64

Villeneuve J P, Bilodeau M, Lepage R, Cote J and Lefebvre M 1996 Variability in hepatic iron concentration measurement from needle-biopsy specimens *J. Hepatol.* **25** 172–7

Wang Z J, Haselgrove J C, Martin M B, Hubbard A M, Li S, Loomes K, Moore J R, Zhao H and Cohen A R 2002 Evaluation of iron overload by single voxel MRS measurement of liver T2 *J. Magn. Reson. Imag.* **15** 395–400

Wielopolski L, Ancona R C, Mossey R T, Vaswani A N and Cohn S H 1985 Nuclear resonance scattering measurement of human iron stores *Med. Phys.* **12** 401–4

Yukawa M, Suzuki-Yasumoto M, Amano K and Terai M 1980 Distribution of trace elements in the human body determined by neutron activation analysis *Arch. Environ. Health* **35** 36–44

Zeisler R, Ostapczuk P, Stone S F and Stoeppler M 1993 Effective tools for trace element characterization of tissue: neutron activation analysis and voltammetry *Sci. Total Environ.* **139/140** 403–10

# GEANT4 Simulation of NSECT for Detection of Iron Overload in the Liver

Anuj J. Kapadia[a], Brian P. Harrawood[a], Georgia D. Tourassi[a,b]
[a]Duke Advanced Imaging Laboratories, Duke University Medical Center, Durham, NC 27705;
[b]Department of Medical Physics, Duke University, Durham, NC 27705

## ABSTRACT

Neutron stimulated emission computed tomography (NSECT) is being proposed as a non-invasive technique to diagnose iron overload in humans. It uses inelastic scatter interactions between incident neutrons and iron nuclei to stimulate gamma-ray emission from iron. Tomographic detection of the emitted gamma-rays yields information about the concentration and spatial distribution of iron in the liver. Early proof-of-concept experiments have shown that NSECT has the potential to quantify clinical quantities of liver iron overload through single-position spectroscopy. However, a tomography application for patient diagnosis has never been tested. This work uses a Monte-Carlo simulation of a tomographic NSECT system to investigate the feasibility of imaging the spatial distribution of liver iron through tomography. A simulation of an NSECT system has been designed in GEANT4 and used to tomographically scan a simulated human liver phantom with high-concentration iron lesions. Images are reconstructed with the MLEM algorithm and analyzed for pixel values within iron regions to determine the statistical significance of detection. Analysis results indicate that a wet iron concentration of 3 mg/g can be detected in surrounding liver tissue with p-value $\leq 0.0001$ for neutron exposure corresponding to a radiation dose of 0.72 mSv. The research performed here demonstrates that NSECT has the ability to image clinically relevant distributions of iron through tomographic scanning.

**Keywords:** Neutron, Spectroscopy, Gamma, Iron-overload, NSECT, Tomography, Simulation, GEANT4.

## 1. INTRODUCTION

Neutron stimulated emission computed tomography (NSECT) system is being developed as a non-invasive technique to quantitatively image the distribution of elements in the human body [1-5]. It uses inelastic scattering interactions between neutrons and target element nuclei to obtain a tomographic image of the element's spatial distribution in the body. NSECT uses the following principle. An incident neutron scatters inelastically with a target atomic nucleus and stimulates the nucleus to emit characteristic gamma radiation. The energy of the emitted gamma-ray is unique to the emitting isotope and can be measured to identify the distribution and concentration of the element in the sample. Translation and rotation of the sample yields tomographic information about the element's spatial distribution in the target. Such quantitative imaging has the potential to diagnose several disorders in the human body that are characterized by differences in element concentration between normal and diseased tissue. Element concentration differences have been observed in liver iron overload [6, 7], Alzheimer's disease [8, 9], and several cancers including breast [10-12], prostate[13] and brain [14-16]. While the imaging of element distribution in all of the above mentioned disorders is within the capabilities of NSECT, the present work is focused on detection of iron overload in the liver.

Iron overload is a condition in which the body's iron stores increase significantly due to iron accumulation through increased dietary absorption (hemochromatosis) or through blood transfusion that form a part of treatment procedures for chronic disorders such as thalassemia major, myelodysplasia and moderate aplastic anemia (transfusional iron overload). While the body has fine techniques for monitoring and controlling the absorption of iron ingested from food in accordance with its iron need, it has no corresponding mechanism to eliminate excess iron in case of overload. The excess quantity is stored in several vital organs in the body such as the liver, heart and spleen, and can lead to extensive tissue damage, liver cirrhosis, cardiac failure, hepatic failure and hepatocellular carcinoma [6, 17, 18].

Accurate measurement of the body's iron content is vital for effective diagnosis and management of iron overload [6, 17]. The measurement is currently obtained through a liver biopsy, which is an uncomfortable procedure. The discomfort and risks associated with biopsy significantly limit its acceptability to patients. NSECT has the ability to obtain an accurate estimate of iron concentration in the liver through a single non-invasive in-vivo scan. It provides an alternative to biopsy

Medical Imaging 2008: Physics of Medical Imaging, edited by Jiang Hsieh, Ehsan Samei,
Proc. of SPIE Vol. 6913, 691309, (2008) · 1605-7422/08/$18 · doi: 10.1117/12.773245

with no associated morbidity. It can be used for repeated monitoring of patients obtaining therapeutic treatments for iron overload.

Preliminary experiments have demonstrated the clinical feasibility of detecting iron overload through a non-invasive 'neutron radio-biopsy'[19]. These experiments have achieved a statistically significant measurement of liver iron in a human iron-overload phantom through a single projection scan with a dose of less than 0.5 mSv. While the single-projection acquisition is appropriate for measuring uniform iron distributions in the liver, a tomographic acquisition is required to image and quantify non-uniform patches of high iron concentration in otherwise normal liver tissue. However, before experimental implementation of a clinical tomography system is begun, it is important to determine the ability of NSECT for detecting non-uniform iron overload in humans with reasonable radiation dose. This work uses a Monte-Carlo simulation to test the feasibility of detecting non-uniform distributions of iron in the liver through a tomographic NSECT scan.

## 2. METHODOLOGY

A Monte-Carlo simulation of a clinical NSECT system is designed in GEANT4. GEANT4 is a programming toolkit to model high-energy physics interactions between particles and matter over a broad range of energies[20]. It has been developed by a worldwide collaboration of over 100 scientists in Europe, Russia, Japan, Canada and the United States. GEANT4 allows precise modeling of interactions that occur between neutrons and a variety of target nuclei at energies of relevance to NSECT. It is an object-oriented programming package which incorporates a powerful set of random number generators, physics units and constants, and provides all the tools required for detector simulation including geometry, tracking and detector response management.

### 2.1 Experimental System

The NSECT simulation is modeled after the experimental system, which uses a Van-de-Graaff accelerator source, high-purity germanium gamma-ray detectors, and a tomographic gantry to accommodate the sample. The experimental system has been described in detail elsewhere [1, 2, 4], and only a brief description is provided here. A Van-de-Graaff accelerator is used to generate mono-energetic neutron beams with energies ranging from 4 MeV and 7.5 MeV for NSECT imaging. Beam width is controlled by a copper collimator with swappable inserts. High-purity germanium (HPGe) gamma-ray detectors are used to generate gamma energy spectra with approximate energy resolution of 1 keV per detector channel. Tomography is performed using the translate-rotate geometry of first generation CT scanners using a gantry to hold and control the sample remotely.

### 2.2 Simulated Model

The simulated NSECT model consists of 3 components – (a) Neutron Source, (b) Gamma Detectors, and (c) Liver Phantom, each designed independently based on the corresponding component of the experimental acquisition system.

#### 2.2.1 Neutron Source

The simulated neutron source produces a 5 MeV mono-energetic neutron beam collimated to 1 cm beam width. These parameters are typical of the beam used in NSECT experiments. Neutrons with 5 MeV of energy are sufficient to excite several energy states in iron as well as the first excited state in carbon in the liver. Carbon can be used to image the location of the liver within the abdomen and also to obtain an image of tissue distribution which can be used for attenuation correction.

#### 2.2.2 Gamma-ray Detectors

The detector system is designed as an array of six germanium crystals that surround the liver sample as shown in figure 1. Four detectors are located at ±45 degrees and ±135 degrees around the sample and two are above and below the sample. The ±45 degree and ±135 degree locations correspond to regions of maximum gamma emission around the sample from electric quadrupole interactions, which are expected to be dominant at this neutron energy. While the experimental setup uses detectors only in the 135 degree positions to minimize detector damage from scattered neutrons, the 45 degree position is included here to increase detection efficiency. The two detectors located above and below the liver sample serve to further increase gamma-ray detection efficiency in the simulated system. Each detector is designed as a cylinder of 30 cm diameter and 10 cm height and is filled with natural density germanium. The detector material is sensitized to track particle transport and energy deposit in its volume.

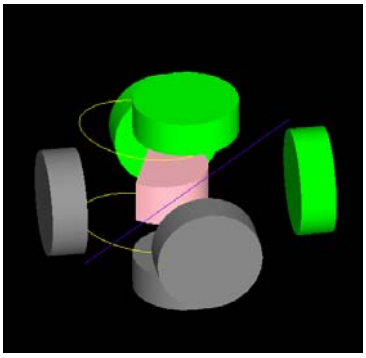

Figure 1. GEANT4 simulation showing the 6-detector array system. The green and gray cylinders are gamma detectors. The liver is shown as a pink model housed in a water-filled torso shown by yellow lines.

### 2.2.3 Liver Phantom

The liver phantom is designed as a combination of a half-cylinder and a trapezoid as shown in figure 2. The major axis of the liver measures 17 cm and the minor axis measures 15 cm. The liver tissue material is modeled on the tissue composition defined in ICRU Report 46 [21], as shown in table 1. Non-uniform iron distribution is modeled as two spherical lesions of 3 cm diameter with concentrations of 5 mg/g and 3 mg/g (wet). These concentration values correspond to iron concentrations reported clinically in liver iron overload in humans. The liver sample is placed inside a simulated torso modeled as an ellipse with 30 cm major axis and 25 cm minor axis. The torso is filled with water to mimic the elastic scattering properties of tissue. Finally, a spine is modeled as a cylindrical tube with 5 cm outer diameter and 1 cm inner diameter, with material definition of skeletal bone tissue from ICRU Report 46 [21] as shown in table 2. The spine provides a dense anatomic structure that can cast a shadow on the iron lesions in certain projections and therefore potentially affect the reconstructed image.

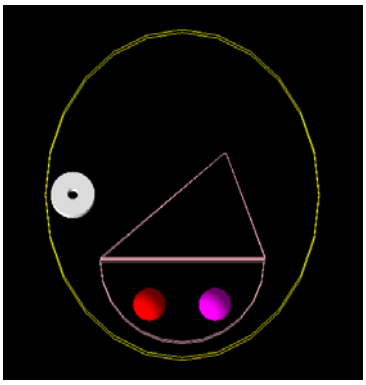

Figure 2. Simulated liver-torso phantom with non-uniform iron overload. The torso is shown as a yellow outline. The liver is shown as a pink outline measuring 17 cm major axis and 15 cm minor axis, and contains two spherical lesions 3 cm in diameter with high iron concentrations – red lesion (5 mg/g) and pink lesion (3 mg/g). The spine is modeled as a white cylindrical tube.

| **Element** | **O** | **C** | **H** | **N** | **P** | **S** | **K** | **Cl** | **Na** | **Fe** | **Density** |
|---|---|---|---|---|---|---|---|---|---|---|---|
| **Normal (%)** | 71.6 | 13.9 | 10.2 | 3.0 | 0.3 | 0.3 | 0.3 | 0.2 | 0.2 | 0.0 | 1060 kg/m$^3$ |

Table 1. Elemental composition of human liver tissue (obtained from ICRU report 46 [21]).

| Element | O | Ca | C | P | N | H | S | Mg | Na | Fe | Density |
|---|---|---|---|---|---|---|---|---|---|---|---|
| Normal (%) | 43.5 | 22.5 | 15.5 | 10.3 | 4.2 | 3.4 | 0.3 | 0.2 | 0.1 | 0.0 | 1920 kg/m$^3$ |

Table 2. Elemental composition of human skeletal bone (obtained from ICRU report 46 [21]).

### 2.3 Tomographic reconstruction

NSECT tomography is performed using the translate-rotate configuration similar to first generation CT scanners, by translating the beam horizontally through the entire sample length, then rotating the beam through a fixed angle and repeating the process. The liver phantom is scanned at 8 angles with 20 spatial steps per angle acquired at 1 cm intervals with the 1 cm neutron beam for a total of 160 projections.

Image reconstruction is performed using the Maximum Likelihood Expectation Maximization (MLEM) algorithm implemented for gamma emission computed tomography [22]. The MLEM algorithm is chosen due to its ability to account for low noise conditions in under-sampled systems and account for non-ideal scanning criteria such as non-uniform sampling and presence of attenuation. Images are reconstructed using the counts in the peak corresponding to $^{56}$Fe at 847 keV.

### 2.4 Statistical Analysis

The reconstructed image is analyzed by testing the average pixel value within each reconstructed lesion against the pixel value in the liver background using a z-score test for difference of means. The z-score test is used to determine the statistical significance of detecting each lesion above the liver background. To calculate the mean pixel value and the standard error in the pixel value within the reconstructed lesions, the entire area corresponding to the original simulated lesion is used. Differences with a two-tailed p-value $\leq 0.05$ are considered statistically significant. Results of statistical analysis of the reconstructed image are shown in table 3.

### 2.5 Dose Calculation

Patient dose in NSECT is a combination of neutron and gamma dose effects. The total delivered dose is calculated by measuring the energy deposited in the liver and surrounding tissue in the GEANT4 simulation, and converting it to equivalent dose as described below. The calculation takes into account three parameters to obtain an accurate estimate of dose: (a) Mass of irradiated tissue, (b) Neutron Q-factor, (c) Liver weighting factor. Each of these values is shown in table 4 in the results of dose calculation. The energy deposited in tissue is measured from the GEANT4 simulation in MeV. The energy in MeV is converted to Joules and divided by the mass of irradiated tissue to obtain the absorbed dose. The absorbed dose is then converted to effective dose by multiplying with the neutron quality factor and liver weighting factor. The calculation can be summarized as:

- Total energy deposited in tissue (from cumulative neutron and gamma effects) $\rightarrow$ Measured (MeV)
- Total energy deposited (J) = Total energy deposited (MeV) x 1.6 x $10^{-13}$ J/MeV
- Absorbed Dose = Total energy deposited / Mass of irradiated tissue
- Effective Dose Equivalent = Absorbed dose x Neutron Q-factor x Liver weighting factor.

The effective dose is calculated for all projections at 1 angle and multiplied by 8 to obtain the total patient dose from the scan. In this study, the dose is calculated separately for the liver and the surrounding abdominal tissue in order to compensate for the difference in irradiated mass within each region, which affects the calculation of effective dose.

## 3. RESULTS

Figure 3 shows the reconstructed image for the tomographic scan with 8 angles, reconstructed using the iterative MLEM algorithm with 15 iterations. The reconstructed image is displayed without any ad-hoc normalization or correction. As can be seen, pixel intensity is primarily distributed in regions corresponding to regions of iron in the liver. Each iron lesion appears brighter than the liver and abdomen background. The lesion with higher iron concentration (5 mg/g) appears brighter than the lesion with lower concentration (3 mg/g). The mean pixel values within the 3 regions are measured and found to be: (i) 5 mg/g lesion = 110.58, (ii) 3 mg/g lesion = 40.88, (iii) liver background = 14.98. Table 3

shows a summary of the statistical analysis of the reconstructed image using the z-score test for difference of means. The standard error is calculated using the standard deviation of pixel values and number of pixels within the original simulated lesion. Each lesion is detected above the background with p-value ≤ 0.0001 using the 8-angle scanning geometry.

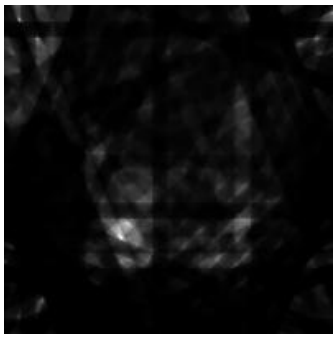

Figure 3. Reconstructed image for the human liver sample. Both lesions are visible above the background and can be detected with p-value ≤ 0.0001.

| Region | Mean pixel value | Std. error | z | p-value |
|---|---|---|---|---|
| **5 mg/g** | 110.58 | 8.44 | 11.33 | 0.0001 |
| **3 mg/g** | 40.88 | 1.12 | 23.11 | 0.0001 |
| **Liver BG** | 14.98 | 0.04 | -- | -- |

Table 3. Summary of statistical analysis of the reconstructed image using a z-score test for difference of means.

Table 4 shows a summary of the dose calculation for the scan. The dose is calculated separately for the liver region and the region corresponding to abdominal tissue by tracking the energy deposited within each individual area. The two regions are treated separately to compensate for the difference in irradiated mass of tissue, which will affect the calculation of effective dose delivered to the organ. For incident neutron energy of 5 MeV, the neutron Q-factor is 10, and the liver weighting factor is 0.05. Using the calculation formula described earlier, the dose delivered to the liver is found to be 0.07 mSv per angle, and dose delivered to the abdomen is found to be 0.02 mSv per angle. The effective dose over the entire mass of illuminated tissue is calculated as a sum of the dose to the liver and abdomen, i.e. 0.09 mSv per angle. The total effective dose delivered to the patient from the NSECT scan with 8 angles using the 6-detector geometry is therefore found to be 0.72 mSv.

| Parameter | Liver | Torso |
|---|---|---|
| Number of Incident Neutrons | 1.07E+08 | 1.07E+08 |
| Total Energy Deposited (MeV) | 3.18E+08 | 1.43E+08 |
| Total Energy Deposited (J) | 5.08E-05 | 2.29E-05 |
| Mass of Liver (kg) | 0.37 | 0.59 |
| Effective Dose (J/kg) Gy | 1.37E-04 | 3.86E-05 |
| Neutron Q-factor | 10 | 10 |
| Liver RBE | 0.05 | 0.05 |
| Effective Dose Equivalent (1 angle) | 0.07 mSv | 0.02 mSv |
| Total Dose Equivalent (8 angles) | 0.09 mSv x 8 angles = 0.72 mSv | |

Table 4. Effective dose delivered from the 8-angle NSECT tomography scan for the liver.

## 4. CONCLUSION

This work presents a simulation of the NSECT system for in-vivo diagnosis of non-uniform iron overload in the liver. A simulation of the NSECT system for tomographic acquisition has been designed and used to image non-uniform iron distribution in a liver phantom. An image is reconstructed from an acquisition with only 8 angles over the entire image space, which provides a good example of the severity of under-sampling in NSECT. The image reconstructed using the MLEM algorithm shows a distribution of pixel intensity that agrees with the distribution of iron concentration in the liver phantom. The result demonstrates that NSECT has the ability to image and quantify localized regions of iron concentration in the liver with excellent statistical accuracy and reasonable levels of patient dose. The reconstructed image validates the performance of the tomography technique and demonstrates the efficacy of MLEM in reconstructing images from severely under-sampled acquisitions. Both lesions detected in the image contain clinically relevant concentrations of iron observed in patients with hemochromatosis and transfusional overload. While the size and shapes of the lesions in patients may not be precise or distinct as in the simulation, the simulated model serves to demonstrate proof of principle for detection of non-uniform iron distribution through tomography. The source and detectors designed in the simulation are based on the Van-de-Graaff accelerator and HPGe detectors used in laboratory experiments. The results of this study, therefore, indicate that NSECT has the potential to obtain clinically relevant liver iron measurements using currently available source and detector technology. Patient dose calculated from the NSECT scan is observed to be within reasonable limits compared to other ionizing imaging modalities. For comparison, a typical abdominal radiograph delivers 4 mSv to the patient[23]. The dose analysis performed in this study indicates that it may be possible to increase the neutron flux by as much as a factor of 10 and remain within the dose limits of an abdominal CT exam (10 mSv)[23]. The increased neutron flux can be used to acquire a greater number of angles to improve image resolution and quantification accuracy further.

## ACKNOWLEDGMENT

We would like to acknowledge the late Carey E. Floyd Jr, who pioneered NSECT and developed it from an experimental idea into a clinically feasibly technique. This work was supported by the Department of Defense (Breast Cancer Research Program) under award number W81XWH-06-1-0484.

## REFERENCES

[1] Floyd, C. E., Jr., Bender, J. E., Sharma, A. C., Kapadia, A., Xia, J., Harrawood, B., Tourassi, G. D., Lo, J. Y., Crowell, A. and Howell, C., "Introduction to neutron stimulated emission computed tomography," Phys Med Biol 51(14), 3375-3390 (2006).

[2] Floyd, C. E., Howell, C. R., Harrawood, B. P., Crowell, A. S., Kapadia, A. J., Macri, R., Xia, J. Q., Pedroni, R., Bowsher, J., Kiser, M. R., Tourassi, G. D., Tornow, W. and Walter, R., "Neutron Stimulated Emission Computed Tomography of Stable Isotopes," in Proceedings of SPIE Medical Imaging, 248-254 (2004).

[3] Kapadia, A. J., Floyd, C. E., Bender, J. E., Howell, C. R., Crowell, A. S. and Kiser, M. R., "Non-invasive quantification of iron 56-Fe in beef liver using neutron stimulated emission computed tomography," in Proceedings of IEEE Nuclear Science Symposium, Medical Imaging Conference, 2232-2234 (2005).

[4] Kapadia, A. J., Sharma, A. C., Bender, J. E., Tourassi, G. D., Howell, C. R., Crowell, A. S., Kiser, M. R., Harrawood, B. P. and Floyd, C. E., "Neutron Stimulated Emission Computed Tomography for Diagnosis of Breast Cancer," IEEE Trans Nuc Sci (in press), (2008).

[5] Kapadia, A. J., Sharma, A. C., Tourassi, G. D., Bender, J. E., Crowell, A. S., Kiser, M. R., Howell, C. R. and Floyd, C. E., "Non-Invasive Estimation of Potassium (39K) in Bovine Liver Using Neutron Stimulated Emission Computed Tomography (NSECT)," in Proceedings of IEEE Nuclear Science Symposium, Medical Imaging Conference, 2076-2078 (2006).

[6] Powell, L., "Hemochromatosis," in [Harrison's Principles of Internal Medicine], edited by D. Kasper, Fawci, AS, Longo, DL, Braunwald, E, Hauser, SL, Jameson, JL, Vol. 2, pp 2298-2303, McGraw Hill, NY, (2005).

[7] Chezmar, J. L., Nelson, R. C., Malko, J. A. and Bernardino, M. E., "Hepatic iron overload: diagnosis and quantification by noninvasive imaging," Gastrointest Radiol 15(1), 27-31 (1990).

[8] Andrasi, E., Farkas, E., Scheibler, H., Reffy, A. and Bezur, L., "Al, Zn, Cu, Mn and Fe levels in brain in Alzheimer's disease," Arch Gerontol Geriatr 21(1), 89-97 (1995).

[9] Bomboi, G., Marchione, F., Sepe-Monti, M., De Carolis, A., Bianchi, V., Medda, E., Pino, A., Bocca, B., Forte, G., D'Ippolito, C. and Giubilei, F., "Correlation between metal ions and clinical findings in subjects affected by Alzheimer's disease," Ann Ist Super Sanita 41(2), 205-212 (2005).
[10] Garg, A., V. Singh, et al., "An elemental correlation study in cancerous and normal breast tissue with successive clinical stages by neutron activation analysis," Biological Trace Element Research 46, 185-202 (1994).
[11] Geraki, K. and Farquharson, M., "Concentrations of Fe, Cu and Zn in breast tissue: a synchrotron XRF study," Phys. Med. Biol 47, 2327-2339 (2002).
[12] Ng, K. H., Bradley, D.A., Looi, L.M., Seman Mahmood, C., Khalik Wood, A., "Differentiation of elemental composition of normal and malignant breast tissue by instrumental neutron activation analysis," Appl. Radiat. Isot. 44(3), 511-516 (1993).
[13] Yaman, M., Atici, D., Bakirdere, S. and Akdeniz, I., "Comparison of trace metal concentrations in malign and benign human prostate," J. Med. Chem. 48, 630-634 (2005).
[14] Civit, T., Houdayer, A. J. and Kennedy, G., "A search for trace elements in some human intracranial tumors by instrumental neutron activation analysis," Biol Trace Elem Res 74(3), 203-210 (2000).
[15] el-Yazigi, A., Al-Saleh, I. and Al-Mefty, O., "Concentrations of zinc, iron, molybdenum, arsenic, and lithium in cerebrospinal fluid of patients with brain tumors," Clin Chem 32(12), 2187-2190 (1986).
[16] Yoshida, D., Ikeda, Y. and Nakazawa, S., "Quantitative analysis of copper, zinc and copper/zinc ratio in selected human brain tumors," J Neurooncol 16(2), 109-115 (1993).
[17] Powell, L. W., "Diagnosis of hemochromatosis," Semin Gastrointest Dis 13(2), 80-88 (2002).
[18] Powell, L. W., George, D. K., McDonnell, S. M. and Kowdley, K. V., "Diagnosis of hemochromatosis," Ann Intern Med 129(11), 925-931 (1998).
[19] Kapadia, A. J., Tourassi, G. D., Sharma, A. C., Crowell, A. S., Kiser, M. R. and Howell, C. R., "Experimental detection of iron overload in liver through neutron stimulated emission spectroscopy," Phys Med Biol (in review), (2008).
[20] Ivanchenko, V. N., "Geant4 toolkit for simulation of HEP experiments," Nuclear Instruments and Methods in Physics Research Section A 502(2-3), 666-668 (2003).
[21] International Commission on Radiation Units and Measurements, [Photon, electron, proton and neutron interaction data for body tissues.], 46, Bethesda, MD, 1992.
[22] Lange, K. and Carson, R., "EM reconstruction Algorithms for Emission and Transmission Tomography," Journal of Computer Assisted Tomography 8(2), 306-316 (1984).
[23] RSNA, [Radiation Exposure in X-ray Examinations], Available at: http://www.radiologyinfo.org, Last Accessed: (2007).

# Validation of a GEANT4 Simulation of Neutron Stimulated Emission Computed Tomography

Anuj J. Kapadia[a], Brian P. Harrawood[a], Georgia D. Tourassi[a,b]
[a]Duke Advanced Imaging Laboratories, Duke University Medical Center, Durham, NC 27705;
[b]Department of Medical Physics, Duke University, Durham, NC 27705

## ABSTRACT

Neutron stimulated emission computed tomography (NSECT) is being proposed as a non-invasive technique to detect concentrations of elements in the body for diagnosis of liver iron overload. Several experiments have been conducted to investigate NSECT's ability to determine iron concentration in liver tissue and evaluate the accuracy and sensitivity of the system. While these experiments have been successful in demonstrating NSECT's capability of quantifying iron and other tissue elements in-vivo, they have been prohibitively time consuming, often requiring as much as 24 hour acquisitions for accurate quantification. Such extensive scan times limit the use of the experimental system for initial feasibility testing and optimization. As a practical alternative, GEANT4 simulations are being developed to investigate system optimization and aid further progress of the experimental technique. This work presents results of a validation study comparing the results of a GEANT4 simulation with experimental data obtained from a sample of iron. A simulation of the NSECT system is implemented in GEANT4 and used to acquire a spectrum from a simulated iron sample. Scanning is performed with a 7.5 MeV neutron beam to stimulate gamma emission from iron nuclei. The resulting gamma spectrum is acquired and reconstructed using high-purity germanium (HPGe) detectors and analyzed for energy peaks corresponding to iron. The simulated spectrum is compared with a corresponding experimental spectrum acquired with an identical source-detector-sample configuration. Five peaks are detected corresponding to gamma transitions from iron in both spectra with relative errors ranging from 4.5% to 17% for different peaks. The result validates the GEANT4 simulation as a feasible alternative to perform simulated NSECT experiments using only computational resources.

**Keywords:** Neutron, Spectroscopy, Gamma, Iron-overload, NSECT, Tomography, Simulation, GEANT4.

## 1. INTRODUCTION

Neutron stimulated emission computed tomography (NSECT) system is being developed as a technique for non-invasive quantification of elements in the human body [1-5]. It uses inelastic scattering interactions between incident neutrons and target element nuclei to determine the element's spatial distribution and concentration in the body.

NSECT uses the following principle. An incident neutron undergoes inelastic scattering with a target atomic nucleus and excites the nucleus to a higher energy level. The excited nucleus spontaneously decays to a lower energy level and emits characteristic gamma radiation with energy unique to the emitting isotope. Measurement of emitted gamma energy and flux can be used to determine the identity and concentration of the emitting element in the sample. A tomographic image of the element distribution can be created by translation and rotation of the sample.

Such quantitative imaging can be applied for diagnosis of several element related disorders in the human body that are characterized by differences in element concentration between normal and diseased tissue. For example, element concentration differences have been observed in liver iron overload [6, 7], Alzheimer's disease [8, 9], and several cancers including breast [10-12], prostate[13] and brain [14-16]. Detection and quantification of elements can be used to diagnose and monitor these disorders in very early stages.

Several experiments have been performed to investigate NSECT's feasibility in detecting elements in biological tissue[3, 5]. While many of these experiments have been largely successful, they have been prohibitively time consuming. For example, a typical scan to detect iron in the liver requires up to 24 hours of data acquisition. Such extensive scan times deem the experimental system impractical for use during initial feasibility testing and system optimization. System optimization involves simultaneous analysis of several variable acquisition parameters such as neutron flux, number of

Medical Imaging 2008: Physics of Medical Imaging, edited by Jiang Hsieh, Ehsan Samei,
Proc. of SPIE Vol. 6913, 69133H, (2008) · 1605-7422/08/$18 · doi: 10.1117/12.773196

gamma detectors and size of neutron beam. It is impractical to investigate the effect of each of these variables with the physical experimental system due to the prohibitively long scan times involved. Therefore, GEANT4 simulations are being developed as an alternative for NSECT development and optimization without the need for specialized sources and gamma detection hardware. Before a GEANT4 simulation can be used to perform iron overload detection studies, it is important to validate the simulated model against experimentally acquired data. This study presents results from a validation experiment for a GEANT4 simulation of NSECT using a natural iron sample containing $^{56}$Fe.

## 2. METHODOLOGY

A simulation of a clinical NSECT system has been developed in GEANT4, a Monte-Carlo programming toolkit that models high-energy physics interactions between particles and matter over a broad range of energies[17]. GEANT4 is developed and managed by a worldwide collaboration of over 100 scientists in Europe, Russia, Japan, Canada and the United States. It allows precise modeling of interactions between neutrons and a variety of target nuclei at energies of relevance to NSECT. The GEANT4 object-oriented programming package includes a powerful set of random number generators, physics units and constants, and provides all the tools required for detector simulation including geometry, tracking and detector response management.

### 2.1 Simulated Model

The simulated model of the NSECT system contains a mono-energetic neutron source, two high-purity germanium (HPGe) gamma-ray detectors, and a sample of natural iron for validation studies. The model is based on the experimental system which uses a Van-de-Graaff accelerator, HPGe gamma detectors and a tomographic gantry for sample positioning[1, 2].

The simulated neutron source is defined as a mono-energetic neutron gun emitting 7.5 MeV neutrons. The gun is placed at an orientation which ensures that every neutron is incident on the target sample. Neutrons at 7.5 MeV are sufficient to excite several energy states in most elements in the body that are of interest to NSECT. For example, a 7.5 MeV neutron can excite carbon at 4.4 MeV, oxygen at 6.1 MeV and several states in iron at 847 keV, 1039 keV, 1238 keV and 1811 keV.

A detector system with two gamma-ray detectors is used in this simulation study. Each of the two gamma detectors is defined as a solid cylinder of HPGe (100% Ge, density= 5.32 g/cm$^3$) measuring 10 cm in diameter and 9 cm in height and located at ±135 degrees with respect to the incident neutron beam. The ±135 degree locations correspond to regions of maximum gamma emission around the sample from electric quadrupole interactions, which are expected to be dominant at this neutron energy. The detector material is sensitized to record the energy of inelastic scatter gamma-rays that are incident on each detector volume.

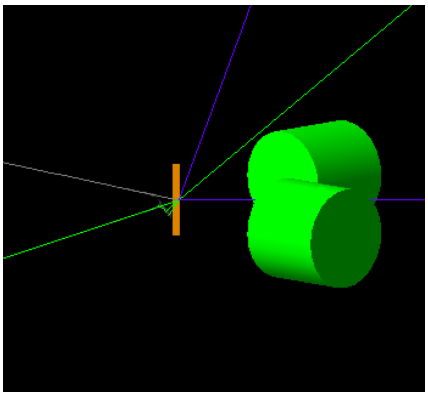

Figure 1. GEANT4 simulation of the NSECT acquisition system. The iron sample is shown in orange with gamma detectors shown as green cylinders. Neutrons enter the system from the right side of the image (blue line). Emitted gamma-rays are shown as green lines while scattered neutrons are seen as blue lines going away from the sample.

The sample in this validation experiment is created as a 3mm thick disc of natural iron containing the three most abundantly found stable isotopes of iron. The circular disc has a 10 cm diameter and 3 mm thickness, natural iron density of 7874 kg/m$^3$, and contains three isotopes of iron in naturally occurring quantities, $^{54}$Fe (5.8%), $^{56}$Fe (91.75%) and $^{57}$Fe (2.45%).

Figure 1 shows the execution of the GEANT4 simulation. The iron sample is shown in orange and gamma detectors are shown as green cylinders. Neutrons enter the system from the right side of the image between the two detectors (depicted by blue lines). Gamma-rays emitted as a result of inelastic scatter are depicted by green lines while scattered neutrons are seen as blue lines going away from the sample. A spectrum is generated from the simulated sample by plotting the gamma counts observed in both detectors vs. the gamma energy.

### 2.2 Experimental Acquisition

A metallic disc of natural iron is scanned with the laboratory NSECT system, which uses a Van-de-Graaff accelerator source, high-purity germanium gamma-ray detectors, and a tomographic gantry to accommodate the sample[1, 2, 4]. Scanning is performed with a 7.5 MeV neutron beam collimated to 1 cm. Two HPGe gamma-ray detectors (with 0.1% energy resolution) located at ± 135 degrees are used to acquire the emitted gamma-rays. An energy spectrum of the gamma emission is generated with a resolution of approximately 1 keV per detector channel. Background correction is performed using the time-of-flight (TOF) correction technique for NSECT[18], where the background noise spectrum is acquired simultaneously and subtracted from the foreground iron signal. The noise-corrected spectrum from natural iron is used for validation of the NSECT system simulated in GEANT4.

### 2.3 Spectral Analysis

Spectral analysis is performed by comparing the simulated and experimental spectra using three criteria: (a) Gamma energy peaks in the simulated spectrum must be observed at energies corresponding to prominent excited state transitions in the target nuclei, (b) Locations of peaks in the simulated spectrum must be in agreement with peak locations in the experimental spectrum, and (c) Number of counts in the peaks must be within reasonable limits of each other.

## 3. RESULTS

Figure 2 and figure 3 show the simulated and experimental spectrum, respectively, from the sample of natural iron. Both spectra show gamma energy peaks for each of the 4 prominent transitions from $^{56}$Fe expected at this neutron energy (847 keV, 1039 keV, 1238 keV and 1811 keV), and from one transition in $^{54}$Fe (1406 keV). The simulated spectrum shows several peaks corresponding to germanium in the detectors (e.g. 834 keV), which are absent in the experimental spectrum due to TOF background correction.

Figure 4 shows the experimental and simulated spectra normalized and overlaid on one another for comparison. As can be seen, the locations and heights of all five gamma energy peaks from iron are in general agreement with each other. Table 1 shows a summary of the differences observed between the two spectra.

| Element | Energy (keV) | Simulated counts (Normalized) | Experimental counts (Normalized) | Difference (%) |
|---|---|---|---|---|
| $^{56}$Fe | 847 keV | 1.000 | 1.000 | 0.00% |
| $^{56}$Fe | 1039 keV | 0.098 | 0.088 | 11.61% |
| $^{56}$Fe | 1238 keV | 0.281 | 0.309 | 9.15% |
| $^{54}$Fe | 1406 keV | 0.037 | 0.045 | 16.95% |
| $^{56}$Fe | 1811 keV | 0.083 | 0.045 | 4.50% |

Table 1. Analysis of the simulated and experimental gamma spectra for the natural iron sample. Peaks for 5 energy transitions in $^{56}$Fe and $^{54}$Fe are seen in both spectra. The percent difference in the peak at 1406 keV can be attributed to poor statistics due to the low concentration of $^{54}$Fe in the sample.

All energy peaks except the peak at 1406 keV are within 15% of the corresponding peak heights in the experimental spectrum. The discrepancy in the 1406 keV peak can be attributed to poor statistics due to the low concentration of the $^{54}$Fe isotope in the sample (5.8%). Two energy peaks at 1238 keV and 1811 keV are within 10% of each other. The result suggests that the gamma lines at 847 keV, 1238 keV and 1811 keV may be suitable for quantification experiments.

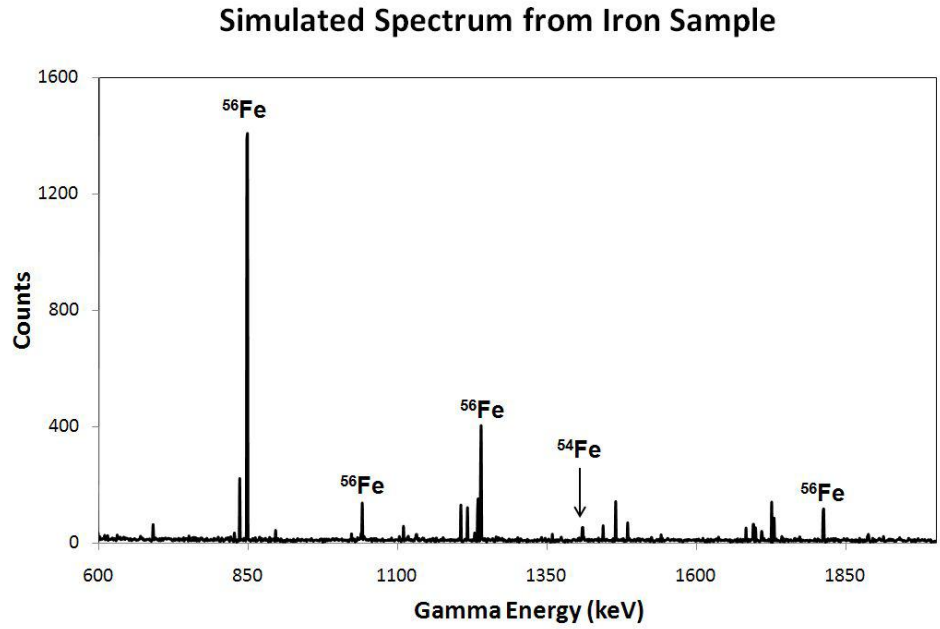


Figure 2. Simulated gamma spectrum for a natural iron sample. Energy peaks corresponding to energy transitions from $^{56}$Fe can be seen at 847 keV, 1039 keV, 1238 keV and 1811 keV and from $^{54}$Fe at 1406 keV. Peaks are also seen for several excited states in germanium, which originate from neutrons scattering onto the HPGe gamma detectors.

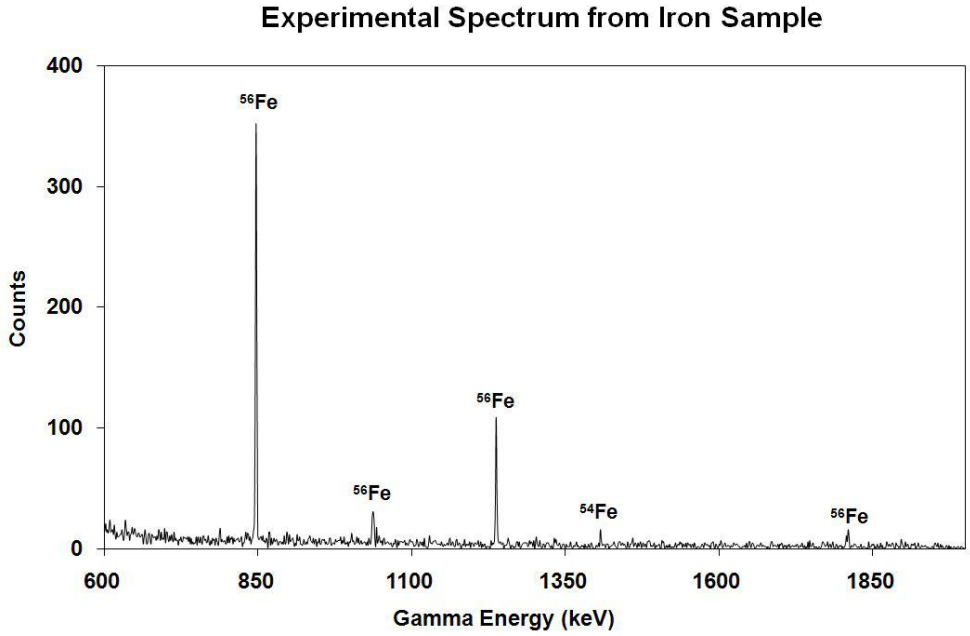


Figure 3. Experimental gamma spectrum for the natural iron sample. Energy peaks are seen from $^{56}$Fe at 847 keV, 1039 keV, 1238 keV and 1811 keV, and from $^{54}$Fe at 1406 keV. Peaks from germanium are absent in this spectrum due to TOF background correction.

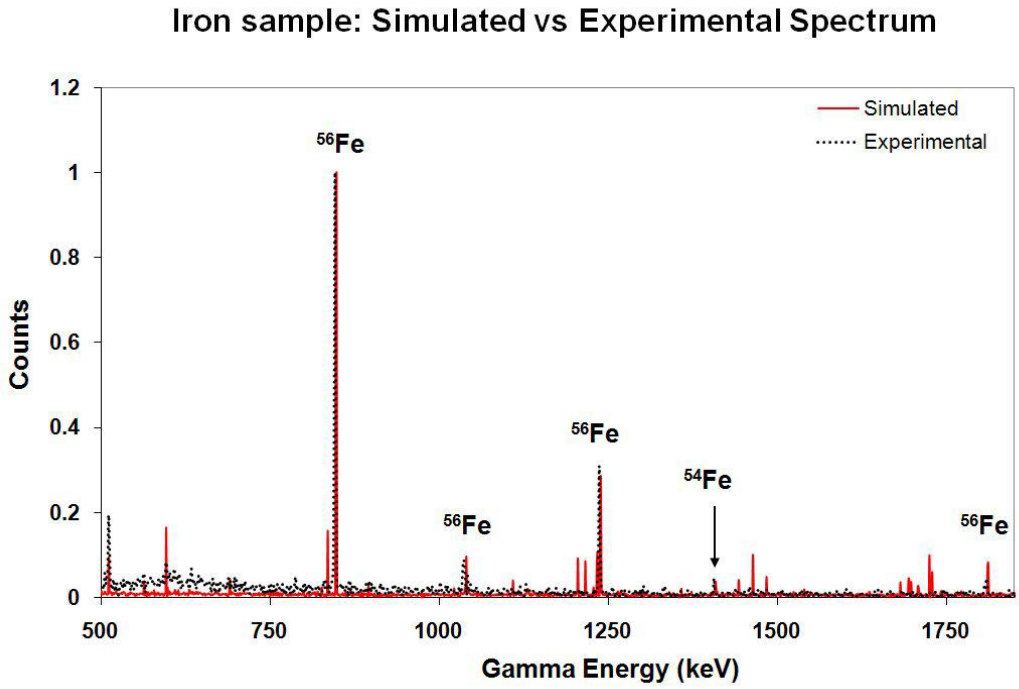


Figure 4. Comparison of simulated and experimental gamma spectra for a natural iron sample. The simulated spectrum is shown as a solid red line, while the experimental spectrum is depicted by an overlaid dotted black line. Energy peaks from all 5 energy transitions in Fe are in excellent agreement with each other. Non-matching energy peaks in the simulated spectrum are due to neutrons scattering onto germanium in the gamma detectors. These peaks are subtracted in the experimental spectrum through TOF background correction.

## 4. CONCLUSION

This work presents successful validation of a Monte-Carlo simulation of the NSECT system. A simulation of the NSECT system has been designed in GEANT4 and validated using a sample of natural iron. Gamma lines from energy transitions in two isotopes of iron ($^{56}$Fe and $^{54}$Fe) are seen in the simulated and experimental spectra. The energies and counts in the gamma are found to be in excellent agreement with each other, showing errors ranging from 4.5% to 17%. The largest error in the system (17.4% for $^{54}$Fe) can be attributed to poor statistics arising from a low isotope concentration in the sample. The result of this study has two important outcomes: (a) It validates the GEANT4 simulation, facilitating its use for future system development and optimization, and (b) It suggests that gamma lines at 847 keV, 1238 keV and 1811 keV may be suitable candidates for investigation in quantification experiments.

## ACKNOWLEDGMENT

We would like to acknowledge the late Carey E. Floyd Jr, who pioneered NSECT and developed it from an experimental idea into a clinically feasibly technique. We would also like to acknowledge Calvin Howell, Alexander Crowell, Matthew Kiser, Anton Tonchev, Anthony Hutcheson and all other contributing members of Triangle Universities Nuclear Laboratory for their help with experimental data acquisition. This work was supported by the Department of Defense (Breast Cancer Research Program) under award number W81XWH-06-1-0484.

## REFERENCES


[1] Floyd, C. E., Jr., Bender, J. E., Sharma, A. C., Kapadia, A., Xia, J., Harrawood, B., Tourassi, G. D., Lo, J. Y., Crowell, A. and Howell, C., "Introduction to neutron stimulated emission computed tomography," Phys Med Biol 51(14), 3375-3390 (2006).

[2] Floyd, C. E., Howell, C. R., Harrawood, B. P., Crowell, A. S., Kapadia, A. J., Macri, R., Xia, J. Q., Pedroni, R., Bowsher, J., Kiser, M. R., Tourassi, G. D., Tornow, W. and Walter, R., "Neutron Stimulated Emission Computed Tomography of Stable Isotopes," in Proceedings of SPIE Medical Imaging, 248-254 (2004).

[3] Kapadia, A. J., Floyd, C. E., Bender, J. E., Howell, C. R., Crowell, A. S. and Kiser, M. R., "Non-invasive quantification of iron 56-Fe in beef liver using neutron stimulated emission computed tomography," in Proceedings of IEEE Nuclear Science Symposium, Medical Imaging Conference, 2232-2234 (2005).

[4] Kapadia, A. J., Sharma, A. C., Bender, J. E., Tourassi, G. D., Howell, C. R., Crowell, A. S., Kiser, M. R., Harrawood, B. P. and Floyd, C. E., "Neutron Stimulated Emission Computed Tomography for Diagnosis of Breast Cancer," IEEE Trans Nuc Sci (in press), (2008).

[5] Kapadia, A. J., Sharma, A. C., Tourassi, G. D., Bender, J. E., Crowell, A. S., Kiser, M. R., Howell, C. R. and Floyd, C. E., "Non-Invasive Estimation of Potassium (39K) in Bovine Liver Using Neutron Stimulated Emission Computed Tomography (NSECT)," in Proceedings of IEEE Nuclear Science Symposium, Medical Imaging Conference, 2076-2078 (2006).

[6] Powell, L., "Hemochromatosis," in [Harrison's Principles of Internal Medicine], edited by D. Kasper, Fawci, AS, Longo, DL, Braunwald, E, Hauser, SL, Jameson, JL, Vol. 2, pp 2298-2303, McGraw Hill, NY, (2005).

[7] Chezmar, J. L., Nelson, R. C., Malko, J. A. and Bernardino, M. E., "Hepatic iron overload: diagnosis and quantification by noninvasive imaging," Gastrointest Radiol 15(1), 27-31 (1990).

[8] Andrasi, E., Farkas, E., Scheibler, H., Reffy, A. and Bezur, L., "Al, Zn, Cu, Mn and Fe levels in brain in Alzheimer's disease," Arch Gerontol Geriatr 21(1), 89-97 (1995).

[9] Bomboi, G., Marchione, F., Sepe-Monti, M., De Carolis, A., Bianchi, V., Medda, E., Pino, A., Bocca, B., Forte, G., D'Ippolito, C. and Giubilei, F., "Correlation between metal ions and clinical findings in subjects affected by Alzheimer's disease," Ann Ist Super Sanita 41(2), 205-212 (2005).

[10] Garg, A., V. Singh, et al., "An elemental correlation study in cancerous and normal breast tissue with successive clinical stages by neutron activation analysis," Biological Trace Element Research 46, 185-202 (1994).

[11] Geraki, K. and Farquharson, M., "Concentrations of Fe, Cu and Zn in breast tissue: a synchrotron XRF study," Phys. Med. Biol 47, 2327-2339 (2002).

[12] Ng, K. H., Bradley, D.A., Looi, L.M., Seman Mahmood, C., Khalik Wood, A., "Differentiation of elemental composition of normal and malignant breast tissue by instrumental neutron activation analysis," Appl. Radiat. Isot. 44(3), 511-516 (1993).

[13] Yaman, M., Atici, D., Bakirdere, S. and Akdeniz, I., "Comparison of trace metal concentrations in malign and benign human prostate," J. Med. Chem. 48, 630-634 (2005).

[14] Civit, T., Houdayer, A. J. and Kennedy, G., "A search for trace elements in some human intracranial tumors by instrumental neutron activation analysis," Biol Trace Elem Res 74(3), 203-210 (2000).

[15] el-Yazigi, A., Al-Saleh, I. and Al-Mefty, O., "Concentrations of zinc, iron, molybdenum, arsenic, and lithium in cerebrospinal fluid of patients with brain tumors," Clin Chem 32(12), 2187-2190 (1986).

[16] Yoshida, D., Ikeda, Y. and Nakazawa, S., "Quantitative analysis of copper, zinc and copper/zinc ratio in selected human brain tumors," J Neurooncol 16(2), 109-115 (1993).

[17] Ivanchenko, V. N., "Geant4 toolkit for simulation of HEP experiments," Nuclear Instruments and Methods in Physics Research Section A 502(2-3), 666-668 (2003).

[18] Floyd, C. E., Sharma, A. C., Bender, J. E., Kapadia, A. J., Xia, J. Q., Harrawood, B. P., Tourassi, G. D., Lo, J. Y., Kiser, M. R., Crowell, A. S., Pedroni, R. S., Macri, R. A., Tajima, S. and Howell, C. R., "Neutron Stimulated Emission Computed Tomography: Background Corrections," Nuclear Instruments and Methods in Physics Research Section B 254, 329 - 336 (2007).

# Detection of Iron Overload with the ORNL Spallation Neutron Source: an MCNPX Simulation Study

Anuj J. Kapadia, Franz X. Gallmeier, Erik B. Iverson and Phillip D. Ferguson

*Abstract*– **In previous work we have demonstrated the use of neutrons to detect iron overload in the liver. We are developing a non-invasive technique to measure liver iron concentration in the human body through neutron inelastic scatter spectroscopy. The measurement is performed using an incident neutron beam that scatters inelastically with iron nuclei in the liver, causing characteristic gamma emission that is used to quantify the tissue iron content. Due to its high neutron flux, the Spallation Neutron Source (SNS) at ORNL presents an attractive option for initial development and optimization of the technique. In this manuscript we describe a simulation study to evaluate feasibility of the SNS beam for iron overload detection in the liver. An MCNPX simulation was developed to model the parameters of the SNS beam and scan a liver phantom with tissue iron content varying from 2 mg/g (mild iron overloaded) to 10 mg/g (severe iron overload). A torso phantom filled with water was placed around the liver and used to simulate scattering effects of the human torso. The emitted gamma spectrum was acquired with a simulated ring detector. Background subtraction was performed by substituting the liver with a water phantom. Background corrected spectra were analyzed to identify gamma lines corresponding to iron in the liver tissue. Statistically significant differences with $p < 0.05$ were identified for the 56Fe gamma line at 847 keV. Counts in the gamma line were found to be higher in the 10 mg/g sample by a factor of 4.72, differing by less than 6% from the expected value of 5. These results demonstrate the feasibility of the SNS beam to determine iron content in liver tissue.**

Manuscript received November 1, 2008. This work was supported by the Department of Defense (Breast Cancer Research Program) under award number W81XWH-06-1-0484 and with funds from the Center for Molecular and Biomolecular Imaging at Duke University.

A. J. Kapadia is with the Department of Biomedical Engineering and the Duke Advanced Imaging Laboratories (DAILabs) of the Department of Radiology, Duke University, Durham, NC 27710, USA (phone: 919-684-1442; fax: 919-684-1491; email: anuj.kapadia@duke.edu).

F. X. Gallmeier is with the Neutron Source Development Group, Spallation Neutron Source, Oak Ridge National Laboratory, Oak Ridge, TN 37831, USA (email: gallmierfz@ornl.gov).

E. B. Iverson is with the Neutron Source Development Group, Spallation Neutron Source, Oak Ridge National Laboratory, Oak Ridge, TN 37831, USA (email: iversoneb@ornl.gov).

P. D. Ferguson is with the Neutron Source Development Group, Spallation Neutron Source, Oak Ridge National Laboratory, Oak Ridge, TN 37831, USA (email: fergusonpd@ornl.gov).

## I. Introduction

LIVER iron overload is a condition that causes serious consequences for the patient through an increase in the body's total iron stores [1]. The excess iron accumulates in several vital organs such as the heart and liver, and may cause extensive tissue damage, liver cirrhosis, cardiac failure, hepatic failure and hepatocellular carcinoma [1, 2]. Definitive diagnosis of iron overload requires an invasive liver-biopsy, an unpleasant procedure with several associated complications including death. In previous work, we have described the use of Neutron stimulated emission computed tomography (NSECT) as a non-invasive technique for iron quantification in the liver [3-6]. The principle of NSECT is briefly described as follows: An incident neutron scattering inelastically with a nucleus of iron in the liver and excites the nucleus to a higher energy state. The excited nucleus is often unstable and therefore rapidly decays to its ground state, emitting a characteristic gamma ray. The energy and flux of the emitted gamma rays can be used to determine the concentration of iron in the liver.

While early experiments demonstrating feasibility of the technique [3, 6-8] have been largely successful, they have been prohibitively time consuming due to the low neutron flux obtained from the Van-de-Graaff accelerator source. NSECT scans with liver samples have often required several hours of scanning per sample. To overcome this limitation of scan time we propose to use a neutron source with significantly higher flux than what has been used thus far. The recently commissioned Spallation Neutron Source (SNS) at Oak Ridge National Laboratory (ORNL) provides an attractive alternative to perform initial system development and optimization due to its significantly higher beam flux. Here we describe a simulation study to evaluate the feasibility of the SNS beam for iron overload detection in the liver.

## II. Motivation

Despite its apparent advantage in flux, the SNS beam presents several parameters with the potential to create practical challenges in performing iron measurements. First, the SNS source contains a large collimator made of natural iron. While the collimation obtained from this collimator is excellent, neutrons scattering in the iron collimator will be detected concurrently with iron in the liver, thereby interfering with the liver iron measurement. Second, as the SNS beam is non-monochromatic a larger number of nuclear interactions are expected in the sample, significantly increasing the noise

in the spectrum. Third, the lack of microsecond beam pulsing eliminates the possibility of time-of-flight (TOF) background correction of the acquired spectra. This project aims at investigating the feasibility of detecting iron overload with the ORNL SNS beam in the presence of the above-mentioned practical challenges.

## III. Method

To investigate the feasibility of iron overload detection with the SNS we have used Monte-Carlo simulations in MCNPX. MCNPX is a general-purpose Monte-Carlo code for three-dimensional and time dependent modeling of the interaction of particles with matter. It has the ability to model a large number of particles over a wide energy range using the latest nuclear cross-section libraries.

The simulated model consists of 3 parts – (a) SNS Beam Source, (b) Gamma-ray Detectors, and (c) Liver phantom. Fig 1 shows a schematic of the simulated model with the three components. Each component is described below.

### A. SNS Beam Source

The neutron source modeled beam parameters, collimation apparatus, and the acquisition area around the beam. The energy distribution of the neutron beam was based on a source neutron spectrum obtained by simulation of the SNS target system in MCNPX. Neutrons entered the system through a collimator made of natural iron providing a collimated beam measuring 2 inches in diameter. A wall of concrete and steel, which also contained some iron, was used to shield the acquisition room. Beam flux was controlled by selecting the number of neutron events executed in the MCNPX code.

### B. Gamma-ray Detectors

The gamma-ray detectors were modeled as 10 cm thick rings of 100 % pure germanium ($^{70}$Ge density= 5.32 g/cm$^3$). Each detector ring was 10 cm deep and 8 cm thick, and placed 30 cm from the sample at angles of 45 and 135 degrees with respect to the beam. These angles were chosen due to the dominant energy transition in iron exhibiting electric quadrupole distributions, which show local maxima at 45 and 135 degrees. Each ring detector was surrounded on three sides by a 3 inch thick shield of lead. A schematic of the detector is shown in Fig 2. Events recorded in the detectors were time-resolved in 2 microsecond intervals as inelastic-scatter gamma emission signal from iron was expected to arrive in the detectors within 2 microseconds of the neutron pulse. Gamma events were energy-binned at 0.5%, i.e. 5 keV intervals at 1 MeV which is typical of a high-purity germanium detector.

### C. Liver Phantom

The liver phantom was modeled in two parts - a human torso and a liver chamber inside the torso. The torso was modeled as a rectangular box measuring 12 x 10 x 7.5 inches and contained water to model the neutron scatter generated in the human body. The liver was modeled as a rectangular box measuring 15 x 10 x 10 cm and was filled with liver tissue material reported in ICRU report 46 (shown in Table 1). Iron overload in the liver was simulated by varying the concentration of iron to correspond to iron overload reported in patients. Two values were used in this study: 2 mg/g corresponding to mild iron overload, and 10 mg/g corresponding to severe clinical overload.

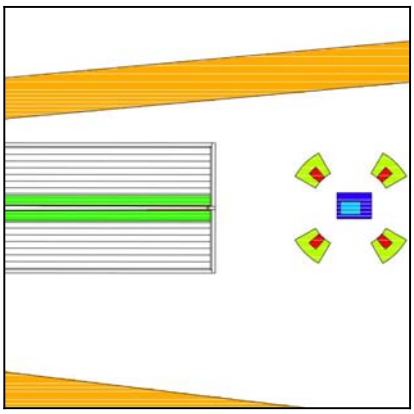

Fig.1. MCNPX simulation of the experiment showing the liver phantom (light blue) inside a water torso (dark blue) with gamma detectors (red) surrounded by a lead shield (light green). Neutrons enter the system from the left through the iron collimator (green tube). The orange bars represent room shielding made of concrete and steel.

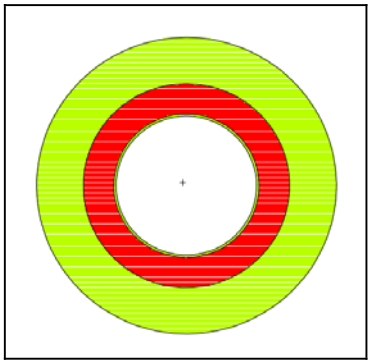

Fig.2. A section through the gamma detector rings. The detector volume (shown in red) is modeled by a germanium ring with 10 cm depth located at 30 cm from the sample. The detector volume is surrounded on three sides by a 3 inch thick lead shield. In the figure, the phantom is placed in the centre of the ring (not seen here as it is outside of the section plane).

The simulation was executed with 1E9 neutron event histories. Gamma spectra were generated for each of the two overload conditions, and counts for energies corresponding to the gamma line from iron at 847 keV were identified and summed. A background noise sample was generated by substituting the liver with water and repeating the scan with the same number of neutron counts used for the liver. The water spectrum was subtracted from the liver signal spectrum to correct for torso-scatter effects and acquisition room effects such as noise signal from iron in the beam collimator and steel walls.

## IV. Results

Figure 3 shows the spectrum from the water sample used to generate an estimate of the spectral background. Prominent

effects observed in the sample include neutron capture on hydrogen (at 2.22 MeV along with single-escape at 1.71 MeV), photon annihilation (511 keV) and inelastic scatter gamma lines from $^{70}$Ge in the detector and $^{208Pb}$ in the detector shield. Additional gamma lines are seen for $^{12}$C in the room and $^{16}$O in the water sample. This spectrum was subtracted from the liver spectra to correct the background effects mentioned.

Figures 4 and 5 show the background corrected gamma spectra from the 2 mg/g and 10 mg/g liver phantoms respectively. Both spectra show gamma lines from $^{12}$C, $^{14}$N, $^{16}$O and $^{56}$Fe in the liver tissues. For both spectra, the gamma line from $^{56}$Fe at 847 keV can be detected above the background with $p \leq 0.05$ (using t-test). In addition, both spectra show some residual background effects after subtraction of the water spectrum.

The ratio of the counts in the 847 keV gamma lines in the two liver samples was measured to obtain an estimate of the quantification error in the system. Table 2 shows a summary of the results. Gamma counts observed in the 10 mg/g sample were found to be a factor of 4.72 higher than the counts in the 2 mg/g sample. This represents an error of less than 6% from the expected value of 5.0 after background correction.

TABLE I
ELEMENTAL COMPOSITION OF THE LIVER PHANTOM (OBTAINED FROM ICRU REPORT 46).

| Element | Normal (%) |
|---|---|
| O | 71.6 |
| C | 13.9 |
| H | 10.2 |
| N | 0.3 |
| P | 0.3 |
| S | 0.3 |
| K | 0.3 |
| Cl | 0.2 |
| Na | 0.2 |
| Fe | 0.0 |
| Density | 1.06 g/cm3 |

TABLE II
RATIO OF COUNTS IN THE 847 KEV GAMMA LINE FROM IRON IN THE TWO LIVER SAMPLES.

| Parameter | Value |
|---|---|
| Counts (10 mg/g) | 6.69E3 |
| Counts (2 mg/g) | 1.42E3 |
| Ratio | 4.72 |
| Expected Ratio | 5.0 |
| Error | 5.53 % |

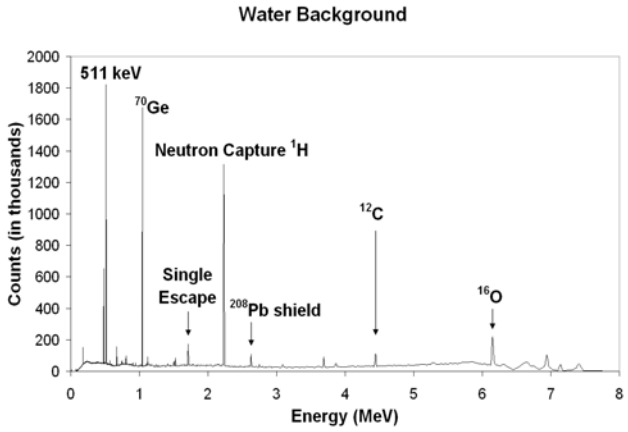


Fig.3. Spectrum corresponding to water phantom with no iron. Gamma lines are observed for $^{12}$C in the room, $^{16}$O in the water, $^{208}$Pb in the shield, $^{70}$Ge in the detector, neutron capture on hydrogen and photon annihilation. This spectrum is used to subtract background effects from the liver spectra.

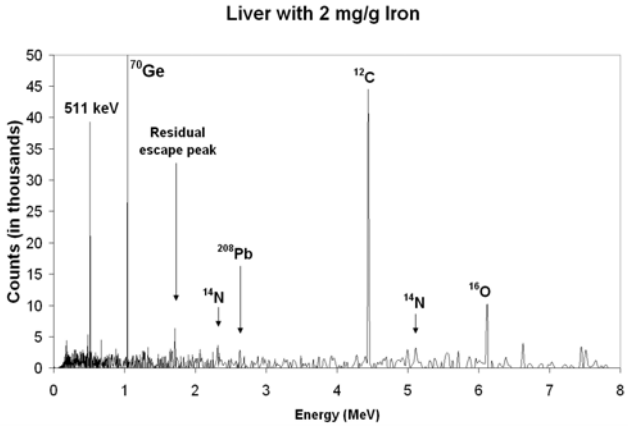


Fig.4. Background corrected spectrum corresponding to an iron overloaded liver with 2 mg/g Fe. Peaks are seen for $^{12}$C, $^{14}$N, and $^{16}$O from the liver tissue and for residual background effects. The peak from $^{56}$Fe is present at 847 keV but is not clearly visible in this figure.

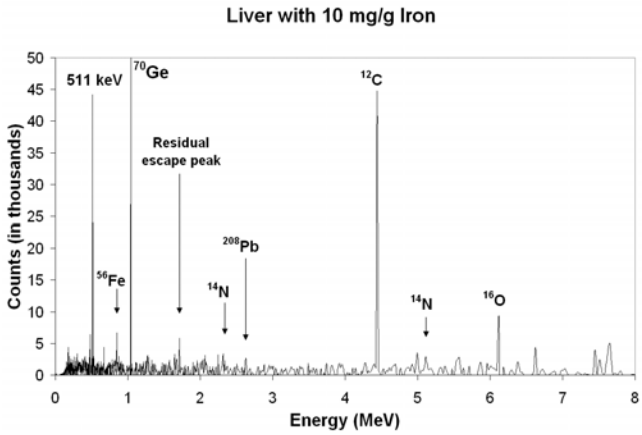


Fig.5. Background corrected spectrum corresponding to an iron overloaded liver with 10 mg/g Fe. Peaks are seen for $^{12}$C, $^{14}$N, $^{16}$O and $^{56}$Fe from the liver tissue and for residual background effects. The peak from $^{56}$Fe is clearly visible in this spectrum.

## V. Conclusion and Future work

The results from this study indicate strong potential for the use of the SNS beam for iron overload detection. Concerns regarding beam parameters such as polychromatic energy, lack of TOF background correction, and strong noise signal from iron collimator are significantly reduced through sample-out background correction. The spectrum from water adequately models and subtracts these background effects.

The results reported here were obtained with only 1E9 neutron events. Typical neutron flux obtained from the SNS is in the range of 1E8 – 1E9 per second for a collimated beam. This observation suggests that it may be possible to perform NSECT experiments with only a few seconds of data acquisition per sample, an enormous improvement over our earlier experiments with 24 – 48 hour acquisitions per sample. Data acquisition experiments using physical samples are currently being planned and will be performed shortly.

## References


[1] L. Powell, "Hemochromatosis," in *Harrison's Principles of Internal Medicine*, 16 ed. vol. 2, D. Kasper, Fawci, AS, Longo, DL, Braunwald, E, Hauser, SL, Jameson, JL, Ed. NY: McGraw Hill, 2005, pp. 2298-2303.

[2] L. W. Powell, "Diagnosis of hemochromatosis," *Semin Gastrointest Dis,* vol. 13, pp. 80-8, Apr 2002.

[3] C. E. Floyd, J. E. Bender, A. C. Sharma, A. J. Kapadia, J. Q. Xia, B. P. Harrawood, G. D. Tourassi, J. Y. Lo, A. S. Crowell, and C. R. Howell, "Introduction to neutron stimulated emission computed tomography," *Physics in Medicine and Biology,* vol. 51, pp. 3375-3390, 2006

[4] A. J. Kapadia, C. E. Floyd, J. E. Bender, C. R. Howell, A. S. Crowell, and M. R. Kiser, "Non-invasive quantification of iron 56-Fe in beef liver using neutron stimulated emission computed tomography," in *IEEE Nuclear Science Symposium, Medical Imaging Conference*, Puerto Rico, 2005 pp. 2232-2234.

[5] A. J. Kapadia, A. C. Sharma, B. P. Harrawood, and G. D. Tourassi, "GEANT4 simulation of an NSECT system for iron overload detection," in *IEEE Nuclear Science Symposium, Medical Imaging Conference*, Honolulu, HI, 2007, pp. 4604 - 4607.

[6] A. J. Kapadia, G. D. Tourassi, A. C. Sharma, A. S. Crowell, M. R. Kiser, and C. R. Howell, "Experimental detection of iron overload in liver through neutron stimulated emission spectroscopy," *Phys Med Biol,* vol. 53, pp. 2633-2649, 2008.

[7] C. E. Floyd, A. J. Kapadia, J. E. Bender, A. C. Sharma, J. Q. Xia, B. P. Harrawood, G. D. Tourassi, J. Y. Lo, A. S. Crowell, M. R. Kiser, and C. R. Howell, "Neutron Stimulated Emission Computed Tomography of a Multi-Element Phantom," *Phys Med Biol,* vol. 53, pp. 2313-2326, 2008.

[8] A. J. Kapadia, A. C. Sharma, J. E. Bender, G. D. Tourassi, C. R. Howell, A. S. Crowell, M. R. Kiser, B. P. Harrawood, and C. E. Floyd, "Neutron Stimulated Emission Computed Tomography for Diagnosis of Breast Cancer," *IEEE Trans Nuc Sci,* vol. 55, pp. 501 - 509, 2008.

# Detection of Iron Overload through Neutron Stimulated Emission Computed Tomography: A Sensitivity Analysis Study

Anuj J. Kapadia[a], Greeshma A. Agasthya[a,b], Georgia D. Tourassi[a,c]
[a]Carl E. Ravin Advanced Imaging Laboratories, Duke University Medical Center, Durham, NC
[b]Department of Biomedical Engineering, Duke University, Durham, NC
[c]Medical Physics Graduate Program, Duke University, Durham, NC

## ABSTRACT

Neutron stimulated emission computed tomography (NSECT) is being developed as a non-invasive technique to diagnose iron overload in the liver. It uses inelastic scatter interactions between fast neutrons and iron nuclei to quantify localized distributions of iron within the liver. Preliminary studies have demonstrated the feasibility of iron overload detection through NSECT using a Monte-Carlo simulation model in GEANT4. The work described here uses the GEANT4 simulation model to analyze iron-overload detection sensitivity in NSECT. A simulation of a clinical NSECT system was designed in GEANT4. Simulated models were created for human liver phantoms with concentrations of iron varying from 0.5 mg/g to 20 mg/g (wet). Each liver phantom was scanned with 100 million neutron events to generate gamma spectra showing gamma-lines corresponding to iron in the liver. A background spectrum was obtained using a water phantom of equal mass as the liver phantom and was subtracted from each liver spectrum. The height of the gamma line at 847 keV (corresponding to $^{56}$Fe) was used as a measure of the detected iron concentration in each background-corrected spectrum. The variation in detected gamma counts was analyzed and plotted as a function of the liver iron concentration to quantify measurement error. Analysis of the differences between the measured and expected value of iron concentration indicate that NSECT sensitivity for detection of iron in liver tissue may lie in the range of 0.5 mg/g – 1 mg/g, which represents a clinically significant range for iron overload detection in humans.

**Keywords:** Neutron, Spectroscopy, Gamma, Iron-overload, NSECT, Tomography, Simulation, GEANT4.

## 1. INTRODUCTION

In previous studies [1-8] we have described the development of neutron stimulated emission computed tomography (NSECT) as a non-invasive technique for quantitative measurement of iron in the human body. Using inelastic scatter spectroscopy, NSECT determines the iron concentration in a target organ by quantitative measurement of gamma radiation emitted from interactions between neutrons and iron nuclei in the organ. The working principle of NSECT for iron overload detection is as follows: Neutrons scattering inelastically with a target iron nucleus in the liver excite the nucleus to a higher energy level stimulating it to emit characteristic gamma radiation. The emitted gamma radiation can be measured to determine the concentration and distribution of iron in the body. A tomographic image can be obtained through translation and rotation of the sample or the beam.

While current NSECT studies have focused primarily on iron-overload detection, it should be mentioned that NSECT has the potential to diagnose several other disorders in the human body that are characterized by differences in element concentration between normal and diseased tissue. For example, element differences have been reported in Alzheimer's disease [9, 10], Wilson's disease [11]and in several cancers including cancer of the breast [12-14], prostate [15] and brain [16-18]. NSECT presents a new potential method of quantifying and diagnosing these element-related disorders through a single non-invasive in-vivo scan. While diagnosis of these disorders is within the abilities of NSECT, given the capabilities of neutron sources and gamma-ray detectors available currently, NSECT exhibits the highest possibility of successful clinical translation for detection of iron-overload in the liver. This study, therefore, focuses on the diagnosis of liver iron overload.

Liver iron overload is a disorder in which the body's total iron stores undergo significant increases due to one of two primary reasons: (a) Hemochromatosis - iron accumulation through increased dietary absorption, or (b) Transfusional Iron Overload - iron accumulation through blood transfusion that form a part of repeated treatment procedures for

chronic disorders such as thalassemia, myelodysplasia and moderate aplastic anemia. While the body possesses well-developed and refined techniques for monitoring and controlling the absorption of dietary iron from food, it lacks a corresponding mechanism to eliminate excess iron in case of overload. The excess iron is accumulated in several vital organs in the body including the liver, heart and spleen, and may lead to extensive tissue damage, liver cirrhosis, cardiac failure, hepatic failure and hepatocellular carcinoma [19-21]. Diagnosis of iron-overload requires accurate measurement of the body's total iron content [19, 20], which is generally estimated using an invasive liver biopsy. Although this diagnostic technique provides excellent measurement accuracy, the discomfort and risks associated with biopsy significantly hinder its acceptance to patients suffering from iron overload disorders. NSECT has the potential to obtain the same measurement through a single non-invasive in-vivo scan without the need for any invasive procedure. It provides an excellent alternative to biopsy with no associated morbidity and only minimal risk from radiation dose.

Preliminary studies using Monte-Carlo simulations have demonstrated the feasibility of clinical NSECT systems for detection of iron overload in the liver. These simulations have also been used to analyze detection accuracy and patient dose for different configurations of the NSECT system [7, 8]. While the results of the simulation studies have demonstrated strong potential for iron overload detection through NSECT, in order for successful clinical translation of the technology it is imperative to analyze the sensitivity limit that can be achieved using currently available source and detector technology. This work investigates the detection sensitivity of an NSECT system in a simulated model of a human liver with iron overload.

## 2. METHODOLOGY

A Monte-Carlo simulation of a clinical NSECT system was designed in GEANT4 - a programming toolkit to model high-energy physics interactions between particles and matter over a broad range of energies [22]. GEANT4 allows precise modeling of a broad range of interactions that occur between neutrons and several target nuclei at energies of relevance to NSECT. In addition, it provides several valuable tools for detector simulation including geometry definition, interaction-tracking and detector response management, making it an ideal tool for investigation of NSECT parameters.

### 2.1 Experimental System

The NSECT simulation developed in this study was modeled after the prototype experimental system, which consisted of a Van-de-Graaff accelerator source, multiple high-purity germanium gamma-ray detectors, and a spectroscopy data acquisition system. Details of the experimental system have been provided in previous work [1, 4, 23]. In the experimental system a monochromatic neutron source (Van-de-Graaff accelerator) was used to generate a mono-energetic beam of neutrons with energy between 4 MeV and 7.5 MeV (typical range of interest to NSECT). Two or more high-purity germanium (HPGe) gamma-ray detectors placed at backward angles of 45 and 135 degrees around the sample were used to detect the emitted gamma-rays and generate gamma energy spectra with energy resolution of 1 keV. The detectors were shielded with a layer of lead (gamma shield) and a layer of borated paraffin wax (neutron shield) for both neutron and gamma effects.

### 2.2 Simulated Model

The simulated NSECT model developed in this study was made up of three modules – (a) Neutron Source, (b) Gamma Detectors, and (c) Liver Phantom. Each module was designed independently and modeled after the corresponding component of the experimental acquisition system. The construction of each module is described below.

#### 2.2.1 Neutron Source

The simulated neutron source was modeled as a finite-width source which produced a 5 MeV mono-energetic neutron beam. The width of the beam was collimated to 1 cm, which is typical of the beam used in NSECT experiments for iron-overload detection. Incident neutron energy was set at 5 MeV as it is sufficient to excite several energy states in iron as well as the first excited state in carbon in the body. The simulated neutron source is shown in Figure 1A as a gray cylindrical object at the lower edge of the image (on the left of the green cylinders).

### 2.2.2 Gamma-ray Detectors

The simulated detector system consisted of an array of six germanium crystals surrounding the liver sample as shown in Figures 1A, 1B and 1C. Although the experimental system typically used 2 to 4 HPGe detectors per acquisition, six detectors were modeled in the simulation to improve detection and computing efficiency. Each of the six detectors was located at 45 degrees and 135 degrees around the sample, corresponding to regions of maximum gamma emission from electric quadrupole interactions around the sample (expected to be dominant in this acquisition). Each detector was modeled as a cylinder of 10 cm diameter and 10 cm height filled with natural density germanium, corresponding to the size and material of the actual HPGe detectors used in NSECT experiments. The detector material was sensitized to track transport of particles through its volume and the energy deposit within the detector.

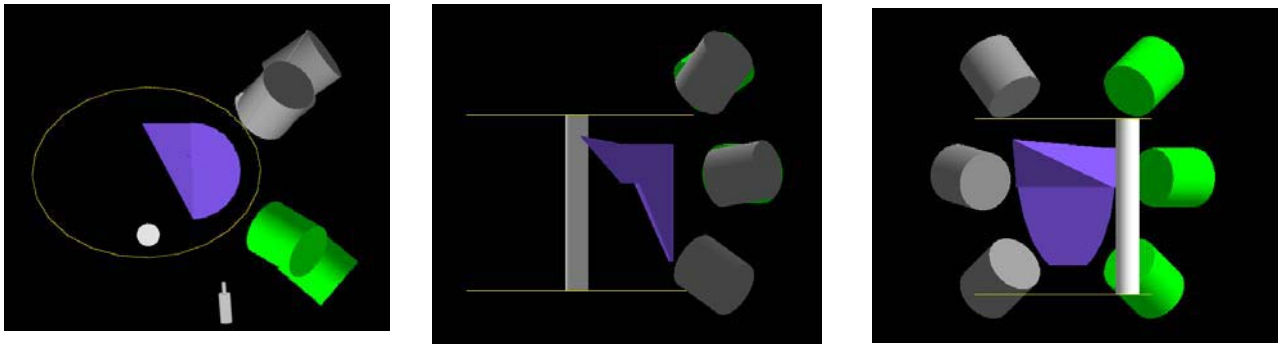

(a) Transverse view (b) Coronal View (c) Sagittal View

Figure 1. GEANT4 simulation of the human liver phantom surrounded by six HPGe detectors. Three views of the phantom are shown. The liver is shown as the blue composite shape housed in an elliptical tube torso (shown by yellow outline). The white cylinder represents the spine. Gamma detectors are shown as green and gray cylinders and are placed at angles of 45 and 135 degrees with respect to the beam. With respect to the geometry in figure 1a, the beam enters the simulation from the lower edge and exits at the upper edge. [Note: This figure is best viewed in color.]

### 2.2.3 Liver Phantom

The liver phantom was designed as a combination of a half-cylinder and two trapezoids as shown in Figure 1. Each of these geometric was simulated individually and then combined to form the composite shape which approximated the shape and volume of an adult human liver. The simulated liver measured 12 cm in height and approximately 1500 $cm^3$ in volume. The liver tissue material was modeled after the tissue composition defined for a healthy adult liver in ICRU Report 46 [24], shown in Table 1. As can be observed in Table 1, normal liver tissue has no significant quantity of iron. Therefore, in order to simulate iron overload conditions, the iron concentration in the liver tissue was artificially increased to correspond to a given degree of iron overload observed in humans. Clinical iron overload is typically defined for iron concentrations ranging from 0.5 mg/g to 6 mg/g (wet) [19, 25], with extreme concentrations up to 10 mg/g reported in certain patients [26, 27]. The liver phantom simulated in this study covers this entire range, simulating iron overload in the following discrete steps: 0.5, 1, 2, 3, 4, 5, 10, 20 mg/g.

The liver sample was placed inside a simulated adult torso modeled as an ellipse with 30 cm major axis and 25 cm minor axis. The torso was filled with water to mimic the elastic scattering properties of tissue. Elastic scatter, which is a significant contributor to noise, has direct implications on the sensitivity of the NSECT system for detection in humans, and is hence an important component of the simulation model.

Finally, a spine was modeled as a cylindrical tube with 5 cm outer diameter and 1 cm inner diameter with material definition of skeletal bone tissue from ICRU Report 46 [24] (shown in Table 2).

Two such phantoms were simulated for this study, one with a torso measuring 30 cm (major axis) and another with a torso measuring 40 cm (major axis). The size of the liver in both models was kept unchanged. The size of the torso in the second model was increased in order to analyze the effect of a larger torso size on iron detection sensitivity (as would be observed in the case of large patients). The two simulated models are shown in Figure 2. The second model was also designed to cover the range of iron-overload in identical discrete steps, i.e. 0.5, 1, 2, 3, 4, 5, 10, 20 mg/g.

Finally, a calibration sample with an iron concentration of 200 mg/g (in aqueous solution) was created to obtain a calibration curve against which the iron concentration measurements in the iron-overload phantoms could be compared.

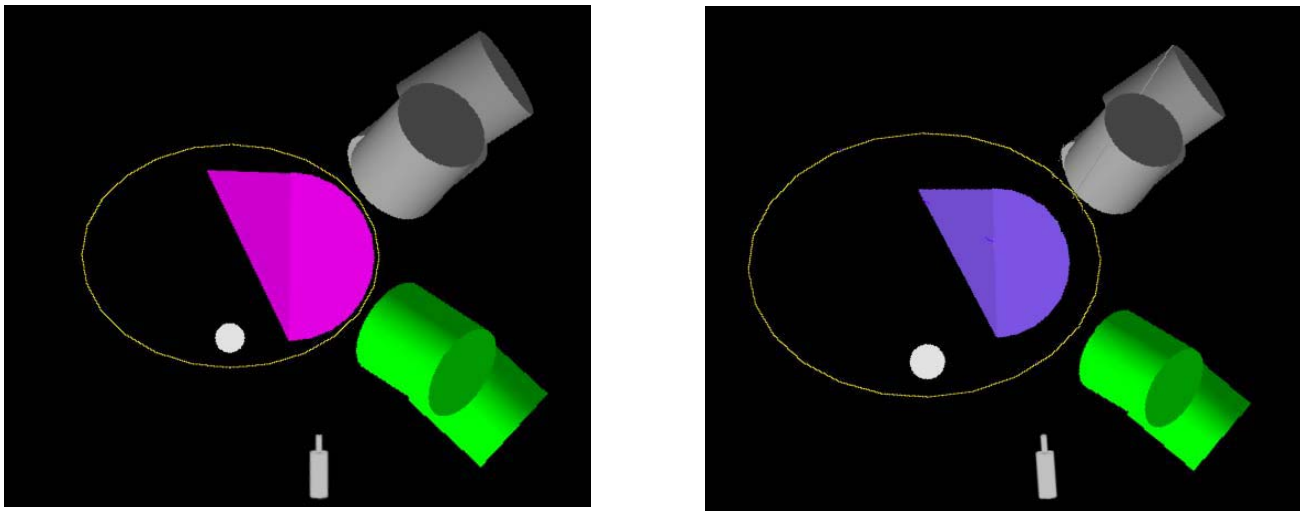

(a) Torso major axis = 30 cm (b) Torso major axis = 40 cm

Figure 2. Simulated liver-torso phantoms with different torso sizes – (a) 30 cm major axis, and (b) 40 cm major axis. The size and volume of the liver in both phantoms is identical. Also visible in the image are the gamma-ray detectors (green and gray cylinders), neutron source and the spine (white circle). [Note: This figure is best viewed in color.]

| **Element** | **O** | **C** | **H** | **N** | **P** | **S** | **K** | **Cl** | **Na** | **Fe** | **Density** |
|---|---|---|---|---|---|---|---|---|---|---|---|
| **Normal (%)** | 71.6 | 13.9 | 10.2 | 3.0 | 0.3 | 0.3 | 0.3 | 0.2 | 0.2 | 0.0 | 1060 kg/m$^3$ |

Table 1. Elemental composition of human liver tissue (obtained from ICRU report 46 [24]).

| **Element** | **O** | **Ca** | **C** | **P** | **N** | **H** | **S** | **Mg** | **Na** | **Density** |
|---|---|---|---|---|---|---|---|---|---|---|
| **Normal (%)** | 43.5 | 22.5 | 15.5 | 10.3 | 4.2 | 3.4 | 0.3 | 0.2 | 0.1 | 1920 kg/m$^3$ |

Table 2. Elemental composition of human skeletal bone (obtained from ICRU report 46 [24]).

### 2.3 Iron concentration measurement

Each liver phantom (i.e. each combination of iron concentration and torso size) was scanned with 100 million neutron events to generate neutron-stimulated gamma emission from the elements present in the simulated phantom. Neutron energy for all scans was maintained at 5 MeV. The emitted gamma-rays were detected in the six HPGe detectors to generate spectra corresponding to each iron overload condition. Background correction for the spectra was performed using a sample-out technique [28, 29], wherein a water phantom was substituted for the liver and scanned to obtain an estimate of background noise. This water phantom was modeled using identical dimensions as the original torso, but contained only water in place of the liver tissue. The phantom was used to obtain an estimate of background effects such as neutron scatter onto the gamma detectors, scatter from components in the acquisition area, and gamma lines arising from neutron capture by hydrogen. These background effects, estimated using the water phantom, were subtracted from the liver-phantom foreground spectra to produce a background corrected spectrum. The resulting background corrected spectra were then analyzed for liver iron content measured through NSECT.

After all iron-overload phantoms had been scanned, the calibration phantom with an iron concentration of 200 mg/g (in aqueous solution) was scanned using 100 million neutron events and background corrected using the same sample-out technique. The calibration phantom was used to establish a ratio of the expected gamma counts and iron concentration

for each phantom. The gamma counts observed in each iron overload measurement were then compared with this ratio to obtain an estimate of the measured iron concentration in the phantom.

For each spectral measurement, the parameter used to compute the measured iron concentration was the number of gamma counts in the gamma line at 847 keV (corresponding to natural iron $^{56}$Fe). The ratio between the iron concentration and the number of gamma counts observed, established with the calibration phantom, was used to determine the measured iron concentration in each of the clinical iron-overload phantoms through a simple comparison. For example, if the 200 mg/g phantom showed 100 counts corresponding to $^{56}$Fe and the overload phantom showed 10 counts in the same gamma line, it could be deduced that the particular overload phantom had a concentration 1/10$^{th}$ of the concentration of the calibration phantom, i.e. 20 mg/g. Using this technique, the iron concentration measured in each iron-overload phantom was determined and compared against its predetermined (simulated) value to obtain an estimate of the difference, i.e. the NSECT measurement error. The trend in observed differences was then used to obtain an estimate of the sensitivity of NSECT for iron overload detection.

### 2.4 Dose Calculation

Following the data acquisition simulations, the total dose delivered through an NSECT scan for 100 million neutrons was calculated as a combination of the neutron and gamma dose by measuring the total energy deposited in the liver and surrounding tissue in the GEANT4 simulation. This technique has been described in detail in several publications [7, 29, 30] and a summary of the calculation is given below:

- Total energy deposited in tissue ($10^7$ neutrons) $\rightarrow$ Measured from GEANT4 simulation (MeV)
- Total energy deposited (J) = Total energy deposited (MeV) x 1.6 x $10^{-13}$ J/MeV
- Absorbed Dose = Total energy deposited / Mass of irradiated tissue
- Effective Dose Equivalent = Absorbed dose x Neutron Q-factor (10) x Liver weighting factor (0.05).

Using this technique, the dose for each 100 million neutron scan with six HPGe detectors was calculated as ~1mSv.

## 3. RESULTS

Figure 3 shows a simulated spectrum from the 5 mg/g iron-overload phantom. Several important gamma lines were observed in the spectrum – $^{56}$Fe at 847 keV, $^{12}$C at 4.4 MeV with two escape peaks, $^{14}$N at 1635 keV and 2312 keV, several states in Ge (from the HPGe gamma detectors) and a residual $^{1}$H gamma line at 2.22 MeV (from neutron capture by hydrogen in water).

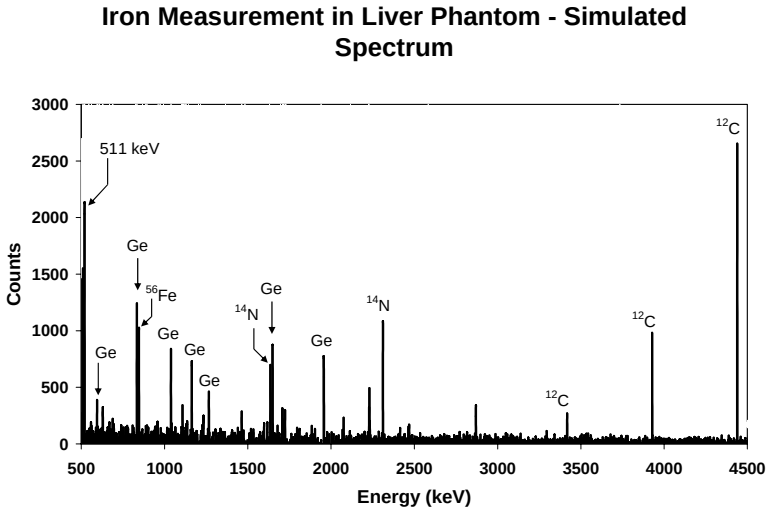


Figure 3. Spectrum corresponding to an iron overloaded liver phantom with 5 mg/g Fe. Gamma lines can be observed for $^{56}$Fe (847 keV), $^{12}$C (4.4 MeV, 3.9 MeV and 3.4 MeV), and $^{14}$N (1635 keV and 2312 keV) in the liver phantom. Also seen are several states in Ge from the HPGe detectors, and a residual gamma line from $^{1}$H (at 2.22 MeV from water in the torso).

As can be seen in Figure 3, after background correction was performed, the gamma line corresponding to iron was clearly visible above background with adequate statistical accuracy ($p \leq 0.001$ measured using a two-tailed t-test for difference of means).

Figures 4 and 5 show the plots of the gamma counts corresponding to the measured and expected iron concentrations in the 30 cm and 40 cm iron overload phantoms, respectively. As can be seen in both figures, the expected and measured counts were found to be in excellent agreement with each other. A summary of the measurement differences observed between the two values is given in Table 3.

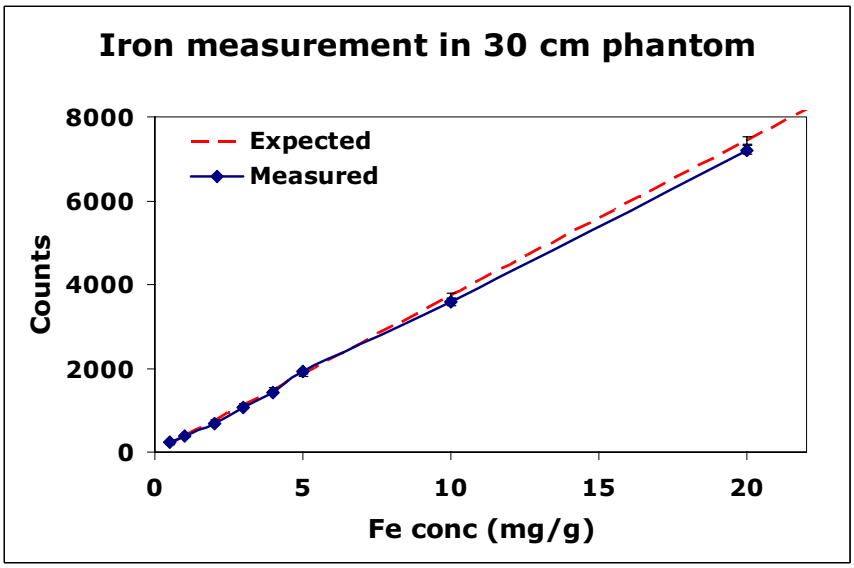


Figure 4. Plot of the gamma counts corresponding to the expected and measured iron concentration in the 30 cm iron overload phantom for the range of iron concentrations studied. The plot corresponding to the expected counts was obtained using the 200 mg/g calibration phantom with the 30 cm torso size.

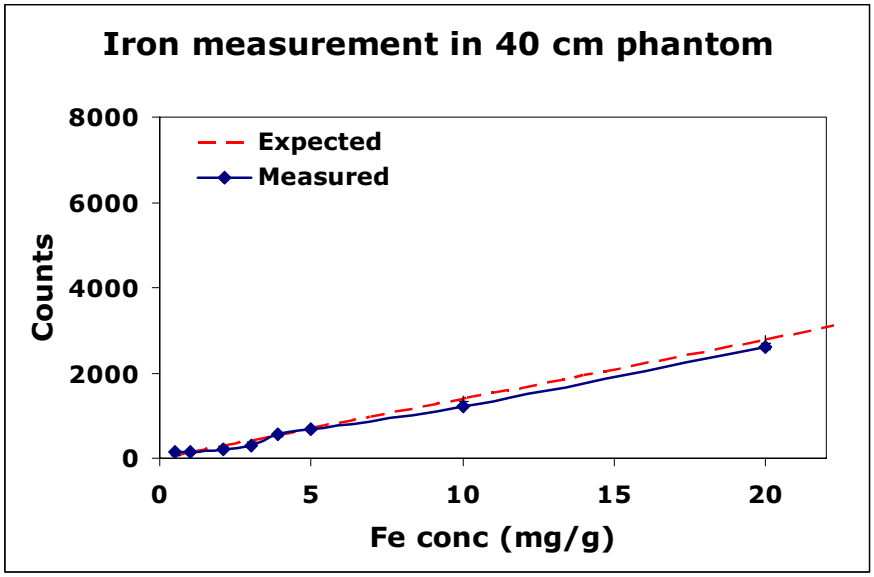


Figure 5. Plot of the gamma counts corresponding to the expected and measured iron concentration in the 40 cm iron overload phantom for the range of iron concentrations studied. The plot corresponding to the expected counts was obtained using the 200 mg/g calibration phantom with the 40 cm torso size.

In addition to the trends between the expected and measured gamma counts in each phantom, it was also observed that gamma counts in the 40 cm torso were approximately a factor of 3 lower than in the 30 cm torso. Since all other parameters in the simulation were maintained constant, this decrease in counts in the larger phantom could be attributed to the increased attenuation and scatter due to the larger torso size. This result is consistent with attenuation calculations corresponding to the larger torso as shown below.

The elastic scatter cross-section for hydrogen for 5.0 MeV neutrons is 1.63 barns, which translates to an attenuation coefficient of $\mu = 0.11$ cm$^{-1}$ (assuming density of 1 g/cm$^3$). Using Beer Lambert's attenuation formula, we have:

$$I_1 = I_0 e^{-\mu . t_1} \text{ and } I_2 = I_0 e^{-\mu . t_2} .$$

A ratio of the two quantities gives:

$$\frac{I_1}{I_2} = e^{-\mu (t_1 - t_2)} \text{, where } \mu = 0.11 \text{ and } (t_1 - t_2) = 10 \text{ cm.}$$

Therefore, the ratio of the expected signal intensity in the two phantoms = 0.33, i.e. the torso with 40 cm major axis is expected to show a factor of 3 lower signal than the torso with major axis 30 cm.

| Iron Concentration (mg/g) | 30 cm | | 40 cm | |
|---|---|---|---|---|
| | Measured conc ± error (mg/g) | Difference (%) | Measured conc ± error (mg/g) | Difference (%) |
| 0.5 | 0.63 ± 0.08 | 26.29% | 1.03 ± 0.18 | 106.75% |
| 1 | 1.00 ± 0.10 | 0.05% | 1.15 ± 0.23 | 14.86% |
| 2 | 1.86 ± 0.14 | 6.90% | 1.58 ± 0.31 | 21.03% |
| 3 | 2.85± 0.18 | 4.88% | 2.22 ± 0.37 | 26.06% |
| 4 | 3.86 ± 0.21 | 3.54% | 4.01 ± 0.44 | 0.14% |
| 5 | 5.19 ± 0.23 | 3.88% | 4.98 ± 0.50 | 0.36% |
| 10 | 9.65 ± 0.32 | 3.46% | 8.72 ± 0.69 | 12.85% |
| 20 | 19.37 ± 0.46 | 3.16% | 18.61 ± 0.98 | 6.93% |

Table 3. Summary of measured iron concentration for the two phantoms along with their difference from the expected concentration value. The difference shows a significant increase between iron concentrations of 1.0 and 0.5 for both sets of phantoms, indicating that the limit of NSECT sensitivity may lie in this range.

## 4. CONCLUSION

This work presents results from a sensitivity analysis study for iron-overload diagnosis in the human body using NSECT. A simulation of the NSECT system was developed and used to scan a set of iron-overload phantoms with degrees of iron overload ranging from mild to severe. Each phantom was scanned with 100 million neutrons corresponding to a dose of 1 mSv, and the iron concentration was determined through a comparison with a high-concentration calibration phantom. The differences between the measured and expected values were found to be consistent for concentrations above 1 mg/g, but were an order of magnitude higher for 0.5 mg/g. This observation indicates that the sensitivity limit for iron-overload detection through NSECT may lie in the range of 0.5 mg/g to 1 mg/g. Consequently, this observation also indicates that NSECT has the potential to accurately quantify iron concentrations above 1 mg/g, which represents a concentration range with high clinical relevance. The results obtained in this study also demonstrate the relationship between attenuation in the torso and the torso size, which suggest the possibility of standardizing iron measurements in patients of different sizes. While the actual value of measured iron concentration will depend on a variety of factors including the torso size, and shape and size of the liver, it may be possible to estimate these parameters (for example through a low dose CT or abdominal x-ray scan for liver shape/size) and include this information in the standardization procedure. Efforts to analyze the effect of liver size on the observed iron signal are currently under way.

## ACKNOWLEDGMENT

This work was supported by the Department of Defense (Breast Cancer Research Program) under award number W81XWH-06-1-0484 and from funds from the Center for Molecular and Biomolecular Imaging at Duke University.

## REFERENCES

[1] Floyd, C. E., Howell, C. R., Harrawood, B. P., Crowell, A. S., Kapadia, A. J., Macri, R., Xia, J. Q., Pedroni, R., Bowsher, J., Kiser, M. R., Tourassi, G. D., Tornow, W. and Walter, R., "Neutron Stimulated Emission Computed Tomography of Stable Isotopes," in Proceedings of SPIE Symposium on Medical Imaging, 248-254 (2004).

[2] Kapadia, A. J., Floyd, C. E., Bender, J. E., Howell, C. R., Crowell, A. S. and Kiser, M. R., "Non-invasive quantification of iron 56-Fe in beef liver using neutron stimulated emission computed tomography," in Proceedings of IEEE Nuclear Science Symposium, Medical Imaging Conference, 2232-2234 (2005 ).

[3] Kapadia, A. J., Sharma, A. C., Tourassi, G. D., Bender, J. E., Crowell, A. S., Kiser, M. R., Howell, C. R. and Floyd, C. E., "Non-Invasive Estimation of Potassium (39K) in Bovine Liver Using Neutron Stimulated Emission Computed Tomography (NSECT)," in Proceedings of IEEE Nuclear Science Symposium, Medical Imaging Conference, 2076-2078 (2006).

[4] Kapadia, A. J., Sharma, A. C., Bender, J. E., Tourassi, G. D., Howell, C. R., Crowell, A. S., Kiser, M. R., Harrawood, B. P. and Floyd, C. E., "Neutron Stimulated Emission Computed Tomography for Diagnosis of Breast Cancer," IEEE Trans Nuc Sci 55(1), 501 - 509 (2008).

[5] Floyd, C. E., Bender, J. E., Harrawood, B. P., Sharma, A. C., Kapadia, A. J., Tourassi, G. D., Lo, J. Y. and Howell, C. R., "Breast cancer diagnosis using Neutron Stimulated Emission Computed Tomography: Dose and Count requirements," in Proceedings of SPIE Symposium on Medical Imaging, 597-603 (2006).

[6] Kapadia, A. J., Tourassi, G. D., Sharma, A. C., Crowell, A. S., Kiser, M. R. and Howell, C. R., "Experimental detection of iron overload in liver through neutron stimulated emission spectroscopy," Phys Med Biol 53, 2633-2649 (2008).

[7] Kapadia, A. J., Harrawood, B. P. and Tourassi, G. D., "GEANT4 simulation of NSECT for detection of iron overload in the liver," in Proceedings of SPIE Symposium on Medical Imaging, 691309 (2008).

[8] Kapadia, A. J., Sharma, A. C., Harrawood, B. P. and Tourassi, G. D., "GEANT4 simulation of an NSECT system for iron overload detection," in Proceedings of IEEE Nuclear Science Symposium, Medical Imaging Conference, 4604 - 4607 (2007).

[9] Andrasi, E., Farkas, E., Scheibler, H., Reffy, A. and Bezur, L., "Al, Zn, Cu, Mn and Fe levels in brain in Alzheimer's disease," Arch Gerontol Geriatr 21(1), 89-97 (1995).

[10] Bomboi, G., Marchione, F., Sepe-Monti, M., De Carolis, A., Bianchi, V., Medda, E., Pino, A., Bocca, B., Forte, G., D'Ippolito, C. and Giubilei, F., "Correlation between metal ions and clinical findings in subjects affected by Alzheimer's disease," Ann Ist Super Sanita 41(2), 205-212 (2005).

[11] Brewer, G., "Wilson Disease," in [Harrison's Principals of Internal Medicine], edited by D. Kasper, Fawci, AS, Longo, DL, Braunwald, E, Hauser, SL, Jameson, JL, Vol. 2, pp 2313-2315, McGraw Hill, NY, (2005).

[12] Garg, A., V. Singh, et al., "An elemental correlation study in cancerous and normal breast tissue with successive clinical stages by neutron activation analysis," Biological Trace Element Research 46, 185-202 (1994).

[13] Geraki, K. and Farquharson, M., "Concentrations of Fe, Cu and Zn in breast tissue: a synchrotron XRF study," Phys. Med. Biol 47, 2327-2339 (2002).

[14] Ng, K. H., Bradley, D.A., Looi, L.M., Seman Mahmood, C., Khalik Wood, A., "Differentiation of elemental composition of normal and malignant breast tissue by instrumental neutron activation analysis," Appl. Radiat. Isot. 44(3), 511-516 (1993).

[15] Yaman, M., Atici, D., Bakirdere, S. and Akdeniz, I., "Comparison of trace metal concentrations in malign and benign human prostate," J. Med. Chem. 48, 630-634 (2005).

[16] Civit, T., Houdayer, A. J. and Kennedy, G., "A search for trace elements in some human intracranial tumors by instrumental neutron activation analysis," Biol Trace Elem Res 74(3), 203-210 (2000).

[17] el-Yazigi, A., Al-Saleh, I. and Al-Mefty, O., "Concentrations of zinc, iron, molybdenum, arsenic, and lithium in cerebrospinal fluid of patients with brain tumors," Clin Chem 32(12), 2187-2190 (1986).

[18] Yoshida, D., Ikeda, Y. and Nakazawa, S., "Quantitative analysis of copper, zinc and copper/zinc ratio in selected human brain tumors," J Neurooncol 16(2), 109-115 (1993).
[19] Powell, L., "Hemochromatosis," in [Harrison's Principles of Internal Medicine], edited by D. Kasper, Fawci, AS, Longo, DL, Braunwald, E, Hauser, SL, Jameson, JL, Vol. 2, pp 2298-2303, McGraw Hill, NY, (2005).
[20] Powell, L. W., "Diagnosis of hemochromatosis," Semin Gastrointest Dis 13(2), 80-88 (2002).
[21] Powell, L. W., George, D. K., McDonnell, S. M. and Kowdley, K. V., "Diagnosis of hemochromatosis," Ann Intern Med 129(11), 925-931 (1998).
[22] Ivanchenko, V. N., "Geant4 toolkit for simulation of HEP experiments," Nuclear Instruments and Methods in Physics Research Section A 502(2-3), 666-668 (2003).
[23] Floyd, C. E., Jr., Bender, J. E., Sharma, A. C., Kapadia, A., Xia, J., Harrawood, B., Tourassi, G. D., Lo, J. Y., Crowell, A. and Howell, C., "Introduction to neutron stimulated emission computed tomography," Phys Med Biol 51(14), 3375-3390 (2006).
[24] International Commission on Radiation Units and Measurements, [Photon, electron, proton and neutron interaction data for body tissues.], 46, Bethesda, MD,, 1992.
[25] Brittenham, G. M. and Badman, D. G., "Noninvasive measurement of iron: report of an NIDDK workshop," Blood 101(1), 15-19 (2003).
[26] Mazza, P., Giua, R., De Marco, S., Bonetti, M. G., Amurri, B., Masi, C., Lazzari, G., Rizzo, C., Cervellera, M., Peluso, A. and et al., "Iron overload in thalassemia: comparative analysis of magnetic resonance imaging, serum ferritin and iron content of the liver," Haematologica 80(5), 398-404 (1995).
[27] Scharfetter, H., Casanas, R. and Rosell, J., "Biological tissue characterization by magnetic induction spectroscopy (MIS): requirements and limitations," IEEE Trans Biomed Eng 50(7), 870-880 (2003).
[28] Floyd, C. E., Sharma, A. C., Bender, J. E., Kapadia, A. J., Xia, J. Q., Harrawood, B. P., Tourassi, G. D., Lo, J. Y., Kiser, M. R., Crowell, A. S., Pedroni, R. S., Macri, R. A., Tajima, S. and Howell, C. R., "Neutron Stimulated Emission Computed Tomography: Background Corrections," Nuclear Instruments and Methods in Physics Research Section B 254, 329 - 336 (2007).
[29] Kapadia, A. J., [Accuracy and Patient Dose in Neutron Stimulated Emission Computed Tomography for Diagnosis of Liver Iron Overload: Simulations in GEANT4]. Dissertation dissertation, Duke University, (2007).
[30] Sharma, A. C., Harrawood, B. P., Bender, J. E., Tourassi, G. D. and Kapadia, A. J., "Neutron stimulated emission computed tomography: a Monte Carlo simulation approach," Phys Med Biol 52(20), 6117-6131 (2007).